NASA TECHNICAL MEMORANDUM

NASA TM X-3424

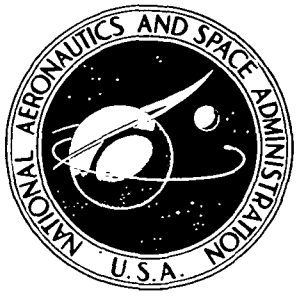

NASA TM X-3424

JET EXHAUST AND SUPPORT INTERFERENCE EFFECTS ON THE TRANSONIC AERODYNAMIC CHARACTERISTICS OF A FIGHTER MODEL WITH TWO WIDELY SPACED ENGINES

William B. Compton III

Langley Research Center
Hampton, Va. 23665

NATIONAL AERONAUTICS AND SPACE ADMINISTRATION • WASHINGTON, D. C. • DECEMBER 1976

1. Report No.	2. Government Accession No.	3. Recipient's Catalog No.
NASA TM X-3424		

4. Title and Subtitle	5. Report Date
JET EXHAUST AND SUPPORT INTERFERENCE EFFECTS ON THE TRANSONIC AERODYNAMIC CHARACTERISTICS OF A FIGHTER MODEL WITH TWO WIDELY SPACED ENGINES	December 1976
	6. Performing Organization Code
7. Author(s)	8. Performing Organization Report No.
William B. Compton III	L-10808
	10. Work Unit No.
9. Performing Organization Name and Address	505-11-41-11
NASA Langley Research Center	11. Contract or Grant No.
Hampton, VA 23665	
	13. Type of Report and Period Covered
12. Sponsoring Agency Name and Address	Technical Memorandum
National Aeronautics and Space Administration	14. Sponsoring Agency Code
Washington, DC 20546	

15. Supplementary Notes

16. Abstract

Jet exhaust, nozzle installation, and model support interference effects on the longitudinal aerodynamic characteristics of a twin-engine fighter model were determined by conducting a wind-tunnel investigation. Realistic jet exhaust nozzle configurations and a reference configuration with a simulated vertical-tail support were tested. Free-stream Mach number was varied from 0.6 to 1.2, and model angle of attack from 0^{o} to 9^{o}. The jet exhaust affected drag more than it affected lift and pitching moment. The largest effects occurred at a Mach number of 0.9 and for the afterburning mode of exhaust nozzle operation. The combined differences between the aerodynamic characteristics of the realistic and reference configurations (which were due to afterbody and nozzle contours, jet operation, and simulated reference support interference) were considerably different from those for the jet interference alone.

17. Key Words (Suggested by Author(s))	18. Distribution Statement
Afterbody drag Jet exhaust effects Jet interference Support interference	Unclassified – Unlimited Subject Category 02

19. Security Classif. (of this report)	20. Security Classif. (of this page)	21. No. of Pages	22. Price*
Unclassified	Unclassified	134	$5.75

*For sale by the National Technical Information Service, Springfield, Virginia 22161

JET EXHAUST AND SUPPORT INTERFERENCE EFFECTS ON THE TRANSONIC AERODYNAMIC CHARACTERISTCS OF A FIGHTER MODEL WITH TWO WIDELY SPACED ENGINES

William B. Compton III
Langley Research Center

SUMMARY

Jet exhaust, nozzle installation, and model support interference effects on the longitudinal aerodynamic characteristics of a twin-engine fighter model were determined by conducting a wind-tunnel investigation. Afterbody configurations representing translating-flap and hinged-flap jet exhaust nozzle configurations were investigated for the jet-off condition and for a wide range of jet pressure ratios. In addition, a reference nozzle configuration was tested with a simulated vertical-tail model support, and with the real vertical tail. The tests were conducted through a Mach number range of 0.6 to 1.2, and with the model at angles of attack of 0° to 9°. The horizontal-tail incidence angle was set at 0°, -5°, and -10°. Free-stream Reynolds number per meter ranged from 10.8×10^6 to 12.4×10^6 depending on the free-stream Mach number and stagnation temperature.

The jet exhaust plume influenced drag more than it influenced lift and pitching moment. The largest jet effects generally occurred at a free-stream Mach number of 0.9 and for the afterburning mode of nozzle operation. The combined differences between the aerodynamic characteristics of the realistic and reference configurations (which were due to afterbody and nozzle contours, vertical tail, jet operation, and simulated reference support interference) were considerably different from those for the jet interference alone. These combined differences were more dependent on angle of attack and horizontal-tail angle and, in the case of drag, were unfavorable.

INTRODUCTION

The result of integrating the propulsion system with the airframe of an advanced fighter airplane has a major influence on the vehicle's performance. This influence, which includes the effects of the interaction between the jet exhaust plume and the complicated flow field near the airplane's afterbody, can affect the aircraft's lift, drag, and thrust. If tail surfaces are located near the jet exhaust nozzles, the stability and control characteristics may also be affected. Therefore, to predict accurately the complete

aerodynamic and performance characteristics of a fighter airplane, tests are conducted on the realistic afterbody with the jet exhaust simulated.

Some earlier work showing the jet effects on the aerodynamic characteristics of general configurations and of typical jet fighter airplanes with closely spaced engines is reported in references 1 to 5. The present investigation was conducted to determine jet exhaust, nozzle installation, and model support effects on the aerodynamic characteristics of a model with widely spaced semipodded engines. The model represented a single seat fighter with a single vertical tail. Two sets of convergent-divergent exhaust nozzles were tested at both normal and afterburner power settings. One set represented a nozzle concept which uses a translating flap to vary geometry, and the other represented a hinged-flap nozzle. The external shapes of the two types were considerably different at the afterburner power settings. Another afterburner and set of nozzles, which represented a flow-through-nacelle model typical of those used in aerodynamic investigations, were also tested. It provided a reference for evaluating nozzle installation and jet effects and was tested both with the regular model vertical tail and with a simulated vertical-tail model support. The simulated vertical-tail support represented a model support technique which would allow aerodynamic tests of complete wind-tunnel models with realistic aft fuselage closure and variations in nozzle geometry.

Tests were made through a Mach number range of 0.6 to 1.2, at angles of attack from 0° to 9°, and for horizontal-tail deflections of 0°, -5°, and -10°. The jet exhaust was simulated with high pressure air and the jet total pressure ratio (ratio of jet total pressure to free-stream static pressure) ranged up to 6.

SYMBOLS

A	area, meters^2
C_D	drag coefficient
$C_{D,a}$	afterbody drag coefficient, $\frac{D_a}{qS}$
$C_{L,a}$	afterbody lift coefficient, $\frac{L_a}{qS}$
$C_{m,a}$	afterbody pitching-moment coefficient, $\frac{M_{Y,a}}{qS\bar{c}}$
$\bar{c}$	mean aerodynamic chord of model wing, meters
D_a	afterbody drag, newtons

d	diameter, meters
F_A	total axial force sensed by balance, newtons
F_a	afterbody axial force, newtons
f	distance from nozzle throat to nozzle exit (see fig. 5), meters
I_A	intercept of bellows pressure tare correction for axial force, meters^2
i	integer
L_a	afterbody lift, newtons
l, m, n	limits of integration
$M_{Y,a}$	afterbody pitching moment, newton-meters
M_∞	free-stream Mach number
p	pressure, newtons/meter^2
q	free-stream dynamic pressure, newtons/meter^2
R	radial distance from nozzle center line to outside contour of nozzle (see figs. 4 and 5), meters
r	radial distance from nozzle center line to inside contour of nozzle (see figs. 4 and 5), meters
S	wing area, meters^2
s_A	slope of bellows pressure tare correction for axial force, meters^2
x	axial distance from nozzle connect station, positive aft (see figs. 4 and 5), meters
x_{cg}	reference point for afterbody moments (see fig. 2)
z	distance from nozzle throat positive aft (see fig. 5), meters

α angle of attack, degrees

β nozzle boattail angle (see figs. 4 and 5), degrees

$\Delta C_{D,a}$ jet exhaust interference on afterbody drag coefficient

$\Delta C_{D,corr}$ difference in drag coefficients between realistic afterbody at scheduled jet pressure ratios and reference afterbody at flow-through jet pressure ratios

$\Delta C_{D,tail}$ difference between drag coefficients for reference afterbody with real tail and with simulated vertical-tail support

$\Delta C_{L,a}$ jet exhaust interference on afterbody lift coefficient

$\Delta C_{L,corr}$ difference in lift coefficients between realistic afterbody at scheduled jet pressure ratios and reference afterbody at flow-through jet pressure ratios

$\Delta C_{L,tail}$ difference between lift coefficients for reference afterbody with real tail and with simulated vertical-tail support

$\Delta C_{m,a}$ jet exhaust interference on afterbody pitching-moment coefficient

$\Delta C_{m,corr}$ difference in pitching-moment coefficients between realistic afterbody at scheduled jet pressure ratios and the reference afterbody at flow-through jet pressure ratios

$\Delta C_{m,tail}$ difference between pitching-moment coefficients for reference afterbody with real tail and with simulated vertical-tail support

δ incidence angle of horizontal tail and inner flap, degrees

ξ nozzle divergence angle (see figs. 4 and 5), degrees

Subscripts:

A axial

a afterbody

b base

corr	correction to reference configuration data for realistic nozzle installation effects
dw	internal divergent wall of supersonic nozzle
e	exit
g	gap
int	internal
j	jet
t	total
tail	tail
th	throat
∞	free stream

APPARATUS AND PROCEDURES

Wind Tunnel

The investigation was conducted in the Langley 16-foot transonic tunnel which is a continuous, single return, atmospheric wind tunnel with an octagonal, slotted test section. The average test-section axial Mach number gradient is less than ± 0.0016 per meter. Measurements of the extent of laminar flow on a highly polished 10° cone indicate a low level of airstream turbulence (ref. 6). Further details of the tunnel can be found in reference 7.

Model

The model represented a single-seat fighter having two widely spaced semipodded engines mounted under the wings and a single vertical tail. For longitudinal control, the horizontal tails rotated together with inner flaps between the engine nacelles and fuselage. The model was supported from the nose by a sting strut, with only the afterbody metric. Figures 1 to 3, respectively, show the model mounted in the tunnel, a three-view drawing of the model, and its general arrangement. A loosely fitting teflon strip inserted into grooves in the metric and nonmetric portions of the model resisted flow through the gap

between these two parts. (See fig. 3.) The jet exhaust for all configurations was simulated with high pressure air. Boundary-layer transition from laminar to turbulent flow was fixed with artificial surface roughness. The grit was applied 1.70 centimeters from the leading edge on two-dimensional surfaces, and 6.35 centimeters from the leading edge on three-dimensional surfaces.

Configurations representing both a translating-flap nozzle and a hinged-flap nozzle in the cruise and afterburning positions were tested. Sketches of these nozzles are presented in figures 4 and 5.

To provide a reference for evaluating the nozzle installation and jet interference effects of the two nozzle concepts, an afterbody typical of those used for wind-tunnel aerodynamic testing was also tested. This configuration had engine nacelles and nozzles (see fig. 6) similar to flow-through configurations. The front of the nacelles was faired over and the jet exhaust was simulated with high pressure air. It also had a simulated vertical-tail model support which was not attached to the model, but fitted into a slot in the afterbody. (See fig. 2.) A fouling circuit indicated when the two were touching. The simulated aerodynamic-test afterbody was also tested with the simulated support removed and the real tail installed on the afterbody. The shape of the engine nacelles was slightly different for each type of nozzle as can be seen from figure 7 which shows cross sections of the model at various stations, and from figure 8 which presents area distributions of the configurations.

The use of a relatively low capacity balance to measure the afterbody drag accurately was desired, and, at the same time, a very small base area at the nozzle exit was needed to closely simulate a real airplane configuration. Therefore, the model was constructed in the following unusual manner. The forward ends of the engines were mounted to the nonmetric part of the model by a gimbal and bellows system. (See fig. 3, detail (a).) This arrangement let the engines swing freely in any direction, but allowed the thrust of the engines to be supported by the nonmetric portion of the model.

The nozzles were made in two pieces: an inner shell, and an outer shell. The outer nozzles attached to the afterbody which was supported by the balance. The inner nozzles attached to the engine plenum chambers, their exits resting inside the exits of the outer nozzles. (See fig. 3.) The surfaces making contact at the nozzle exits were teflon coated to reduce friction. The inner nozzle extended approximately 0.132 centimeter downstream of the outer nozzle to prevent the internal cavity of the model from being pressurized by the jet exhaust. Figure 9 shows the inner and outer pieces of a set of nozzles, and figure 10 shows the assembled set installed on the model. An analysis of the data obtained showed that tunnel vibrations (or deliberately induced vibrations when reference data zeros were being recorded) sensed by the model overcame any static friction forces at the nozzle exit. Thus, errors due to these friction forces were essentially zero.

Test Matrix and General Procedure

Wind-tunnel tests were made on airplane afterbody configurations representing a translating-flap nozzle and a hinged-flap nozzle, and an aerodynamic flow-through reference configuration. The tests were conducted through a Mach number range of 0.6 to 1.2, at angles of attack from 0° to 9°, and for horizontal-tail deflections of 0°, -5°, and -10°. The total pressure of the jet exhaust, which was simulated with high pressure air, ranged up to six times the free-stream static pressure. The free-stream Reynolds number per meter ranged from 10.8×10^6 to 12.4×10^6 depending on the free-stream Mach number and temperature. The blockage of the model and support system was 0.243 percent of the wind-tunnel cross-sectional area.

During a tunnel run, the free-stream Mach number was held constant while a sweep of the desired jet pressure ratios at each angle of attack was made. Data were recorded at discrete values of jet pressure ratio with all test parameters being essentially constant. Approximately five samples of data were recorded within 1 second and averaged at each data point.

Measurements and Instrumentation

The forces and moments on the model afterbody shell were measured by a six-component strain gage balance. To determine the magnitude of pressure tare forces, static pressures were measured internal and external to the metric-gap seal and in the afterbody cavity. When tests were made with the simulated vertical-tail support, pressures were measured on the front and rear faces of the afterbody slot into which the dummy tail fitted. Static pressures were also measured on the walls of the divergent portion of the afterburning nozzles.

The stagnation pressure of the flows simulating the jet exhausts was measured ahead of each nozzle throat with total pressure rakes. Pressures were measured with individual transducers remotely located from the model, and the readings of all quantities were recorded simultaneously.

Data Reduction

The force and moment coefficients on the model afterbody are presented with respect to the model stability axes. The location of the moment center is indicated in figure 2. The balance readings, which indicated the total forces and moments on the model afterbody, were corrected for pressure tare forces at the metric gap and on the inside of the afterbody shell. When applicable, the corrections were also made for the slot for the dummy tail. When the jet was operating, the balance readings were also corrected for bellows tare forces due to pressure differences between the internal and external surfaces of the bellows. (See fig. 3.) For example, afterbody axial force was obtained from the equation:

$$F_a = -F_A - \sum_{i=1}^{n} \left(p_{g,i} - p_\infty\right)A_{g,i} - \sum_{i=1}^{m} \left(p_{int,i} - p_\infty\right)A_{int,i}$$

$$- \sum_{i=1}^{l} \left(p_{b,i} - p_\infty\right)A_{b,i} - \left(s_A \frac{p_{t,j}}{p_{int}} - I_A\right)p_{int}$$

where F_A is the total axial force sensed by the balance. The second and third terms correct for pressure tare forces on the afterbody rim at the metric gap and the interior of the afterbody. The fourth term accounts for the small additional afterbody force which would be present if there were no gap between the external and internal nozzles. (See figs. 3 to 6.) The last term is the bellows tare correction term. The bellows tare correction was usually zero for the axial force and was small for the normal force and pitching moments when compared with the other corrections.

The model angle of attack was assumed equal to the tunnel strut angle. Since the loads measured by the balance did not act on the entire model, but only on the afterbody, a correction for the sting deflection was not made. The error in the model angle of attack caused by failing to make this correction is estimated to be less than 0.2° at the worst conditions.

The skin-friction drag coefficient of the vertical tail was calculated by using the Karman-Schoenherr incompressible formula with the Sommer and Short reference temperature method for compressibility correction. (See refs. 8 and 9.) This skin-friction drag coefficient was then multiplied by the vertical-tail form factor (1.11) to get the vertical-tail drag coefficient at subsonic speeds.

PRESENTATION OF RESULTS

The kinds of incremental forces and moments presented are:

(1) Those due to jet interference on the real afterbodies

$$\Delta C_{D,a} = C_{D,\text{real afterbody at scheduled values of } p_{t,j}/p_\infty} - C_{D,\text{real afterbody jet off}}$$

(2) Those showing the differences between the data for the real afterbodies at scheduled jet pressure ratios, and the reference afterbody at flow-through pressure ratios

$$\Delta C_{D,corr} = C_{D,\text{real afterbody at scheduled values of } p_{t,j}/p_\infty} - C_{D,\text{reference afterbody at flow-through values of } p_{t,j}/p_\infty}$$

The drag of the reference afterbody was measured in the presence of the simulated vertical-tail support, but the drag of the simulated support was not included in the measurements. The real afterbody drag included the drag of the real tail. For drag, a negative increment means favorable jet interference or nozzle installation effects.

(3) A third comparison is made between the afterbody drag of the real afterbody at scheduled jet pressure ratios, and at jet pressure ratios typically obtained with flow-through nacelles. For this comparison only the jet pressure ratio was varied.

RESULTS AND DISCUSSION

Basic Jet Effects

Reference configuration.- Figure 11 presents the basic data for the reference configuration with the simulated vertical-tail support. The data for the reference afterbody with the real vertical tail installed (here the vertical-tail forces are included on the balance) are presented in figure 12. The figures show that the values of the aerodynamic coefficients depend on jet operation, the free-stream Mach number, the model angle of attack, horizontal-tail deflection angle, and the type of vertical tail.

Although the values of the afterbody aerodynamic coefficients for the two configurations are at different levels, the jet effects on the coefficients follow the same trends. In the range of jet pressure ratios presented, which is typical of flow-through nacelles, the most significant effect of the jet exhaust is a reduction in drag from the jet-off condition to the jet-on condition. The magnitude of the reduction, which depended on the free-stream Mach number, was approximately 0.0020 to 0.0035 in drag coefficient. This initial drag reduction did not occur at the supersonic Mach number of 1.2. (See fig. 11(e), for example.) The jet pressure ratios were probably not high enough to separate the boattail flow, and reference 10 indicates that with attached supersonic flow on the boattail, the jet exhaust has very little effect on afterbody pressures.

Generally, the lift and pitching moments were insensitive to jet operation. However, at horizontal-tail (the inner flaps are always included) settings of -5° and -10°, the pitching-moment coefficients did change as much as 0.0007 from the jet-off to the jet-on condition at the subsonic Mach numbers. Jet operation had very little effect on these parameters at a free-stream Mach number of 1.2.

Translating-flap nozzles.- Data for the translating-flap nozzle configurations and hinged-flap nozzle configurations were taken at jet pressure ratios up to real engine

values. The basic data for the translating-flap nozzle in the cruise and afterburning configurations are presented in figures 13 and 14, respectively. Similar to the results for the reference nozzles, the most significant effect of the jet exhaust is a reduction in drag from the jet-off to the jet-on condition. The pressure ratios tested for this nozzle concept were large enough to give the typical drop in afterbody drag as pressure ratio was increased. At scheduled jet pressure ratios (see fig. 15), the jet effects on drag are favorable and range from a drag coefficient reduction of about 0.0010 to 0.0050 depending on the jet pressure ratio, free-stream Mach number, angle of attack, and configuration. The lift and pitching moments were affected very little by the jet exhaust plume with the nozzles in the cruise position. For the afterburning configurations, at the more negative tail angles, lift and pitching moment changed slightly as the jet was turned on.

The following table gives reductions in afterbody drag from the jet-off condition and for ($\alpha = 0^{\circ}$; $\delta = 0^{\circ}$):

M_∞	$C_{D,\text{scheduled } p_{t,j}/p_\infty} - C_{D,\text{same afterbody, jet off}}$		$C_{D,\text{scheduled } p_{t,j}/p_\infty} - C_{D,\text{same afterbody at flow-through } p_{t,j}/p_\infty}$	
	Jet interference	Percent afterbody drag	Jet interference	Percent afterbody drag
Translating-flap nozzles cruise configuration ($\alpha = 0^{\circ}$; $\delta = 0^{\circ}$)				
0.6	-0.0009	-7.6	0.0007	6.0
.8	-.0018	-15.7	.0004	3.5
.85	-.0023	-20.5	.0001	.9
.9	-.0022	-18.2	.0003	2.5
Afterburning configuration				
0.6	-0.0026	-23.6	0.0009	8.3
.8	-.0041	-41.8	-.0005	-5.1
.85	-.0050	-53.8	-.0011	-11.8
.9	-.0044	-41.5	-.0004	-3.8
1.2	-.0030	-10.9	-.0027	-9.8

It also gives the differences between the afterbody drag at scheduled jet pressure ratios and at jet pressure ratios typically obtained with flow-through nacelles. All drags used in calculating the increments were for the translating-flap nozzle afterbody; only the jet pressure ratios varied. The percentages are based on the values of afterbody drag at the scheduled pressure ratios. Based on the jet-off drag, jet effects range from 7.6 percent to 20.5 percent of the cruise nozzle afterbody drag. At $M_\infty = 0.85$ (fig. 14 (c)), jet effects are 53.8 percent of the afterburning nozzle drag. The jet effects are much smaller when they are related to flow-through jet pressure ratios. In this case, the largest listed value of jet interference for the translating-flap cruise nozzles was only 3.5 percent of the afterbody drag at a free-stream Mach number of 0.80. The largest value for the afterburning configuration was 11.8 percent of the afterbody drag at $M_\infty = 0.85$.

Hinged-flap nozzles.- The basic data for the hinged-flap nozzles are presented in figure 16 for the cruise nozzle configuration, and in figure 17 for the afterburning configuration. Generally, the jet exhaust influenced the afterburning nozzle drag less, and the cruise nozzle drag slightly more than it did for the translating-flap configurations. Otherwise jet effects were basically the same as for the translating-flap nozzles. Values of jet interference on afterbody drag for the hinged-flap nozzle configurations were obtained from the data of figures 16 and 17 and are presented in the following table:

M_∞	$C_{D,\text{scheduled } p_{t,j}/p_\infty} - C_{D,\text{same afterbody, jet off}}$		$C_{D,\text{scheduled } p_{t,j}/p_\infty} - C_{D,\text{same afterbody at flow-through } p_{t,j}/p_\infty}$	
	Jet interference	Percent afterbody drag	Jet interference	Percent afterbody drag
Hinged-flap nozzles cruise configuration ($\alpha = 0^\circ$; $\delta = 0^\circ$)				
0.6	-0.0018	-17.1	0.0009	8.6
.8	-.0020	-20.2	.0001	1.0
.85	-.0024	-24.7	-.0003	-3.1
.9	-.0029	-29.6	-.0004	-4.1
Afterburning configuration				
0.6	-0.0018	-16.8	0.0007	6.5
.8	-.0026	-25.7	-.0003	-3.0
.85	-.0030	-30.3	-.0007	-7.1
.9	-.0038	-37.6	-.0008	-7.9
1.2	-.0023	-8.3	-.0021	-7.6

Jet interference related to total airplane drag.- Reference 11 indicates that the afterbody drag of a modern jet fighter is approximately 40 percent of the total airplane drag at zero lift. For efficient cruise, the drag due to lift is approximately equal to the zero lift drag. Using these approximations, one can estimate the ratio of the jet effects to the total cruise drag of the airplane. Sketches (a) and (b), respectively, show these

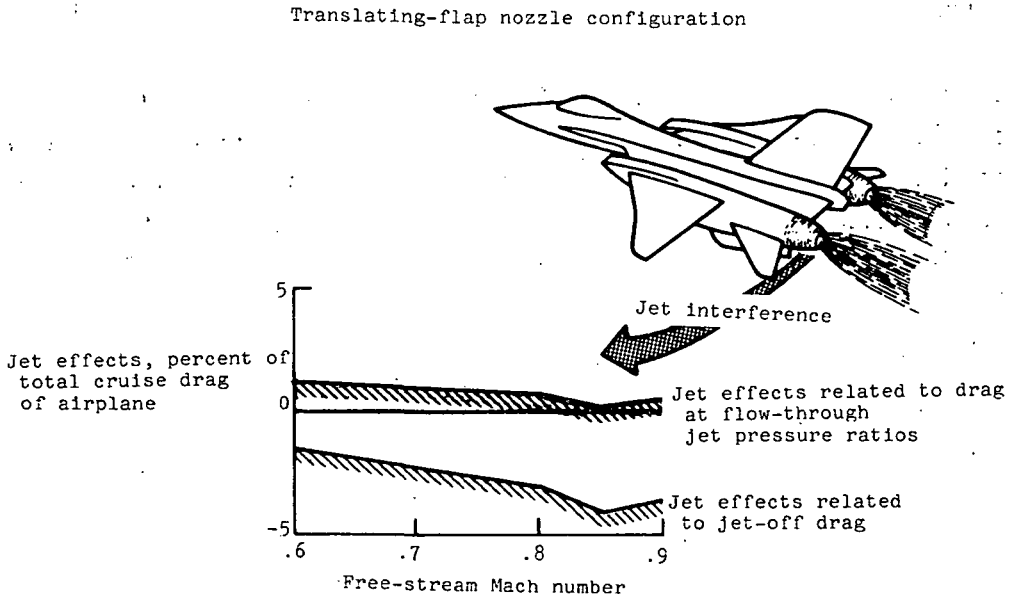

Sketch (a)

Hinged-flap nozzle configuration

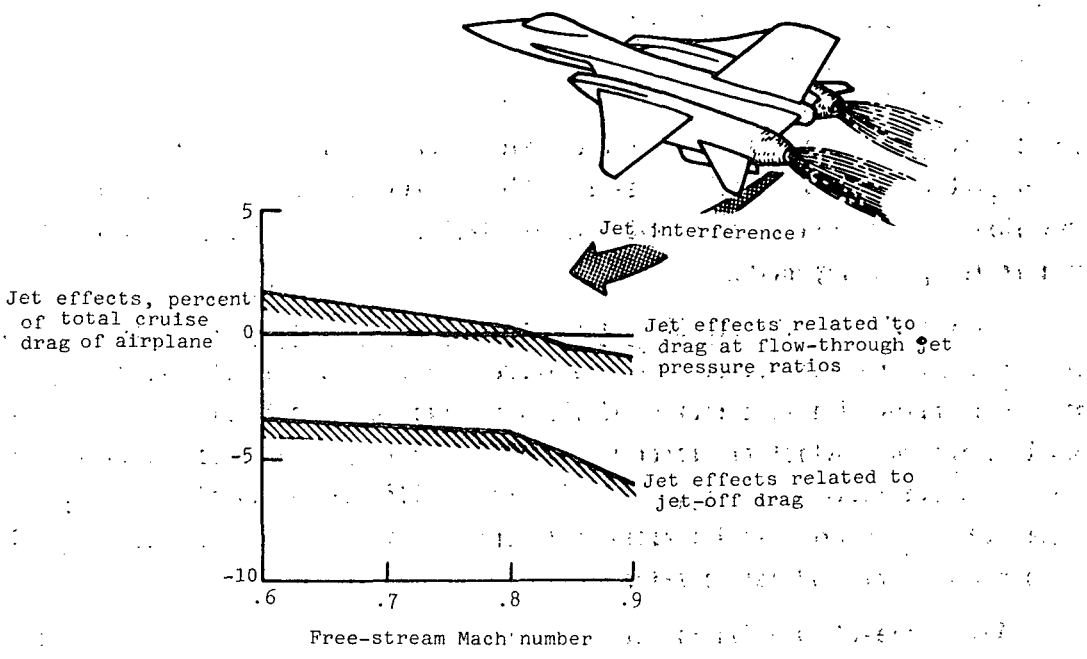

Sketch (b)

estimates for the translating-flap and hinged-flap nozzle configurations. The shaded areas represent a possible reduction in afterbody drag due to hot exhaust effects. (See ref. 12.) Like the preceding tables, all drags used in calculating the increments for each sketch were for the same afterbody; only the jet pressure ratios varied.

The drag increments related to jet-off drag would represent errors in airplane drag due to complete failure to represent the jet exhaust plume during a model test. Those related to the drag at flow-through jet pressure ratios represent errors due to incorrectly simulating the jet exhaust plume. These results indicate that if the afterbody is correctly represented, fairly good estimates of airplane drag at cruise conditions can be obtained with flow-through nacelles. (See ref. 11.) However, they also indicate that the jet exhaust plume should be represented by some means, even if only with flow-through nacelles. This condition applies to theoretical calculations as well as to wind-tunnel investigations.

Parameters Affecting Jet Exhaust Interference

The jet exhaust plume affects the flow over the afterbody by presenting a body which the external flow must negotiate, that is, plume blockage, and by entraining fluid from the the vicinity of the afterbody. The magnitude of these effects on the longitudinal aerodynamic coefficients was determined for specific values of jet pressure ratio obtained from figure 15, a typical fan-jet pressure ratio schedule. These values of jet interference were

related to jet-off values. (For example, see relation $\Delta C_{D,a}$ in the section entitled "Presentation of Results.") Factors affecting the magnitude of these values are discussed below.

Effect of angle of attack on jet interference.- Figure 18 shows the effect of angle of attack on jet interference. Generally, jet effects were insensitive to model angle of attack, especially for the lift and pitching-moment coefficients. For drag, however, there were some exceptions. An example is the translating-flap nozzle in the afterburning position at $M_\infty = 0.6$ and $\delta = -10^\circ$. (See fig. 18(b).) But these isolated instances do not seem to follow a consistent pattern with either Mach number, horizontal-tail deflection angle, or nozzle operating mode.

Effect of free-stream Mach number on jet interference.- Figure 19 shows the effect of free-stream Mach number on jet interference. The absolute value of the jet effects on drag increases with an increase of Mach number in the subsonic speed range. The largest interference, which occurred at $M_\infty = 0.9$, was two to three times its $M_\infty = 0.6$ value, that is approximately $\Delta C_{D,a}$ of -0.002 or -0.005 compared with a $\Delta C_{D,a}$ of -0.001 to -0.003 at $M_\infty = 0.6$. At the supersonic speed, $M_\infty = 1.2$, jet interference dropped off from its maximum absolute value.

With free-stream Mach number, the variation of the jet effects on lift and pitching moment is usually negligible. For a tail incidence angle of -5°, however, these effects sometimes change as much as $|0.01|$ between $M_\infty = 0.6$ and 0.9, and between $M_\infty = 0.9$ and 1.2. Like the case for drag, the largest jet effects occurred at the highest subsonic Mach number 0.9.

Effect of horizontal-tail deflection on jet interference.- Figure 20 shows that the variation of jet interference with horizontal-tail angle is small. Tail deflection influenced jet interference on drag the most, and the largest effects usually occurred for the nozzles in their afterburning positions.

Effect of nozzle operating mode.- The influence of the jet exhaust on all three aerodynamic parameters investigated $\left(C_{D,a}, C_{m,a}, \text{ and } C_{L,a}\right)$ is up to twice as large for the afterburning nozzle configurations as it is for the cruise nozzle configurations. Figure 19 illustrates this effect. In addition, jet interference was more sensitive to free-stream Mach number for the afterburning mode of nozzle operation than it was for the cruise mode of operation. Compare figure 19(a) with figure 19(b) and figure 19(c) with figure 19(d). These effects could possibly be explained in the following manner.

For unseparated internal nozzle flow, the larger exit divergence angles of these afterburning configurations result in higher initial jet plume angles than those for the cruise configurations. Reference 12 demonstrates the importance of the initial jet plume angle in determining the extent of the plume blockage effects on afterbody pressures.

Therefore, the blockage effect of the afterburning nozzle exhaust plume should be greater than that for the cruise nozzle plume.

The plume angle, however, is not the full explanation for the phenomenon. Figures 21 and 22 show results of the hinged-flap afterburning nozzle exhausting into a quiescent atmosphere. They indicate that the jet total pressure ratio must be close to 3 for nonseparated internal flow. An examination of figures 13 to 17 shows that the afterburning configurations are more sensitive to jet operation for both nonseparated and separated internal nozzle flow. Calculations were made by using the results of reference 13. For the translating-flap nozzles, the calculations indicate that the larger initial diameter of the afterburning exhaust plume (see figs. 4 and 5) may be a partial explanation of the increased jet interference at the low pressure ratios. However, in the case of the hinged-flap nozzles, the calculations did not support this explanation. Probably it is a combination of the greater initial plume angle and larger jet plume size that results in the afterburning configurations being more sensitive to jet operation than the cruise configurations.

The increase in jet interference in the afterburning position is more pronounced for the translating-flap nozzles than that for the hinged-flap nozzles. The higher internal divergence angle, 28°, and higher external boattail angle, 14°, of the translating-flap afterburning configuration (compared with 9° and 8° for the hinged-flap afterburning configuration) would lead one to expect these results.

Increments Between Reference and Realistic Configurations

Previously, the jet interference for a configuration has been determined by considering the drag at different values of jet pressure ratio. The increments were computed for a fixed afterbody. In this section of the report, the reference afterbody is used as a baseline for determining drag increment. Figures 23 to 25 show the difference between the longitudinal aerodynamic coefficients of the realistic afterbodies and those of the reference afterbody with the simulated vertical-tail support. (See fig. 2(a).) The real afterbody data and the reference afterbody data used in constructing these figures were obtained, respectively, at the typical fan jet and flow-through pressure ratios in figure 15.

The drag of the simulated vertical-tail support was not measured on the afterbody drag balance. Thus, it represented a support technique which would allow aerodynamic tests of complete wind-tunnel models with realistic aft fuselage closure and variations in nozzle geometry. These differences in figures 23 to 25 would then represent effects of afterbody closure, jet interference based on flow-through-nacelle values of $p_{t,j}/p_{\infty}$, and interference due to this model support technique.

Effect of angle of attack. - The effect of angle of attack on $\Delta C_{D,corr}$, $\Delta C_{m,corr}$, and $\Delta C_{L,corr}$ is shown in figure 23. The real afterbodies usually had higher drag than the reference configuration. The magnitude of this difference generally increased with angle of attack, except for a horizontal-tail deflection angle of -10°, and was a much

stronger function of angle of attack than jet interference. In general, the lift and pitching-moment coefficients varied very little with angle of attack except for the afterburning nozzle positions at a Mach number of 1.2.

Effect of free-stream Mach number.- The differences between the aerodynamic coefficients of the real afterbody configurations and the reference configuration are presented as a function of Mach number in figure 24. The drag coefficient difference generally has a reflex between free-stream Mach numbers of 0.80 and 0.85. For a horizontal-tail angle of 0°, the greatest differences between the drag coefficients of the real and reference afterbodies were on the order of 0.004 to 0.007 and occurred at a Mach number of 1.2. Except for the preceding case, the variation of $\Delta C_{m,corr}$ and $\Delta C_{L,corr}$ with Mach number was usually small. For that case, the absolute magnitudes of $\Delta C_{m,corr}$ and $\Delta C_{L,corr}$ were from 0.005 to 0.020.

Effect of horizontal-tail deflection.- Figure 25 presents $\Delta C_{D,corr}$, $\Delta C_{m,corr}$, and $\Delta C_{L,corr}$ as a function of horizontal-tail deflection. Unlike jet interference, these parameters are generally highly dependent on the horizontal-tail incidence, especially the drag parameter. In some instances, $\Delta C_{D,corr}$ changed as much as 0.004 for a change in tail deflection of 5°, whereas the pitching moment and lift parameters generally changed 0.01 for the same variation in tail angle. Although the individual case depended on free-stream Mach number and model angle of attack, $\Delta C_{m,corr}$ usually had a maximum value at a horizontal-tail deflection between -5° and -10°, for the subsonic Mach numbers.

Effect of simulated vertical-tail support and afterbody shape.- Figures 23 to 25 have presented the differences between the data for the realistic nozzle configurations with the jet operating at scheduled pressure ratios, and the reference configuration with the jet at flow-through pressure ratios. These differences would account for corrections to the data for a similar aerodynamic model. They are due to differences between the jet exhaust plume effects at flow-through and scheduled jet pressure ratios, effect of afterbody contours and vertical tail, and interference of this simulated support system. For drag, there are large differences between these corrections and between pure jet interference. The following table (on next page) shows these differences for a model angle of attack and tail deflection of 0°. The preceding discussions have also pointed out the dependence of these corrections on model angle of attack and horizontal-tail deflection, whereas jet plume effects by themselves (based on the jet-off condition) varied very little with these parameters.

Figures 26 and 27 show the effect of afterbody shape on drag for the jet-off condition and at flow-through jet pressure ratios. Both the realistic and reference afterbodies had the real vertical tail installed. The simulated tail support was not present. At the flow-through pressure ratios, the increments in drag due to afterbody shape were as high as 0.0014 at a Mach number of 0.9. Figure 28 shows increments in afterbody drag due to

Nozzle position	M_∞	$C_{D,\text{scheduled}}\ p_{t,j}/p_\infty - C_{D,\text{same afterbody at flow-through}}\ p_{t,j}/p_\infty$	$C_{D,\text{scheduled}}\ p_{t,j}/p_\infty - C_{D,\text{reference afterbody at flow-through}}\ p_{t,j}/p_\infty$
Translating-flap nozzles ($\alpha = 0^\circ$; $\delta = 0^\circ$)			
Cruise	0.6	0.0007	0.0018
	.8	.0004	.0001
	.85	.0001	.0003
	.9	.0003	.0017
Afterburning	0.6	0.0009	0.0008
	.8	-.0005	-.0010
	.85	-.0011	-.0015
	.9	-.0004	0
	1.2	-.0027	.0044
Hinged-flap nozzles ($\alpha = 0^\circ$; $\delta = 0^\circ$)			
Cruise	0.6	0.0009	0.0003
	.8	.0001	-.0009
	.85	-.0003	-.0012
	.9	-.0004	-.0007
Afterburning	0.6	0.0007	0.0006
	.8	-.0003	-.0007
	.85	-.0007	-.0009
	.9	-.0008	-.0005
	1.2	-.0021	.0044

changing jet pressure ratio from scheduled to flow-through values. For subsonic speeds, the increments varied very little with angle of attack and were generally only of the order of ±0.0005 at the higher Mach numbers. Thus, these figures indicate that at the higher subsonic Mach numbers, $\Delta C_{D,corr}$ is a stronger function of afterbody shape than of precisely matching jet pressure ratio.

Figure 29 shows the differences between the aerodynamic coefficients for the reference afterbody configuration with the real tail installed and with the dummy tail. The drag of the real tail was measured on the afterbody balance, whereas the drag of the dummy tail was not. At the subsonic Mach numbers, these differences generally follow the same trends as the corrections presented in figures 23 to 25, especially for $\Delta C_{D,tail}$ which, like $\Delta C_{D,corr}$, changes with both angle of attack and horizontal-tail deflection angle. This condition suggests that a large part of $\Delta C_{D,corr}$ is due to the removal of the simulated vertical-tail support and installation of the real tail. Included on the plots in figure 29 is the calculated drag of the real vertical tail for the subsonic Mach numbers. The calculated vertical-tail drag does not necessarily have the same value as $\Delta C_{D,tail}$. This condition further suggests that $\Delta C_{D,tail}$ is partially due to differences in the afterbody flow field caused by the presence of the two different vertical tails. Therefore, at subsonic Mach numbers, $\Delta C_{D,corr}$ appears to be mainly due to differences in afterbody configuration and to simulated support interference. The effect of changing jet pressure ratio from flow-through to scheduled values appears to be of less importance.

Comparison of Translating-Flap and Hinged-Flap Nozzles

Figure 30 presents a comparison of the afterbody drag coefficients for the translating-flap and hinged-flap nozzle configurations at a horizontal-tail angle of 0°. At low angles of attack and subsonic Mach numbers, the hinged-flap nozzle configuration generally has the lower drag. However, in choosing a nozzle, the relative thrust of the

two nozzle types and their drags at the mission Mach number and at airplane trim conditions must be considered.

CONCLUSIONS

A wind-tunnel investigation was conducted to determine the jet exhaust, nozzle installation, and support interference effects on the transonic aerodynamic characteristics of a twin-engine air superiority fighter model. In addition to realistic afterbody configurations, a reference configuration was tested with a simulated vertical-tail support, and with the real vertical tail.

1. Results of the investigation indicate that in the range of jet pressure ratios typical of flow-through nacelles, the most significant jet effects occurred from the jet-off to the jet-on conditions. In this range of pressure ratios, jet effects were essentially limited to subsonic Mach numbers.

2. The greatest jet interference usually occurred at a free-stream Mach number of 0.9.

3. When related to jet-off conditions, jet operation decreased the drag of the realistic configurations up to 50 airplane drag counts. When related to values of drag at flow-through jet pressure ratios, jet interference was usually less than 10 drag counts at subsonic Mach numbers. At supersonic Mach numbers, it was on the order of 20 airplane drag counts.

4. Jet interference on the lift and pitching-moment coefficients was limited to small changes which occurred with the change from jet-off to jet-on conditions and was readily apparent only for the afterburning configurations.

5. The interference of the jet exhaust plume on all the aerodynamic parameters was more pronounced with the afterburning nozzle configurations than with the cruise configurations.

6. The combined differences between the aerodynamic characteristics of the realistic and reference configurations (due to afterbody and nozzle contours, jet operation, and the simulated reference support interference) were considerably different than those for the jet interference alone. These combined differences were usually more dependent on angle of attack and horizontal-tail angle and, in the case of drag, were unfavorable. At subsonic speeds, they are attributed mainly to differences in afterbody configuration and to simulated support interference.

Langley Research Center
National Aeronautics and Space Administration
Hampton, VA 23665
September 13, 1976

REFERENCES

1. Pendergraft, Odis C., Jr.; and Schmeer, James W.: Effect of Nozzle Lateral Spacing on Afterbody Drag and Performance of Twin-Jet Afterbody Models With Convergent-Divergent Nozzles at Mach Numbers up to 2.2. NASA TM X-2601, 1972.

2. Lee, Edwin E., Jr.; and Runckel, Jack F.: Performance of Closely Spaced Twin-Jet Afterbodies With Different Inboard-Outboard Fairing and Nozzle Shapes. NASA TM X-2329, 1971.

3. Berrier, Bobby Lee; and Wood, Frederick H., Jr.: Effect of Jet Velocity and Axial Location of Nozzle Exit on the Performance of a Twin-Jet Afterbody Model at Mach Numbers up to 2.2. NASA TN D-5393, 1969.

4. Mercer, Charles E.; and Reubush, David E.: Sting and Jet Interference Effects on Longitudinal Aerodynamic Characteristics of a Twin-Jet, Variable-Wing-Sweep Fighter Model at Mach Numbers to 2.2. NASA TM X-2825, 1973.

5. Berrier, Bobby L.; and Maiden, Donald L.: Effect of Nozzle-Exhaust Flow on the Longitudinal Aerodynamic Characteristics of a Fixed-Wing, Twin-Jet Fighter Airplane Model. NASA TM X-2389, 1971.

6. Dougherty, N. S., Jr.; and Steinle, Frank W., Jr.: Transition Reynolds Number Comparisons in Several Major Transonic Tunnels. AIAA Paper No. 74-627, July 1974.

7. Corson, Blake W., Jr.; Runckel, Jack F.; and Igoe, William B.: Calibration of the Langley 16-Foot Transonic Tunnel With Test Section Air Removal. NASA TR R-423, 1974.

8. Peterson, John B., Jr.: A Comparison of Experimental and Theoretical Results for the Compressible Turbulent-Boundary-Layer Skin Friction With Zero Pressure Gradient. NASA TN D-1795, 1963.

9. Sommer, Simon C.; and Short, Barbara J.: Free-Flight Measurements of Turbulent-Boundary-Layer Skin Friction in the Presence of Severe Aerodynamic Heating at Mach Numbers From 2.8 to 7.0. NACA TN 3391, 1955.

10. Compton, William B., III: Jet Effects on the Drag of Conical Afterbodies at Supersonic Speeds. NASA TN D-6789, 1972.

11. Runckel, Jack F.: Interference Between Exhaust System and Afterbody of Twin-Engine Fuselage Configurations. NASA TN D-7525, 1974.

12. Compton, William B., III: Effects of Jet Exhaust Gas Properties on Exhaust Simulation and Afterbody Drag. NASA TR R-444, 1975.

13. Cahn, Maurice S.: An Experimental Investigation of Sting-Support Effects on Drag and a Comparison With Jet Effects at Transonic Speeds. NACA Rep. 1353, 1958.

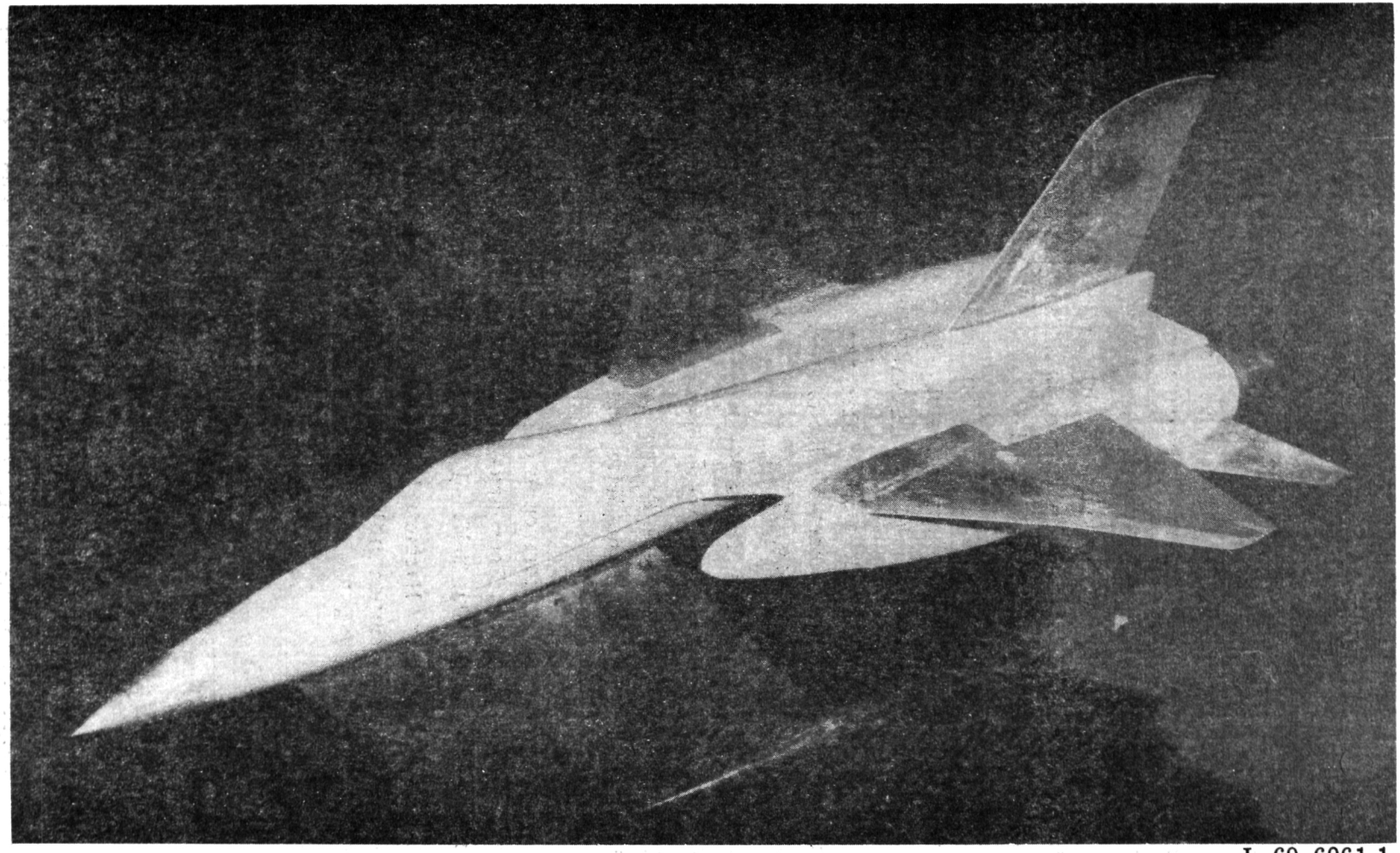

L-69-6061.1

Figure 1.- Model installed in the tunnel. (Realistic afterbody configuration.)

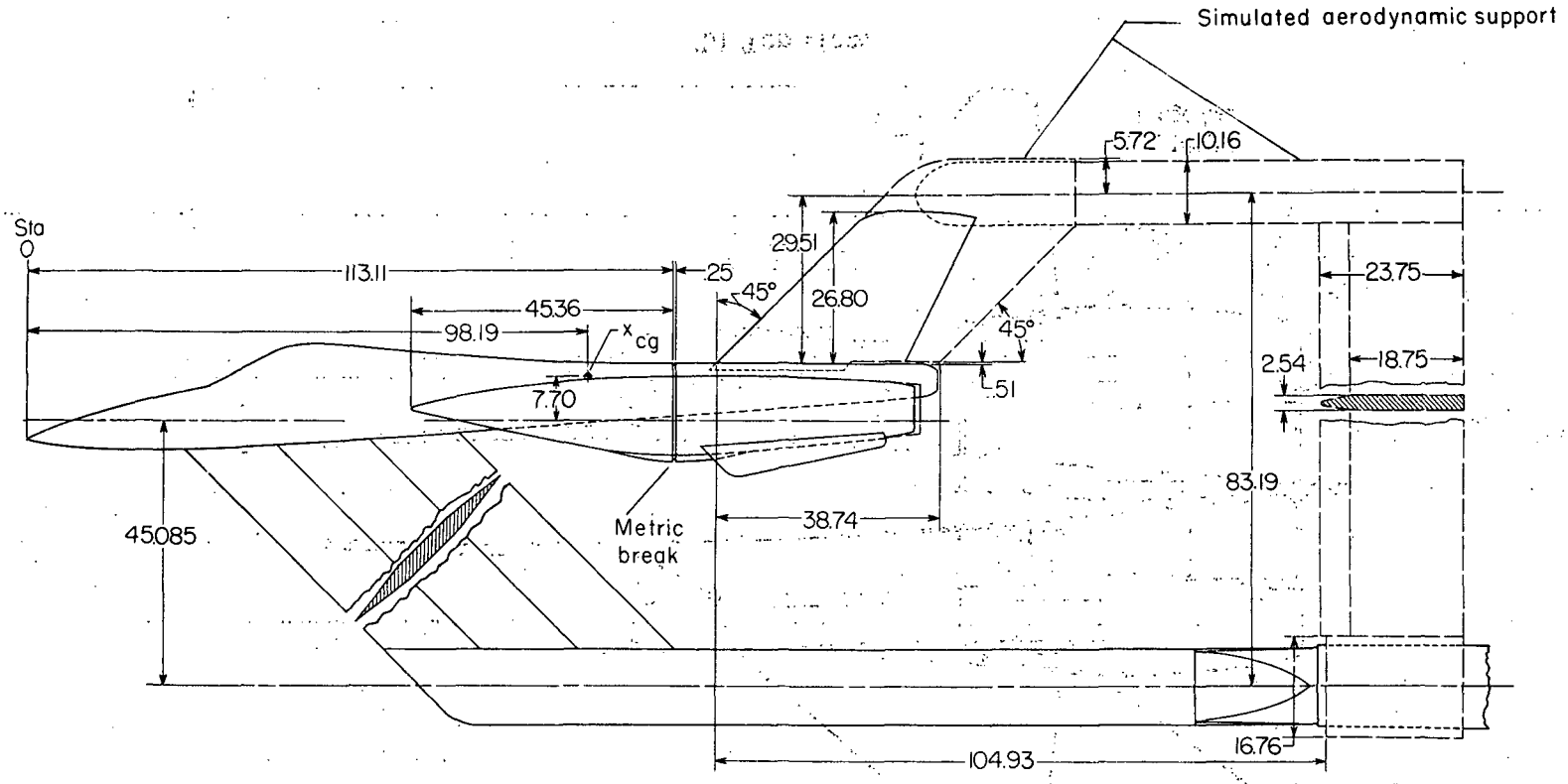

(a) Side view.

Figure 2.- Model and support system. All dimensions are in centimeters unless otherwise noted.

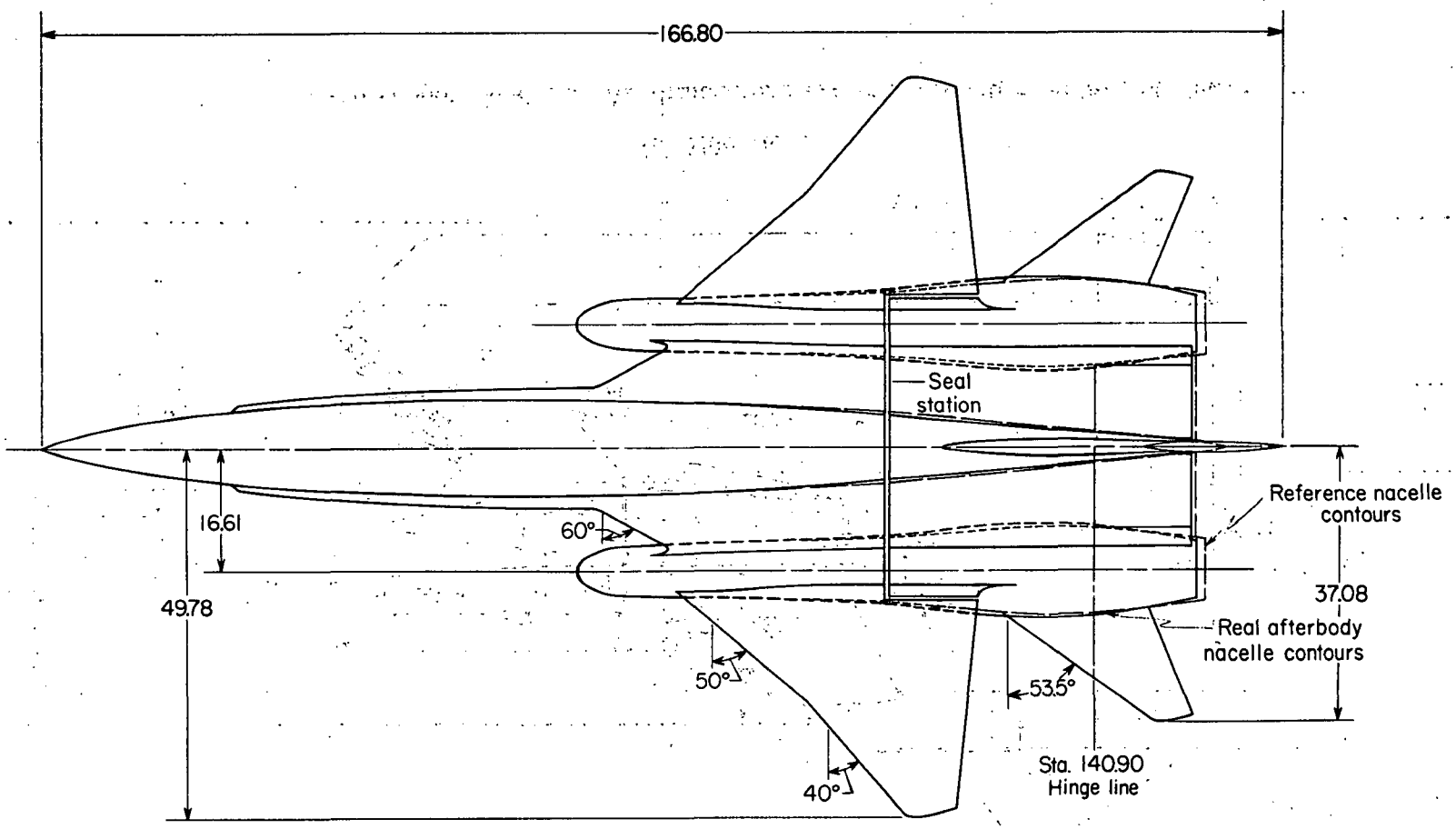

(b) Top view.

Figure 2.- Continued.

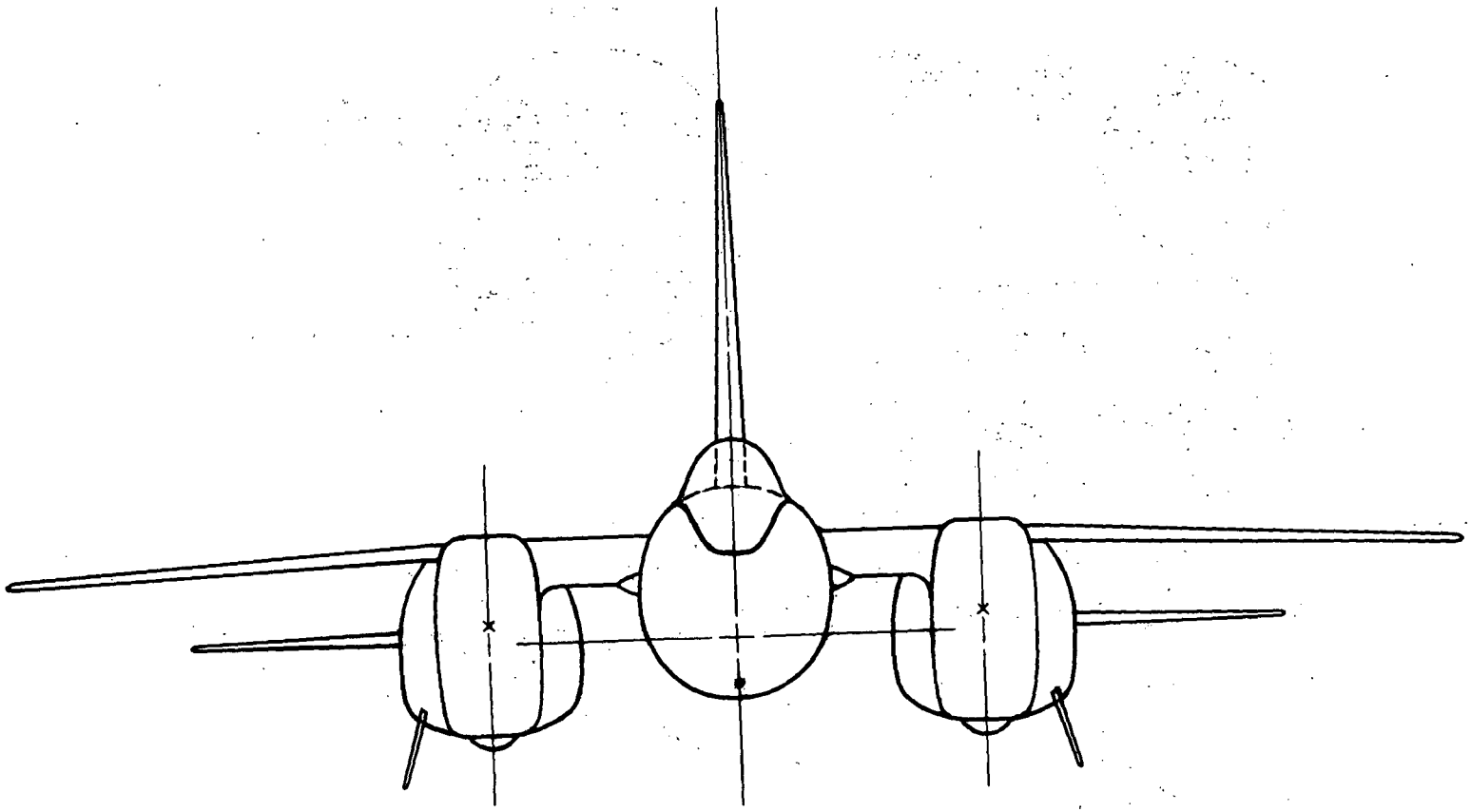

(c) Front view.

Figure 2.- Concluded.

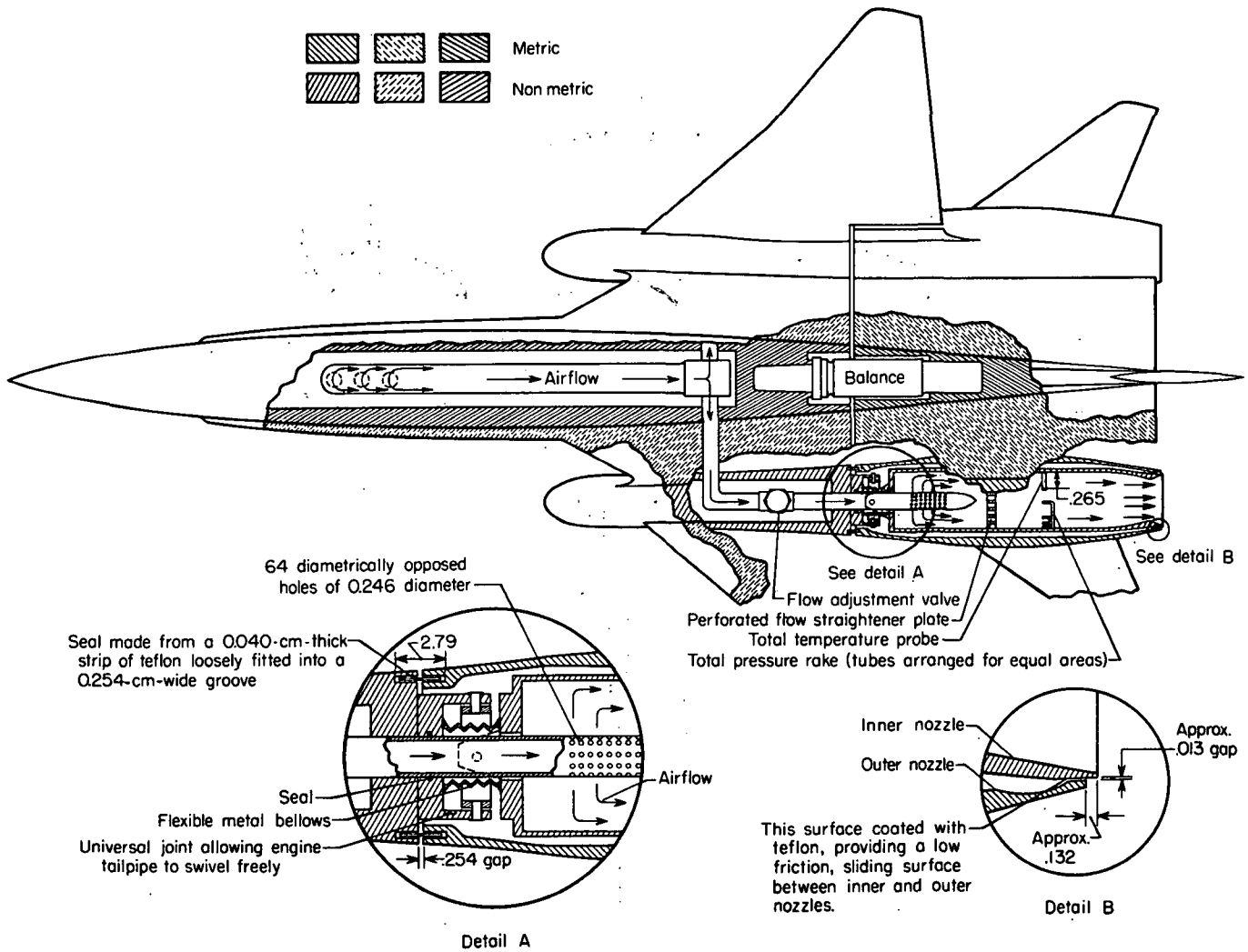

Figure 3.- General arrangement of model. All dimensions are in centimeters unless otherwise noted.

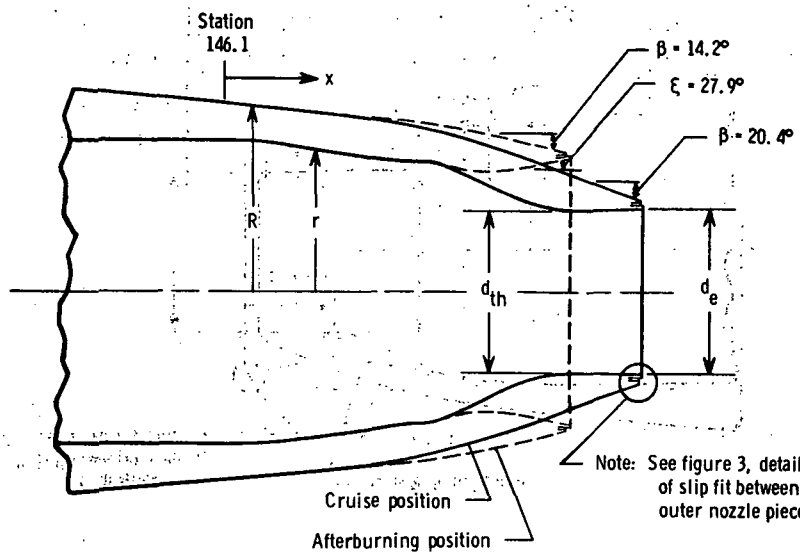

Coordinates					
Cruise position			Afterburning position		
A_{th} = 15.547 ; A_e/A_{th} = 1.095			A_{th} = 34.391 ; A_e/A_{th} = 1.276		
x	R	r	x	R	r
0	5.13		0	5.13	
3.52	4.78		3.52	4.78	
3.71	4.76		3.71	4.76	
3.89	4.74		3.89	4.74	
3.98	4.71		3.93	4.74	
4.38	4.67		4.31	4.72	
4.78	4.60		4.73	7.71	
5.19	4.51	3.58	5.19	4.67	3.58
4.69	4.38	3.58	5.75	4.61	3.58
6.20	4.26	3.42	6.16	4.55	3.46
6.66	4.13	3.24	6.58	4.49	3.37
7.11	3.98	3.04	7.01	4.41	3.33
7.40	3.88	2.90	7.41	4.32	3.31
7.56	↑	2.82	7.44	4.32	3.31
7.97	|	2.62	7.54	↑	3.31
8.39	|	2.47	7.72	Linear	3.32
8.80	|	2.35	7.83	↓	3.34
9.21	Linear	2.26	9.32	3.90	↑
9.38	|	2.24	9.32	3.84	Linear
9.50	|	2.23	9.54	3.79	↓
9.60	|	2.22			3.71
9.67	↓	2.23			
11.28	2.44				
11.44		2.31			

Figure 4.- Translating-flap nozzle. All dimensions are in centimeters unless otherwise noted.

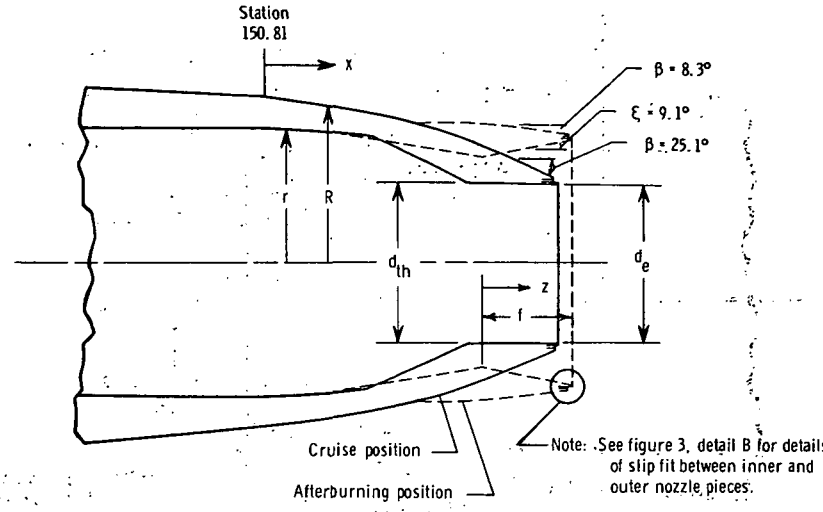

Coordinates	
Hinged-flap nozzle positions	
x	R
-1.34	4.76
.77	4.76
1.13	4.76
1.31	4.75
1.49	4.75
1.85	4.73
2.21	4.70
2.39	4.68
2.57	4.66
2.75	4.64
2.93	4.62
3.11	4.60
3.29	4.57
3.43	4.54
3.66	4.51
3.84	4.47
4.02	4.44
4.20	4.40
4.38	4.36

x	Cruise position A_{th} = 18.840 A_e/A_{th} = 1.017		Afterburning position A_{th} = 33.000 A_e/A_{th} = 1.269	
	R	r	R	r
4.55	4.32			
4.71				
4.76	4.27		4.27	
4.83				
4.92	4.23			
4.97	4.22		4.27	
5.19	4.16		4.27	
5.40	4.10		4.26	
5.61	4.04		4.25	
5.82	3.97		4.23	
6.03	3.90		4.22	
6.24	3.83		4.20	
6.46	3.75		4.18	
6.52		2.45		
6.67	3.67		4.15	
6.77				3.24
6.88	3.59		4.13	
7.09	3.51		4.10	
7.30	3.41		4.06	
7.50	3.33	Linear		
7.51	↑		4.03	
7.52				
7.56	Linear		4.02	Linear
7.60	↓		↑	
9.08	2.59		Linear	
9.17		2.47		
9.21			3.78	
9.27				3.65
9.33				
9.40				

Figure 5.- Hinged-flap nozzle. All dimensions are in centimeters unless otherwise noted.

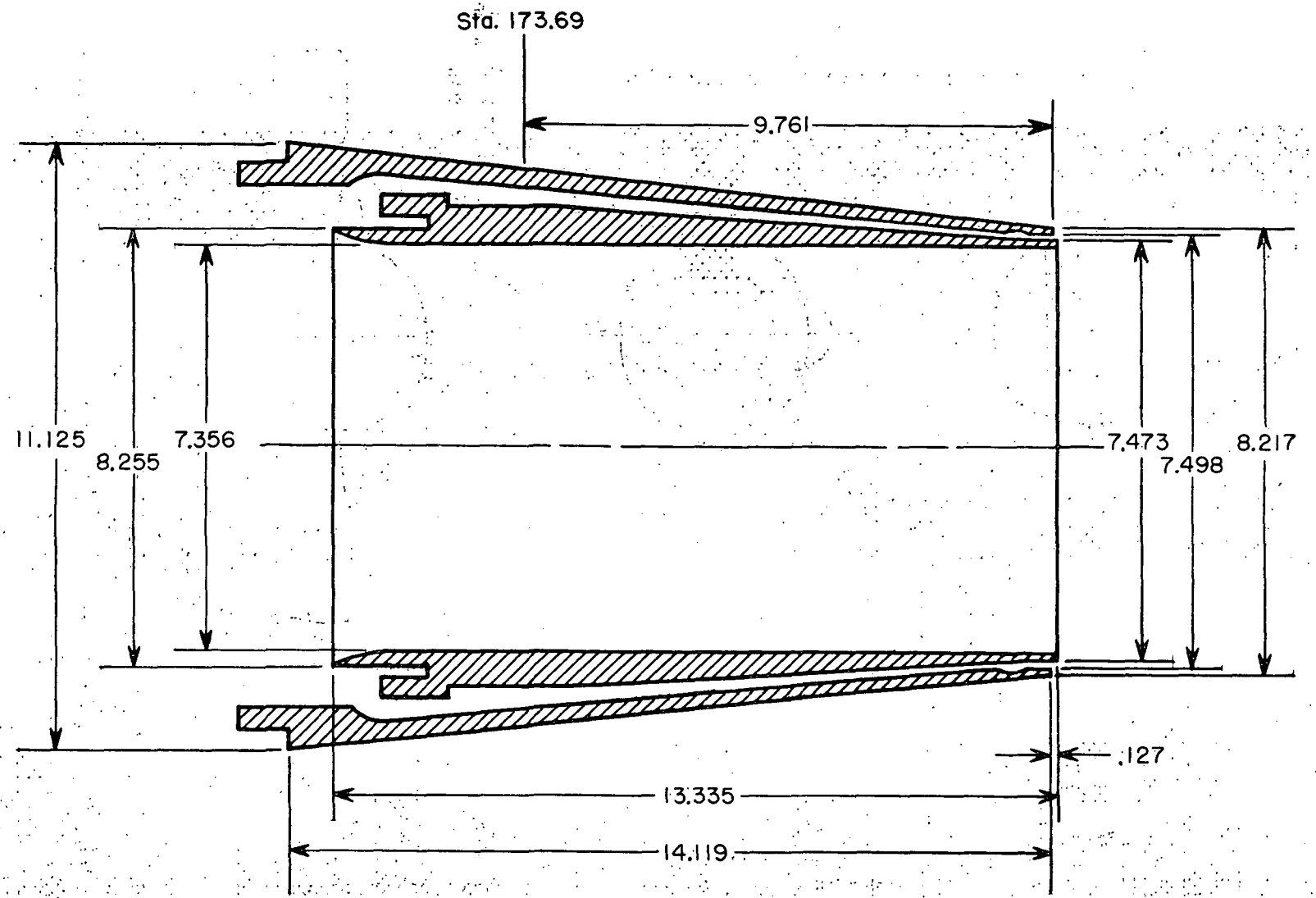

Figure 6.- Reference nozzle. All dimensions are in centimeters unless otherwise noted.

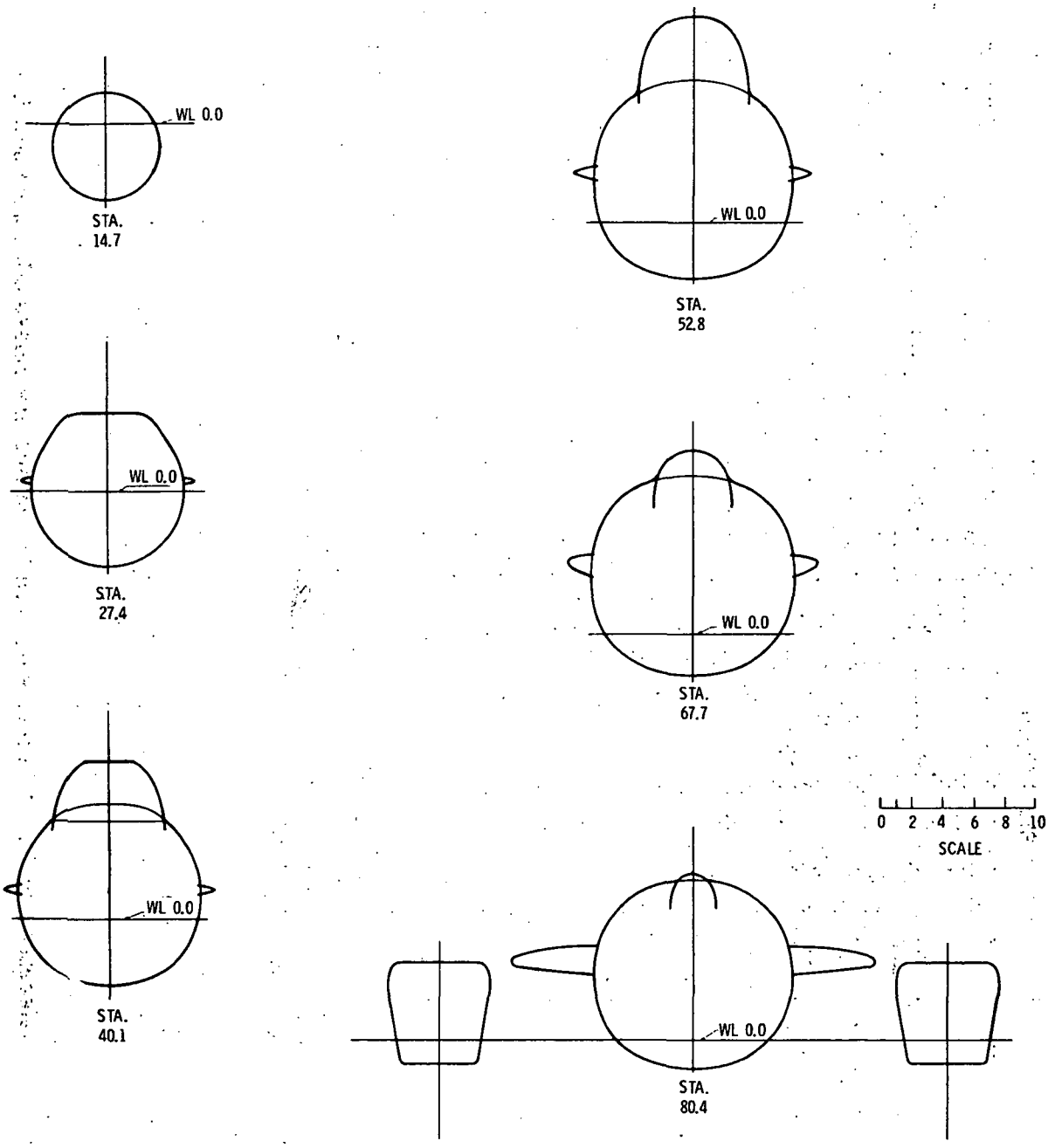

(a) Stations 14.7 to 80.4.

Figure 7.- Cross sections of model. All dimensions are in centimeters unless otherwise noted. WL denotes water line.

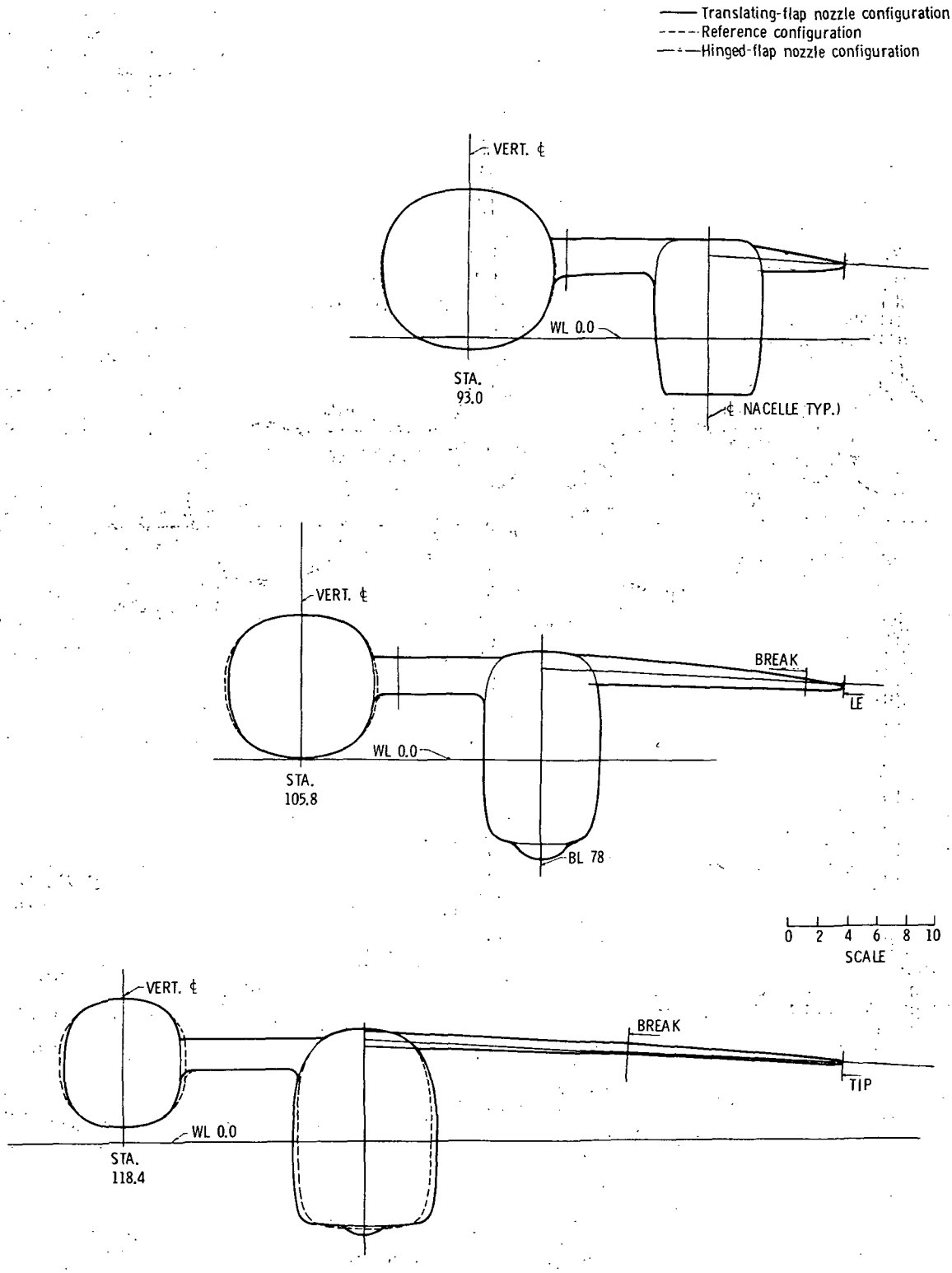

(b) Stations 93.0 to 118.4.

Figure 7.- Continued.

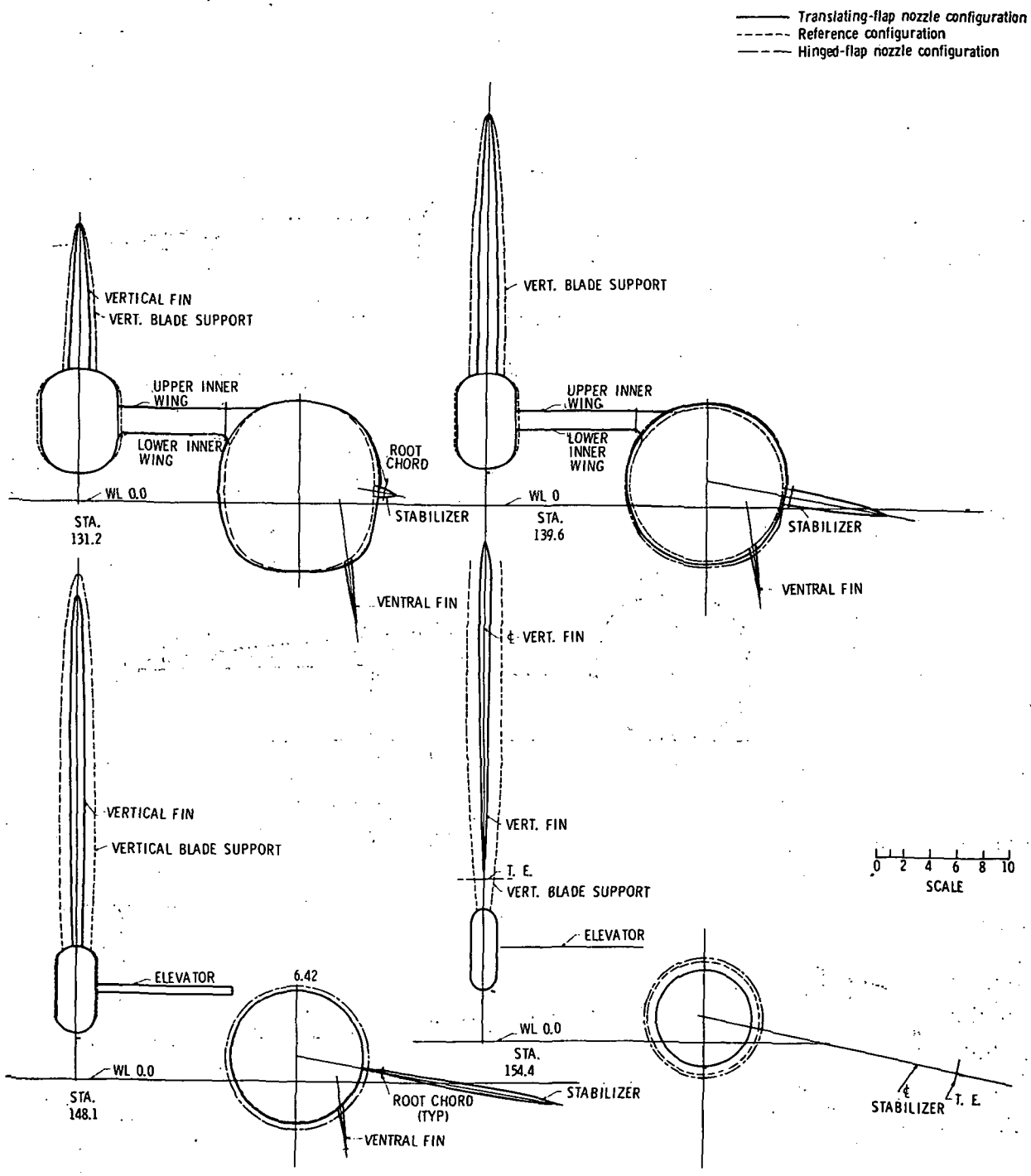

(c) Stations 131.2 to 154.4.

Figure 7.- Concluded.

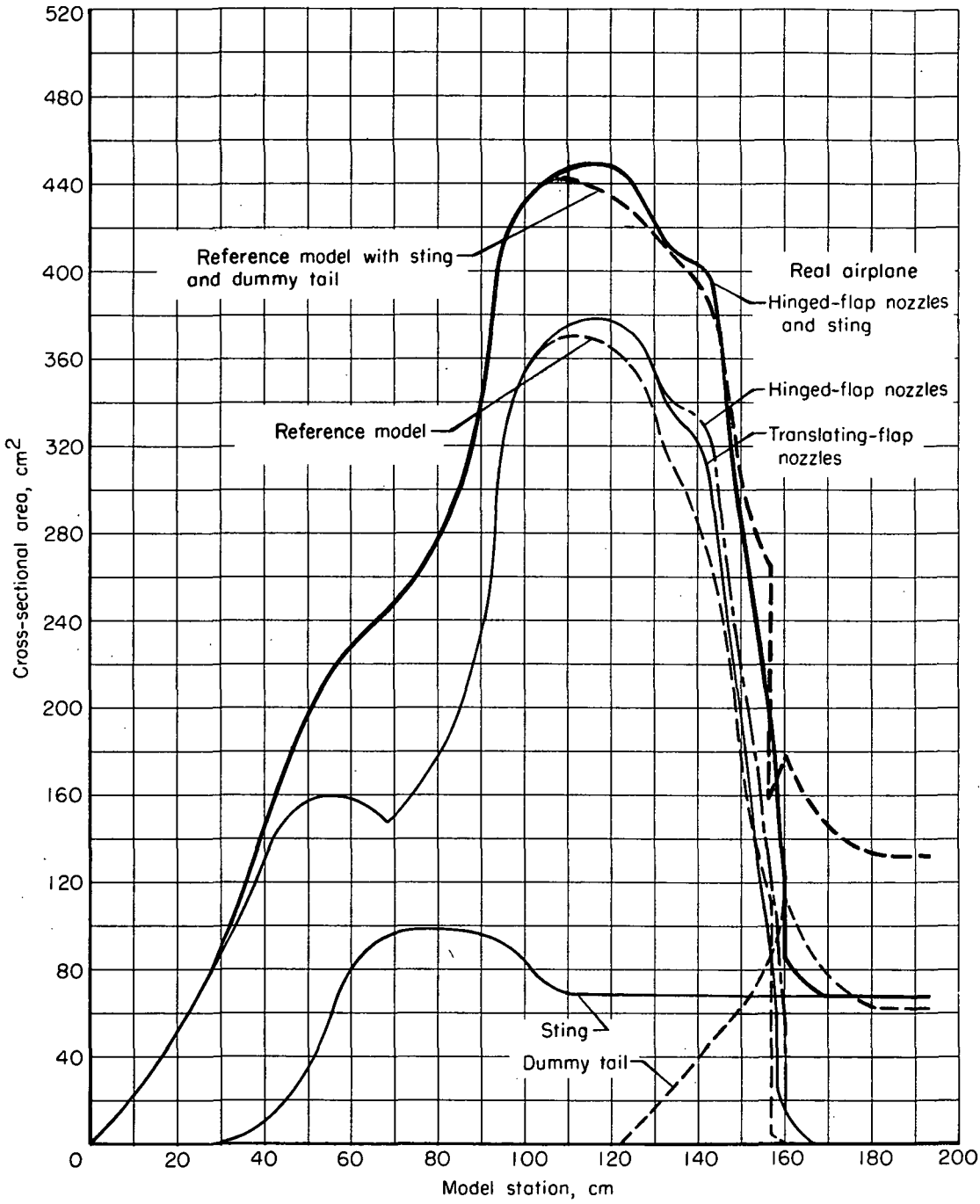

Figure 8.- Cross-sectional area distributions of model and support system.

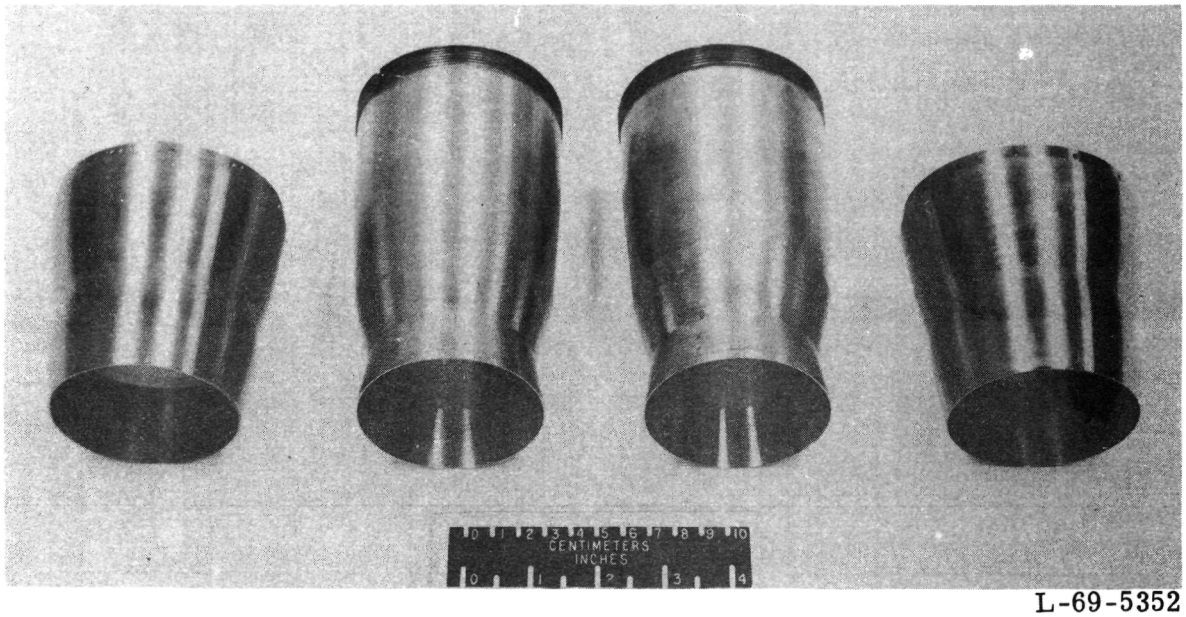

L-69-5352

Figure 9.- Typical set of jet exhaust nozzles showing inner and outer pieces.

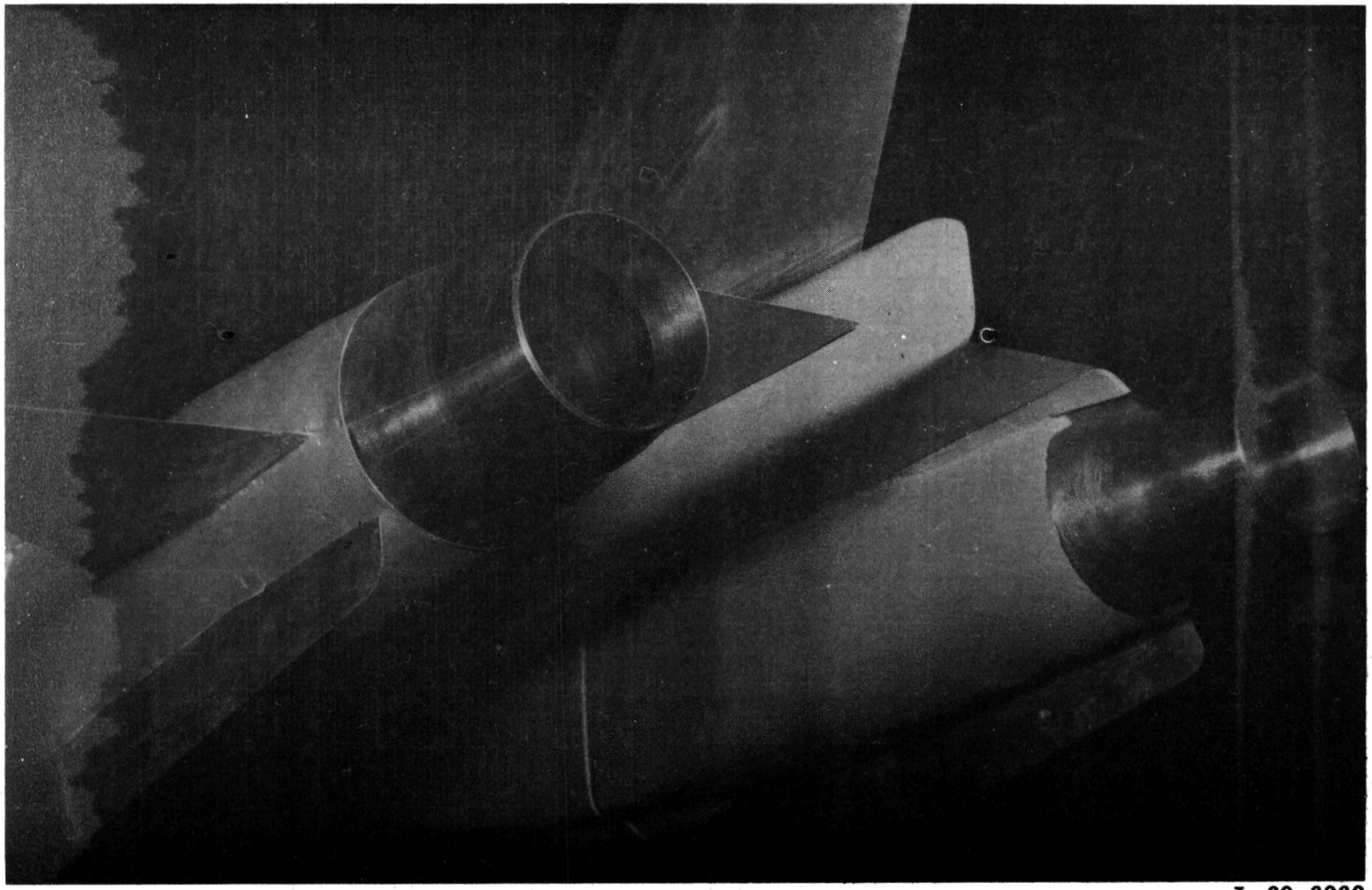

L-69-6060

Figure 10.- Jet exhaust nozzles installed on model.

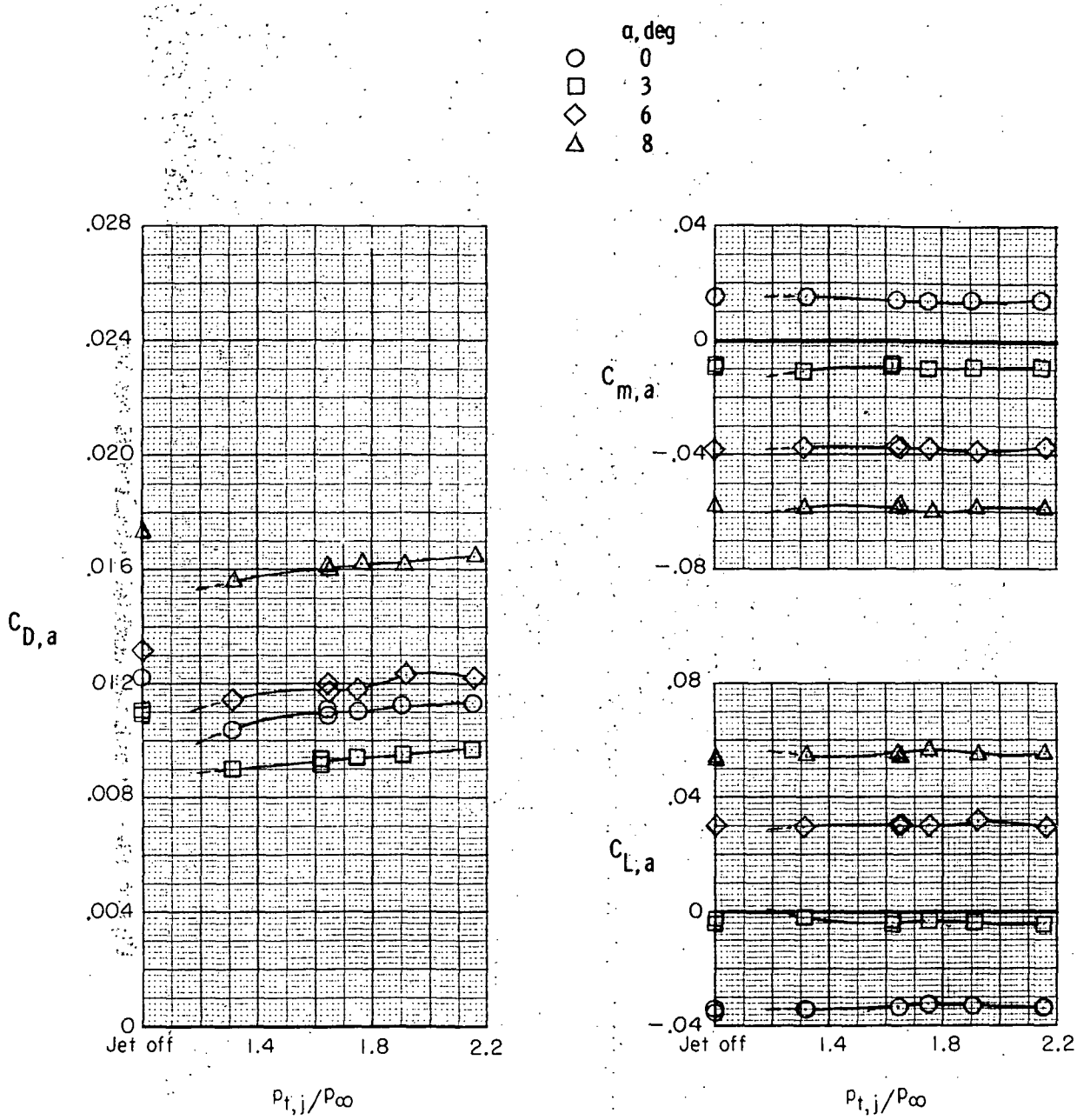

(a) $\delta = 0^o$; $M_\infty = 0.60$.

Figure 11.- Effect of jet total pressure ratio on aerodynamic characteristics of reference configuration with simulated vertical-tail support. Dashed lines indicate extrapolated data.

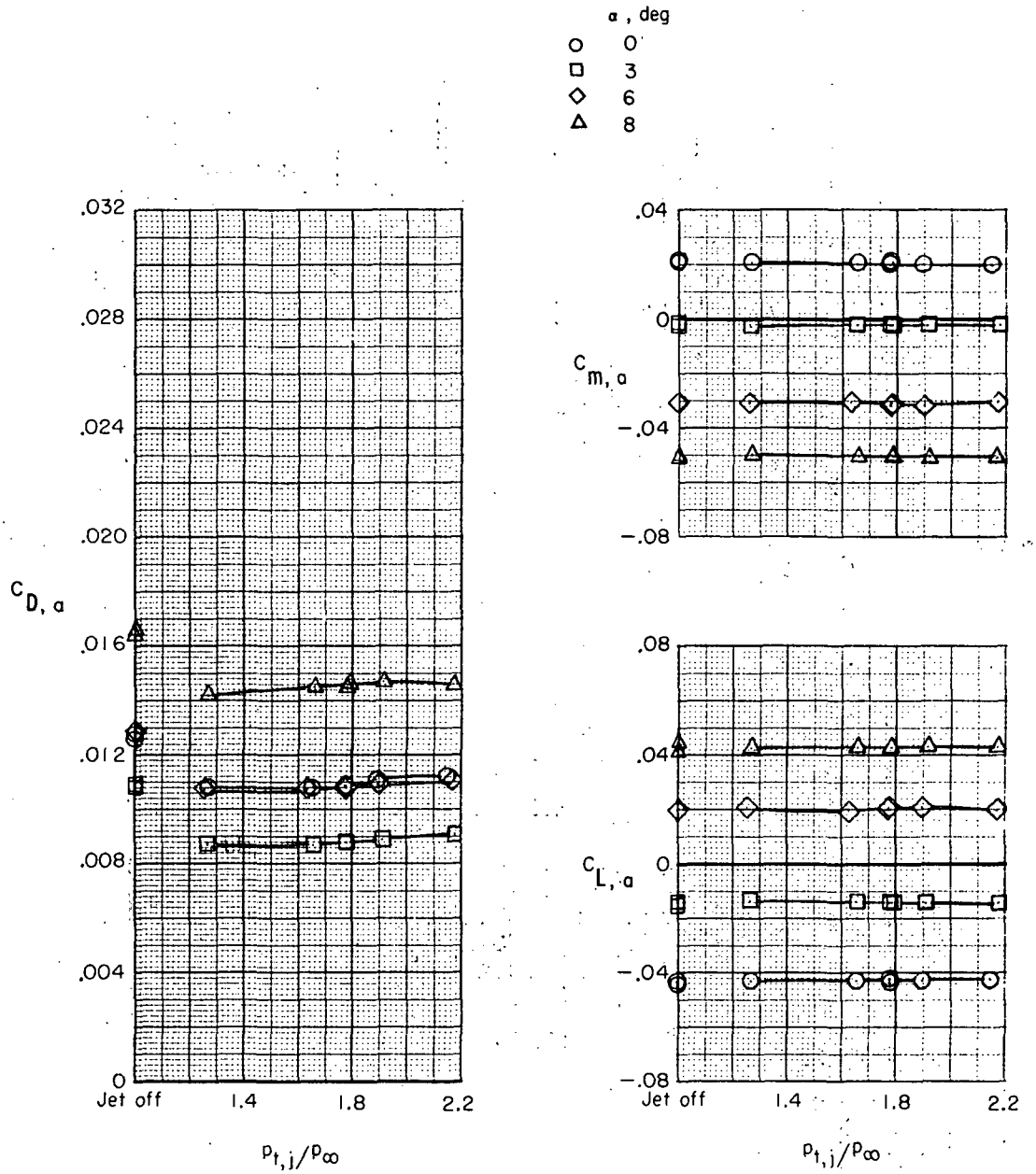

(b) $\delta = 0^o$; $M_\infty = 0.80$.

Figure 11. - Continued.

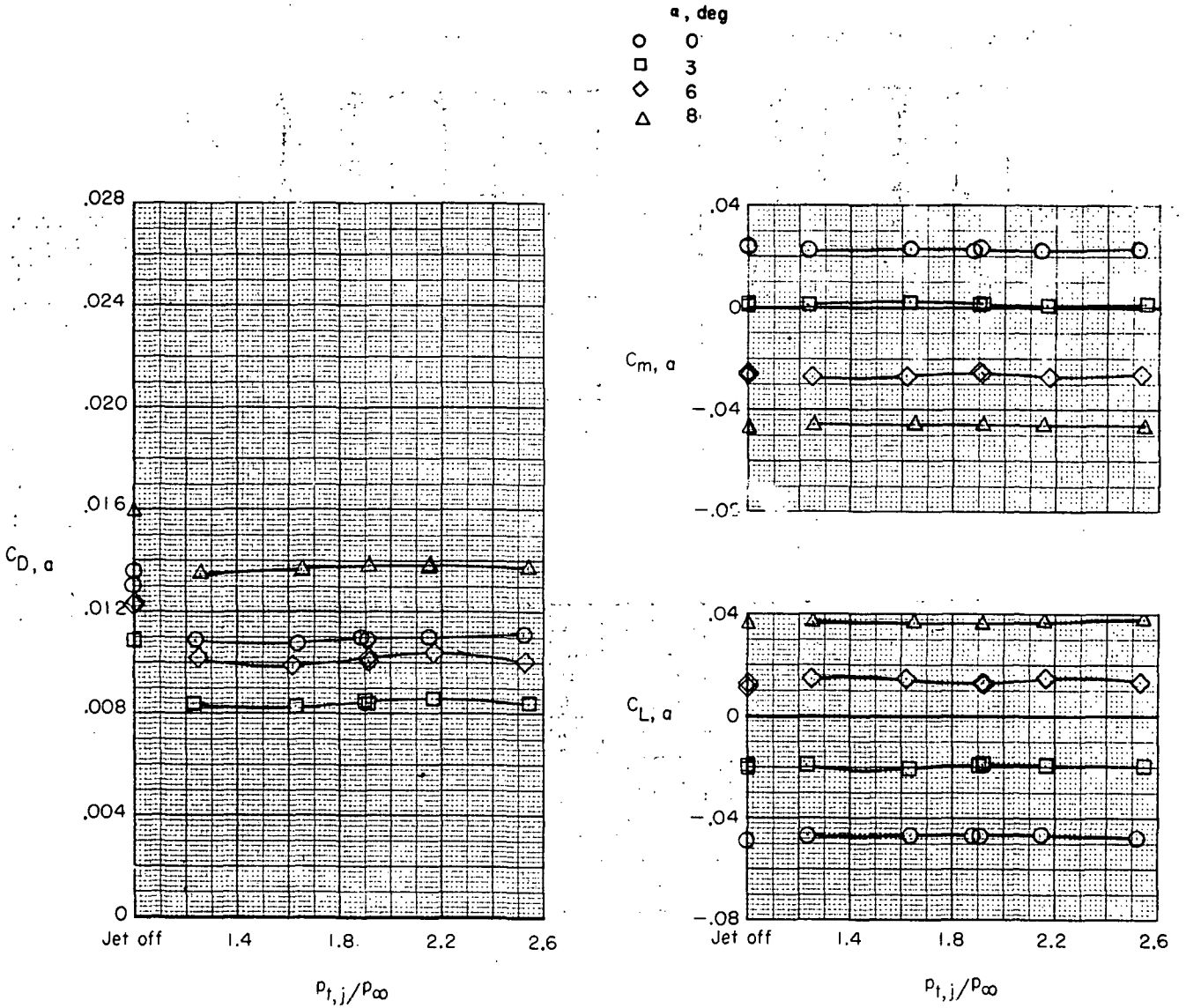

(c) $\delta = 0^o$; $M_\infty = 0.85$.

Figure 11.- Continued.

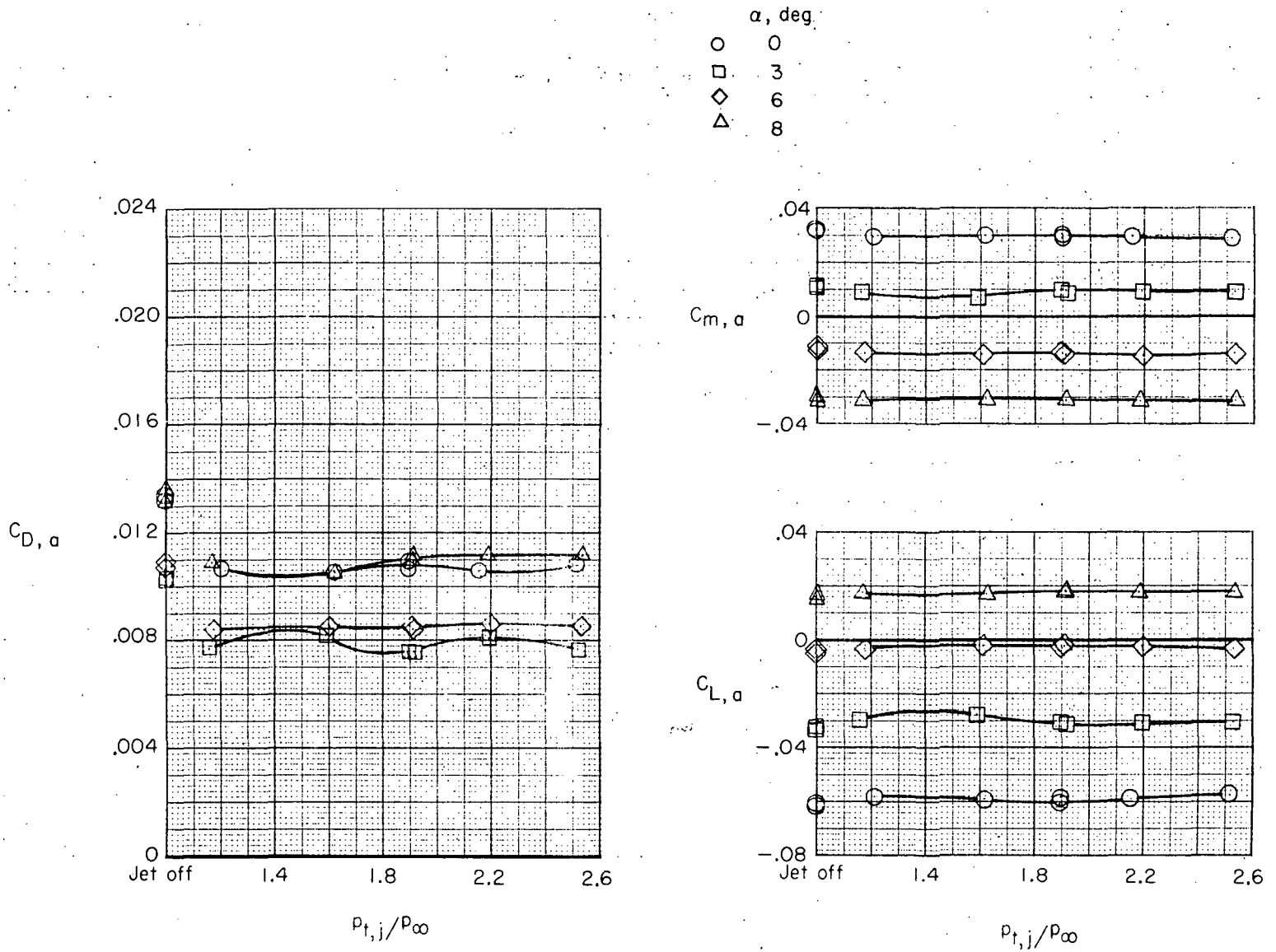

(d) $\delta = 0^o$; $M_\infty = 0.90$.

Figure 11.- Continued.

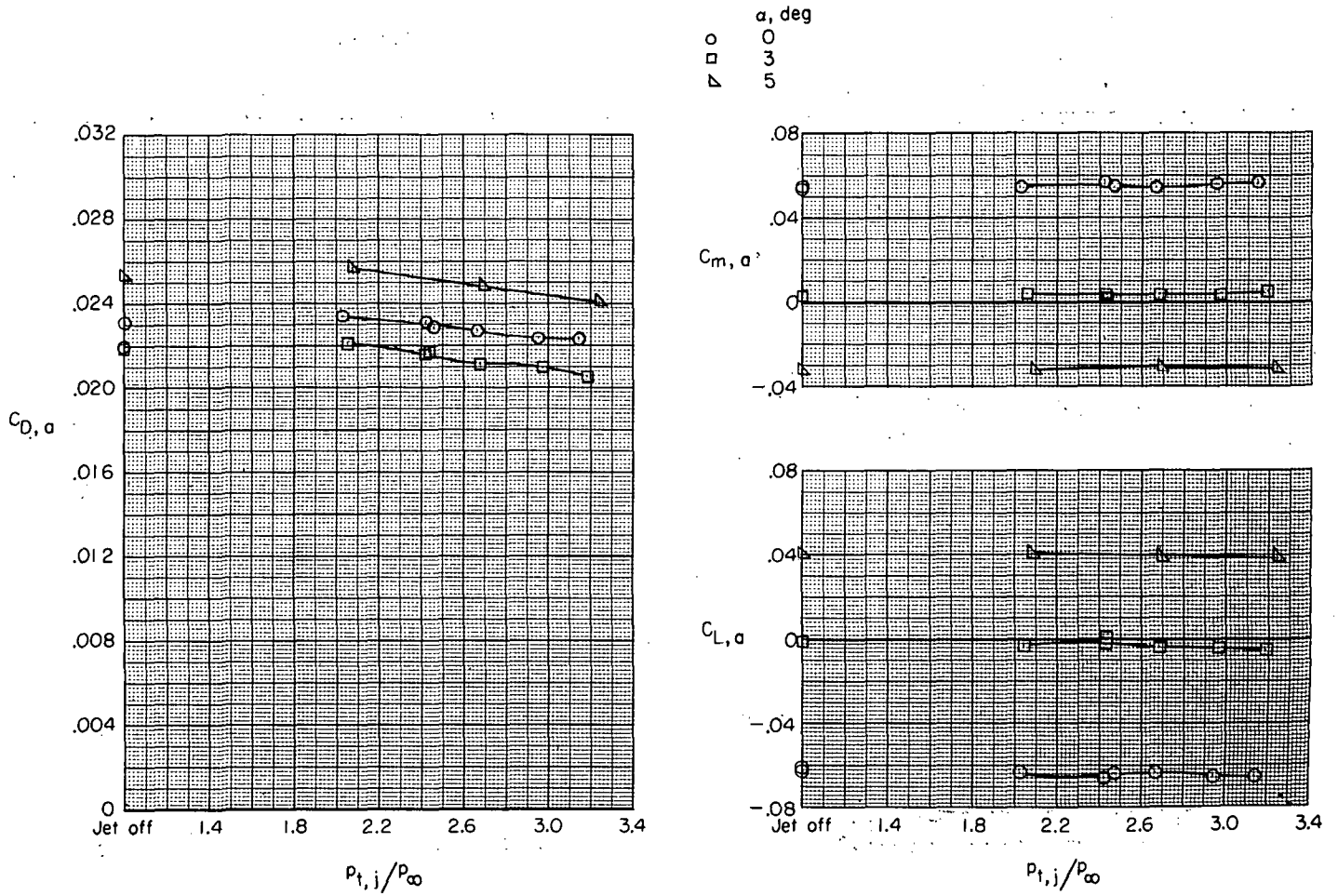

(e) $\delta = 0^o$; $M_\infty = 1.20$.

Figure 11.- Continued.

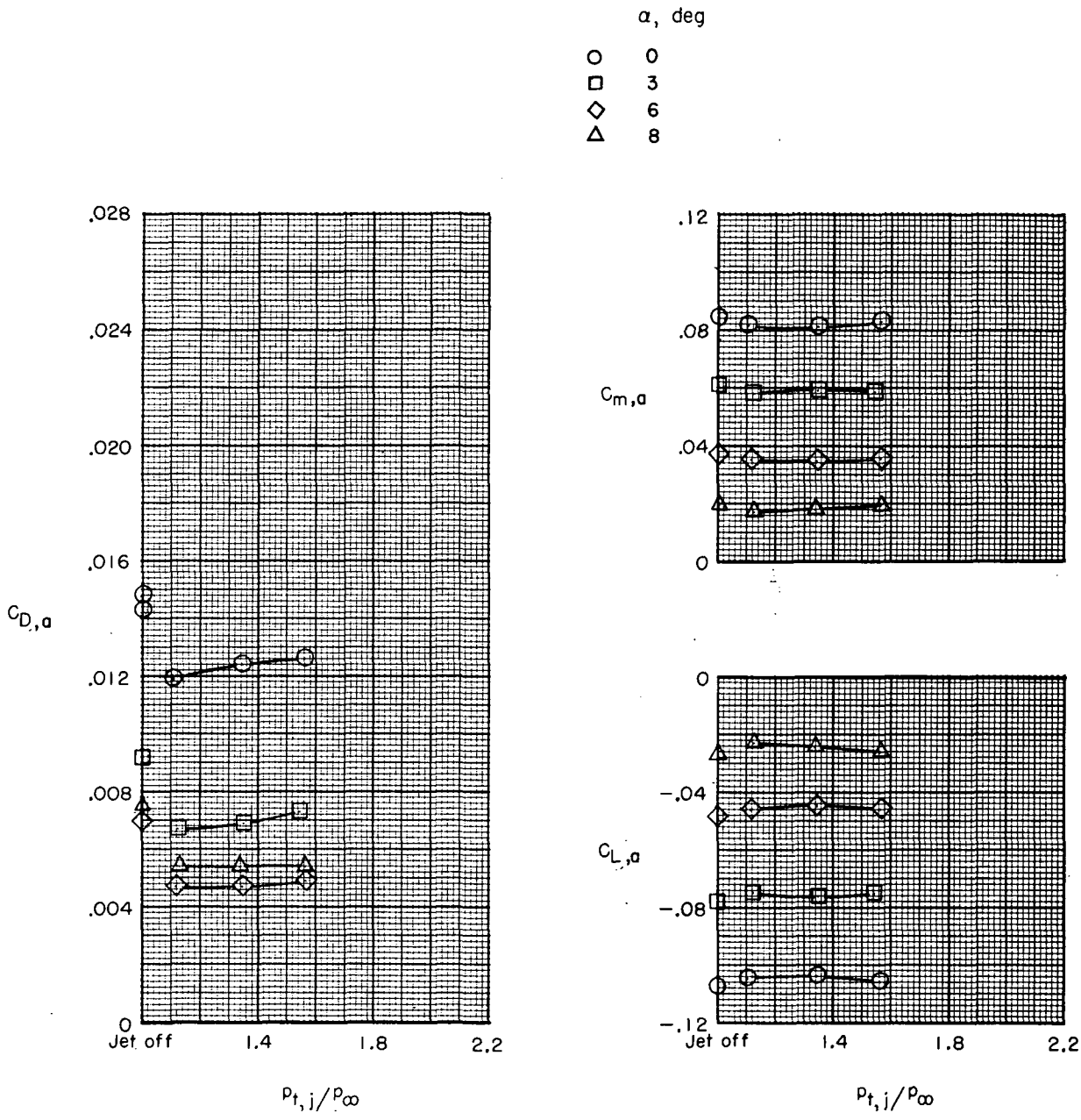

(f) $\delta = -5^o$; $M_\infty = 0.60$.

Figure 11.- Continued.

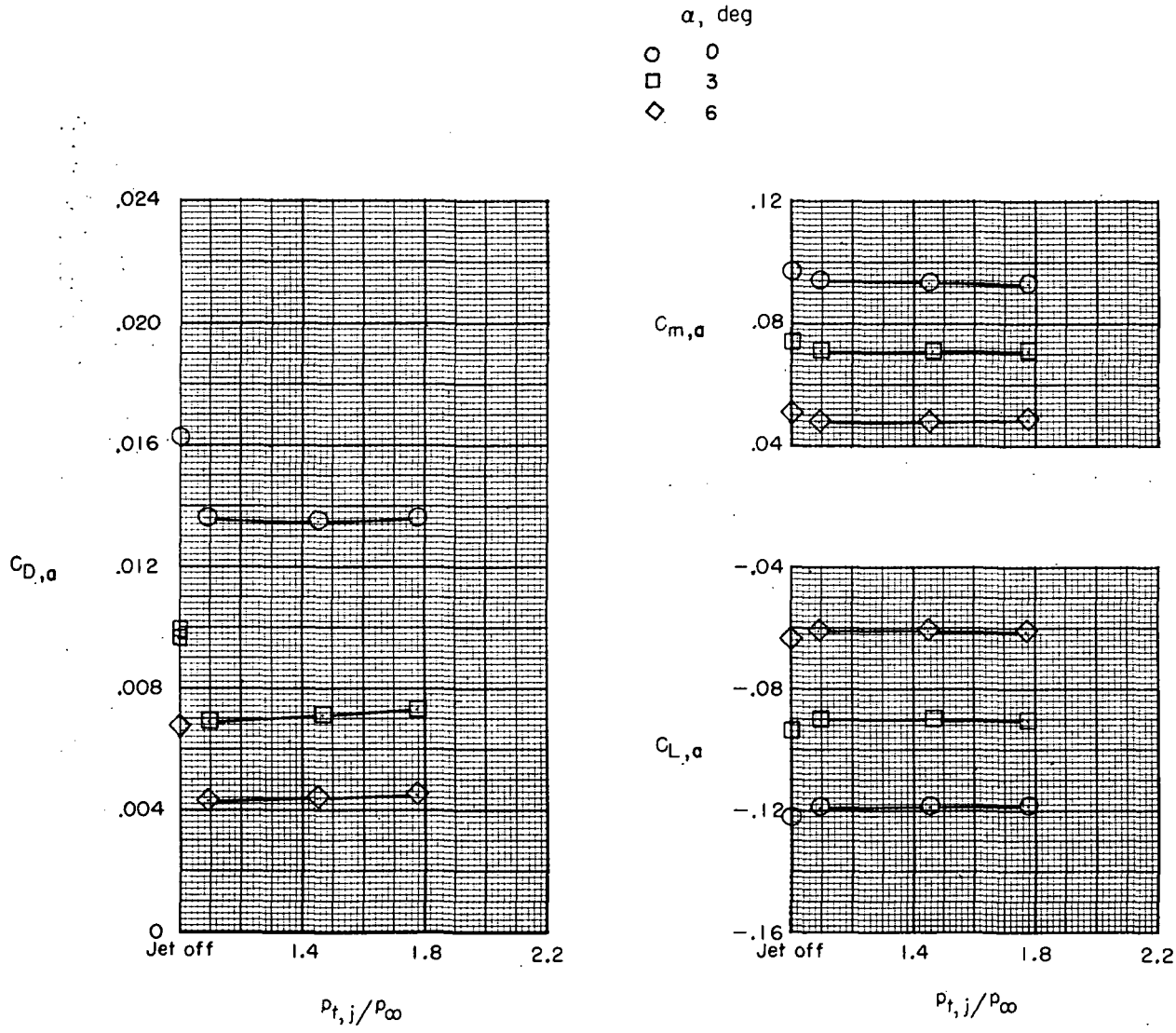

(g) $\delta = -5^o$; $M_\infty = 0.80$.

Figure 11. - Continued.

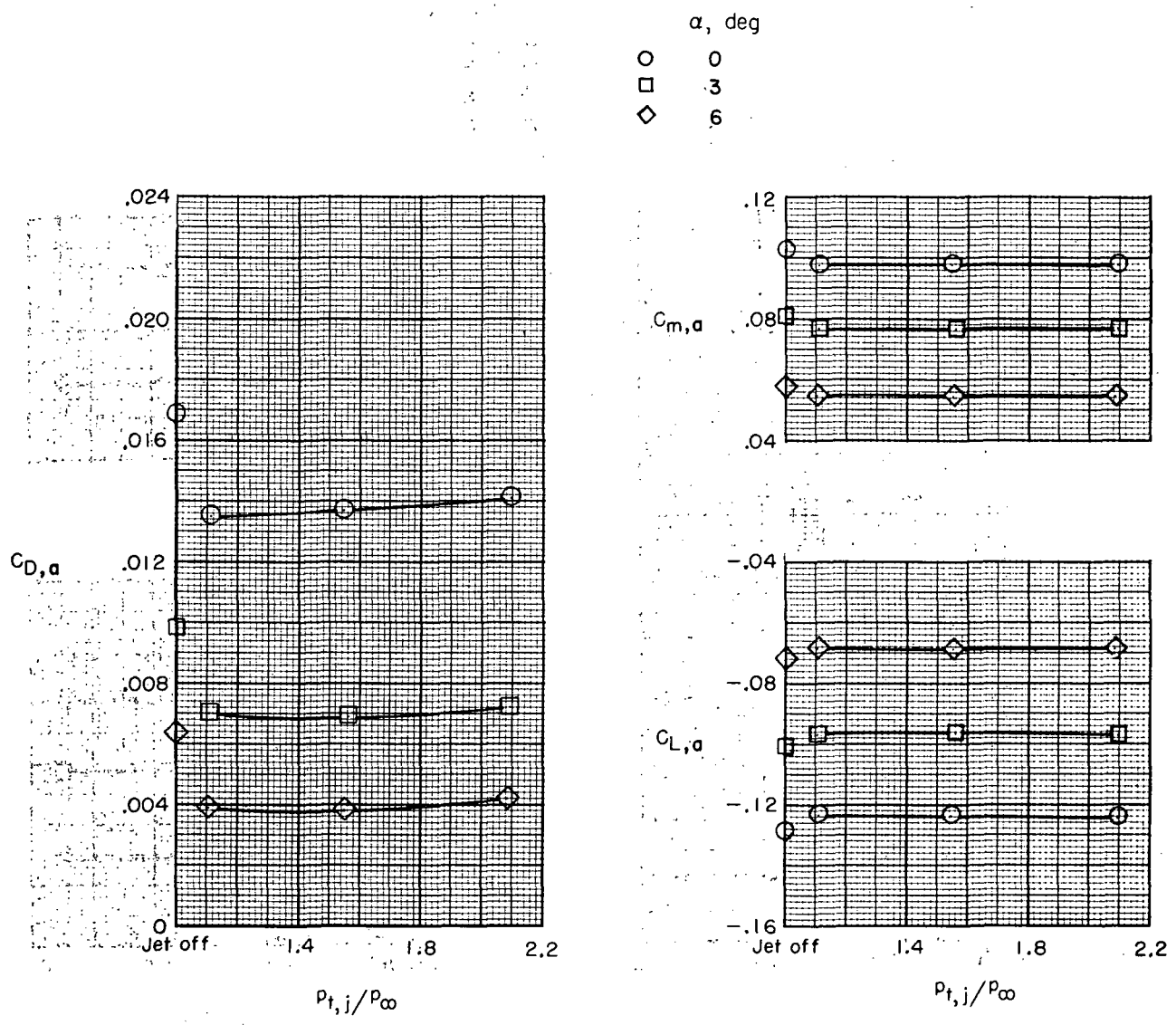

(h) $\delta = -5^o$; $M_\infty = 0.85$.

Figure 11.- Continued.

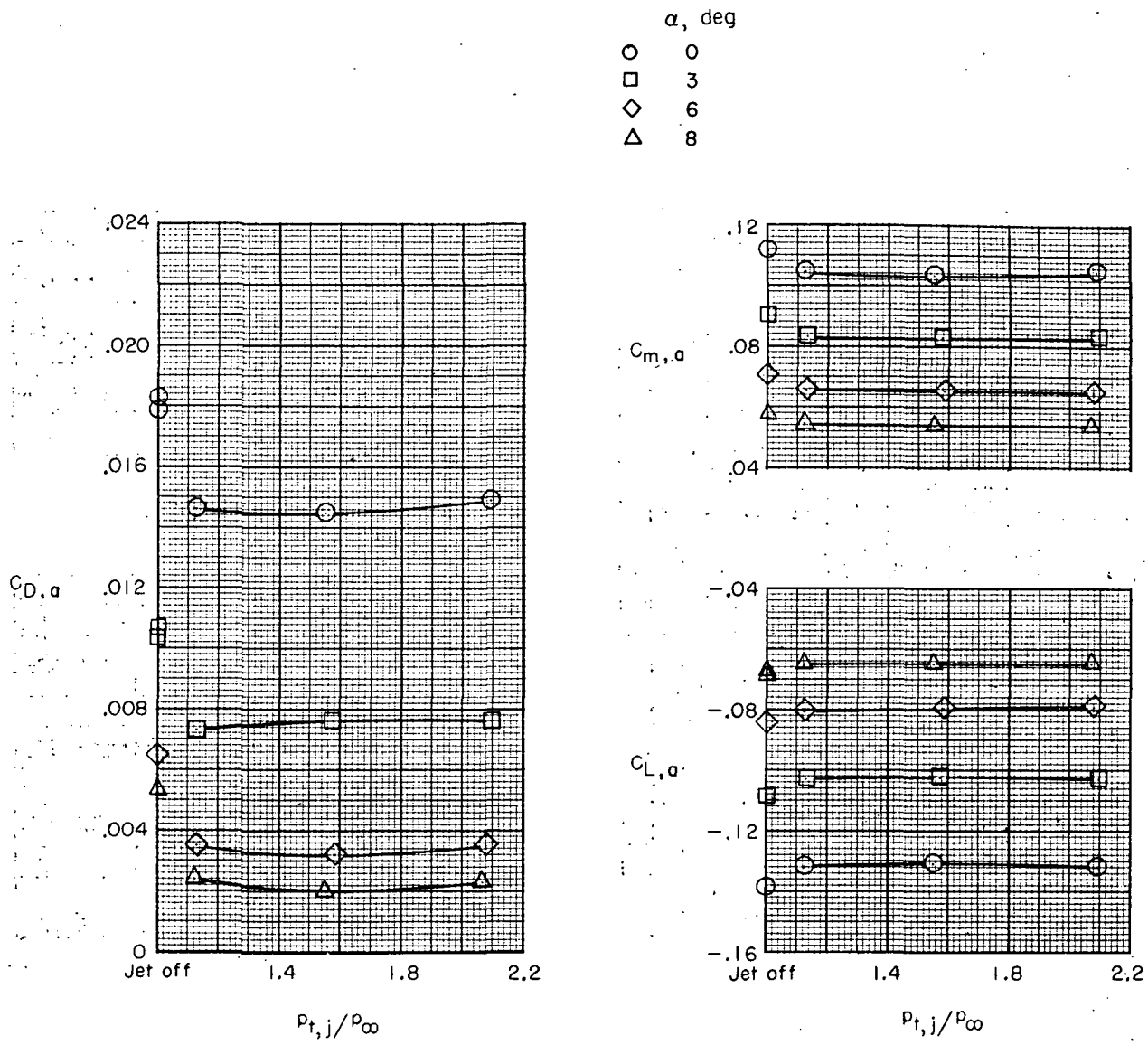

(i) $\delta = -5^{o}$; $M_\infty = 0.90$.

Figure 11.- Continued.

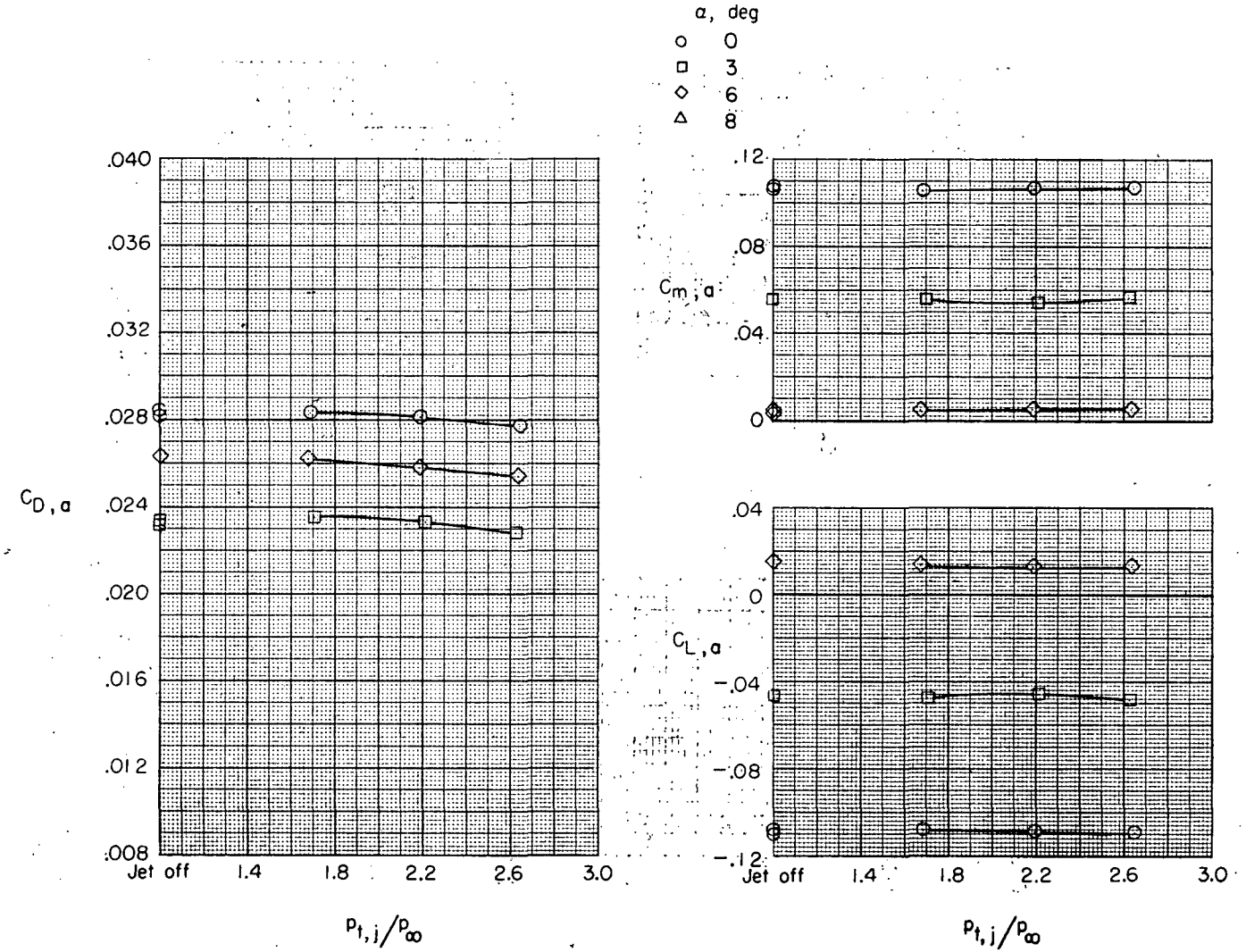

(j) $\delta = -5^o$; $M_\infty = 1.20$.

Figure 11.- Continued.

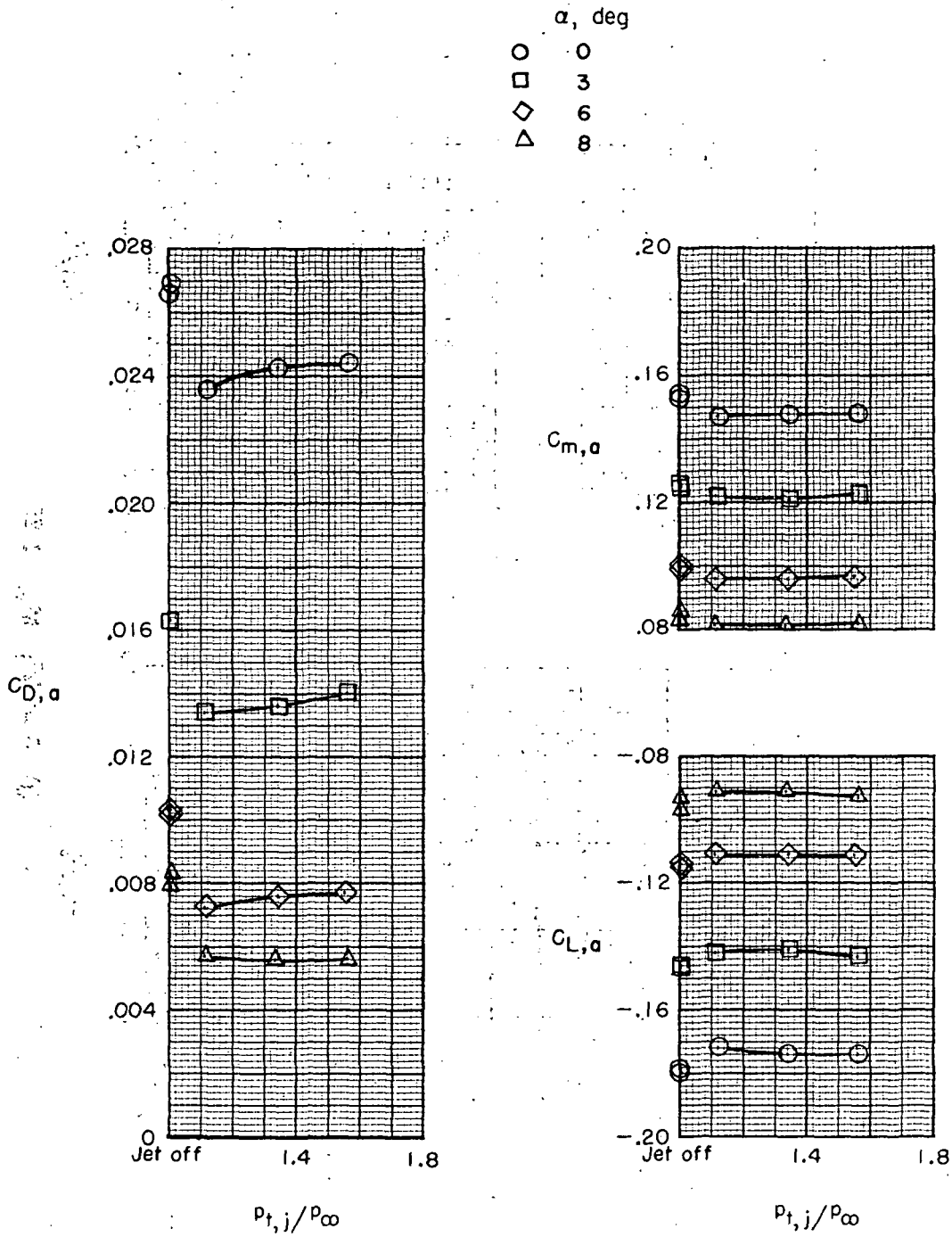

(k) $\delta = -10^{o}$; $M_\infty = 0.60$.

Figure 11.- Continued.

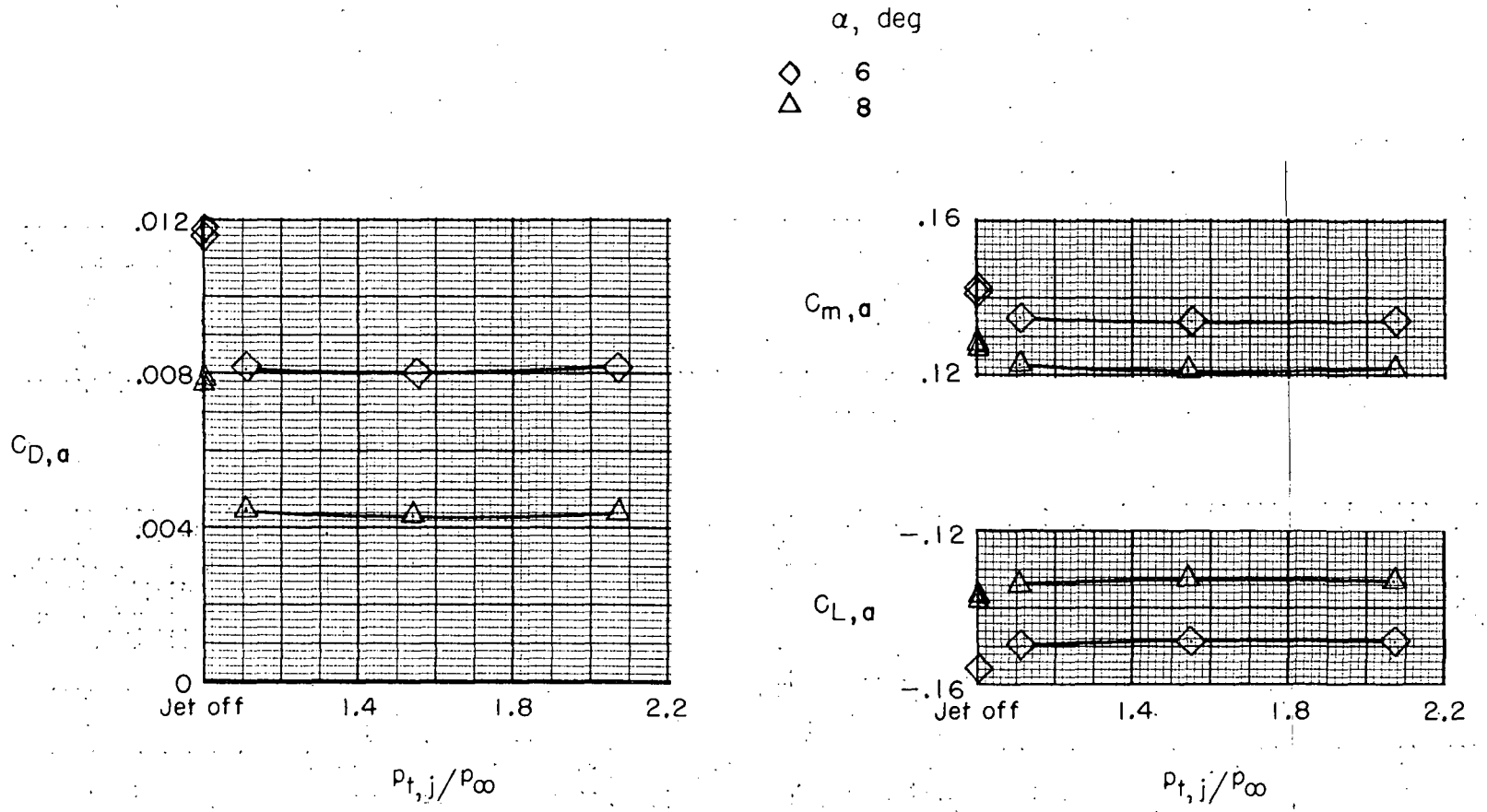

(l) $\delta = -10^o$; $M_\infty = 0.90$.

Figure 11. - Concluded.

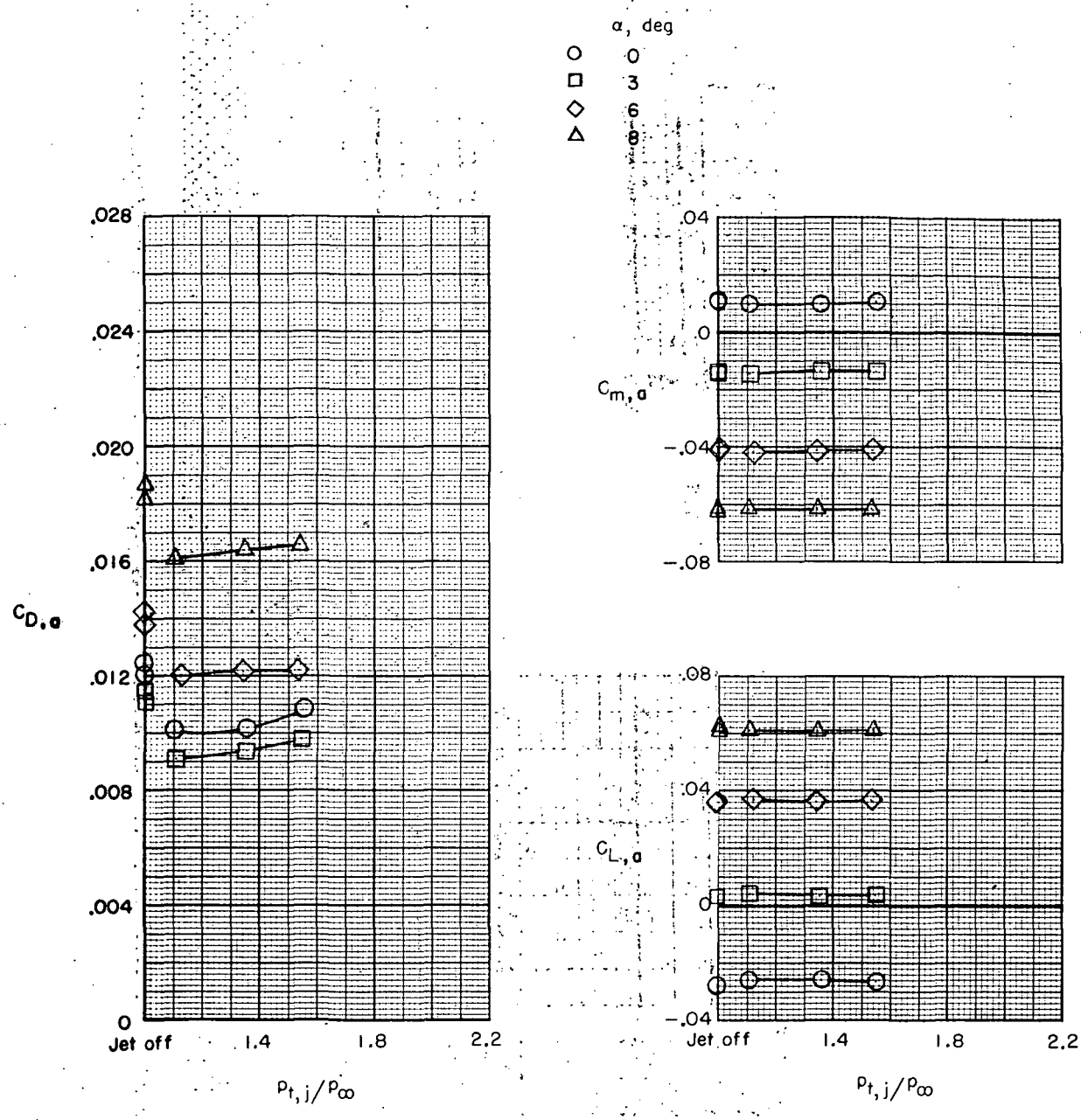

(a) $\delta = 0^o$; $M_\infty = 0.60$.

Figure 12. - Effect of jet total pressure ratio on aerodynamic characteristics of reference afterbody with real vertical tail installed.

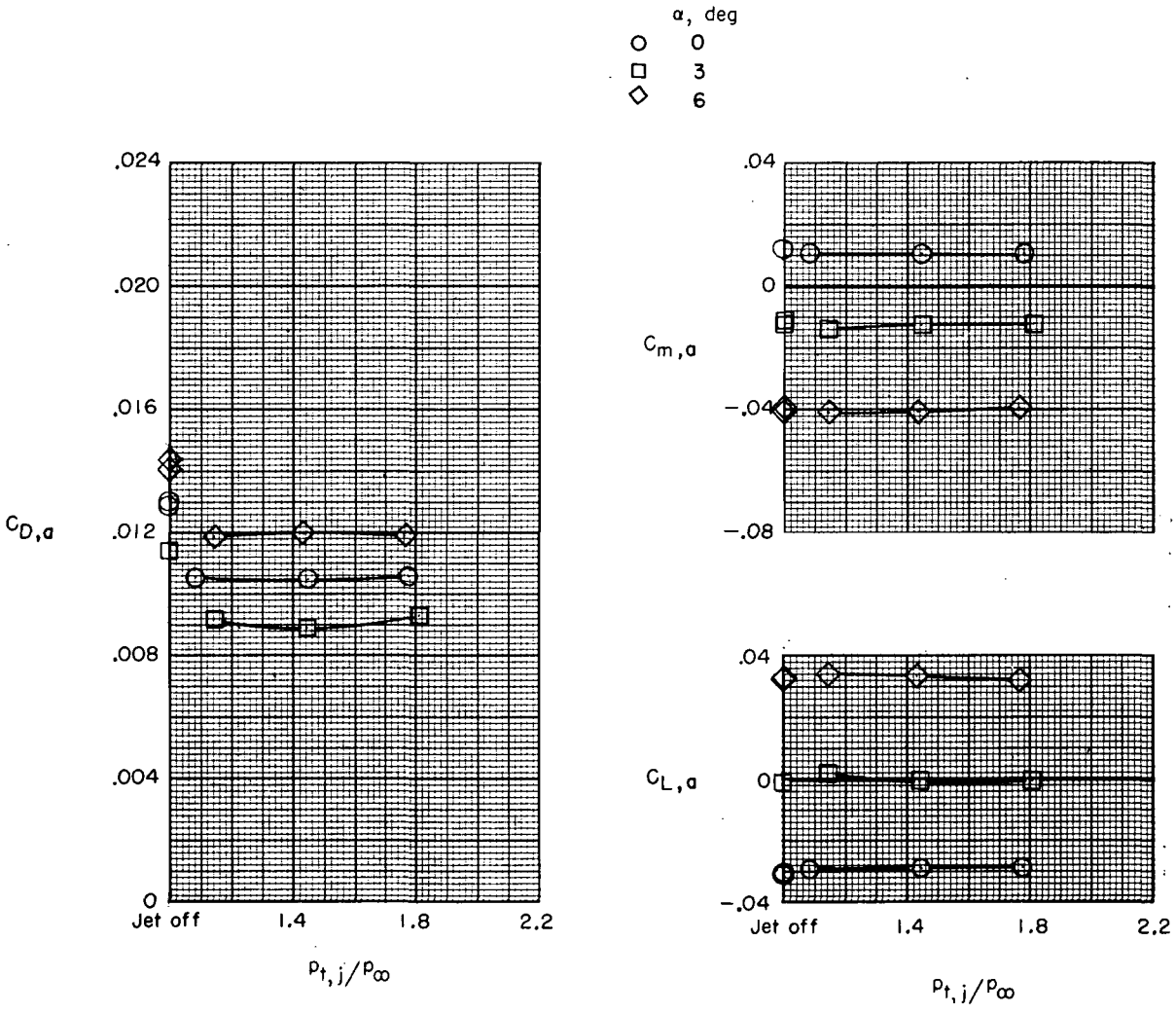

(b) $\delta = 0^o$; $M_\infty = 0.80$.

Figure 12.- Continued.

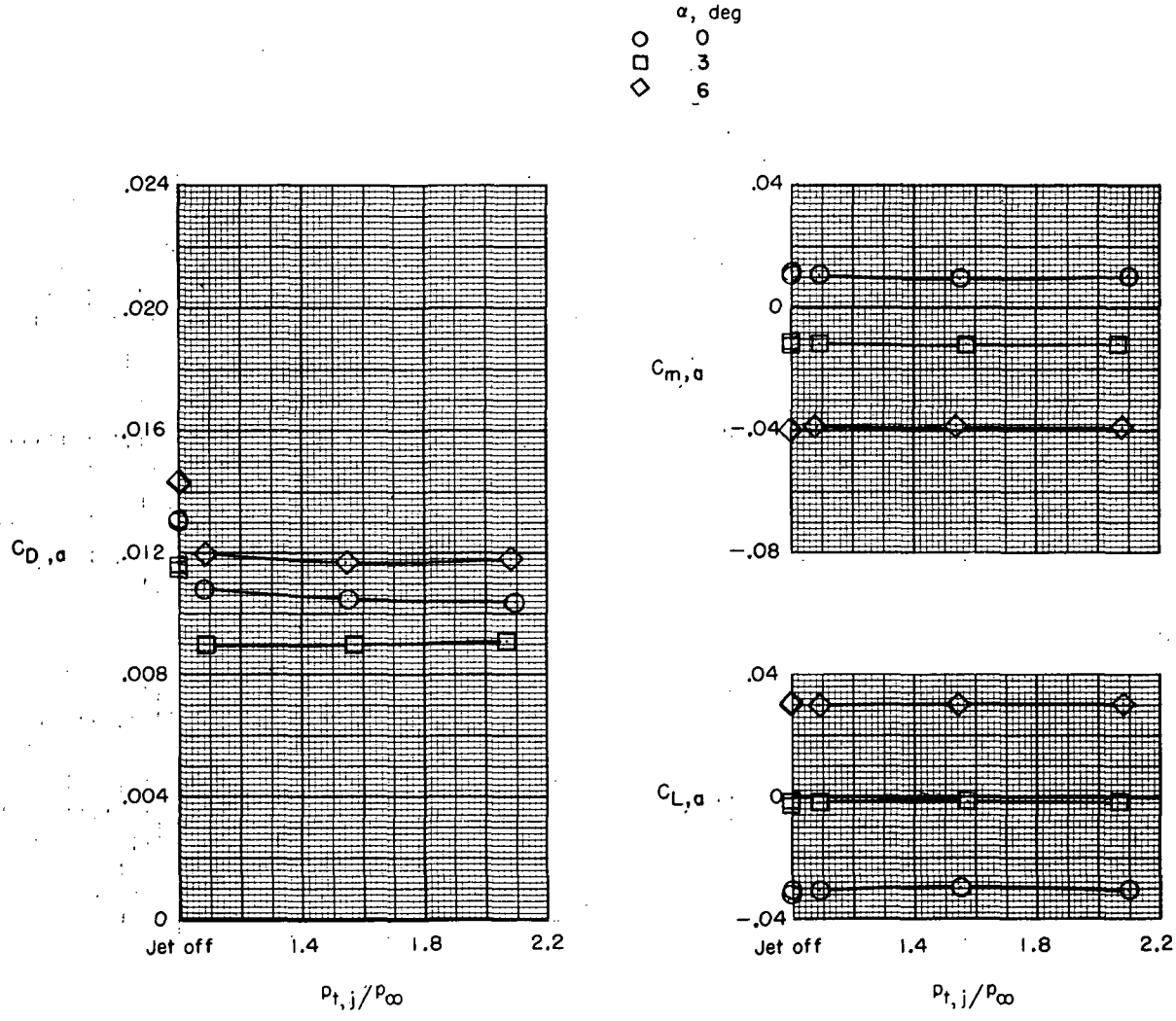

(c) $\delta = 0^O$; $M_\infty = 0.85$.

Figure 12.- Continued.

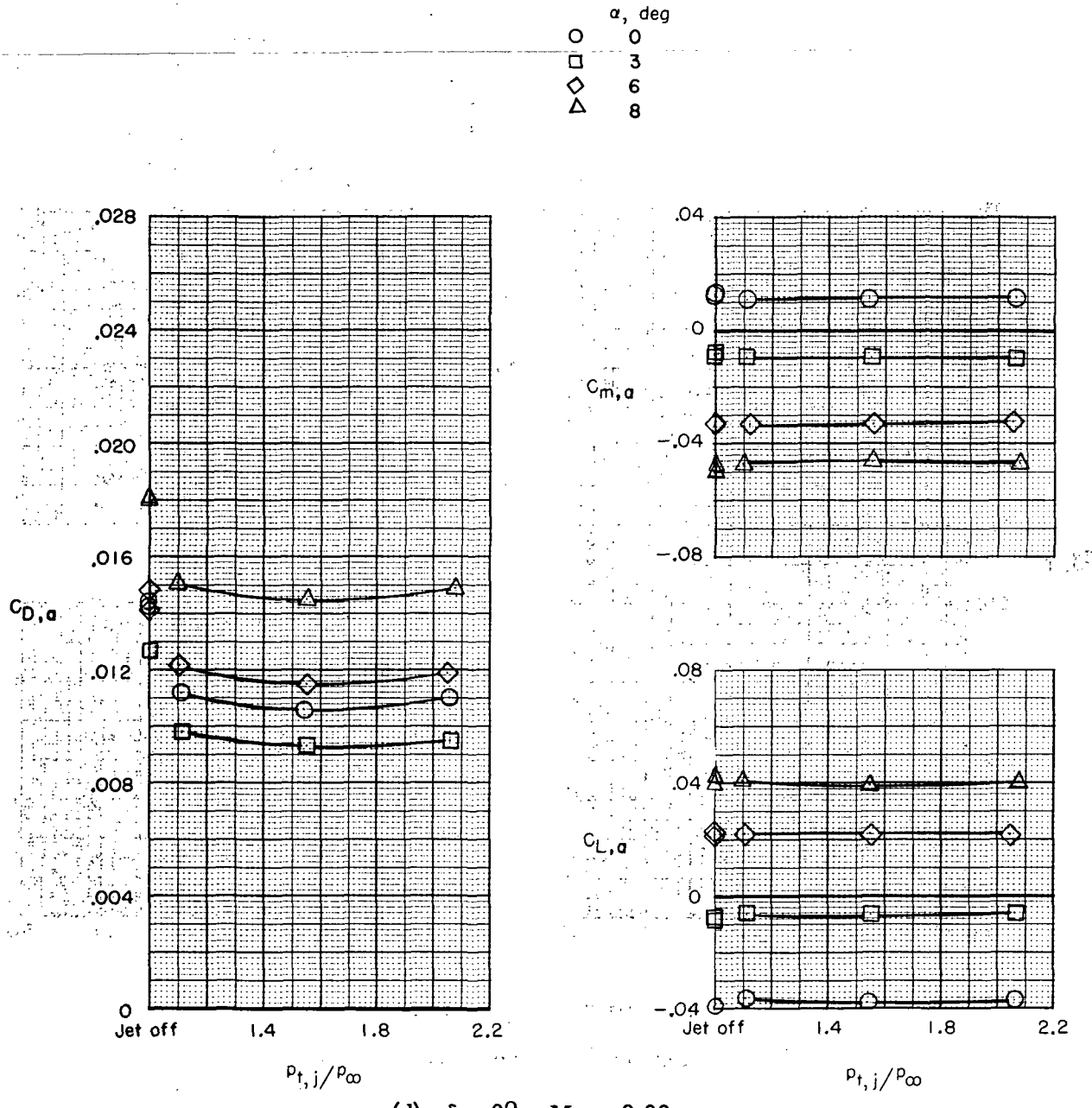

(d) $\delta = 0^o$; $M_\infty = 0.90$.

Figure 12.- Continued.

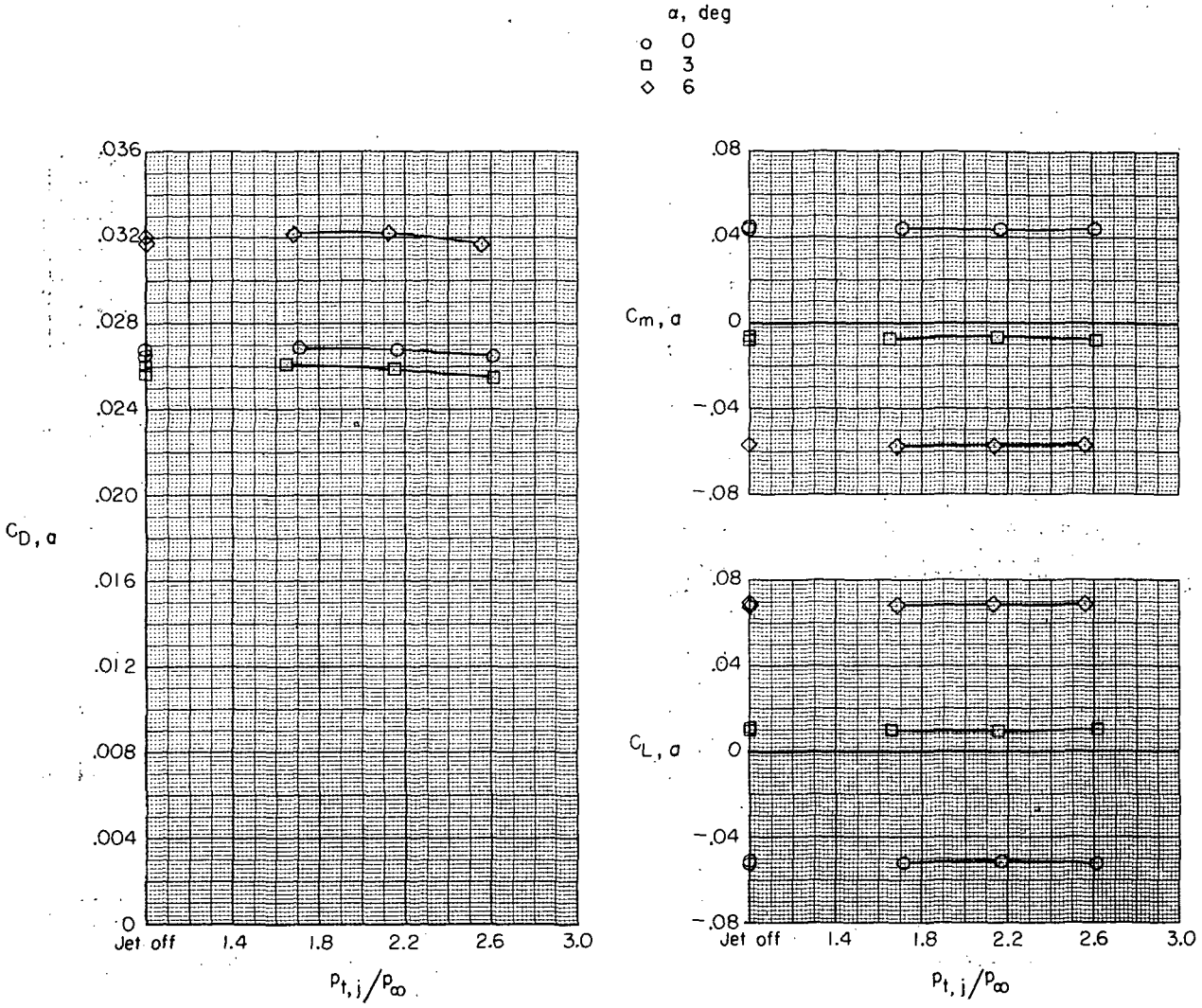

(e) $\delta = 0^O$; $M_\infty = 1.20$.

Figure 12.- Continued.

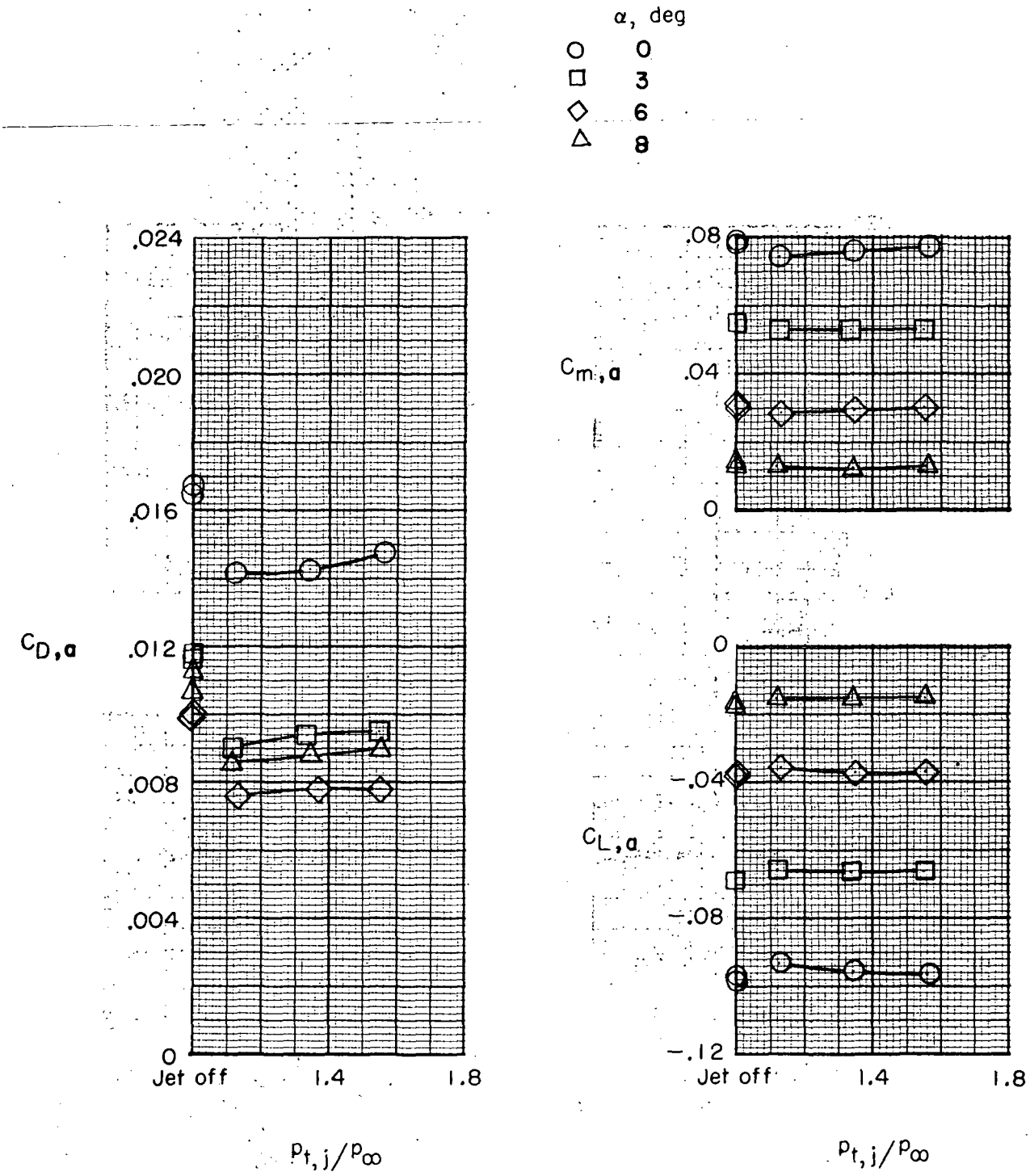

(f) $\delta = -5^o$; $M_\infty = 0.60$.

Figure 12.- Continued.

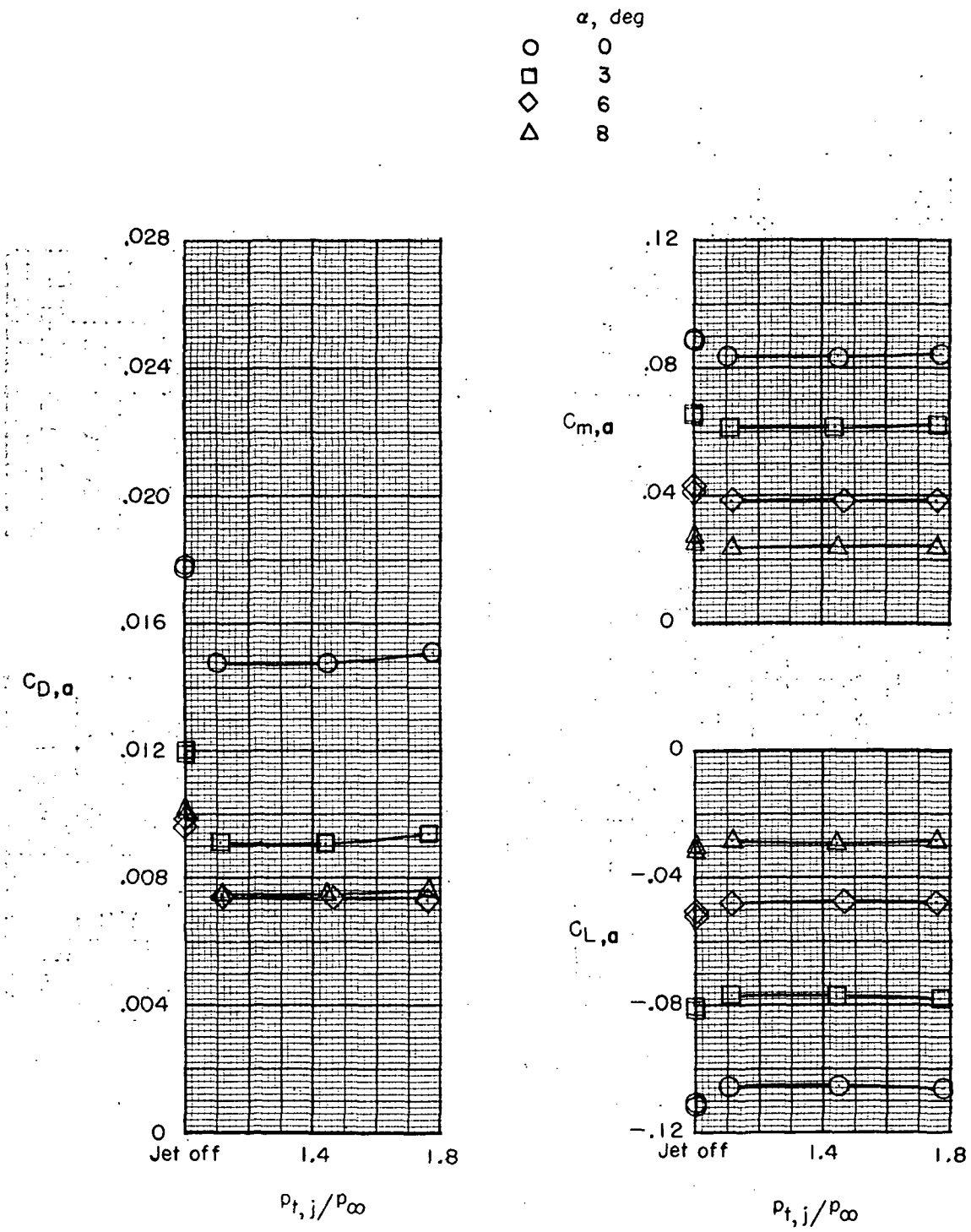

(g) $\delta = -5^o$; $M_\infty = 0.80$.

Figure 12.- Continued.

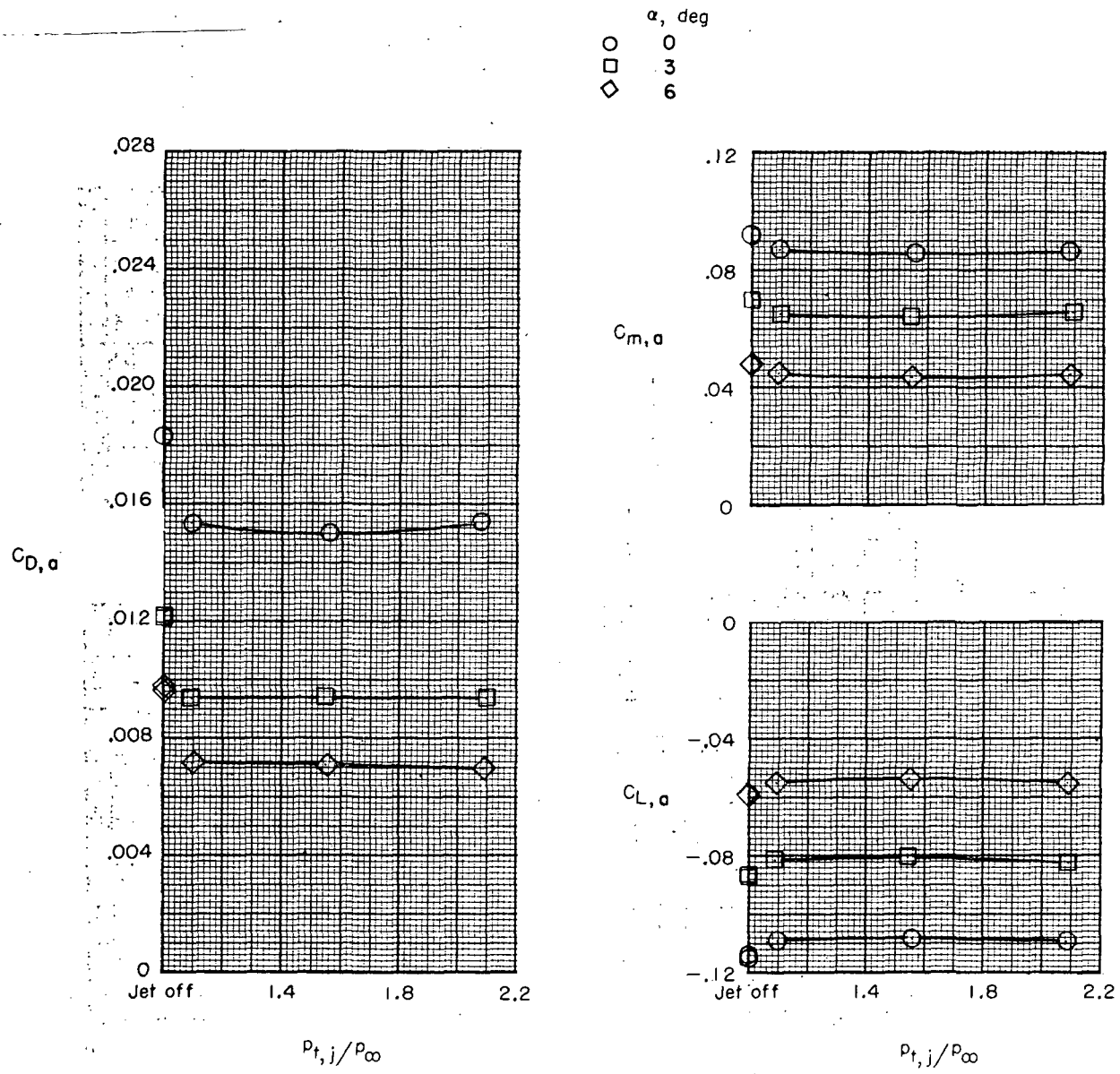

(h) $\delta = -5^{O}$; $M_\infty = 0.85$.

Figure 12.- Continued.

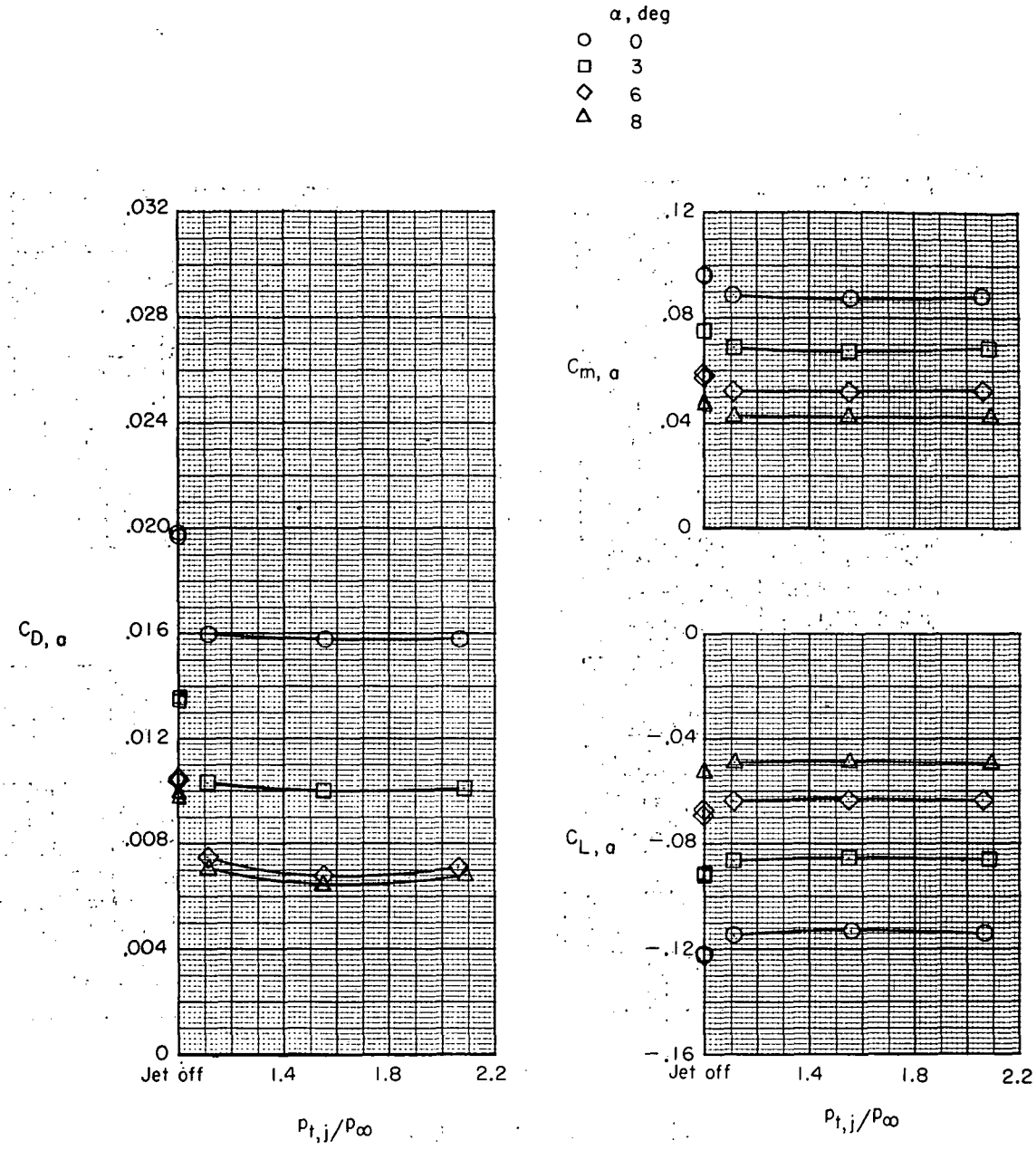

(i) $\delta = -5^o$; $M_\infty = 0.90$.

Figure 12.- Continued.

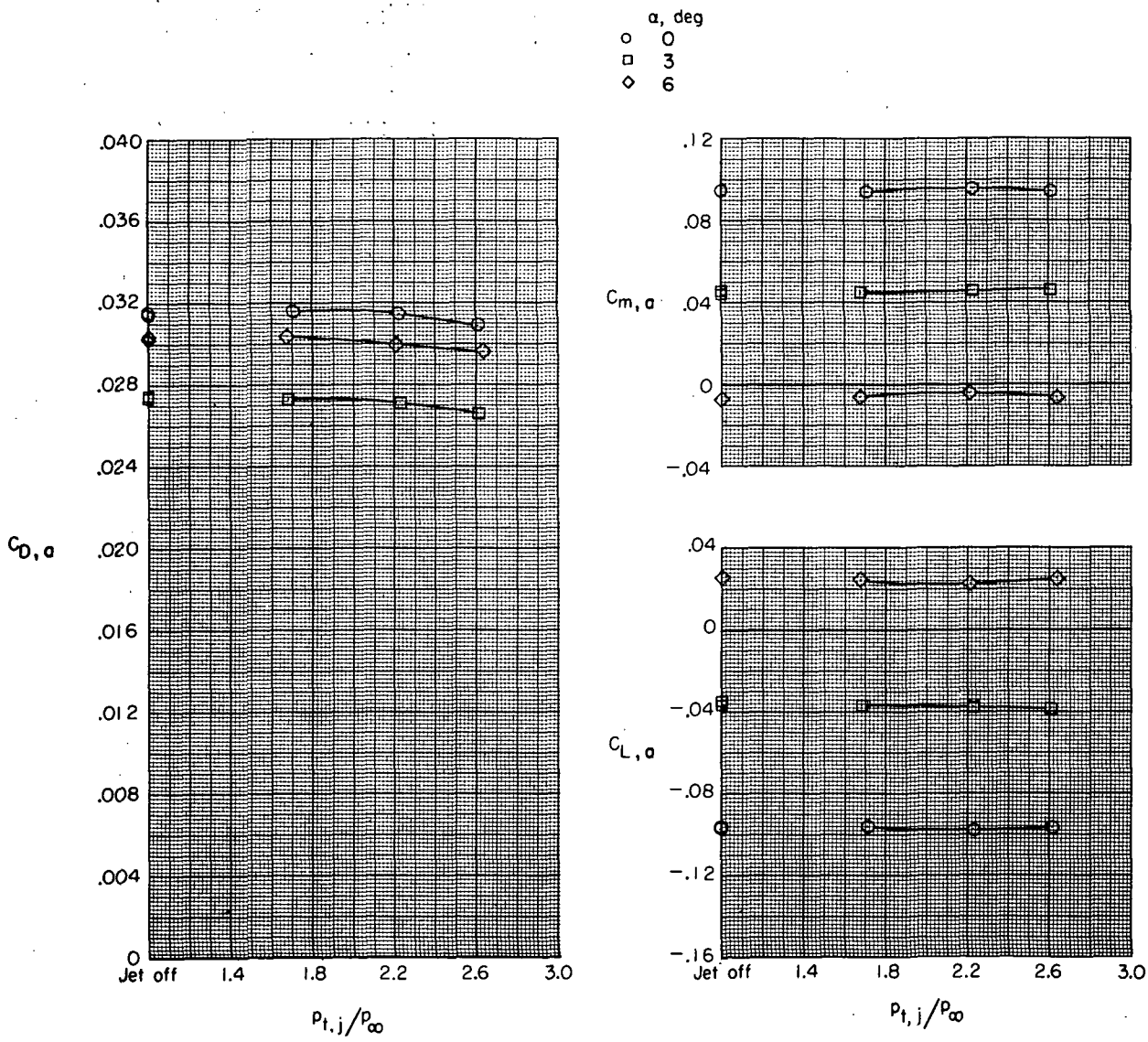

(j) $\delta = -5^{o}$; $M_\infty = 1.20$.

Figure 12.- Concluded.

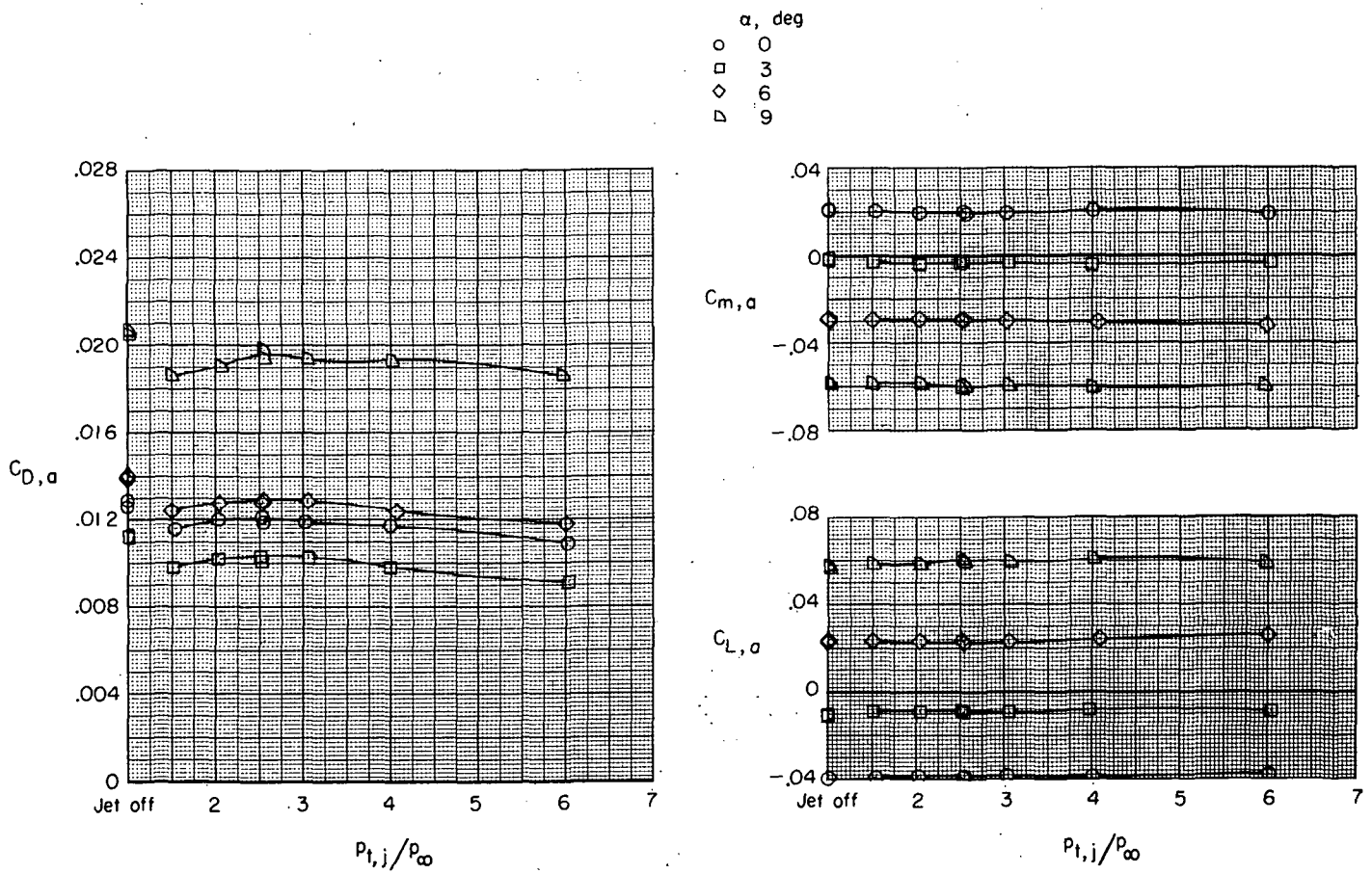

(a) $\delta = 0^o$; $M_\infty = 0.60$.

Figure 13.- Effect of jet total pressure ratio on aerodynamic characteristics of translating-flap nozzle configuration in cruise position.

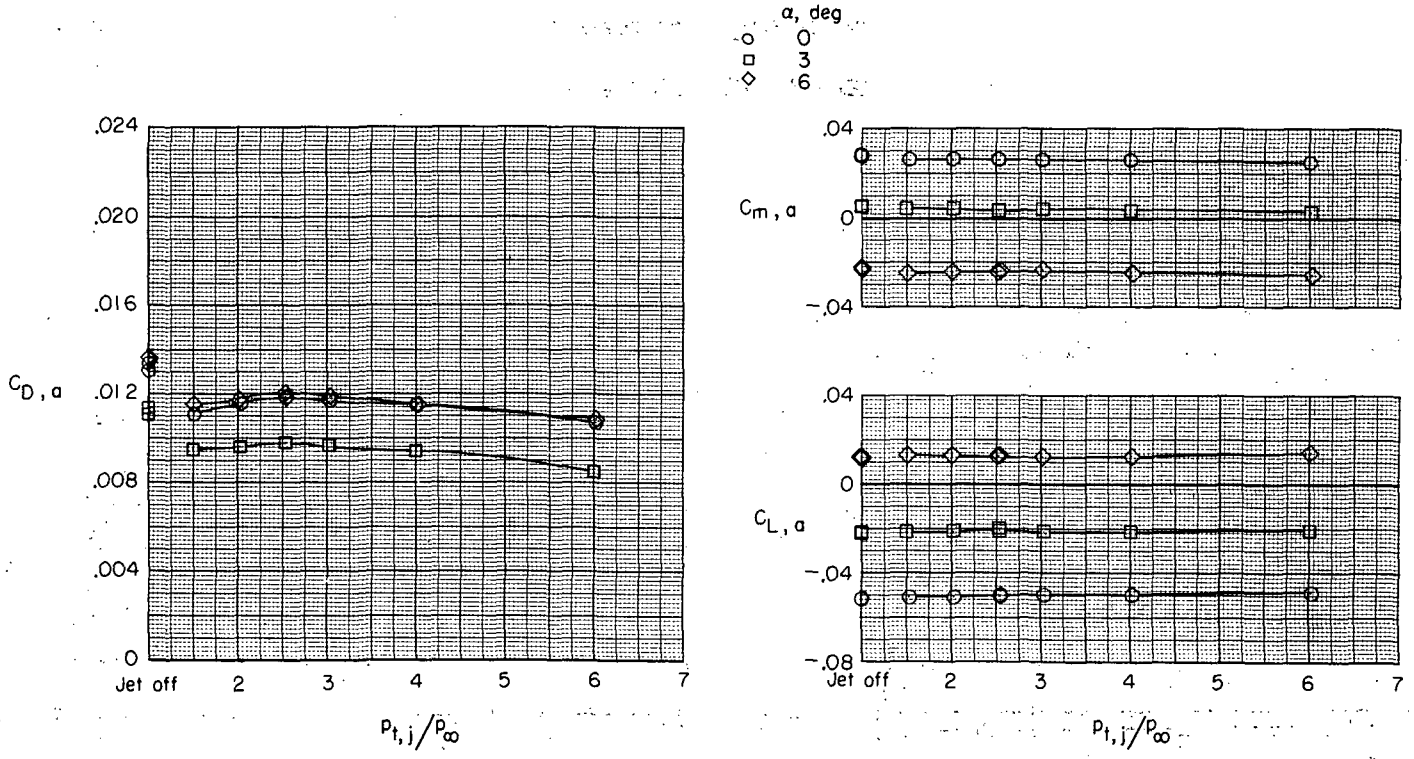

(b) $\delta = 0^o$; $M_\infty = 0.80$.

Figure 13.- Continued.

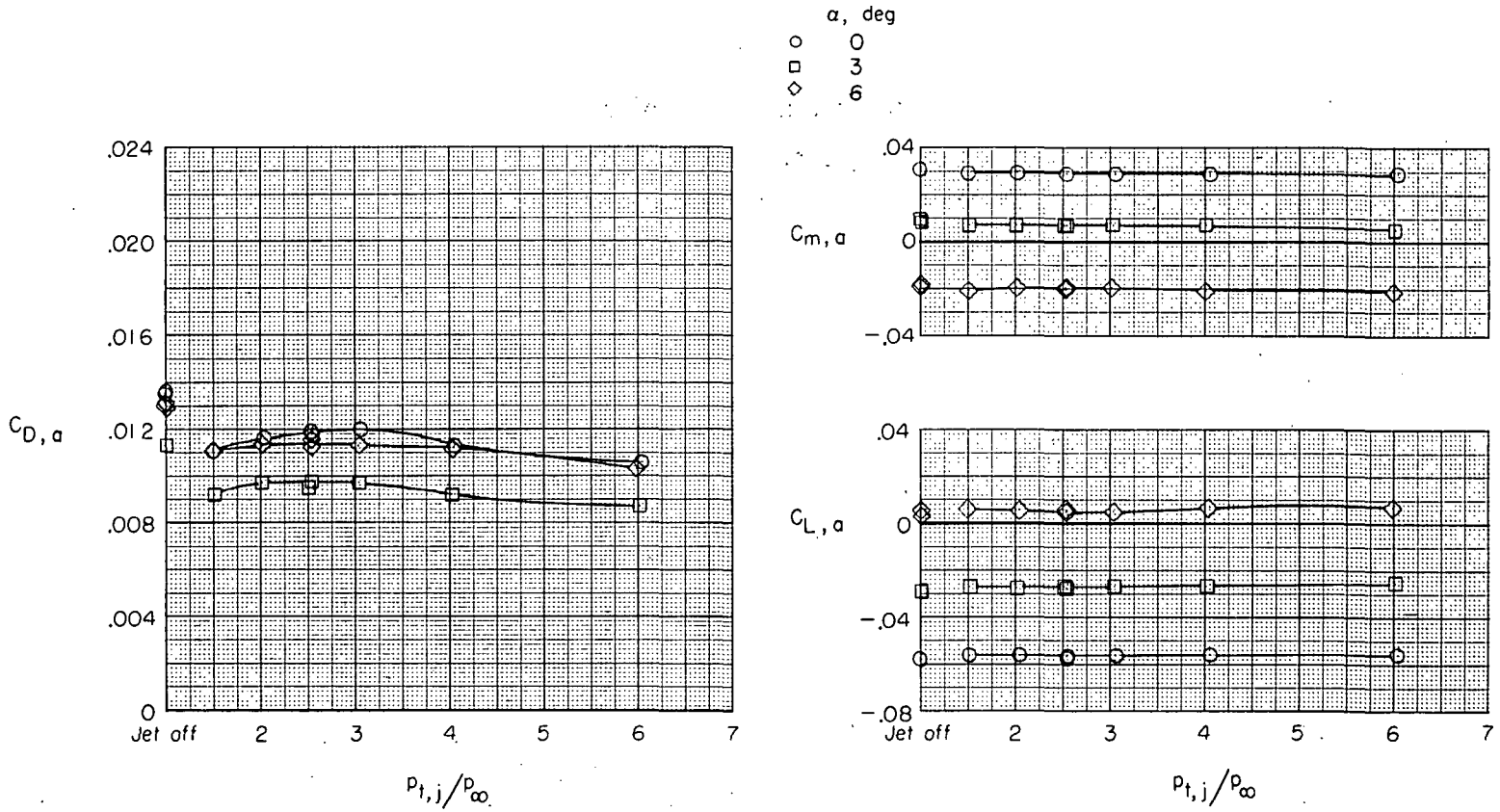

(c) $\delta = 0^o$; $M_\infty = 0.85$.

Figure 13.- Continued.

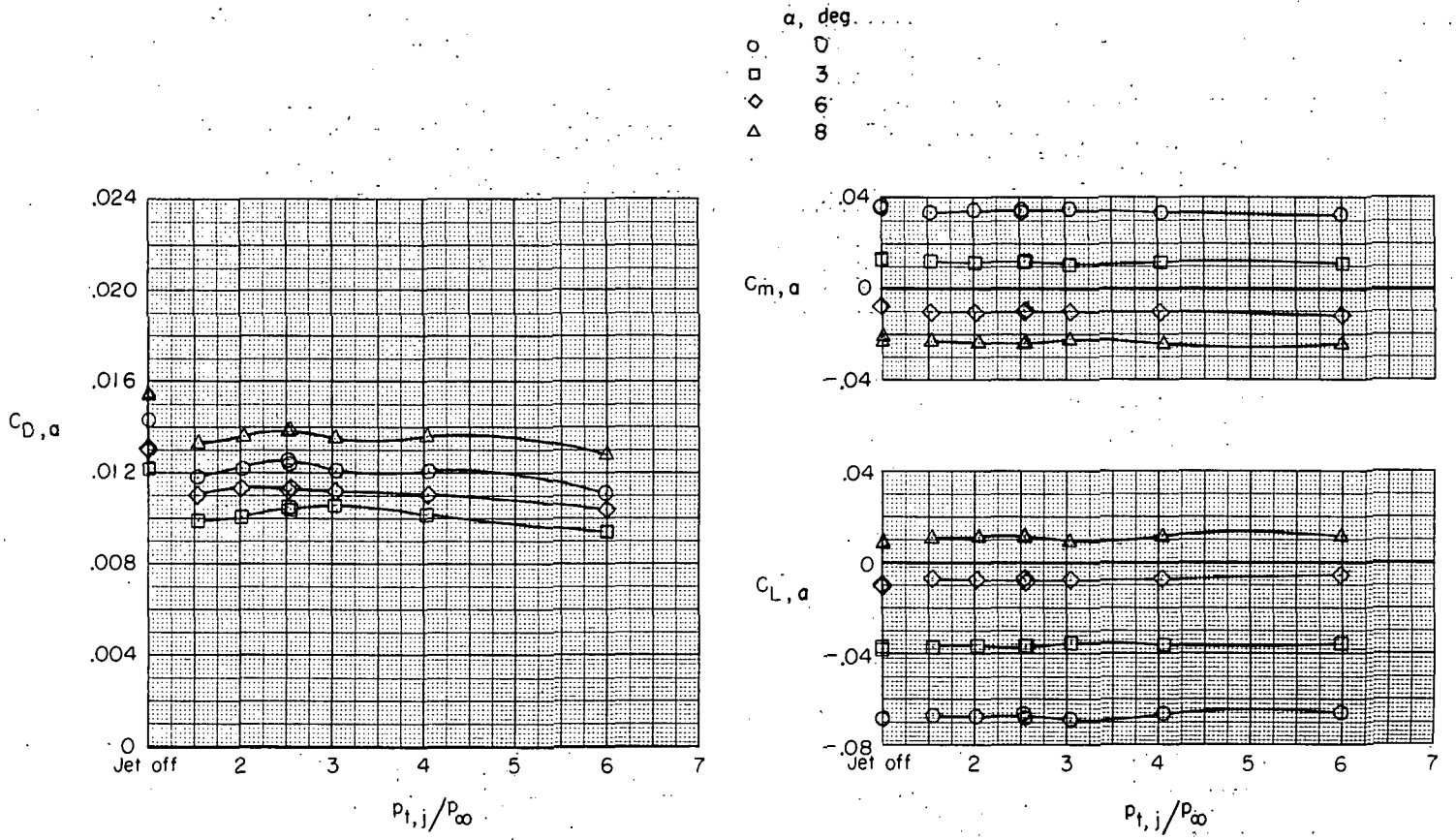

(d) $\delta = 0^o$; $M_\infty = 0.90$.

Figure 13.- Continued.

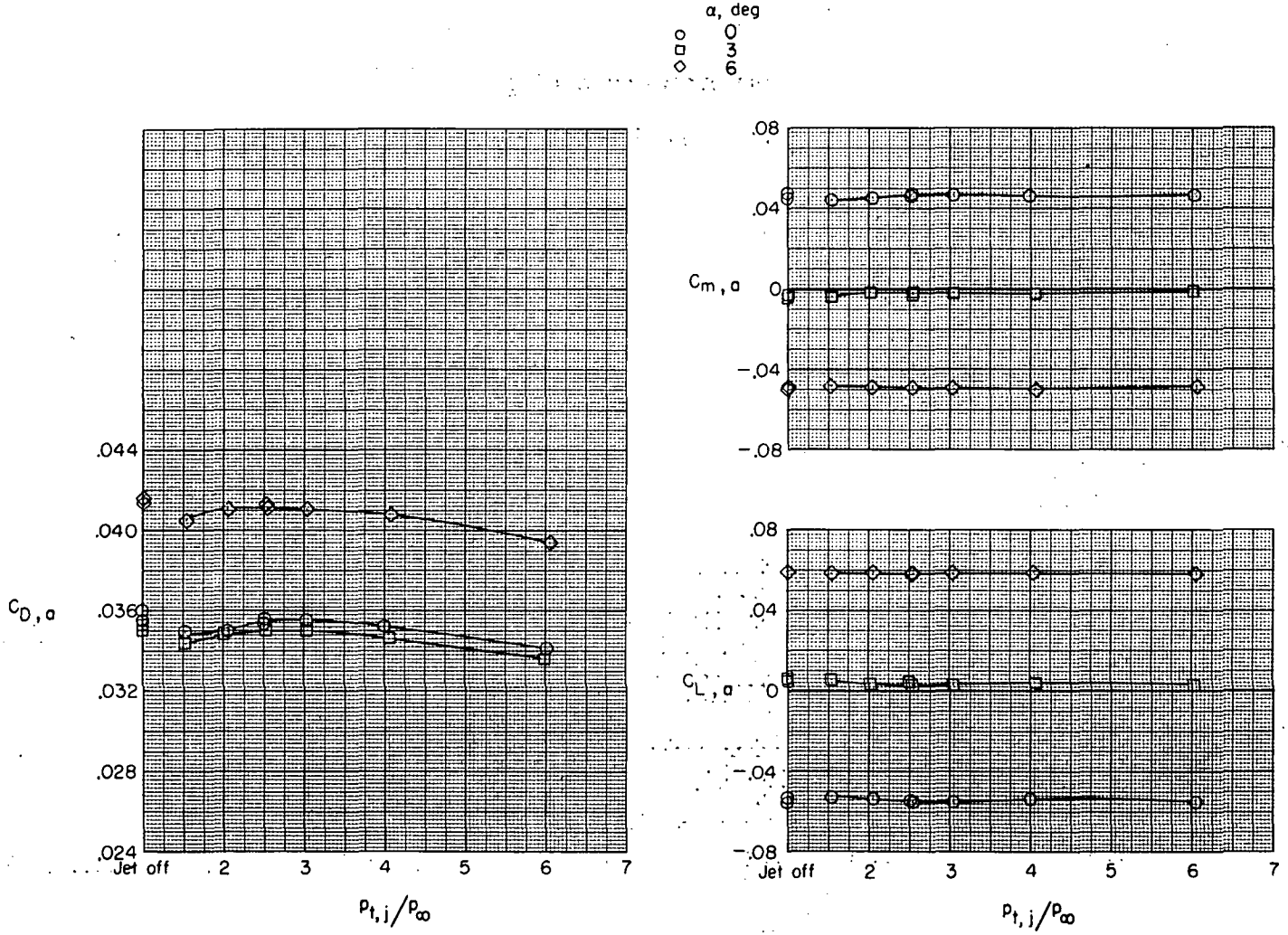

(e) $\delta = 0^o$; $M_\infty = 1.20$.

Figure 13.- Continued.

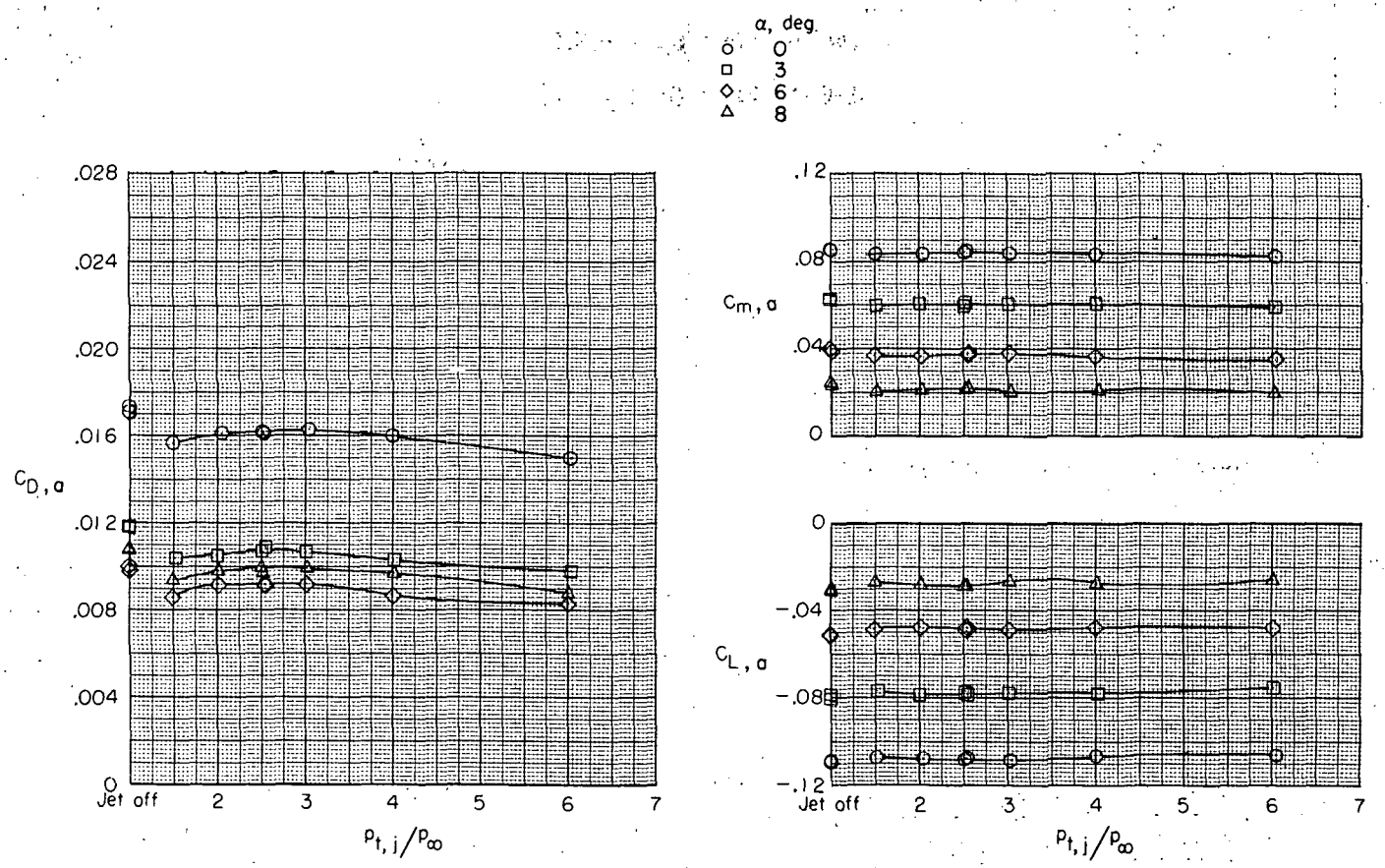

(f) $\delta = -5^o$; $M_\infty = 0.60$.

Figure 13.- Continued.

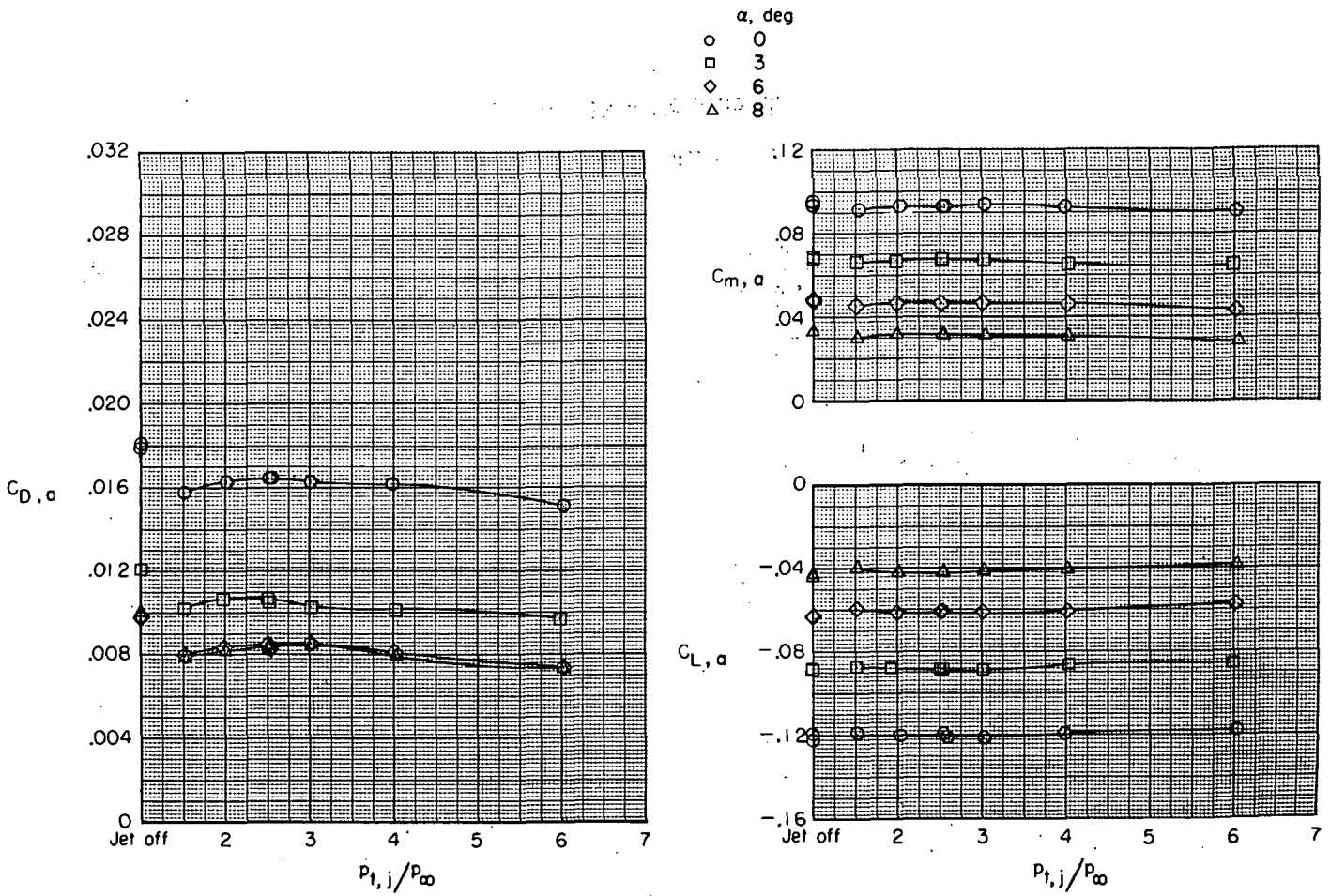

(g) $\delta = -5^{o}$; $M_\infty = 0.80$.

Figure 13.- Continued.

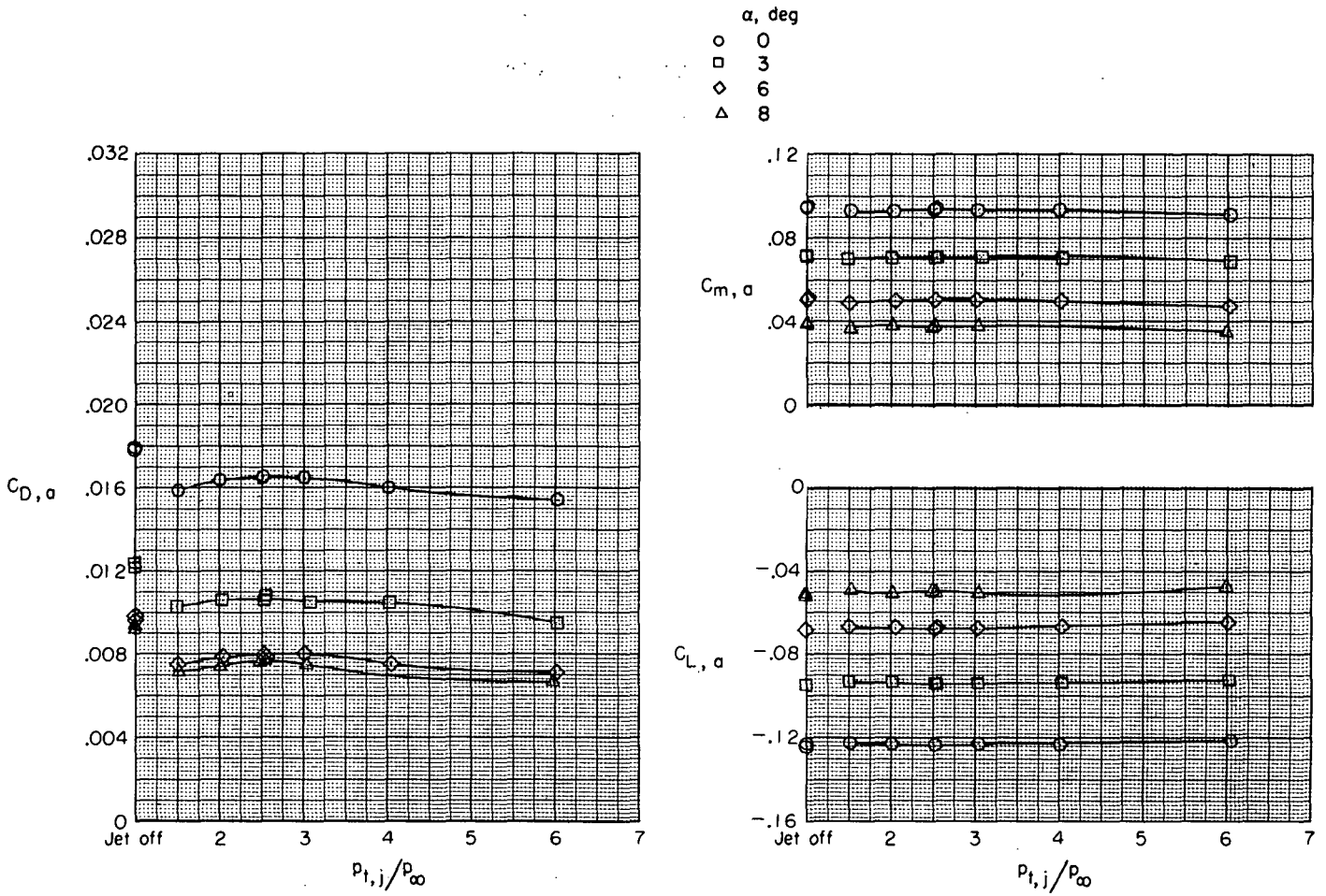

(h) $\delta = -5^o$; $M_\infty = 0.85$.

Figure 13.- Continued.

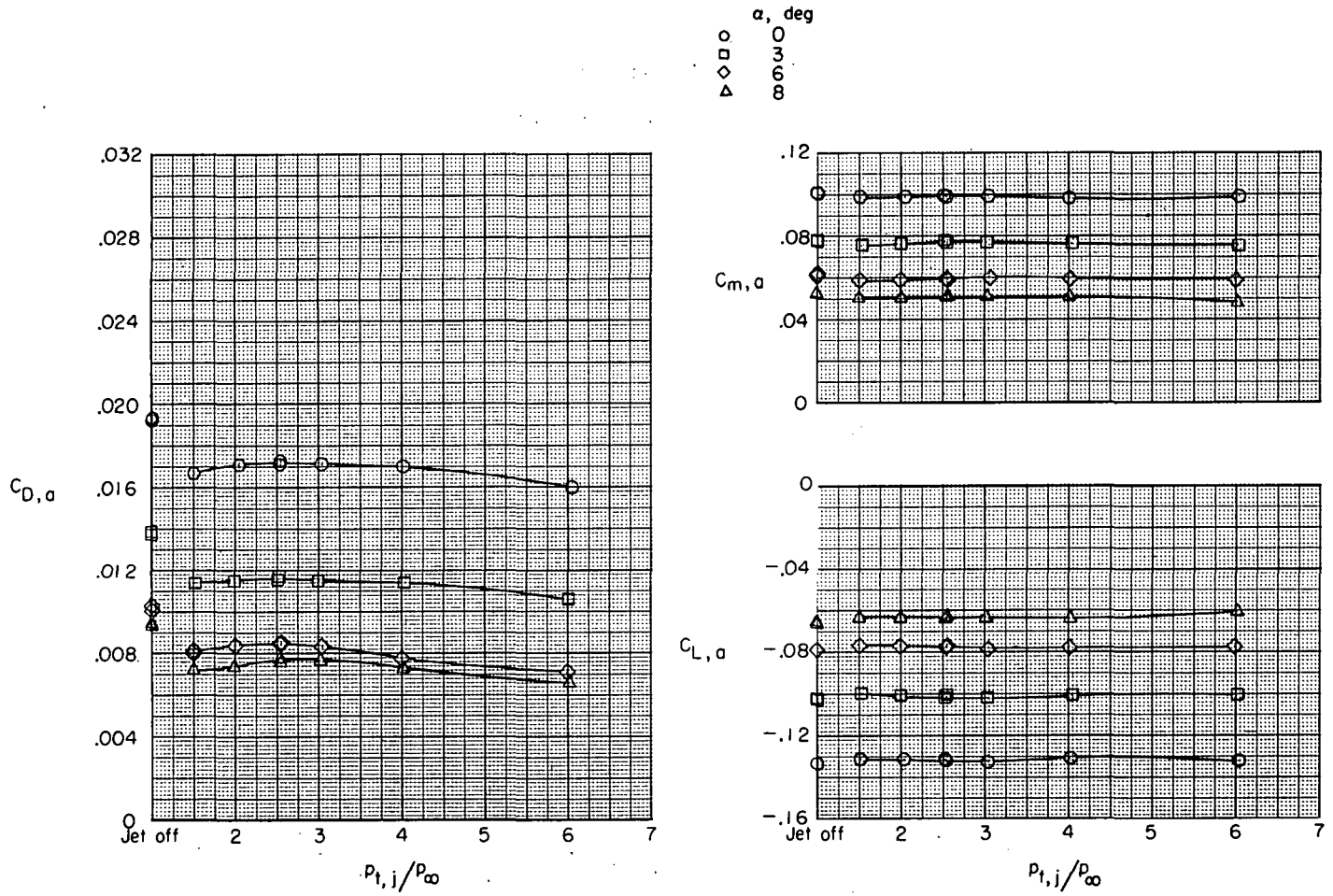

(i) $\delta = -5^o$; $M_\infty = 0.90$.

Figure 13.- Continued.

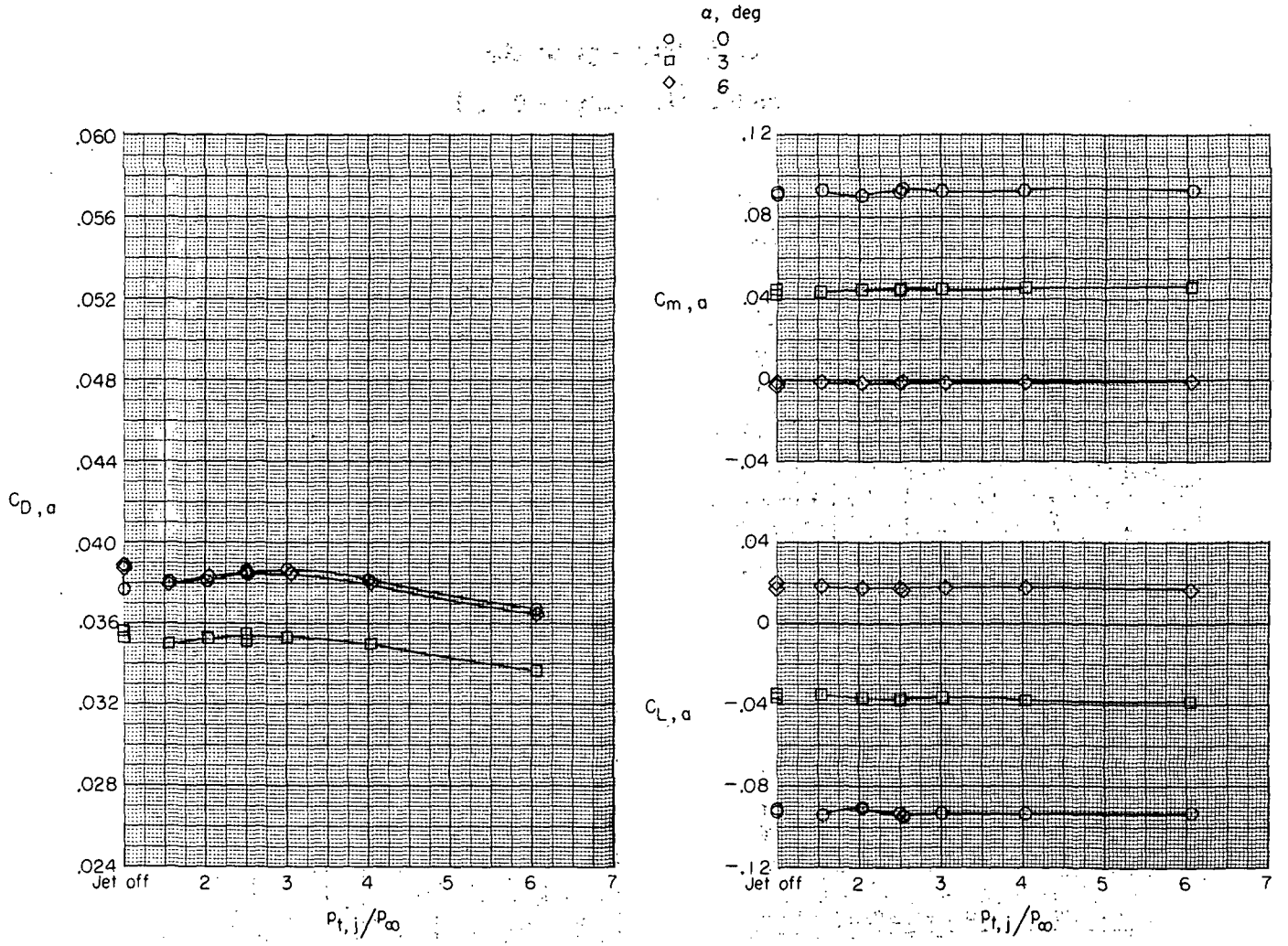

(j) $\delta = -5^o$; $M_\infty = 1.20$.

Figure 13.- Continued.

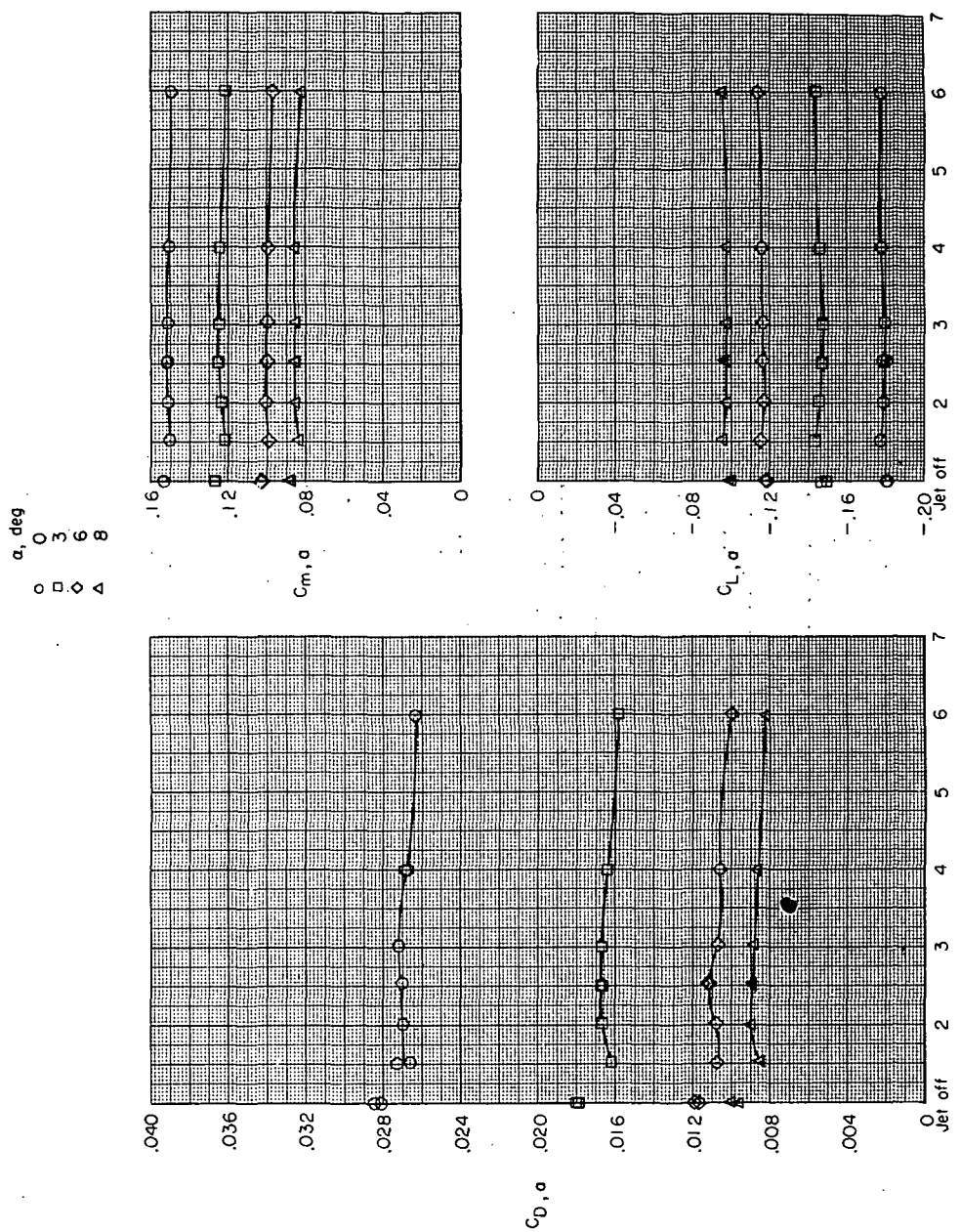

(k) $\delta = -10^o$; $M_\infty = 0.60$.

Figure 13.- Continued.

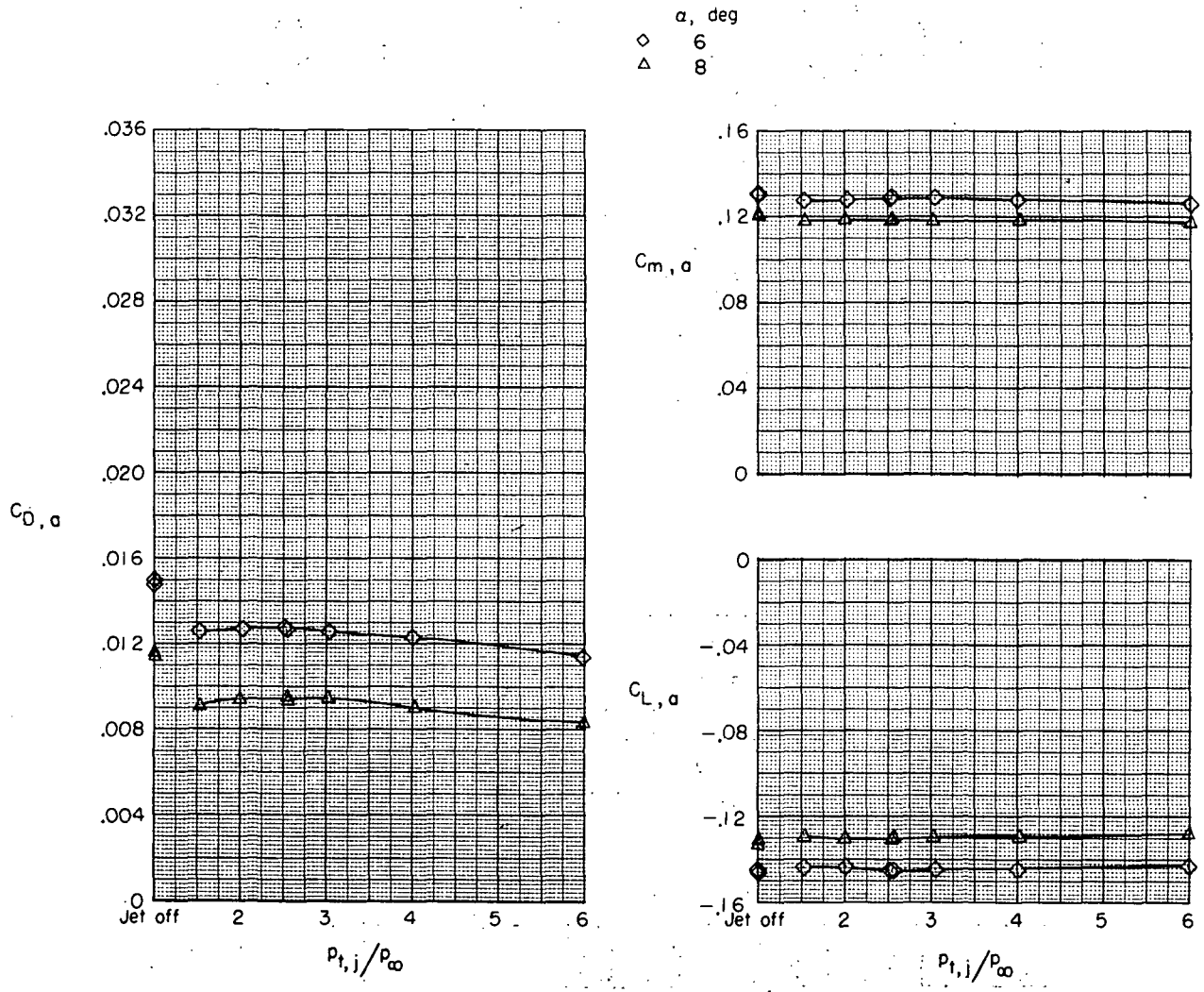

(l) $\delta = -10^{o}$; $M_\infty = 0.90$.

Figure 13.- Concluded.

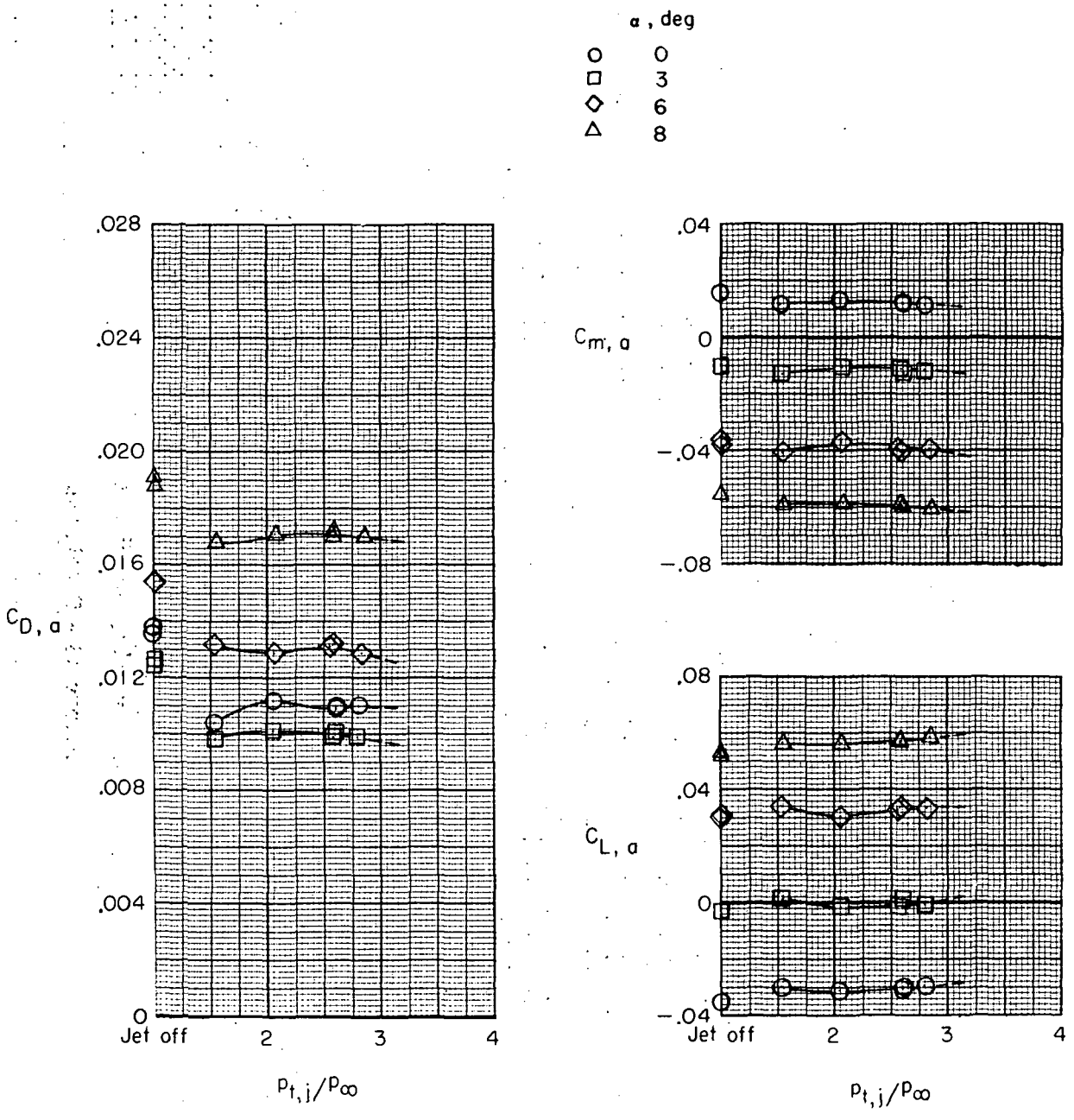

(a) $\delta = 0^o$; $M_\infty = 0.60$.

Figure 14.- Effect of jet total pressure ratio on aerodynamic characteristics of translating-flap nozzle configuration in afterburning position. Dashed lines indicate extrapolated data.

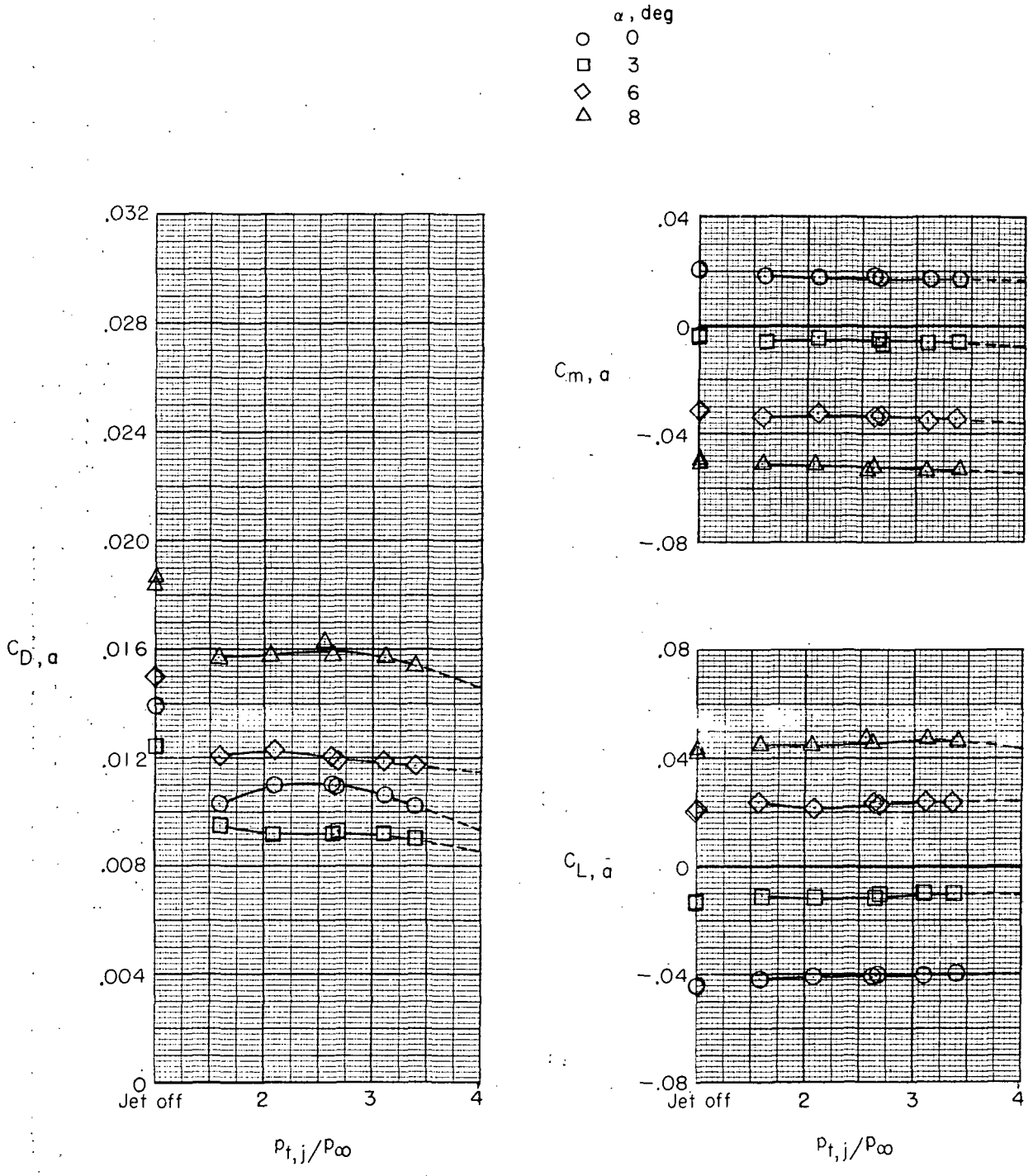

(b) $\delta = 0^o$; $M_\infty = 0.80$.

Figure 14.- Continued.

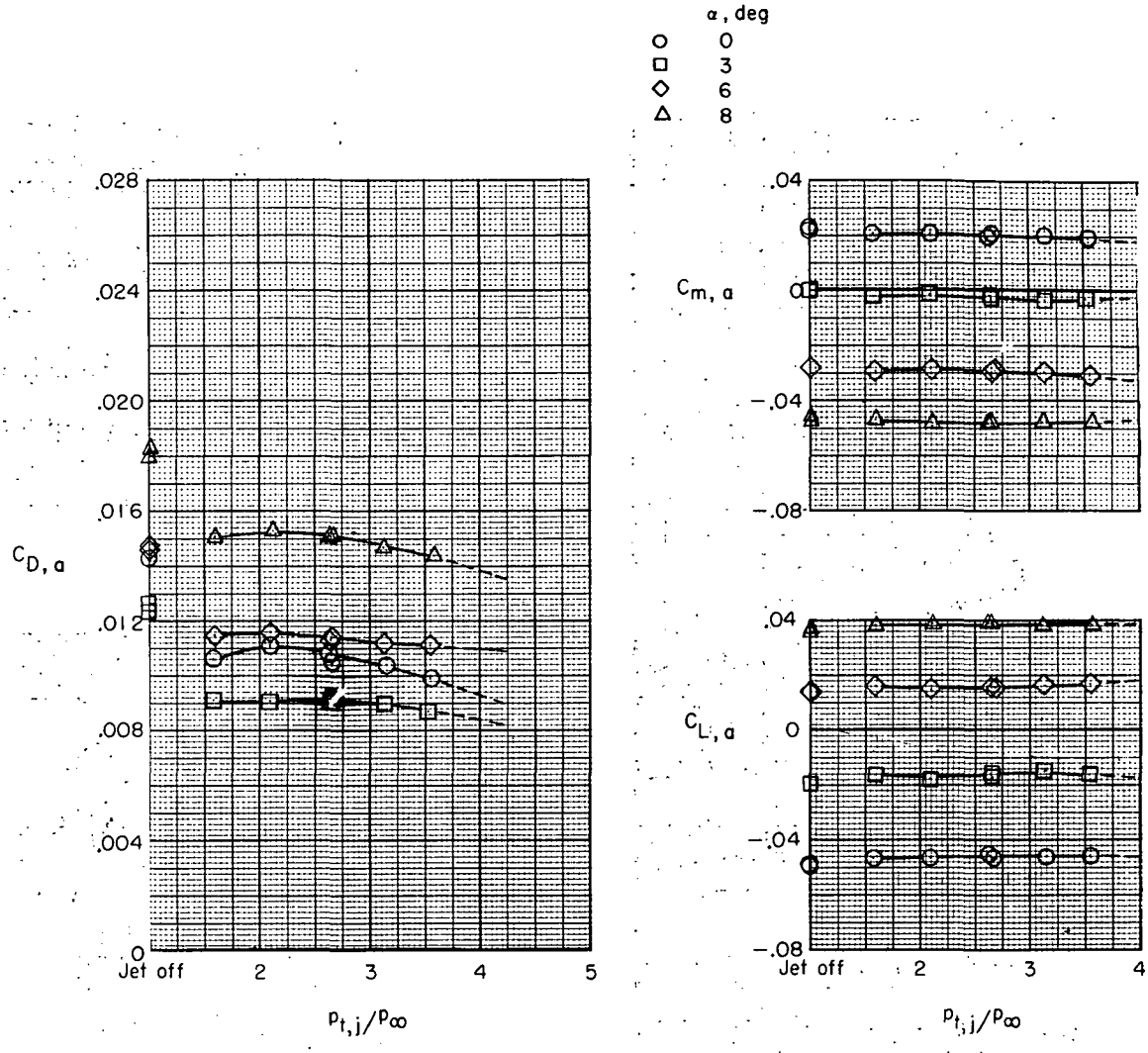

(c) $\delta = 0^o$; $M_\infty = 0.85$.

Figure 14.- Continued.

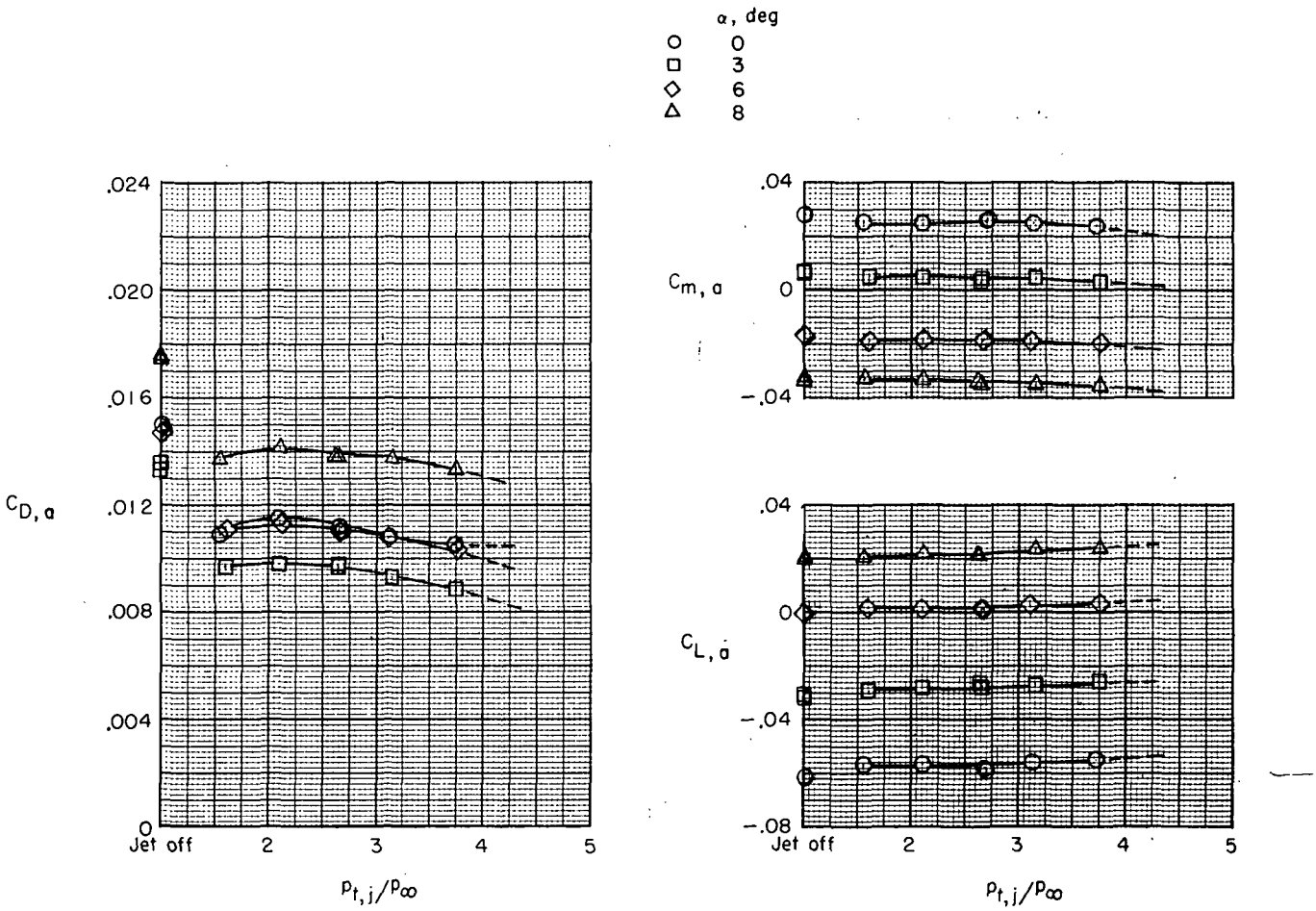

(d) $\delta = 0^{o}$; $M_\infty = 0.90$.

Figure 14.- Continued.

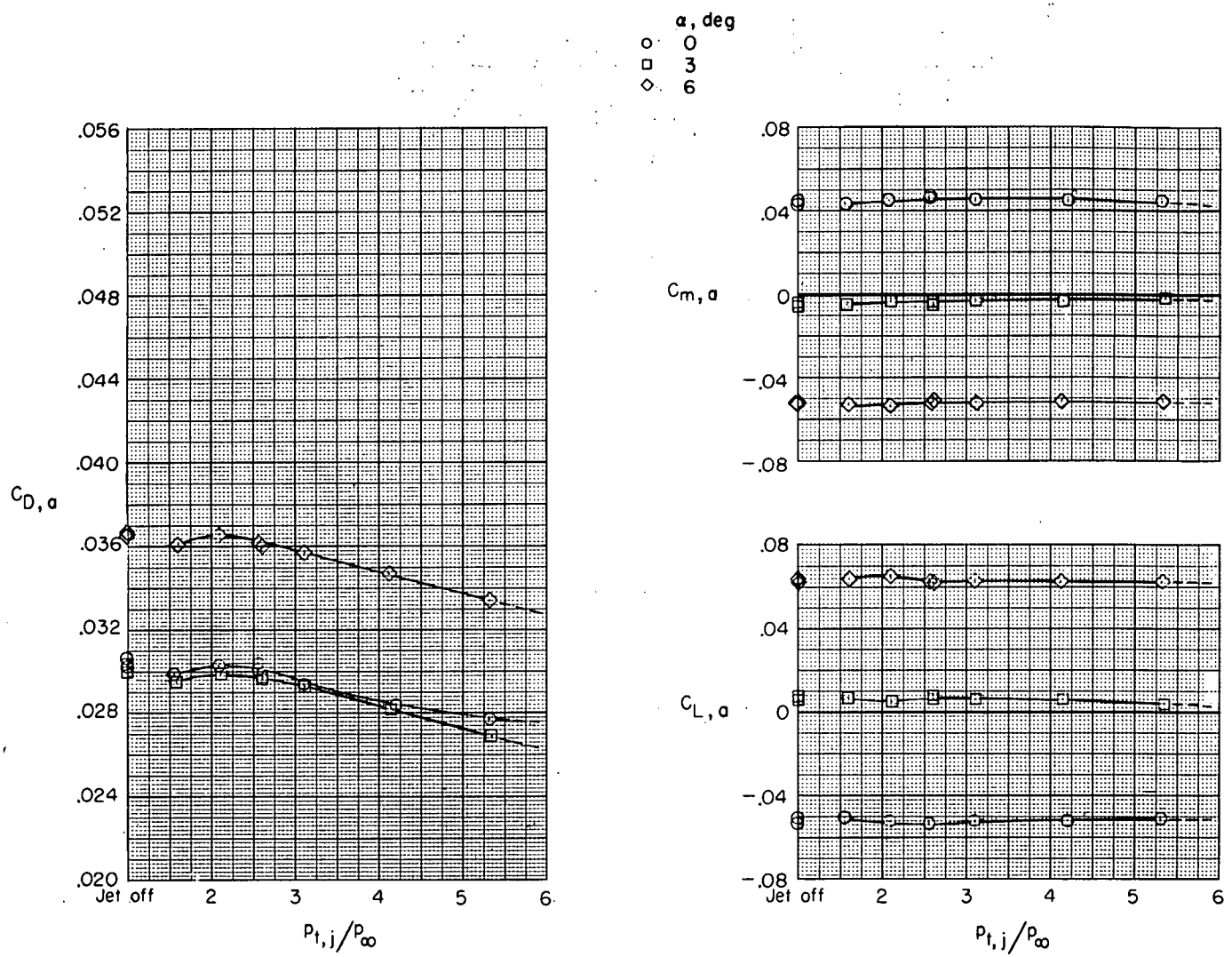

(e) $\delta = 0^o$; $M_\infty = 1.20$.

Figure 14.- Continued.

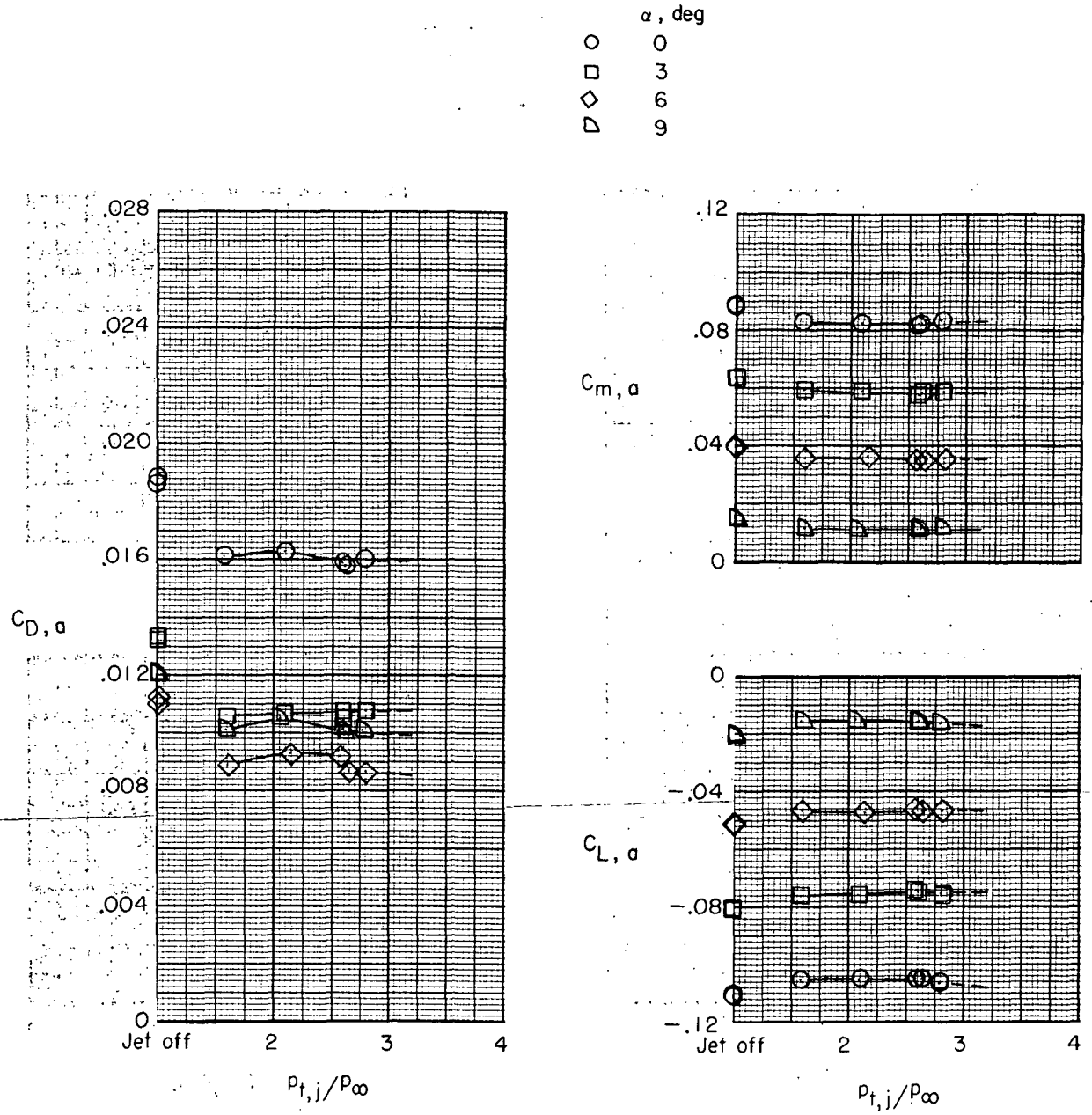

(f) $\delta = -5^o$; $M_\infty = 0.60$.

Figure 14.- Continued.

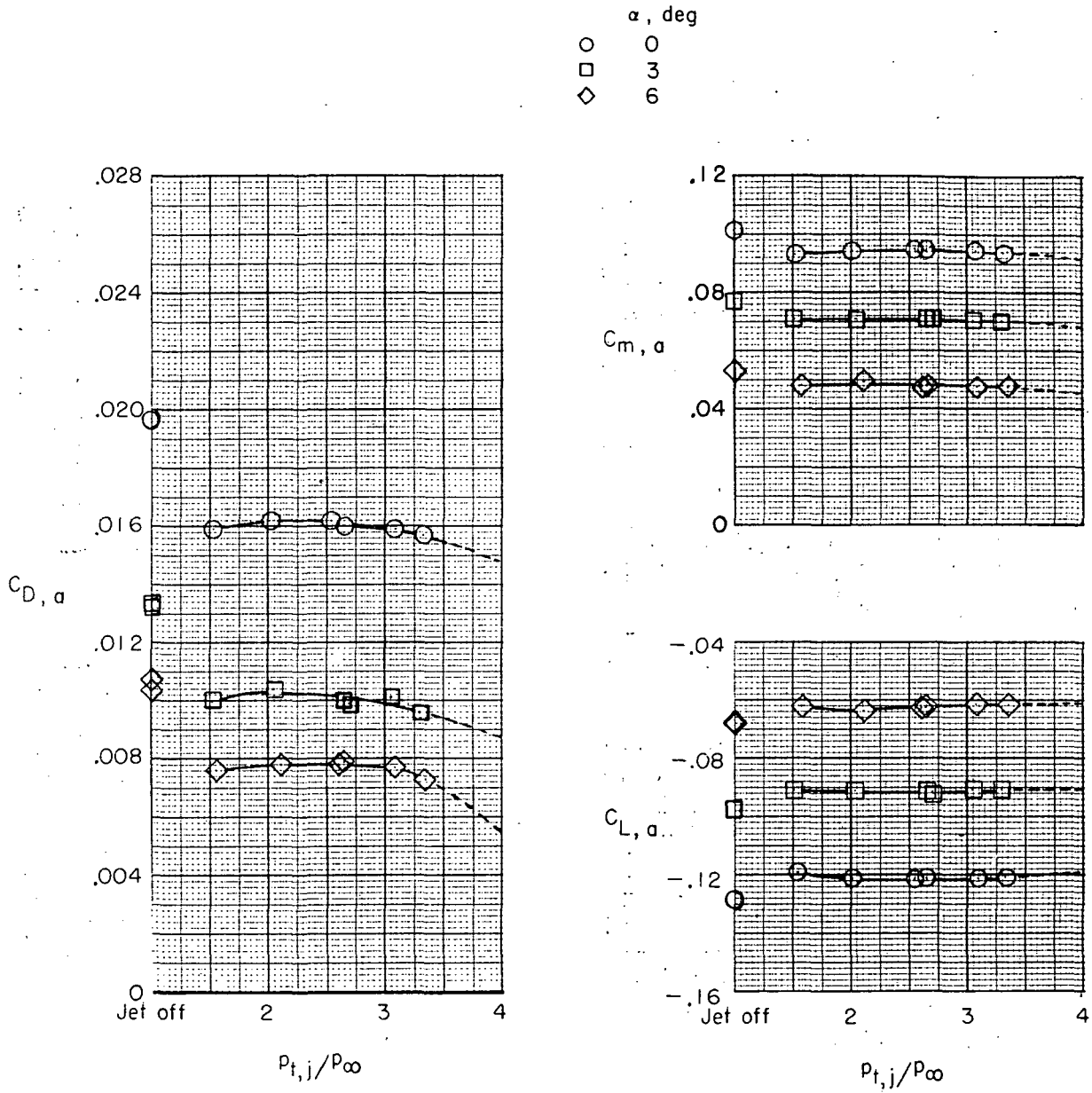

(g) $\delta = -5^o$; $M_\infty = 0.80$.

Figure 14.- Continued.

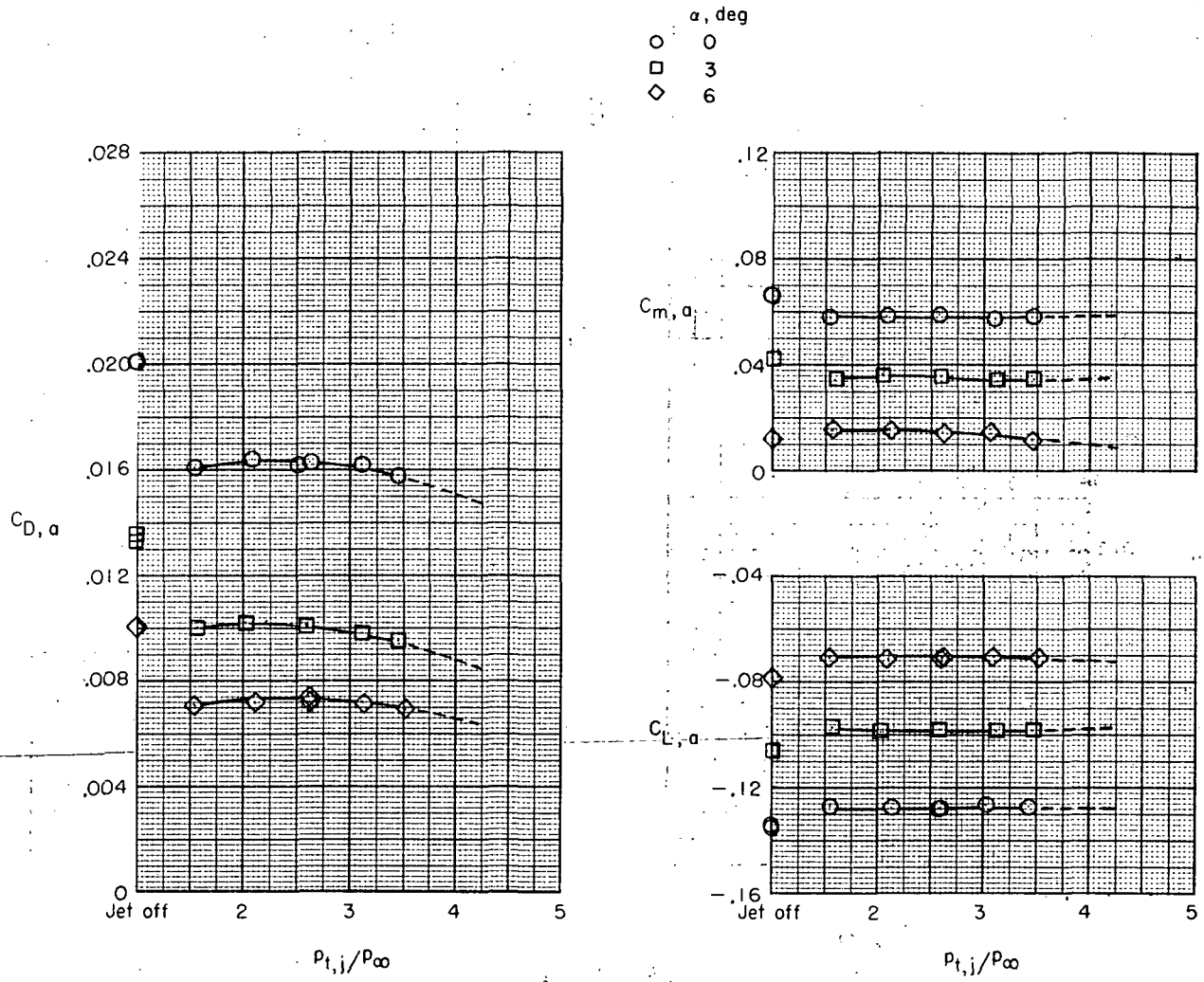

(h) $\delta = -5^o$; $M_\infty = 0.85$.

Figure 14.- Continued.

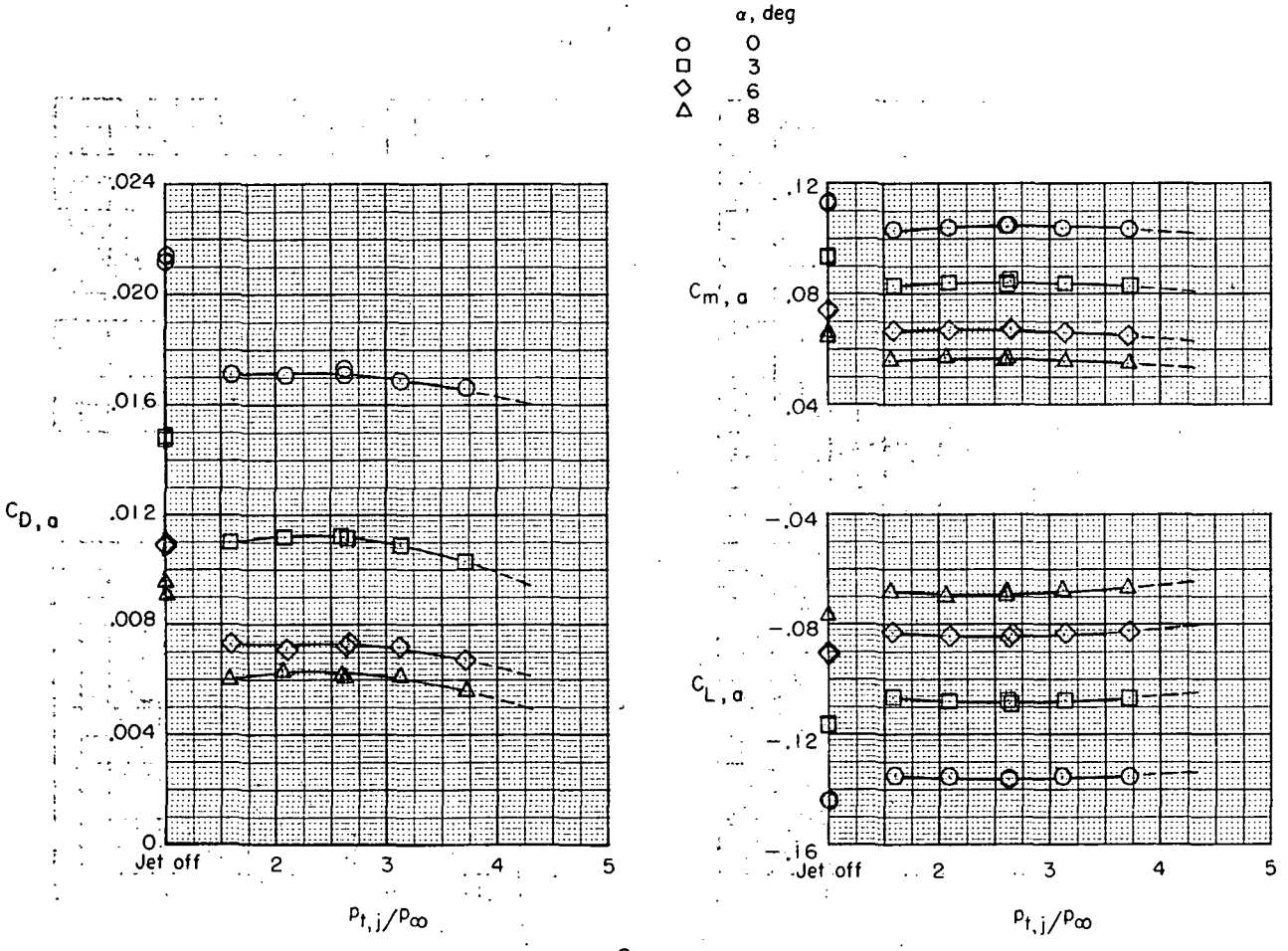

(i) $\delta_e = -5^o$; $M_\infty = 0.90$.

Figure 14.- Continued.

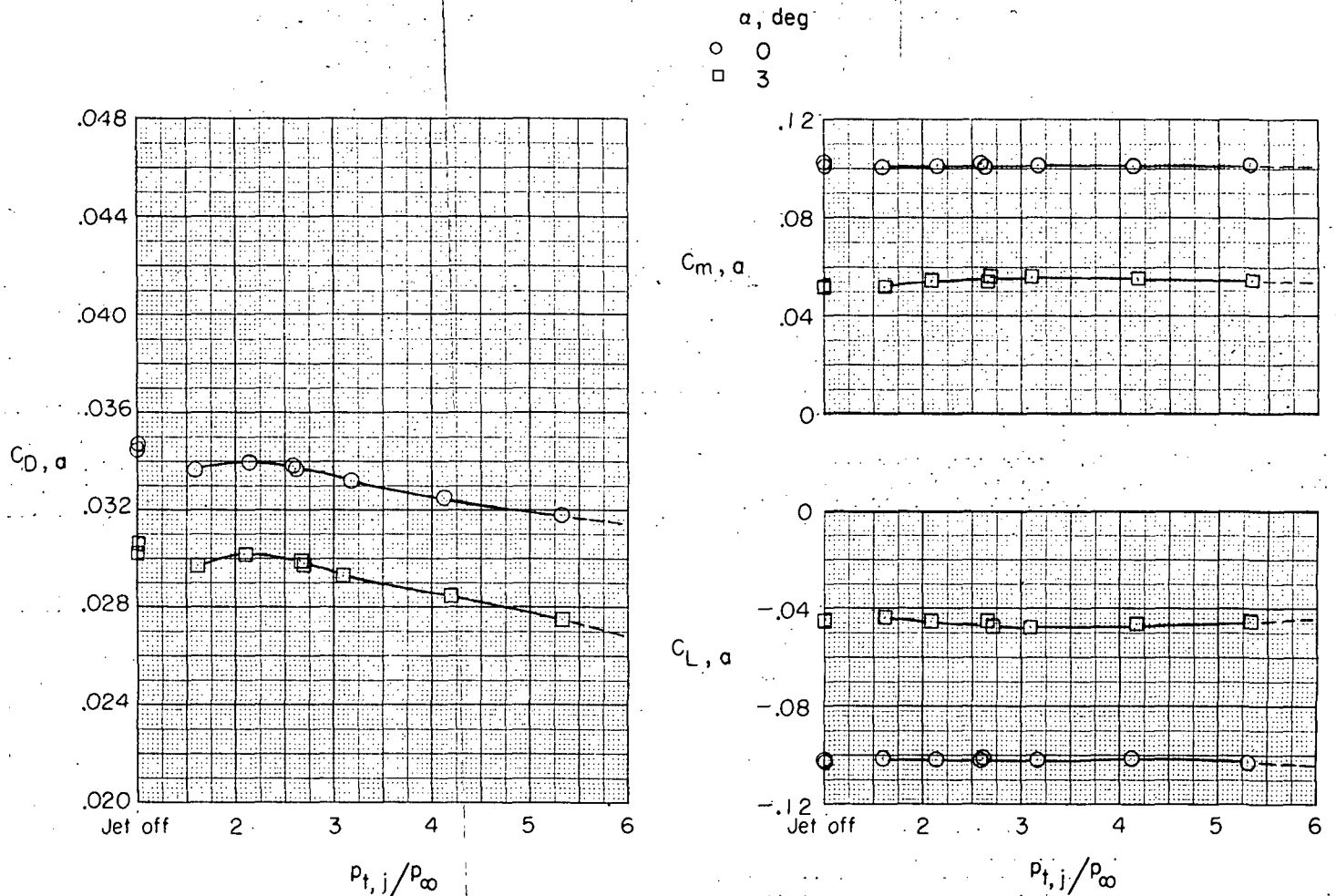

(j) $\delta = -5^o$; $M_\infty = 1.20$.

Figure 14.- Continued.

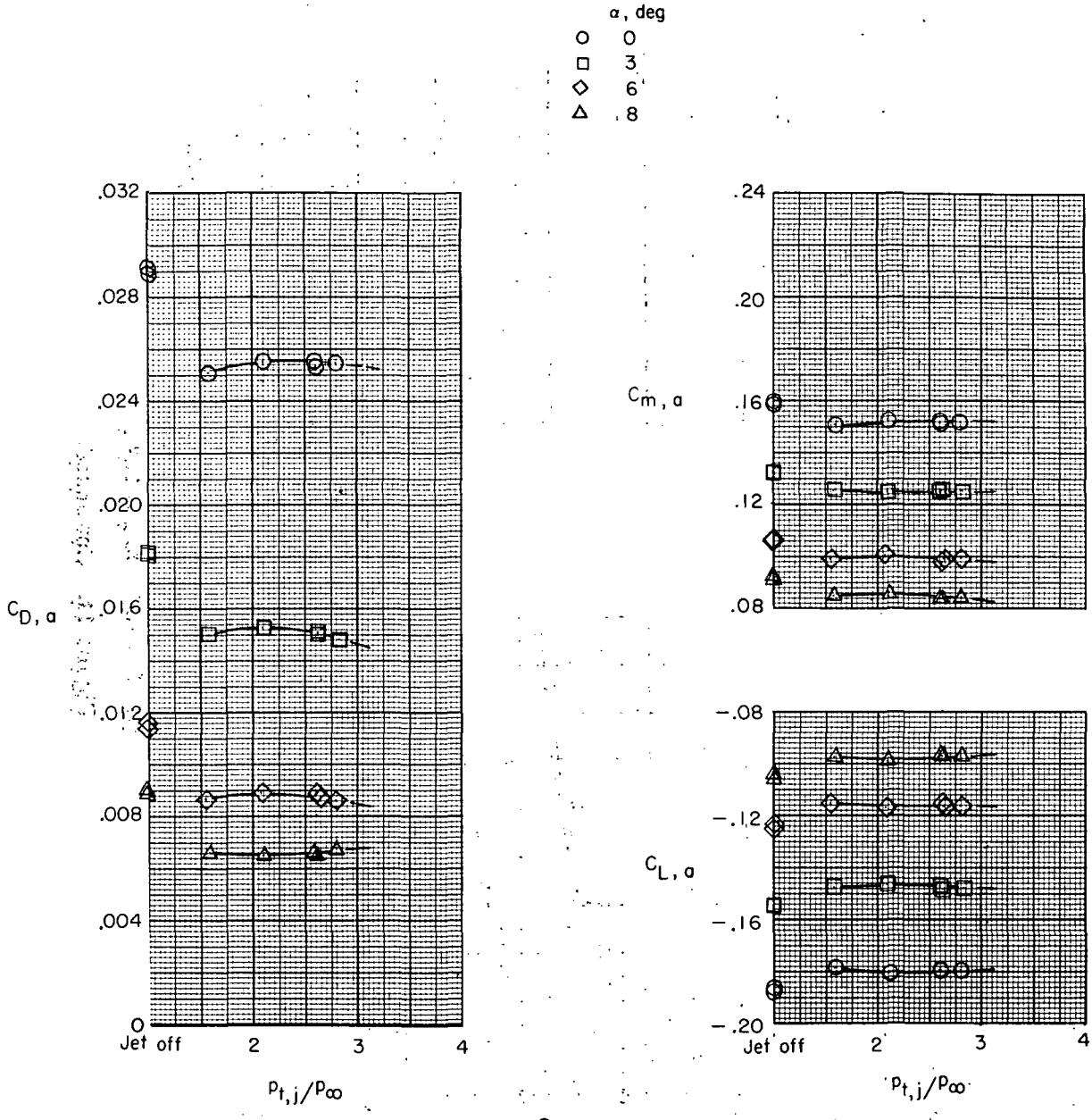

(k) $\delta = -10^{o}$; $M_\infty = 0.60$.

Figure 14. - Continued.

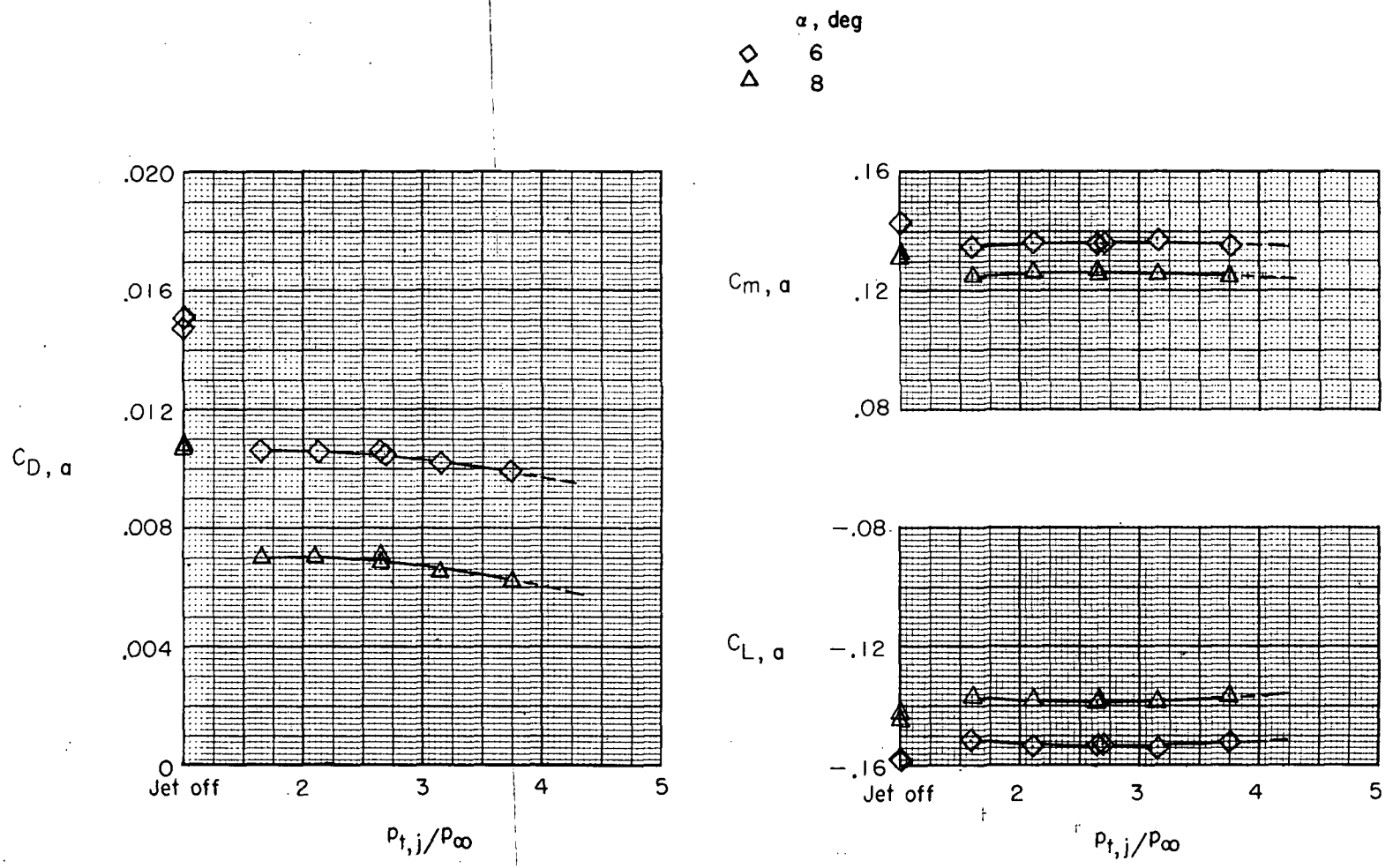

(l) $\delta = -10^o$; $M_\infty = 0.90$.

Figure 14.- Concluded.

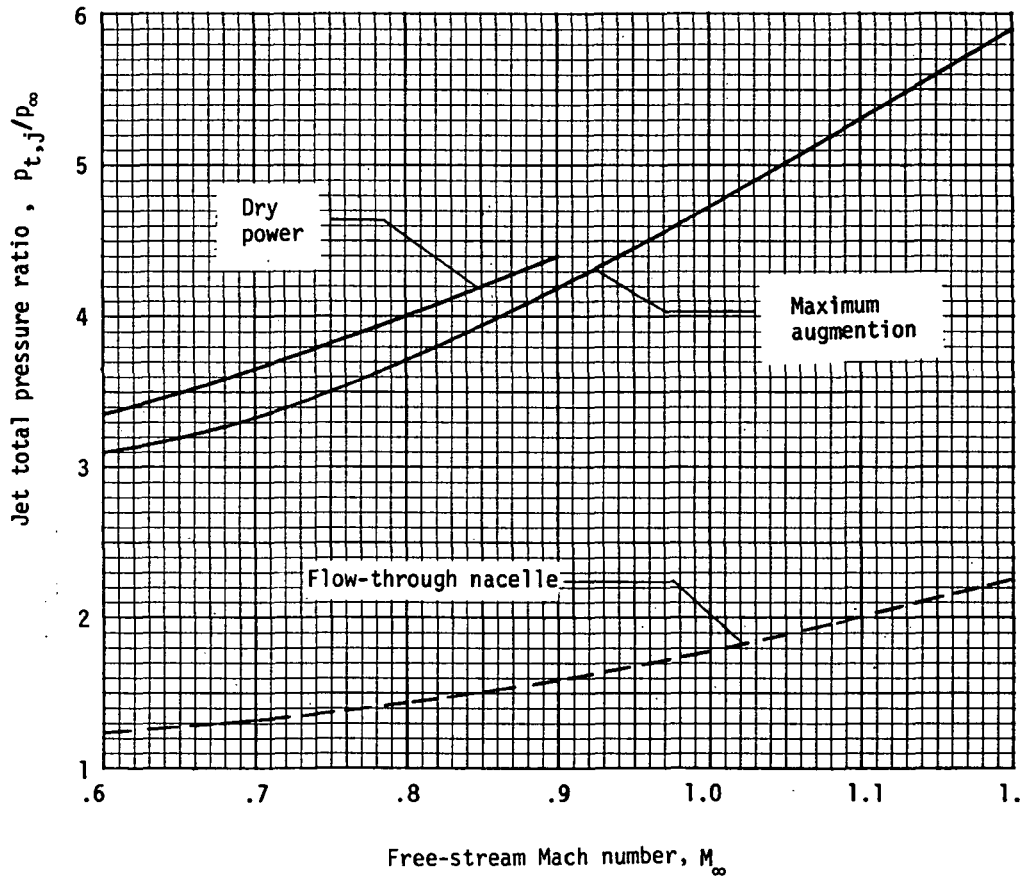

Figure 15.- Typical fan jet total pressure ratio schedule for a fighter airplane with a turbofan engine.

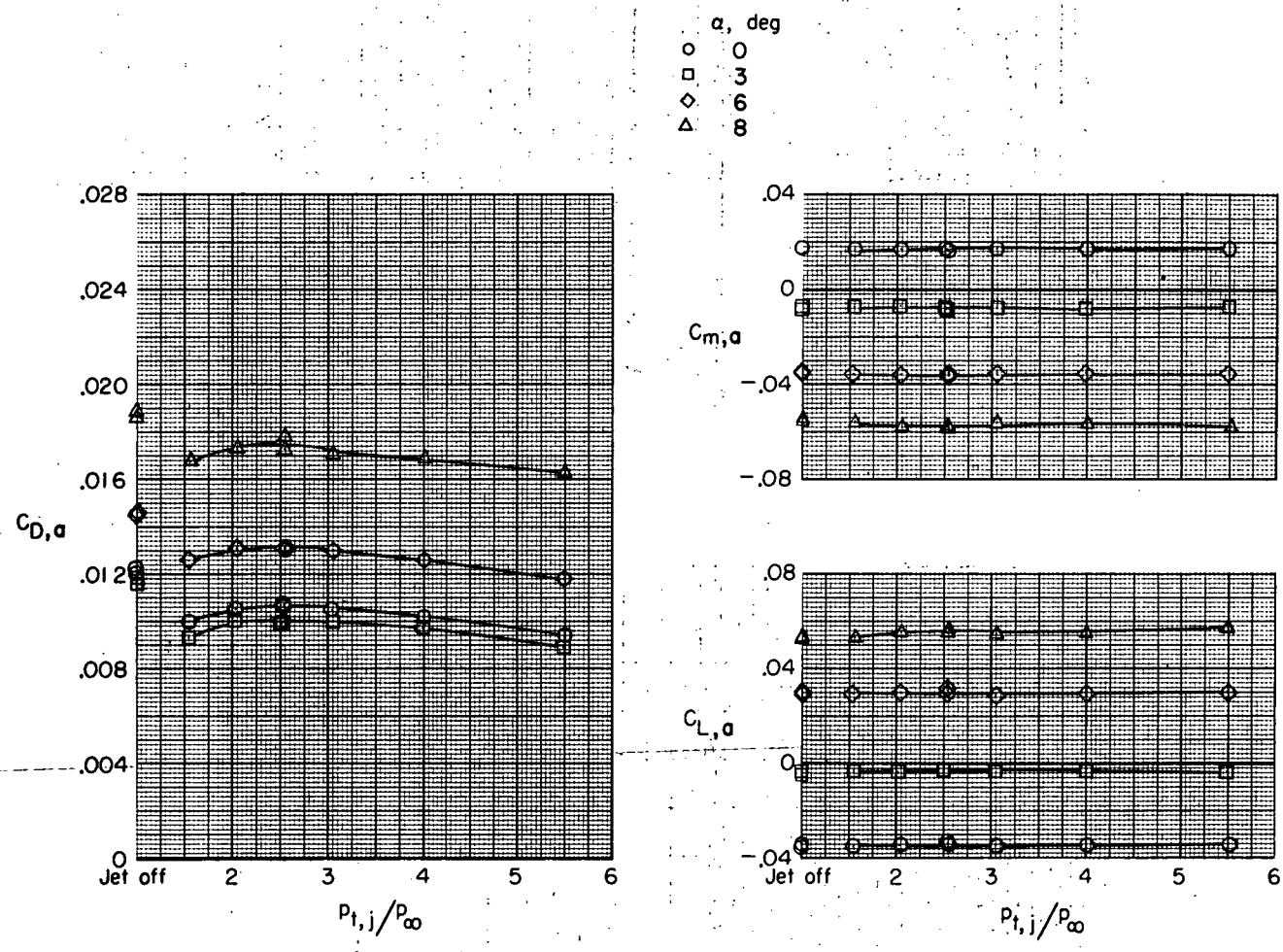

(a) $\delta = 0^o$; $M_\infty = 0.60$.

Figure 16.- Effect of jet total pressure ratio on aerodynamic characteristics of hinged-flap nozzle configurations in cruise position.

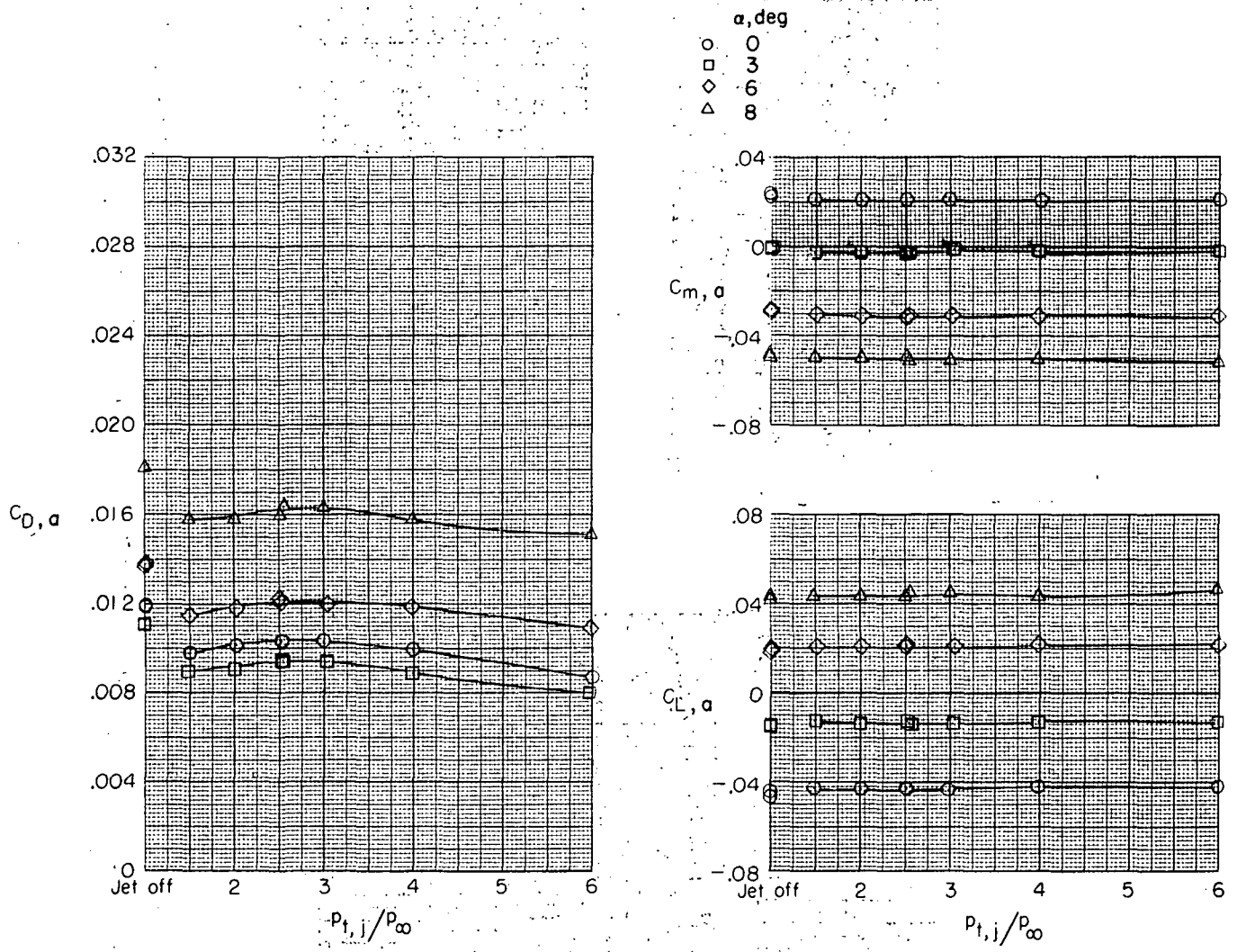

(b) $\delta = 0^o$; $M_\infty = 0.80$.

Figure 16.- Continued.

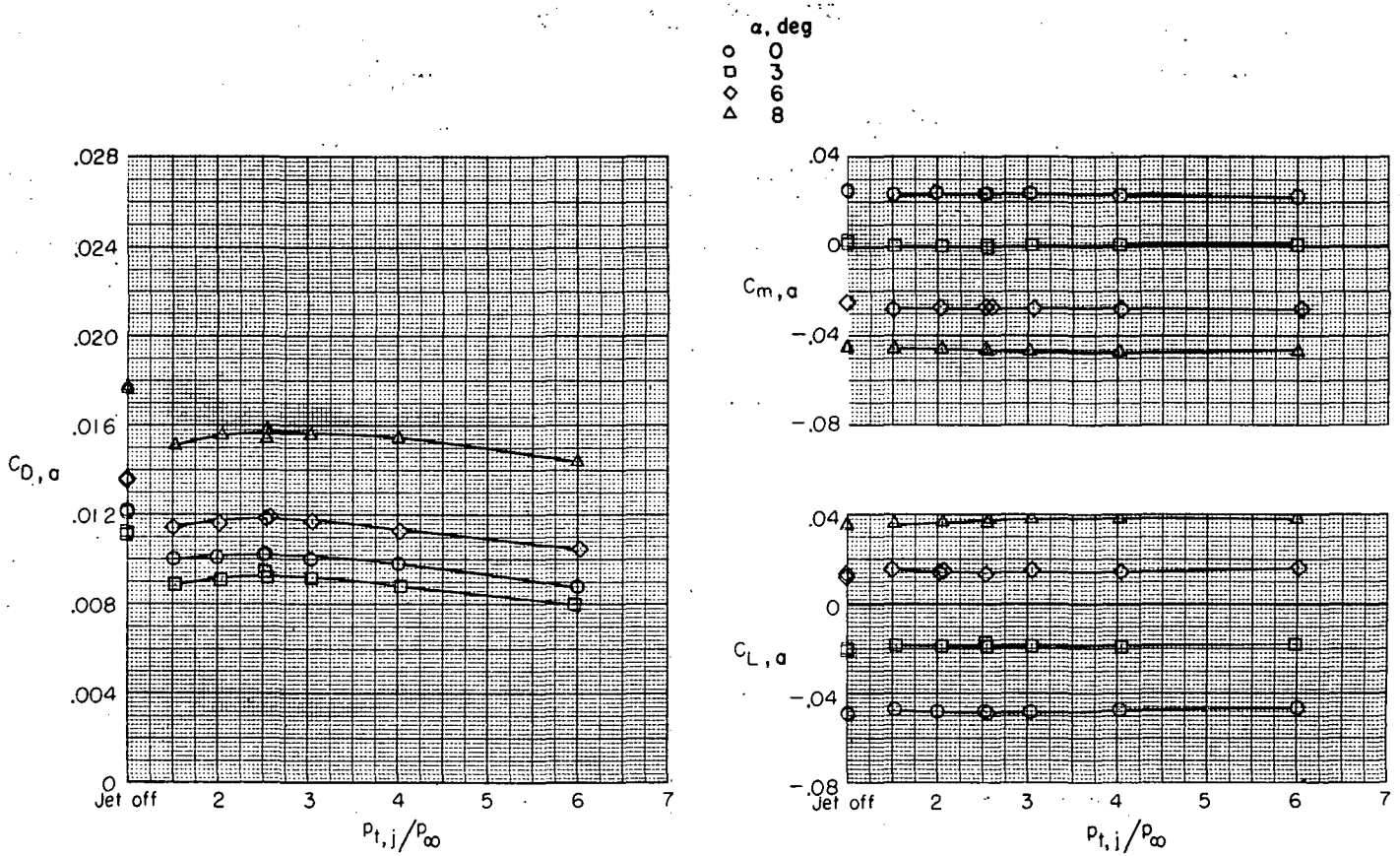

(c) $\delta = 0^o$; $M_\infty = 0.85$.

Figure 16.- Continued.

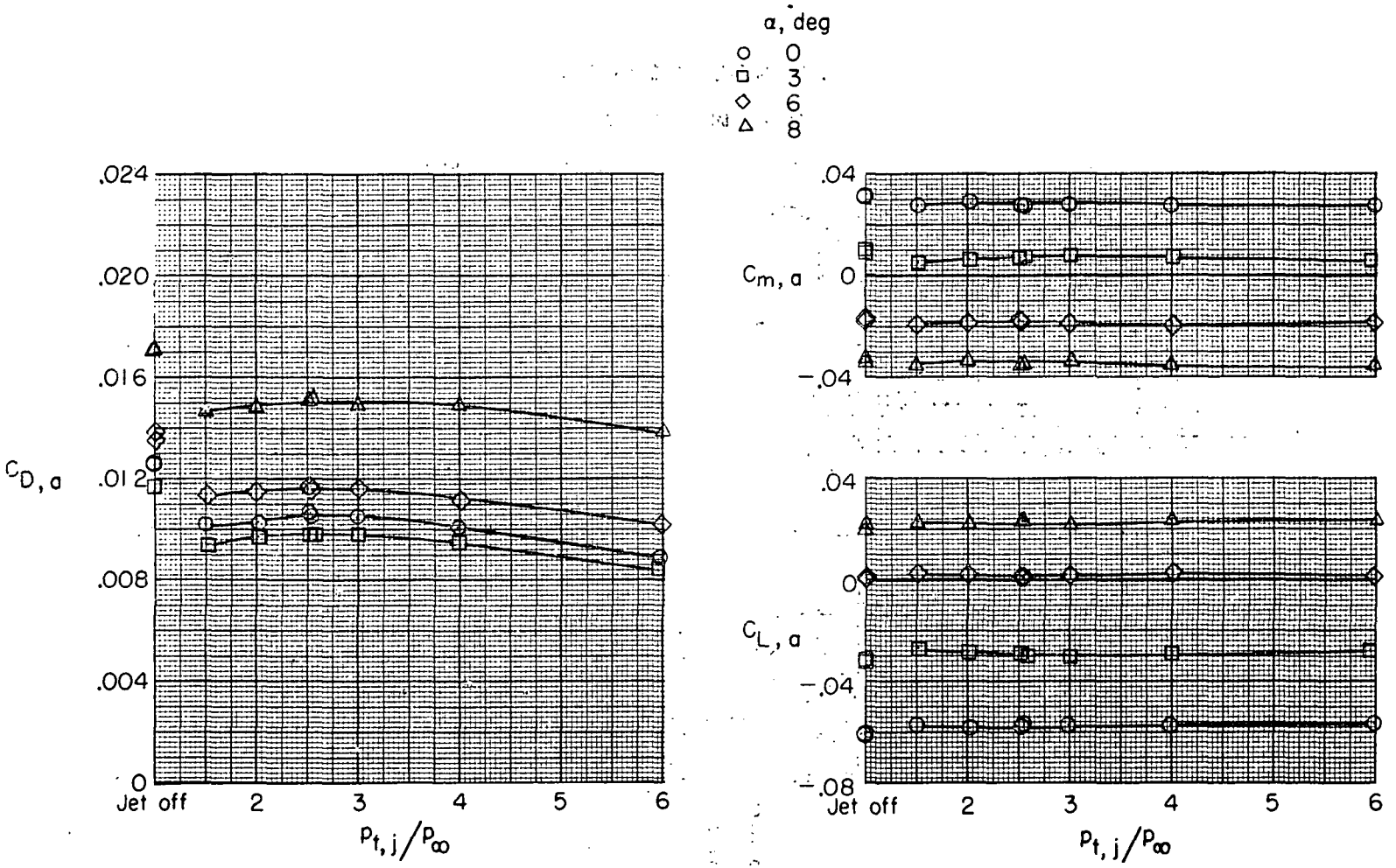

(d) $\delta = 0^o$; $M_\infty = 0.90$.

Figure 16.- Continued.

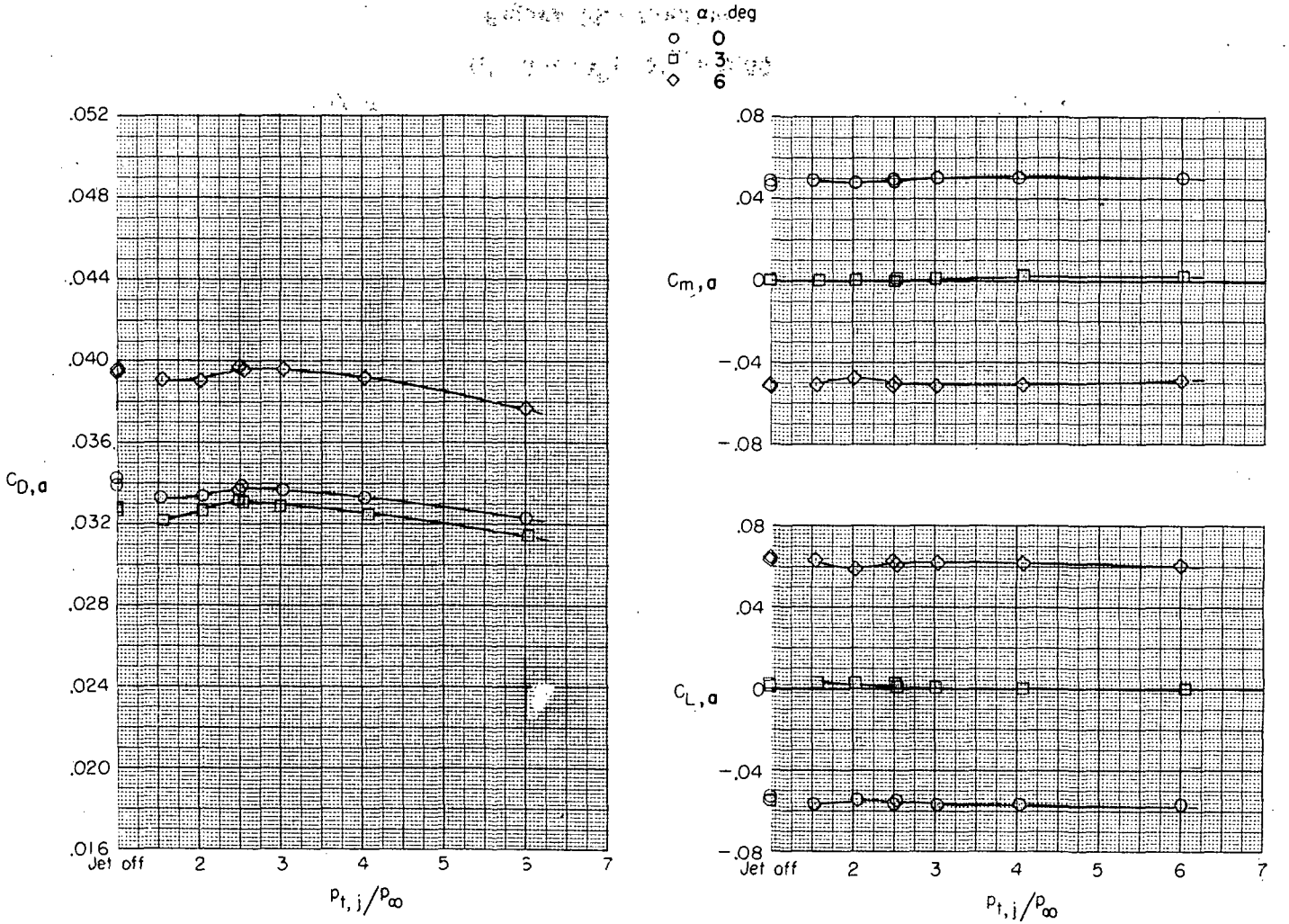

(e) $\delta = 0^o$; $M_\infty = 1.20$.

Figure 16.- Continued.

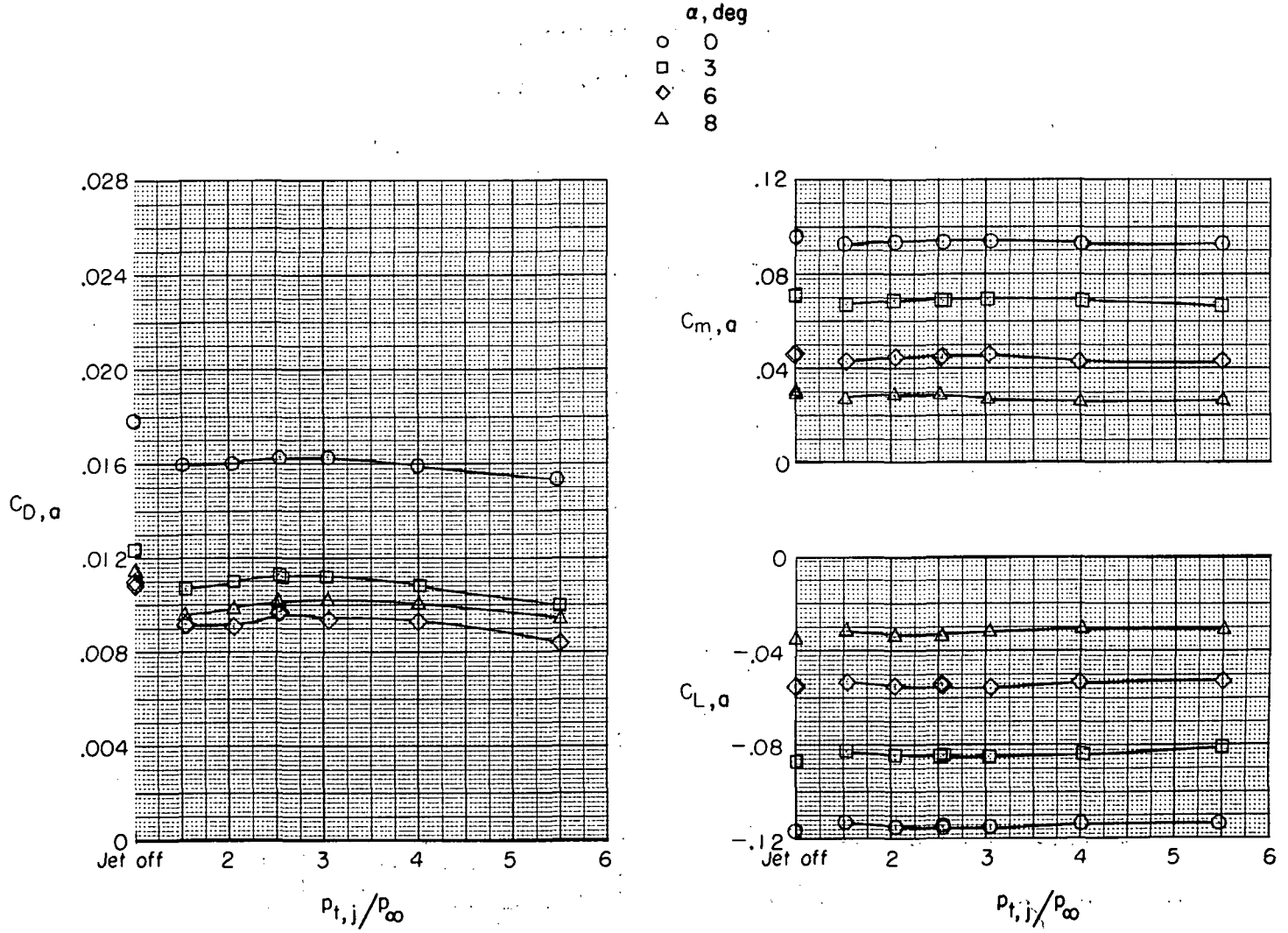

(f) $\delta = -5^o$; $M_\infty = 0.60$.

Figure 16.- Continued.

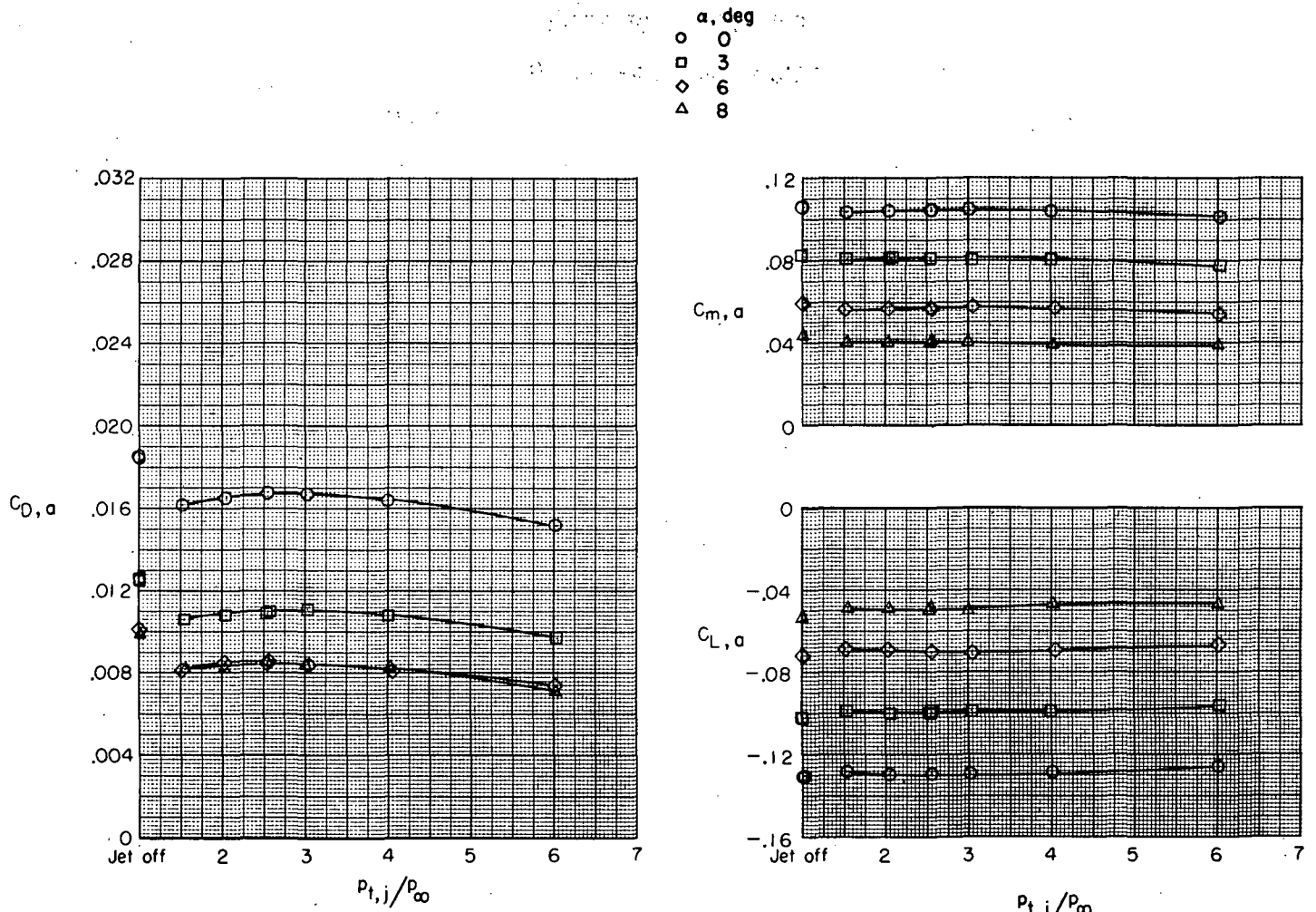

(g) $\delta = -5^o$; $M_\infty = 0.80$.

Figure 16.- Continued.

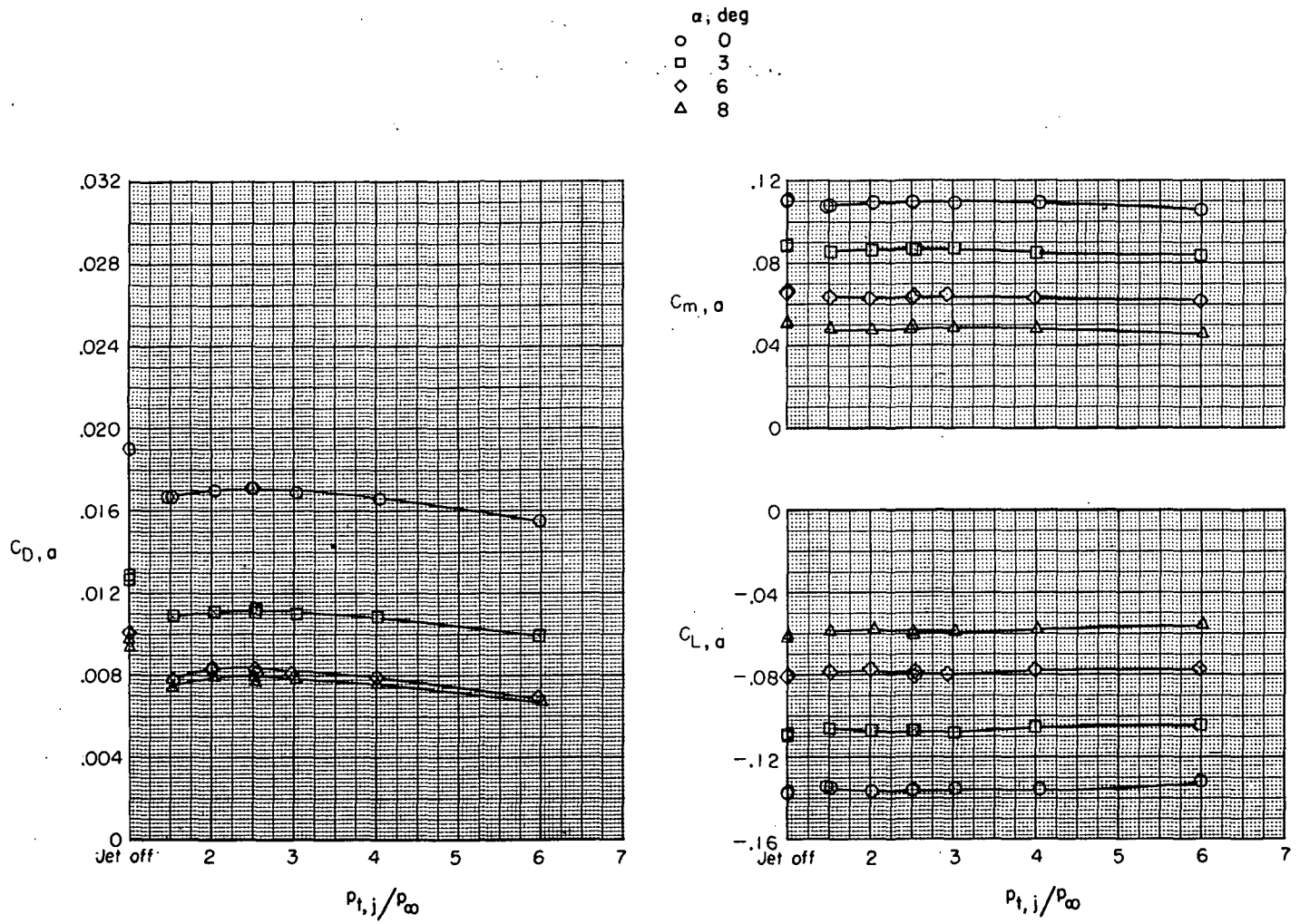

(h) $\delta = -5^o$; $M_\infty = 0.85$.

Figure 16.- Continued.

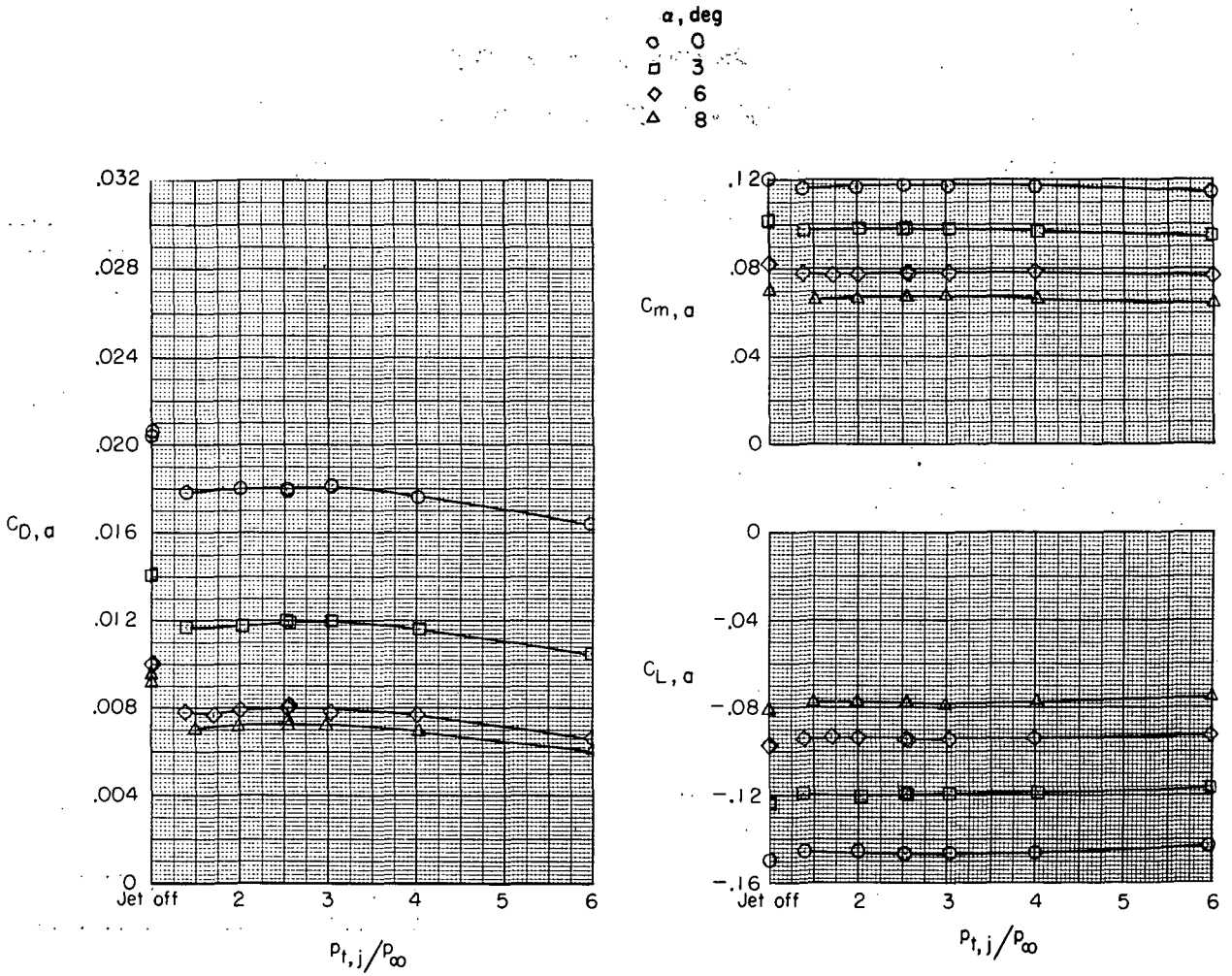

(i) $\delta = -5^o$; $M_\infty = 0.90$.

Figure 16.- Continued.

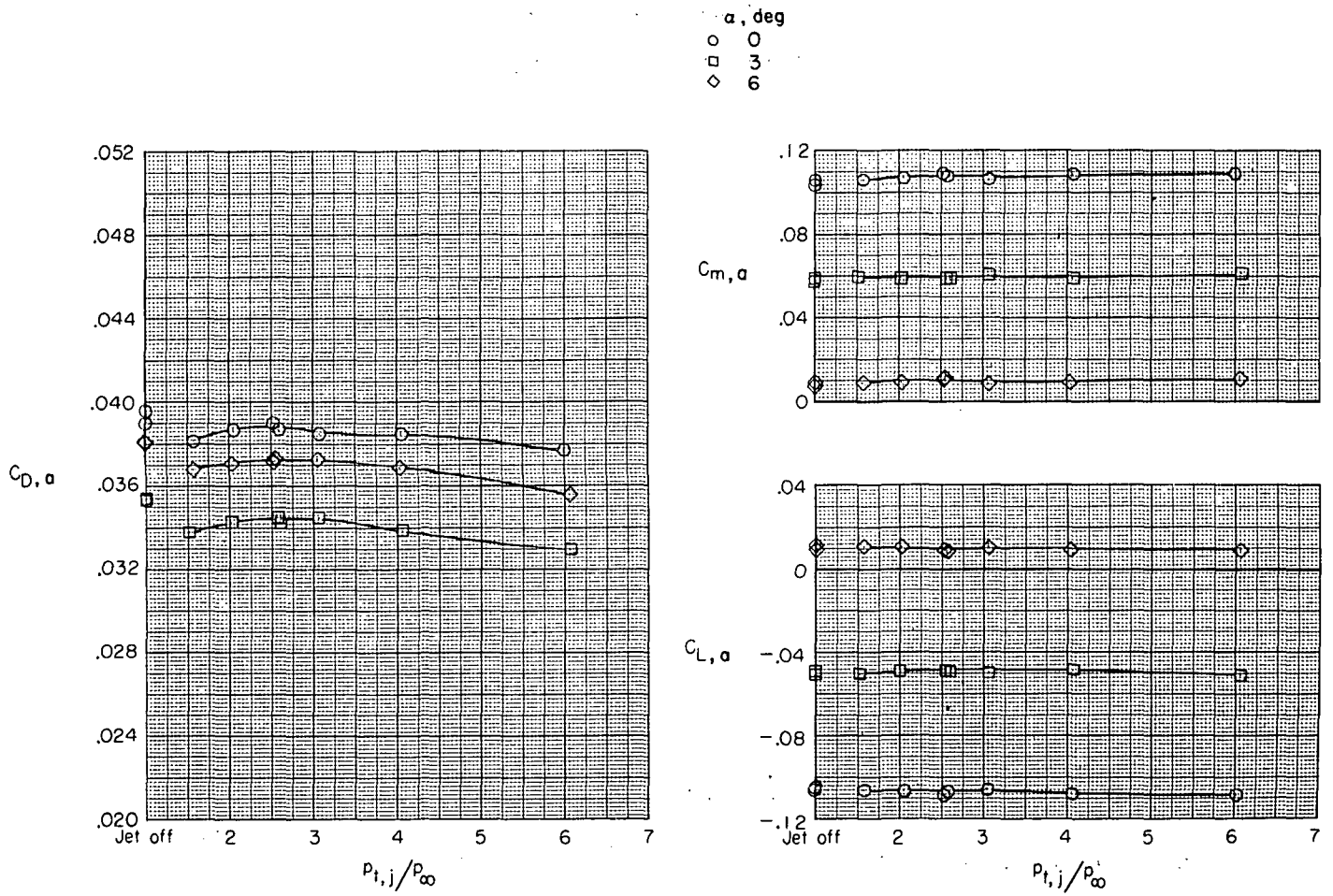

(j) $\delta = -5^o$; $M_\infty = 1.20$.

Figure 16.- Continued.

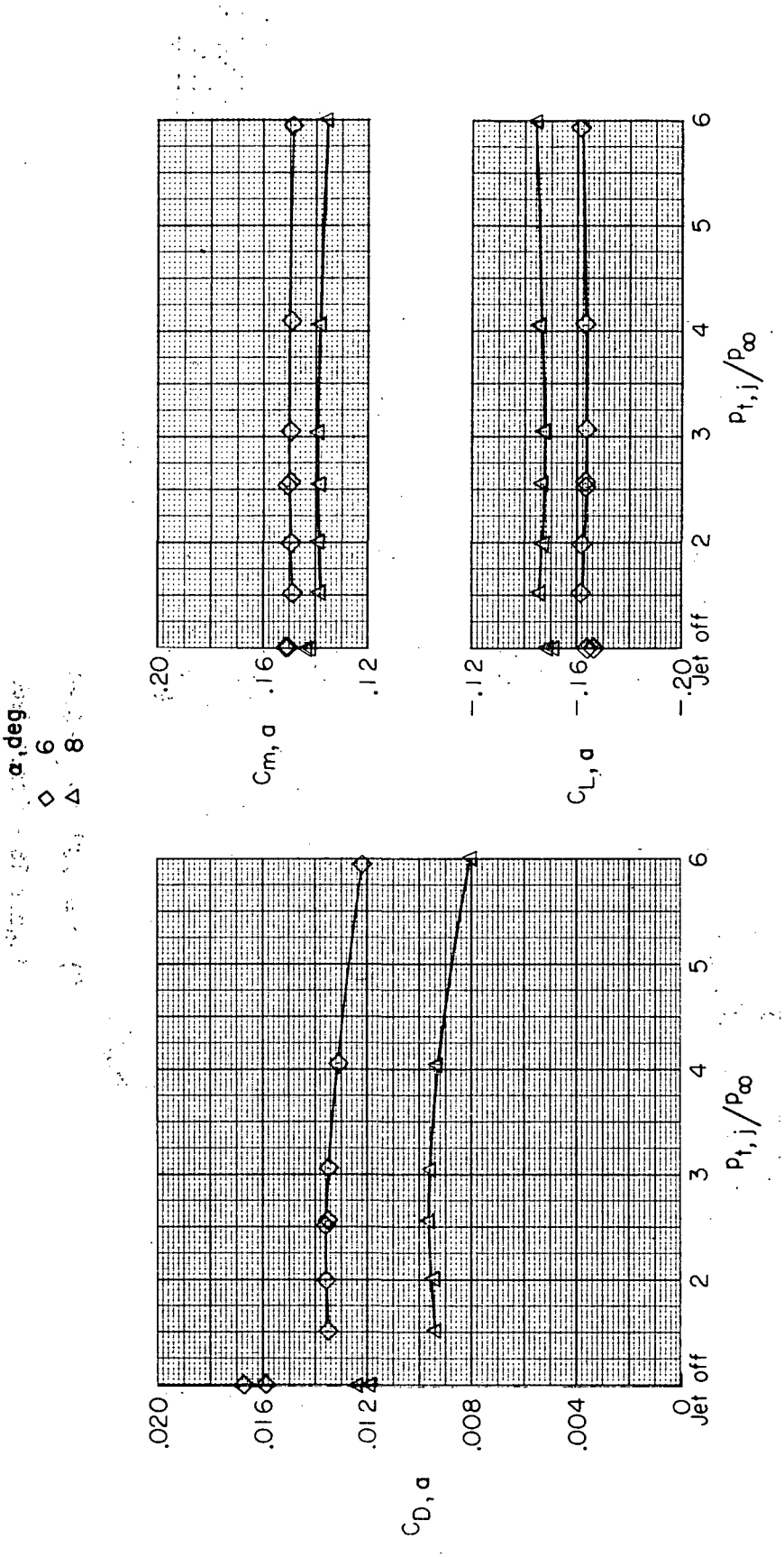

(k) $\delta = -10^\circ$; $M_\infty = 0.60$.

Figure 16.- Continued.

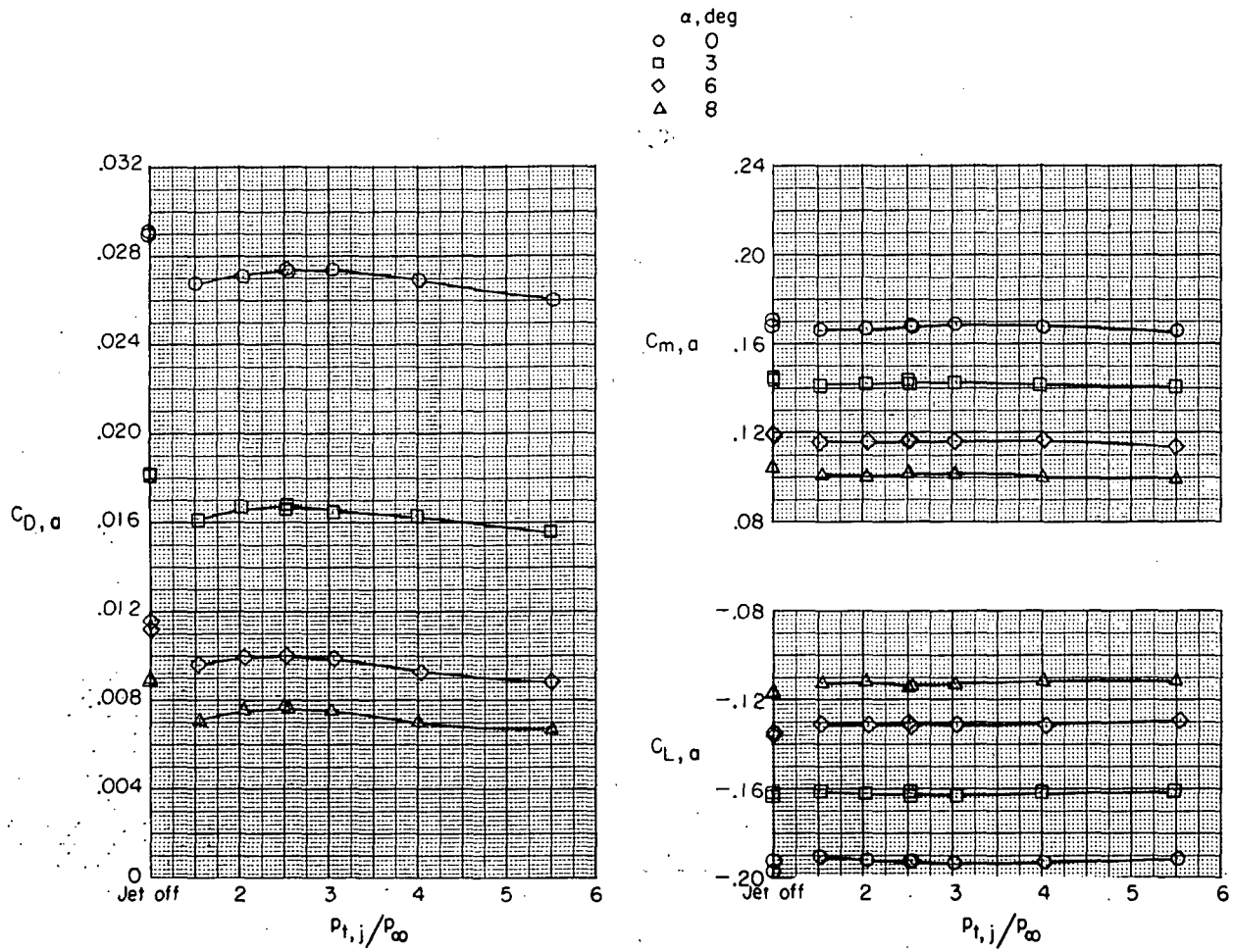

(l) $\delta = -10^o$; $M_\infty = 0.90$.

Figure 16.- Concluded.

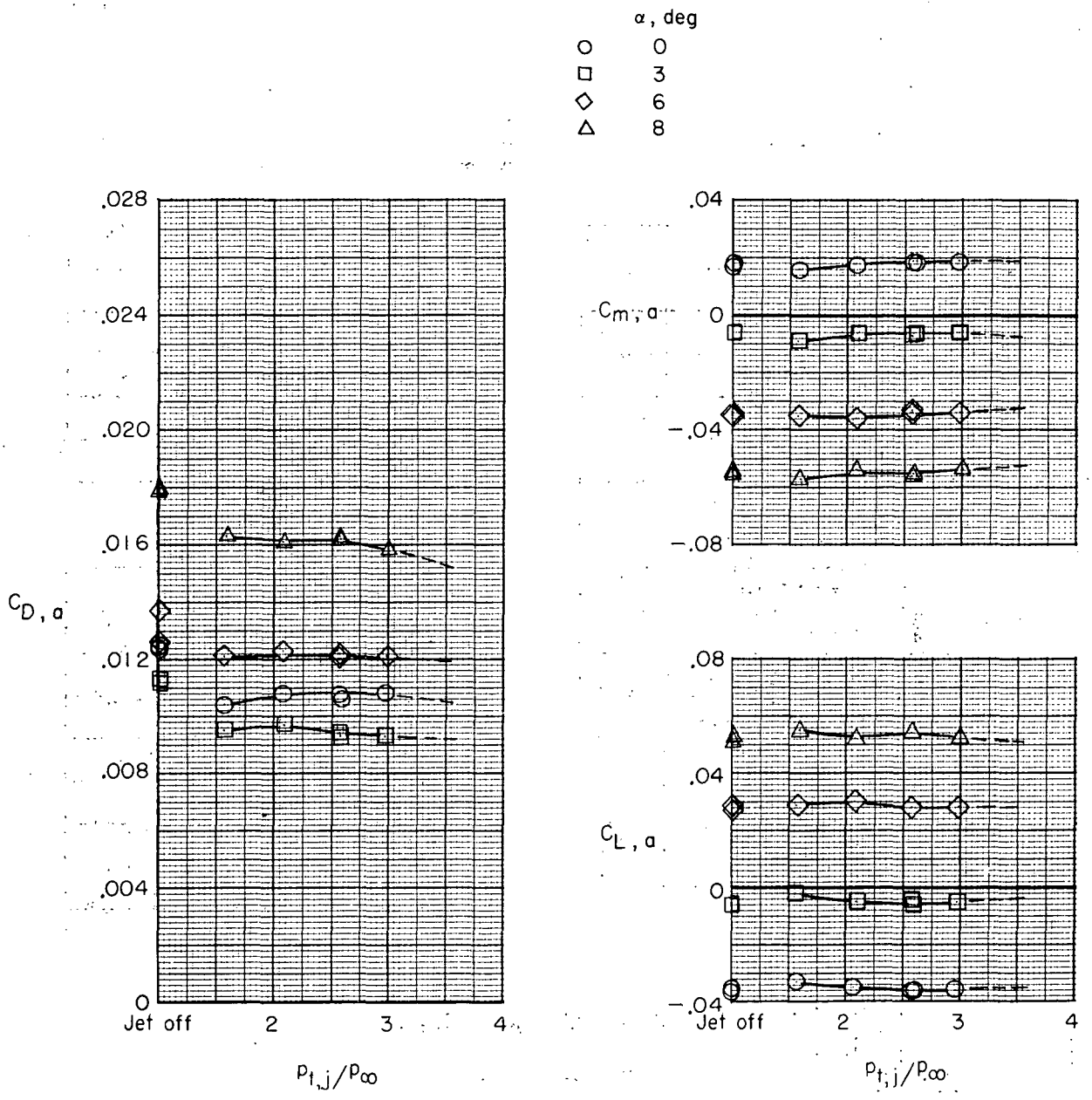

(a) $\delta = 0^o$; $M_\infty = 0.60$.

Figure 17.- Effect of jet total pressure ratio on aerodynamic characteristics of hinged-flap nozzle configuration in afterburning position. Dashed lines indicate extrapolated data.

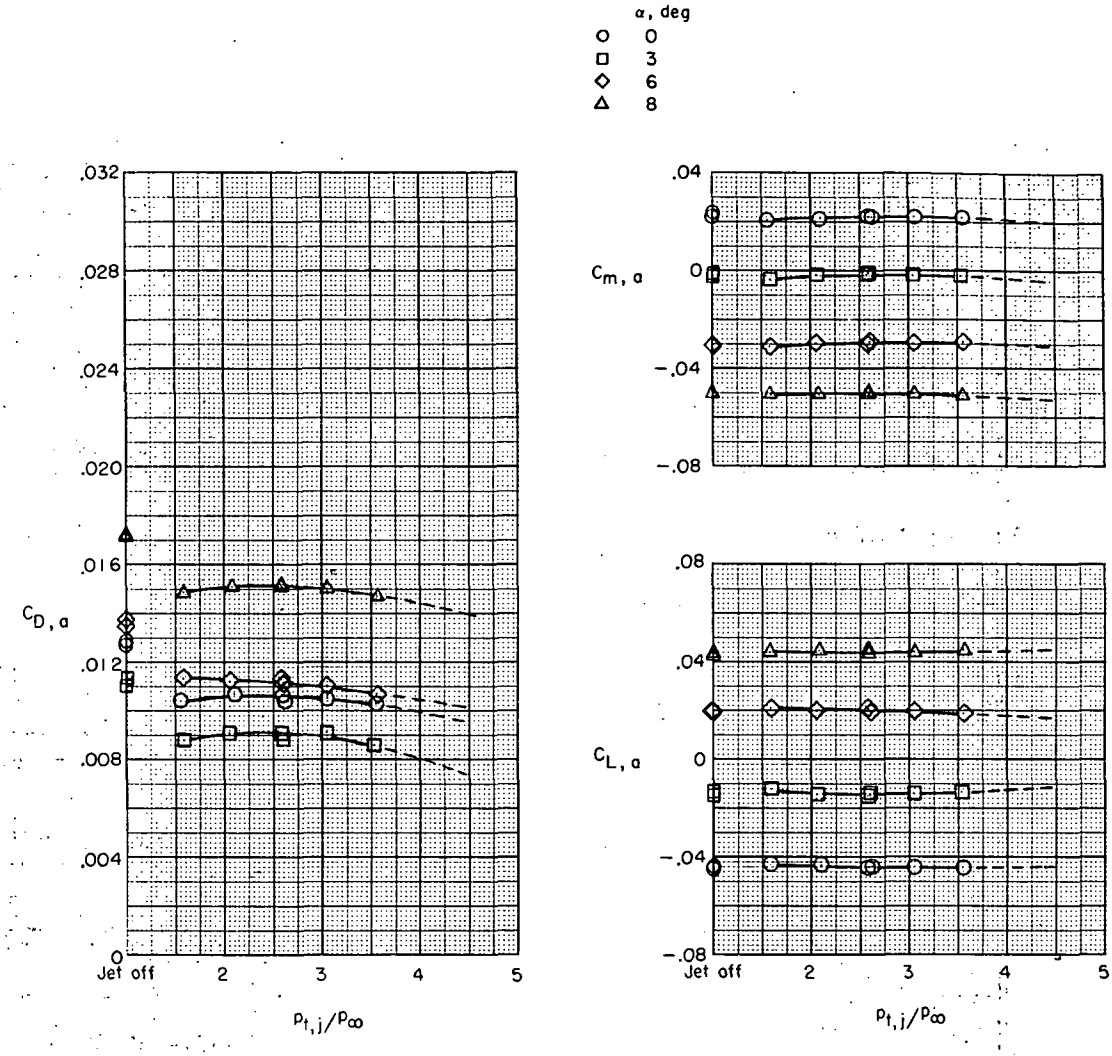

(b) $\delta = 0^o$; $M_\infty = 0.80$.

Figure 17.- Continued.

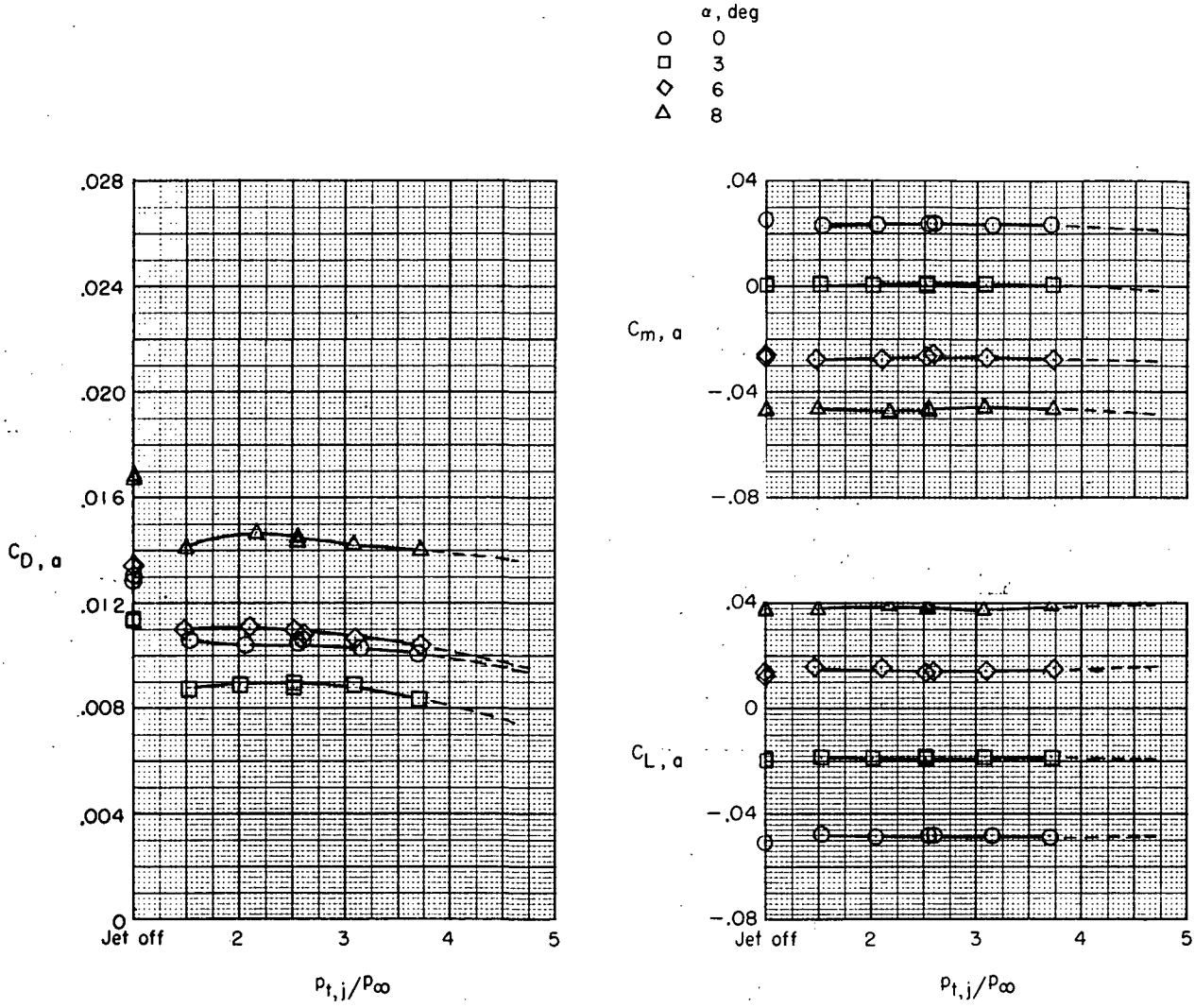

(c) $\delta = 0^o$; $M_\infty = 0.85$.

Figure 17.- Continued.

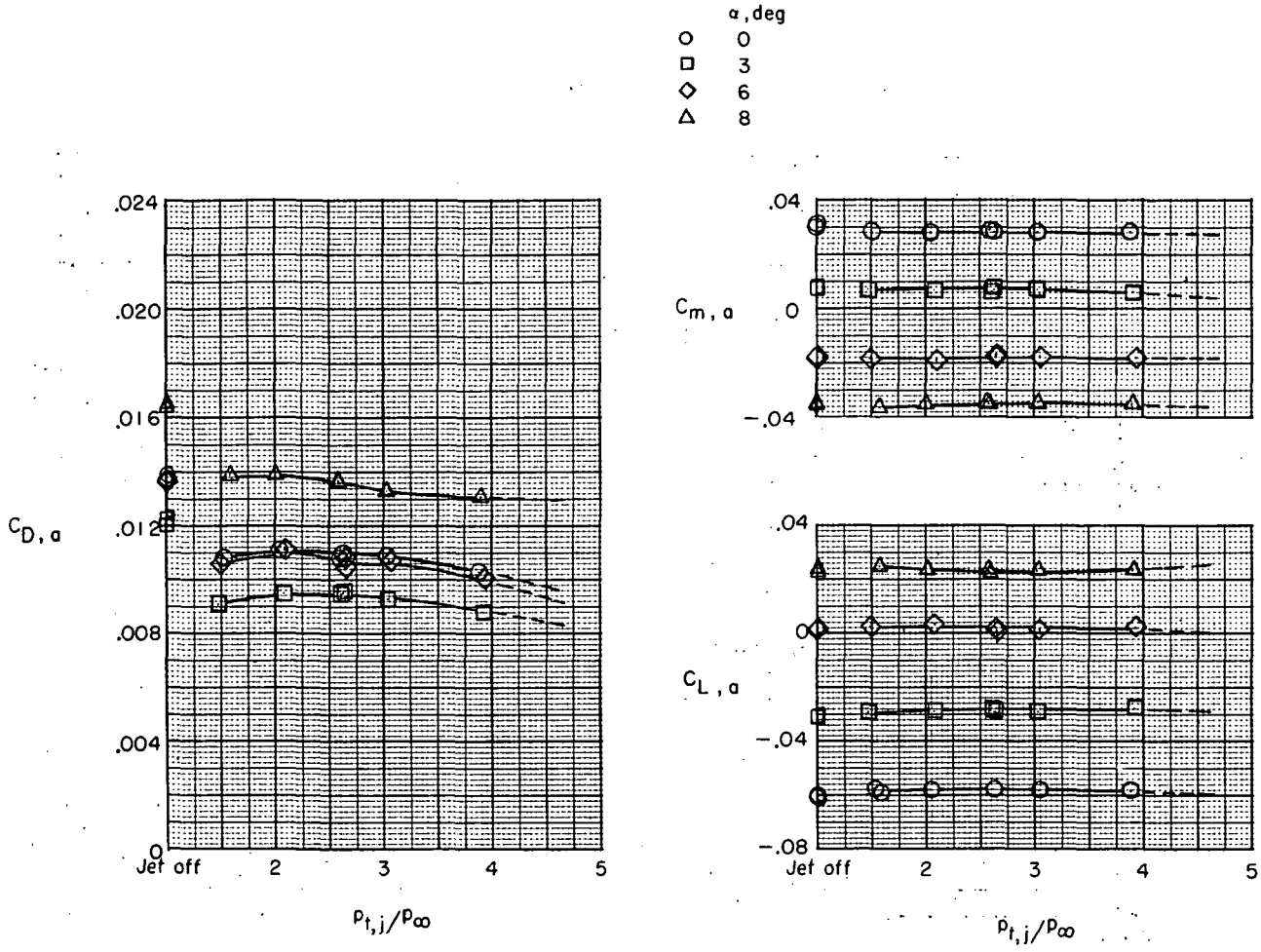

(d) $\delta = 0^o$; $M_\infty = 0.90$.

Figure 17.- Continued.

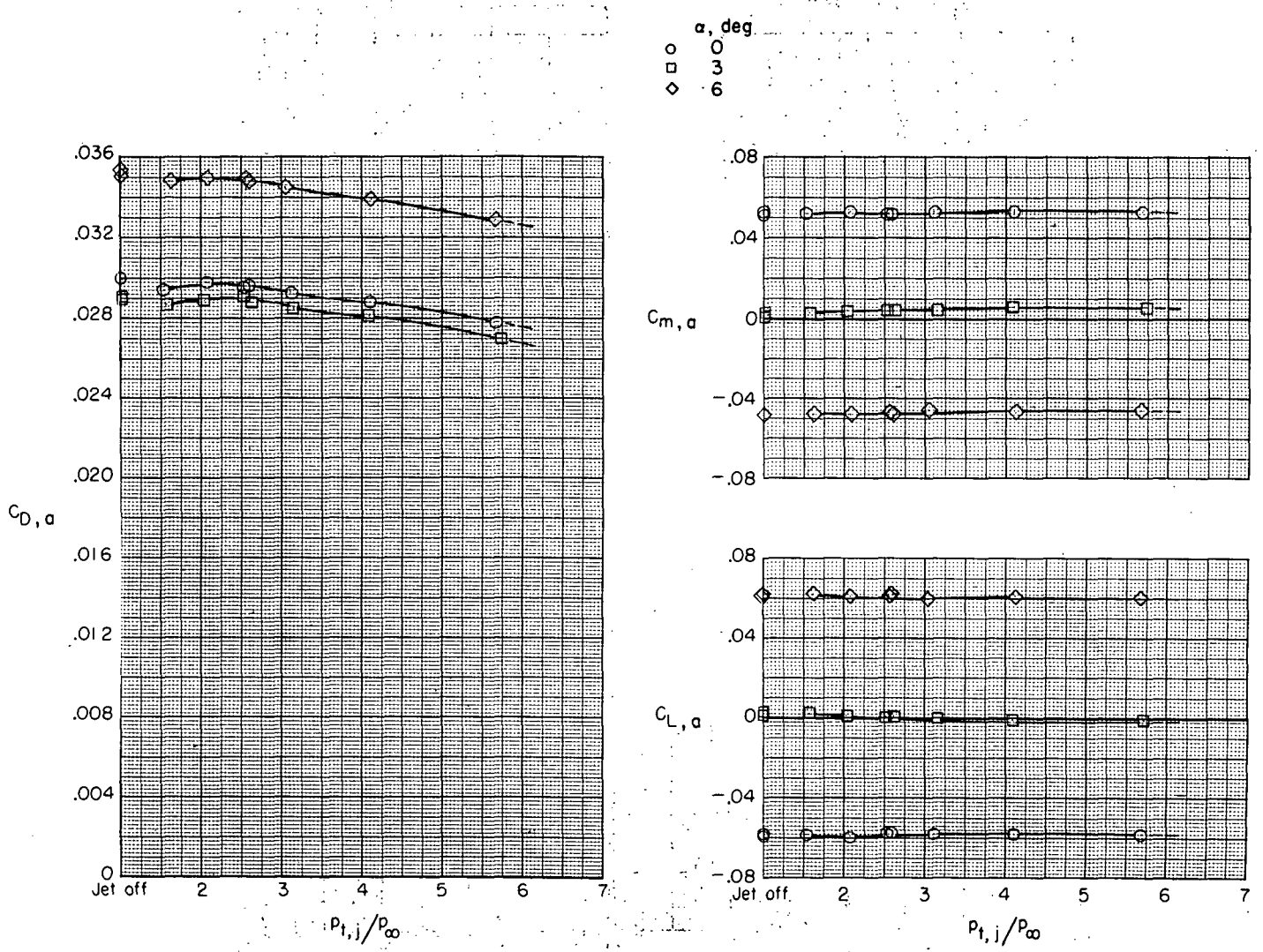

(e) $\delta = 0^O$; $M_\infty = 1.20$.

Figure 17.- Continued.

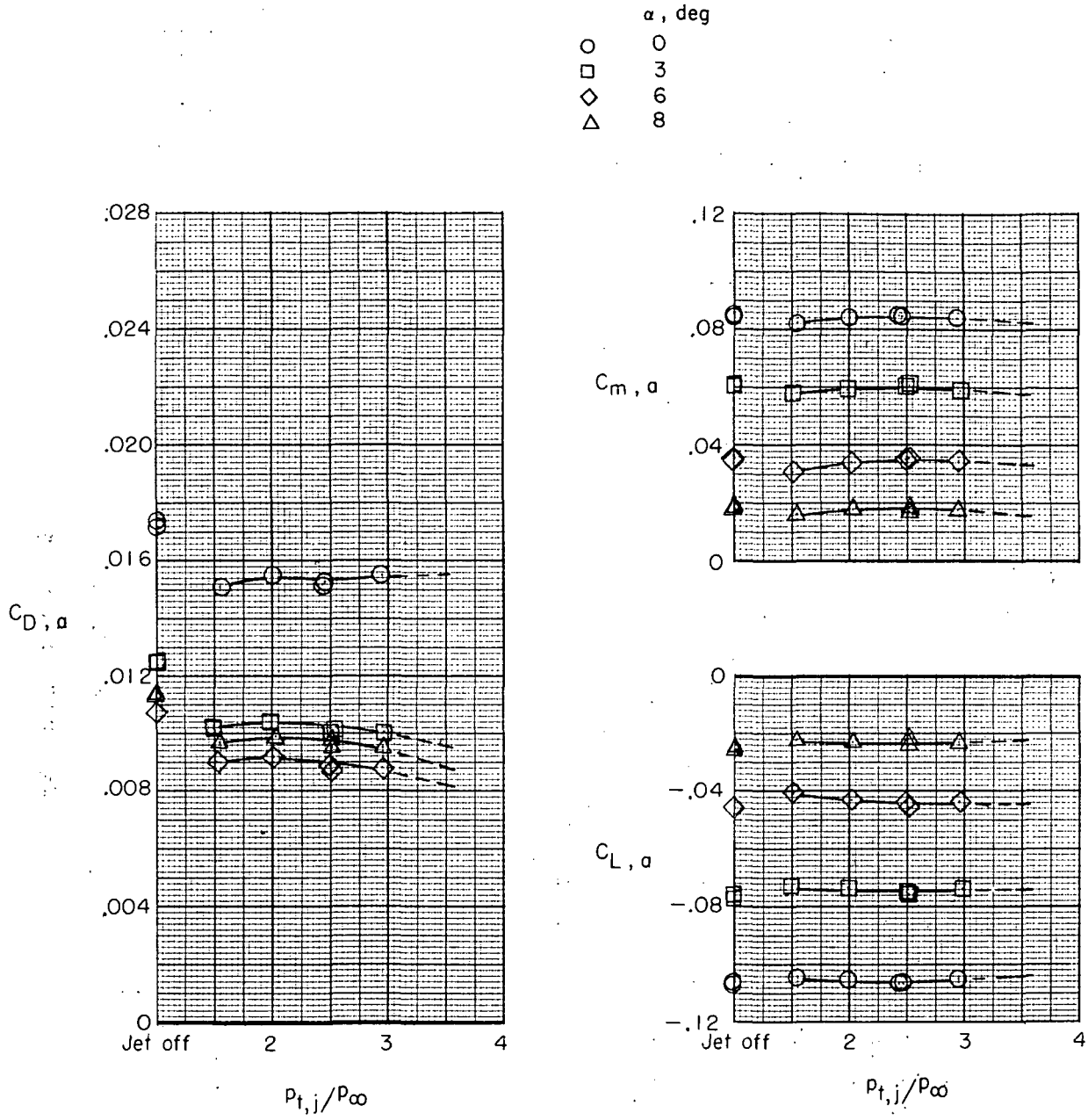

(f) $\delta = -5^o$; $M_\infty = 0.60$.

Figure 17.- Continued.

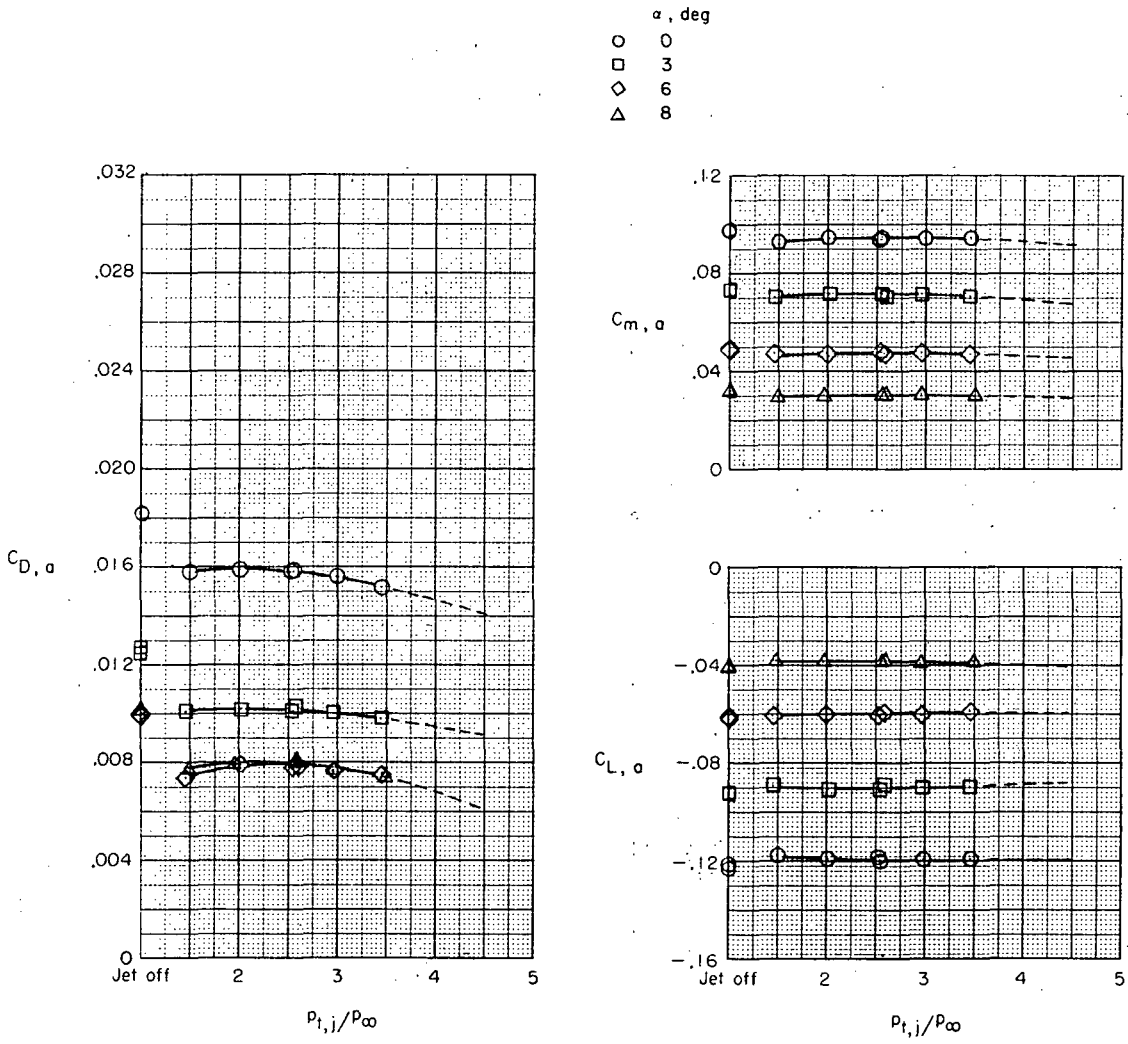

(g) $\delta = -5^o$; $M_\infty = 0.80$.

Figure 17.- Continued.

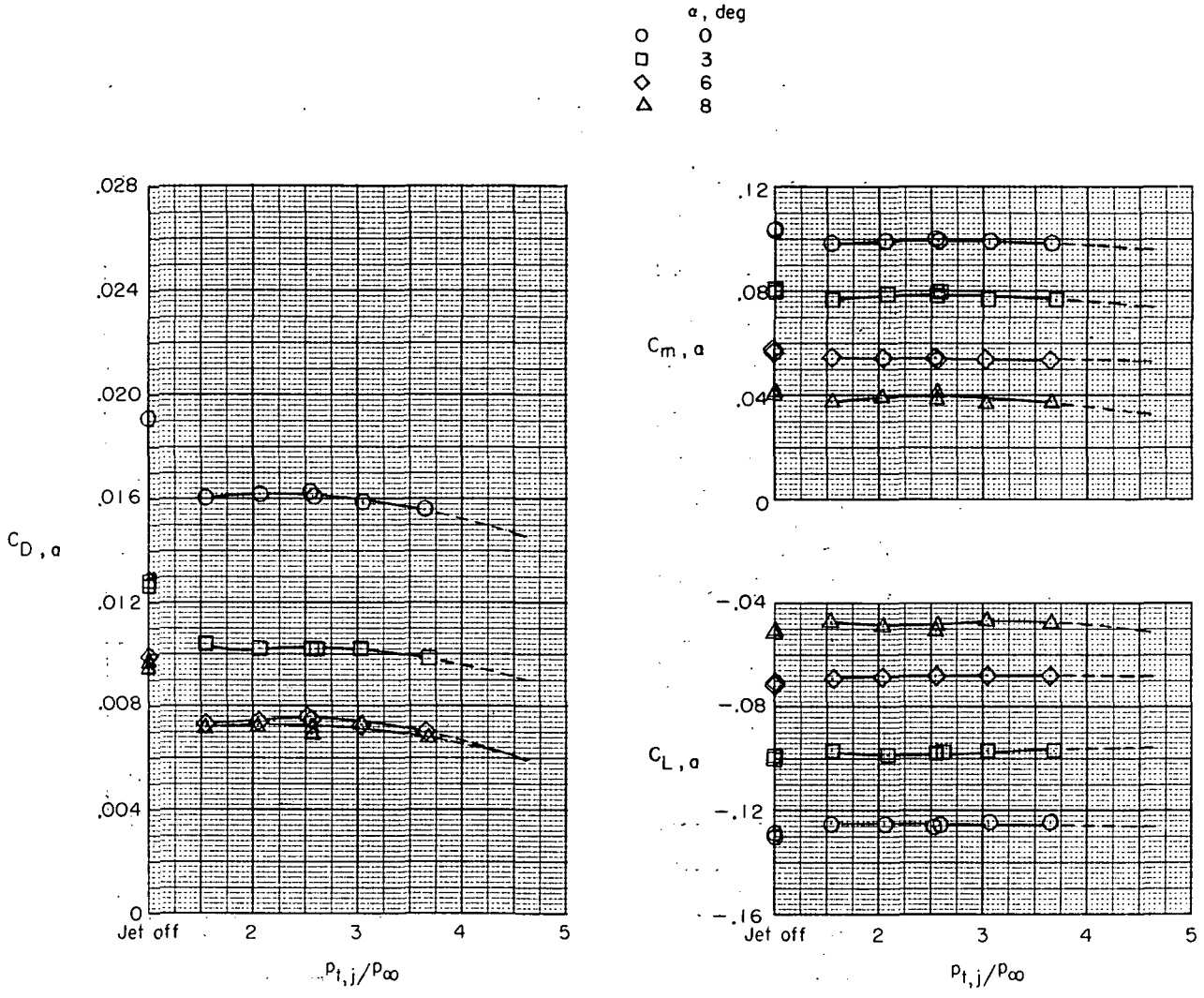

(h) $\delta = -5^o$; $M_\infty = 0.85$.

Figure 17.- Continued.

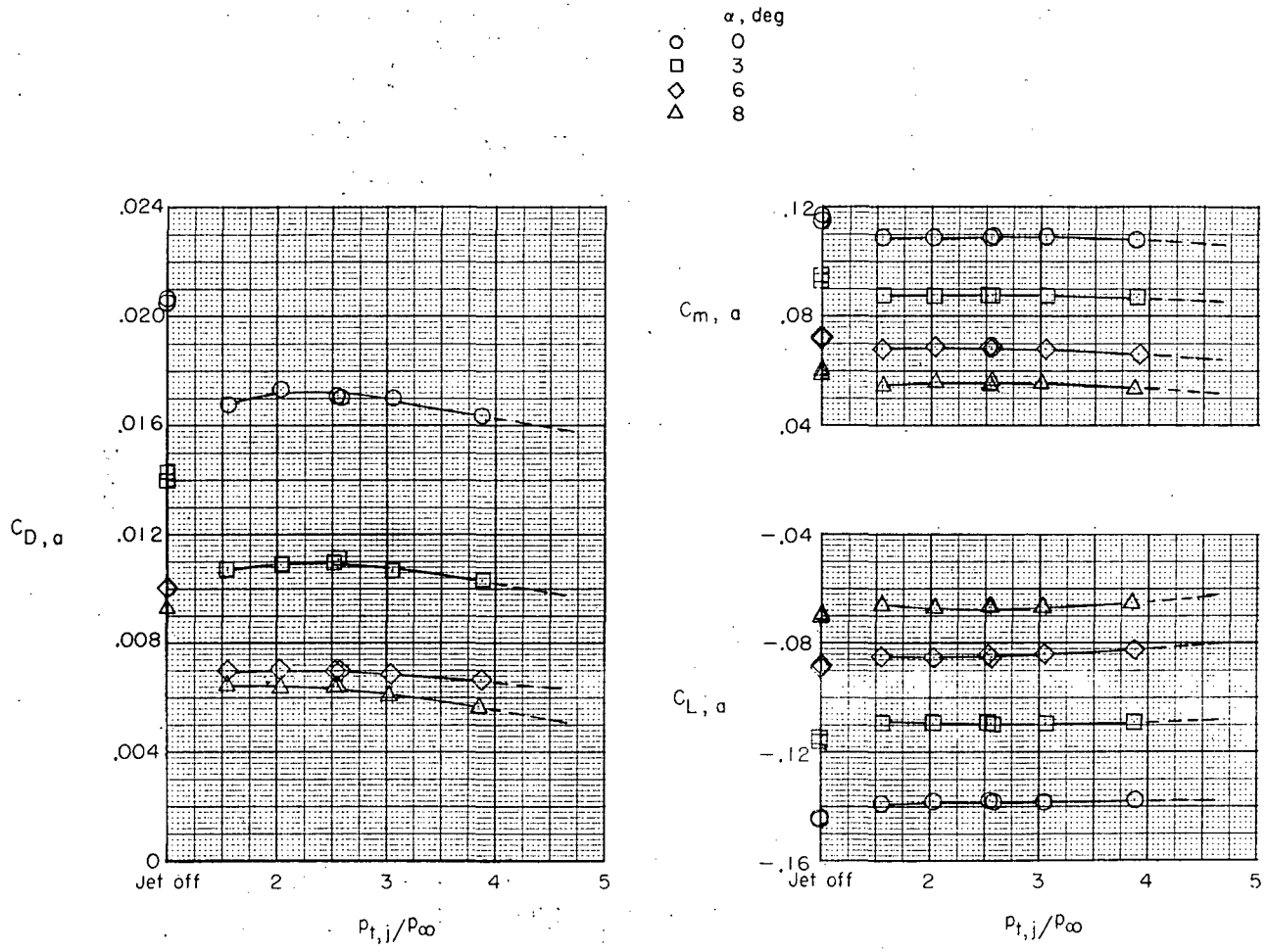

(i) $\delta = -5^o$; $M_\infty = 0.90$.

Figure 17.- Continued.

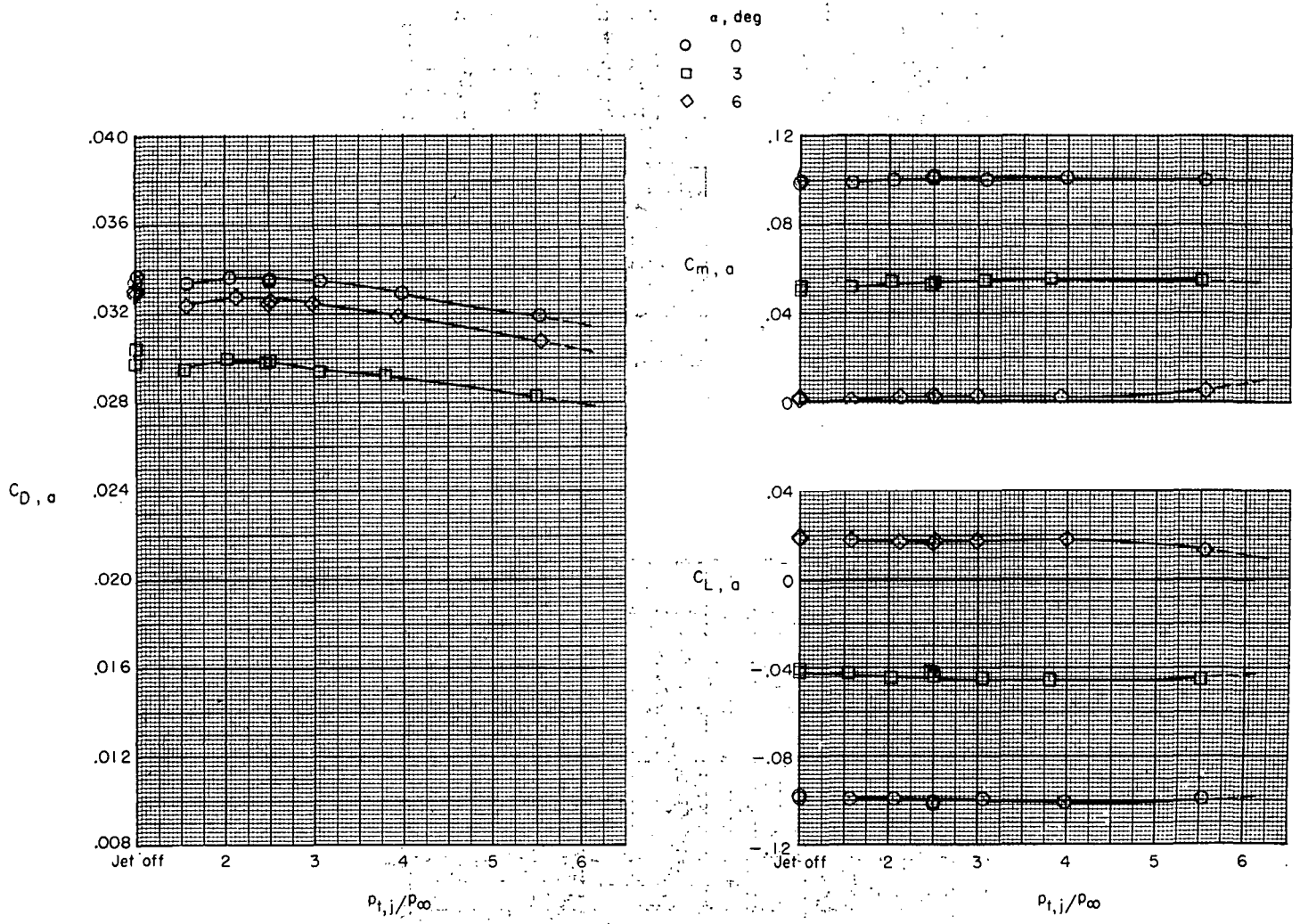

(j) $\delta = -5^o$; $M_\infty = 1.20$.

Figure 17.- Continued.

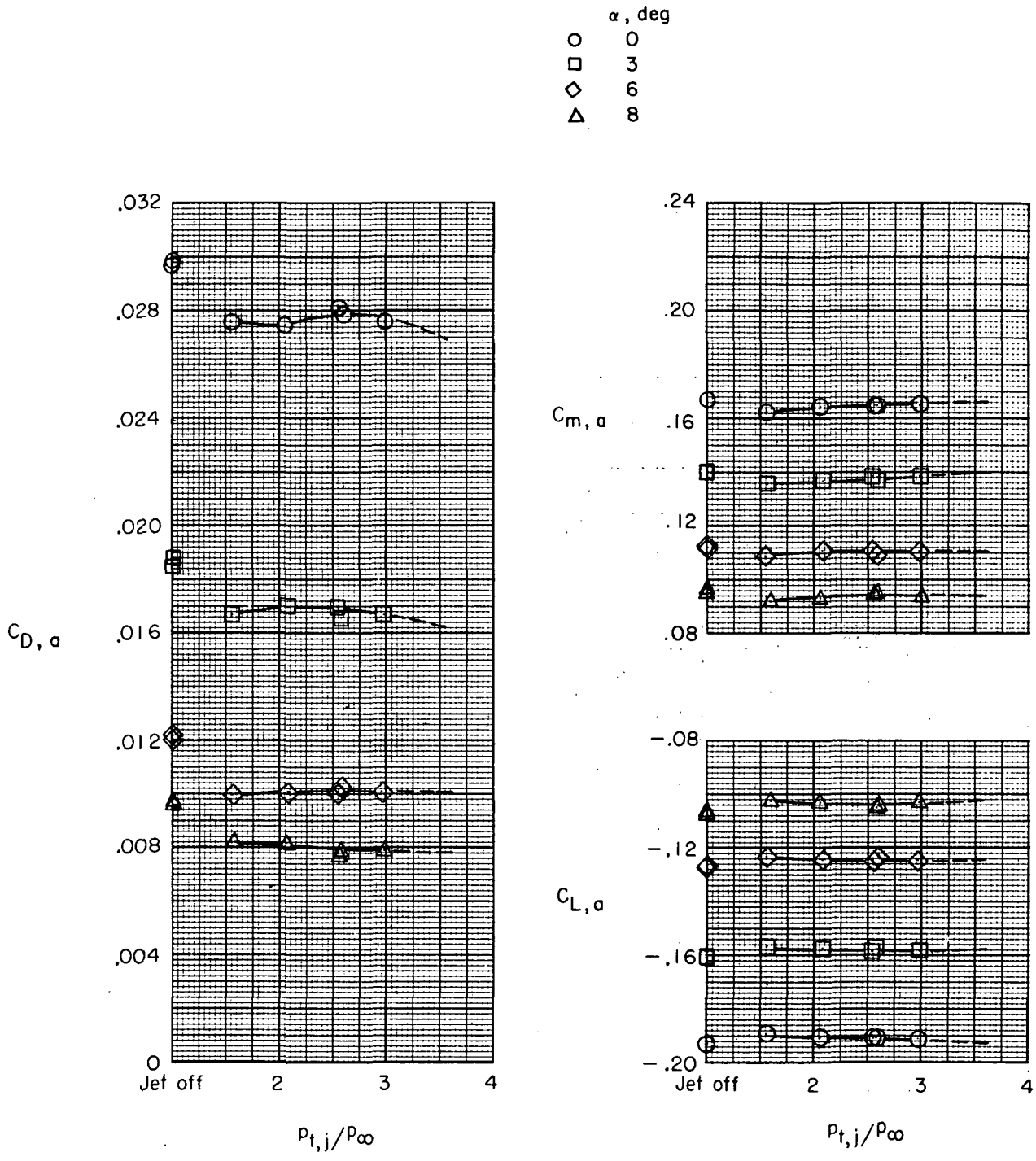

(k) $\delta = -10^o$; $M_\infty = 0.60$.

Figure 17.- Continued.

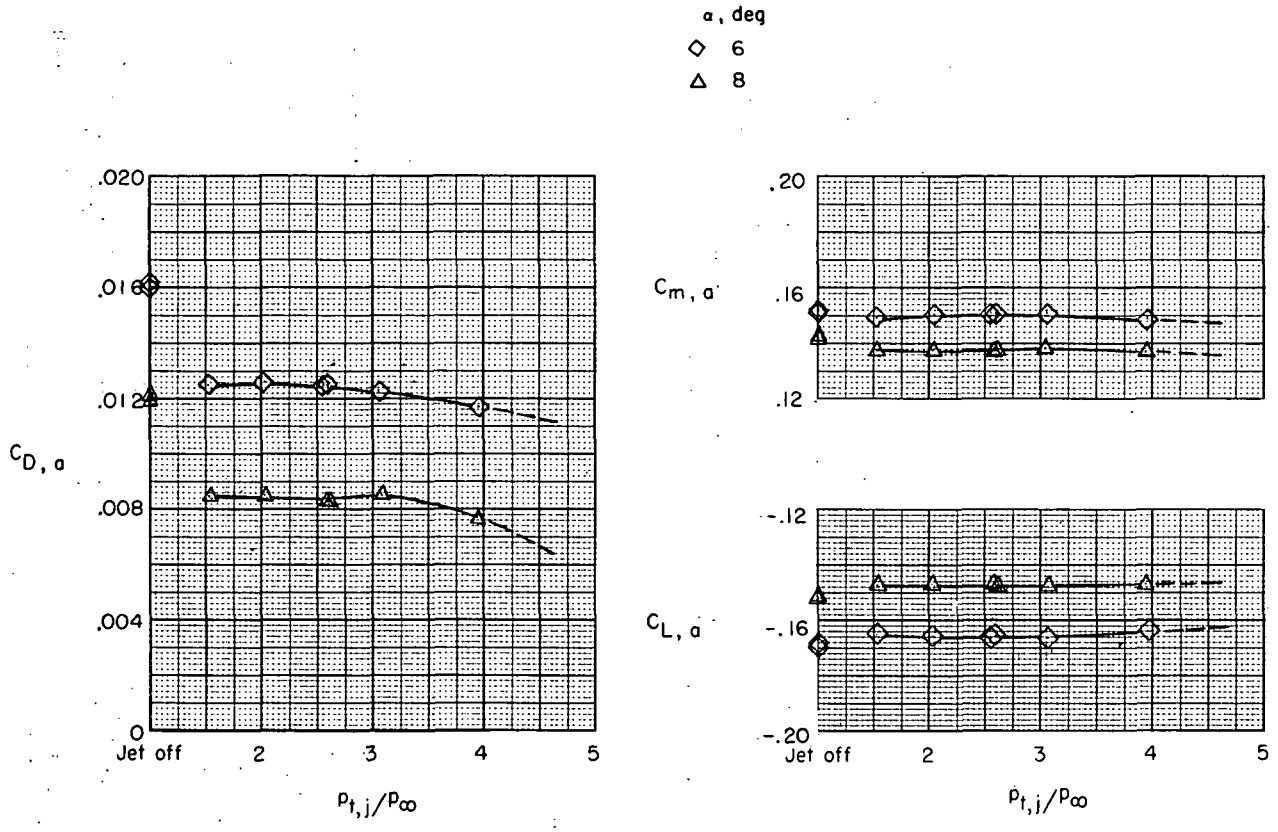

(l) $\delta = -10^o$; $M_\infty = 0.90$.

Figure 17.- Concluded.

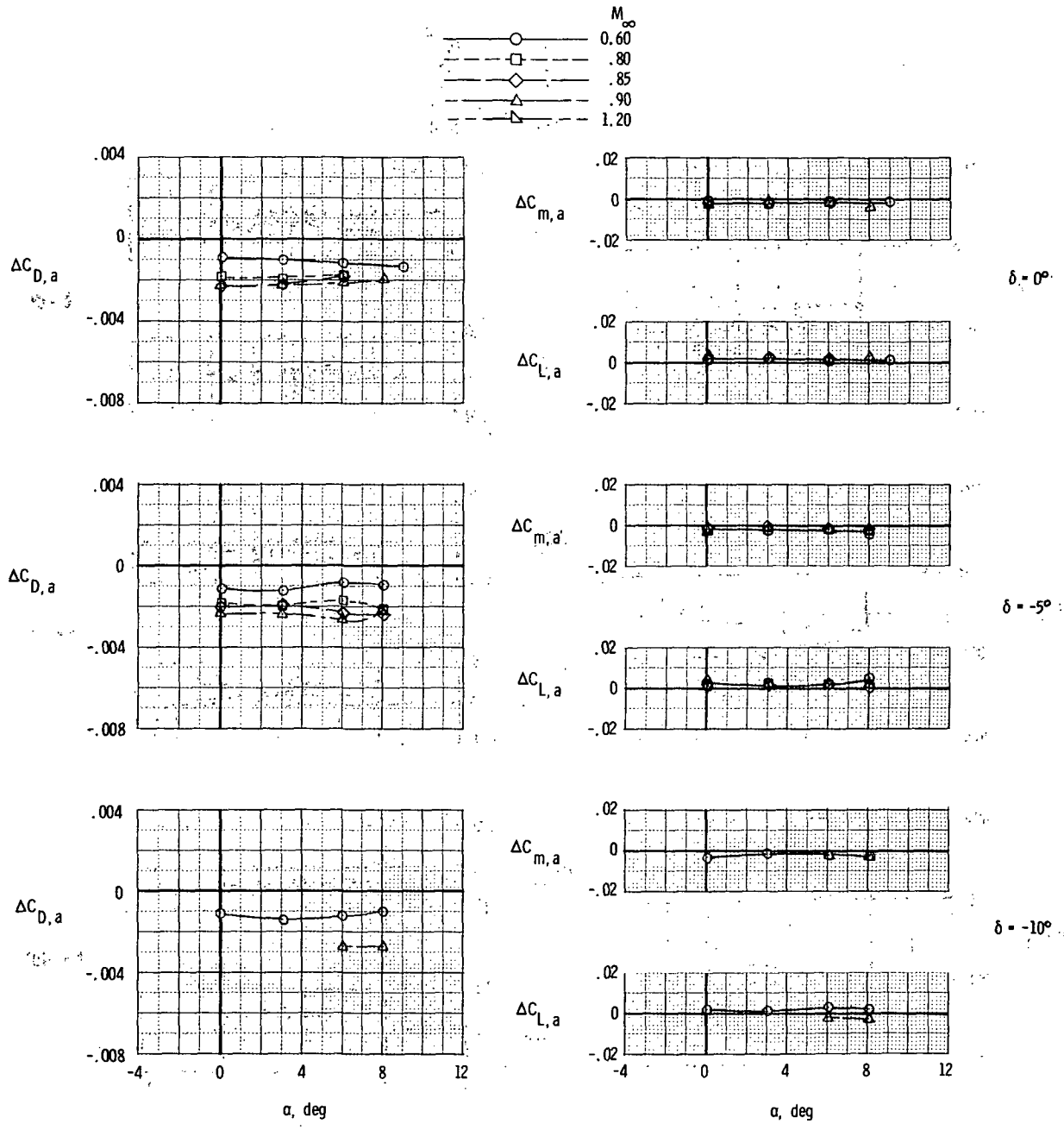

(a) Translating-flap nozzle cruise position.

Figure 18.- Effect of angle of attack on incremental aerodynamic characteristics of various configurations. Increments are due to jet interference with jet operating at scheduled pressure ratios.

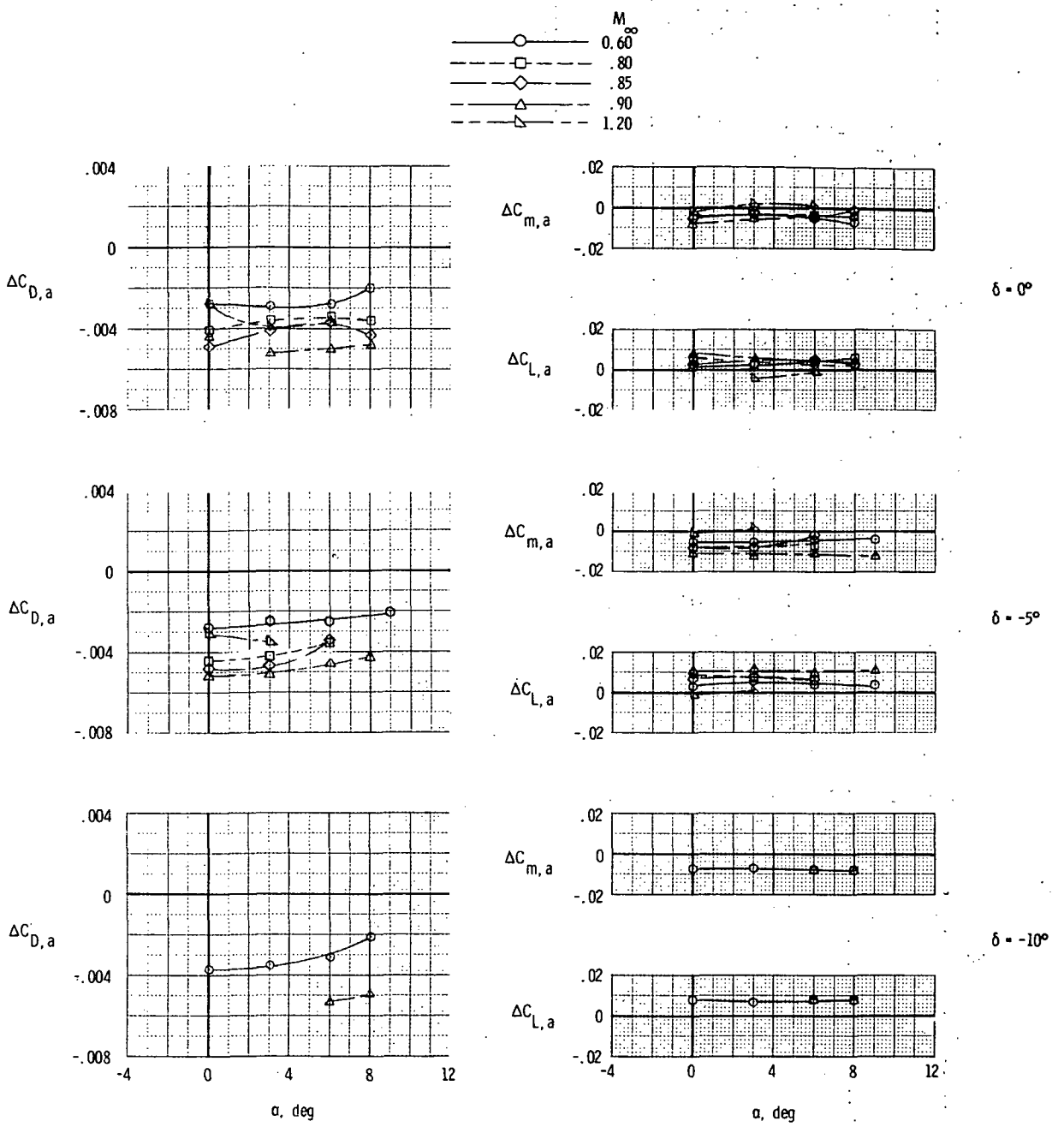

(b) Translating-flap nozzle afterburning position.

Figure 18.- Continued.

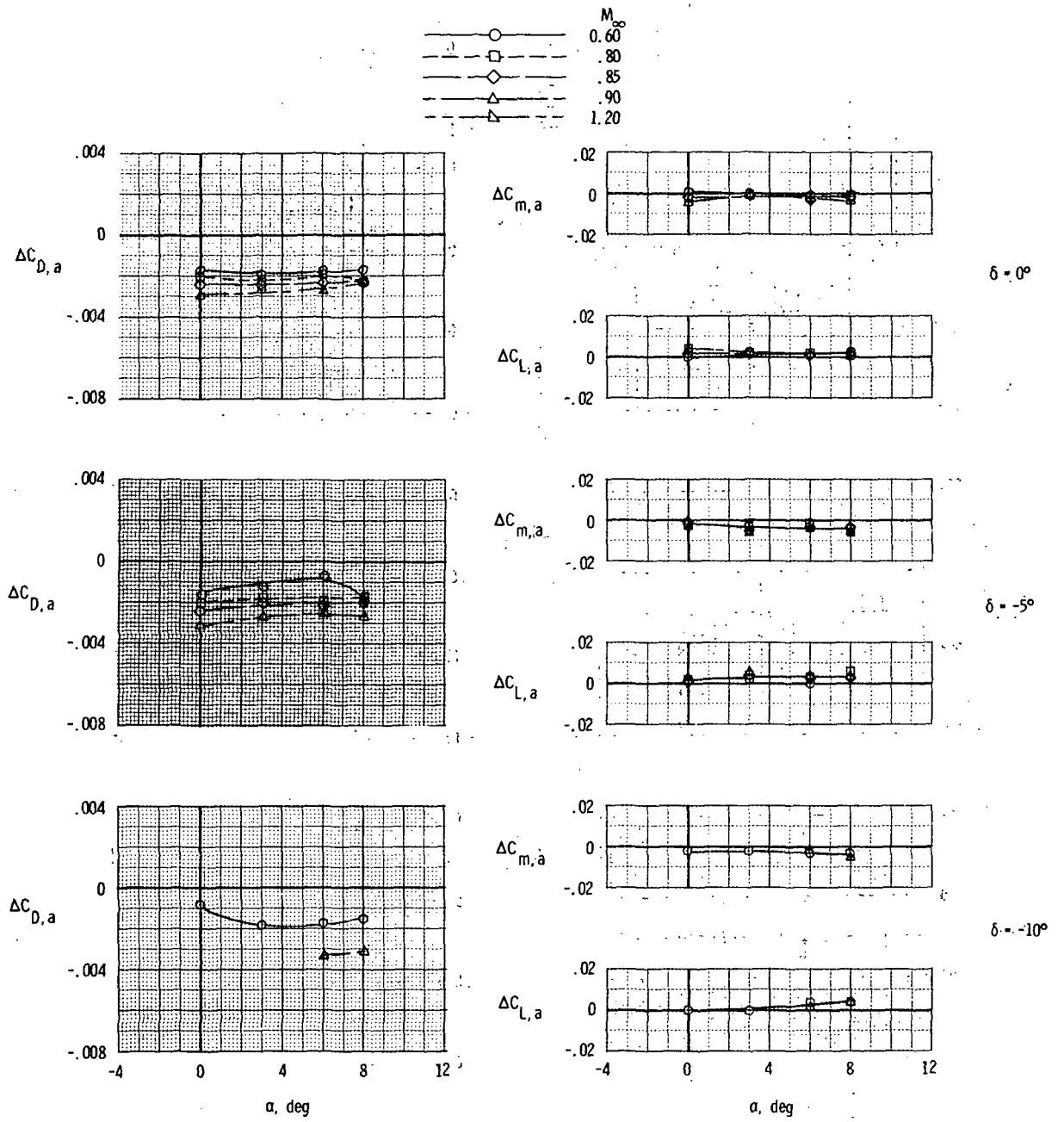

(c) Hinged-flap nozzle cruise position.

Figure 18.- Continued.

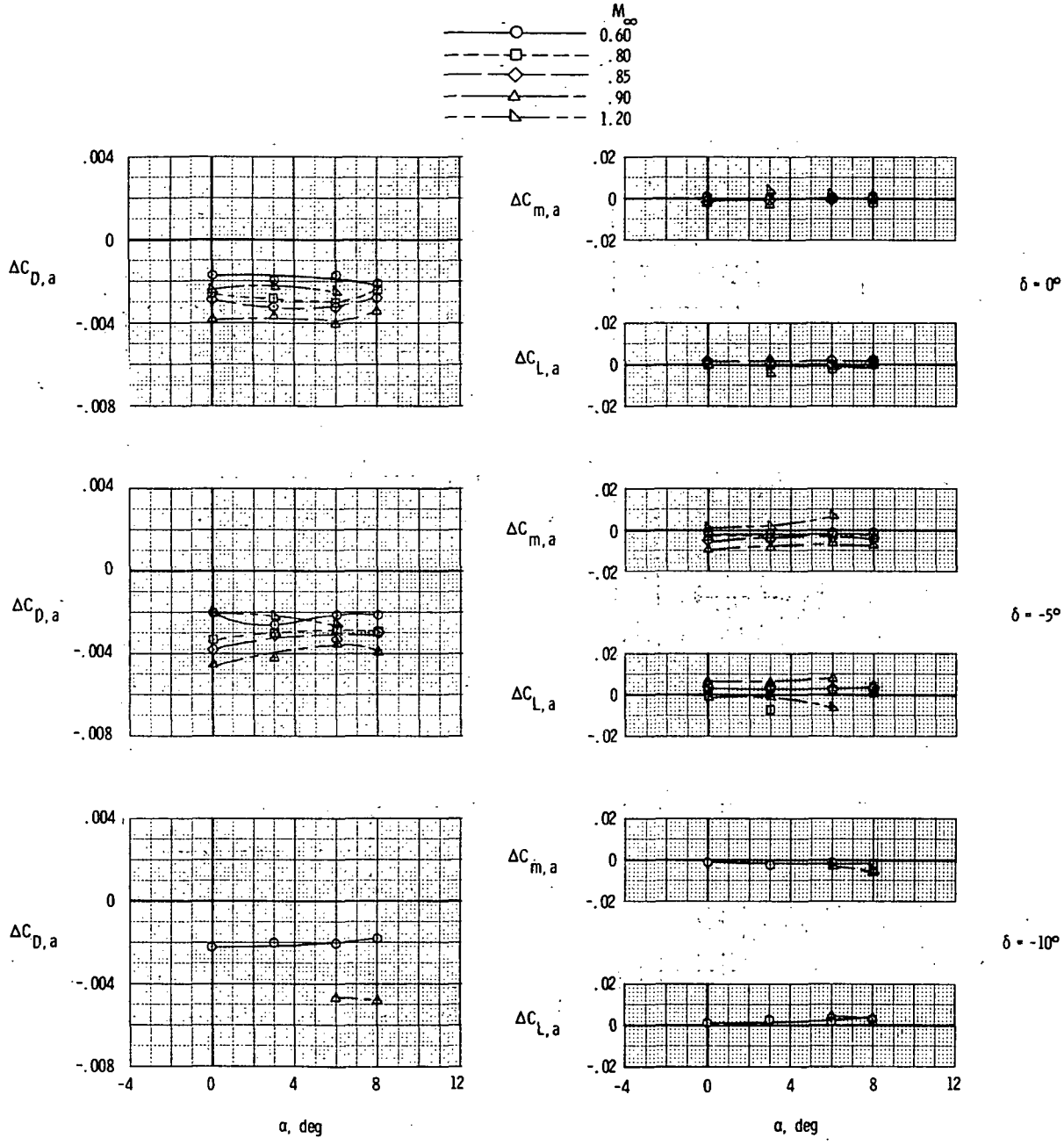

(d) Hinged-flap nozzle afterburning position.

Figure 18.- Concluded.

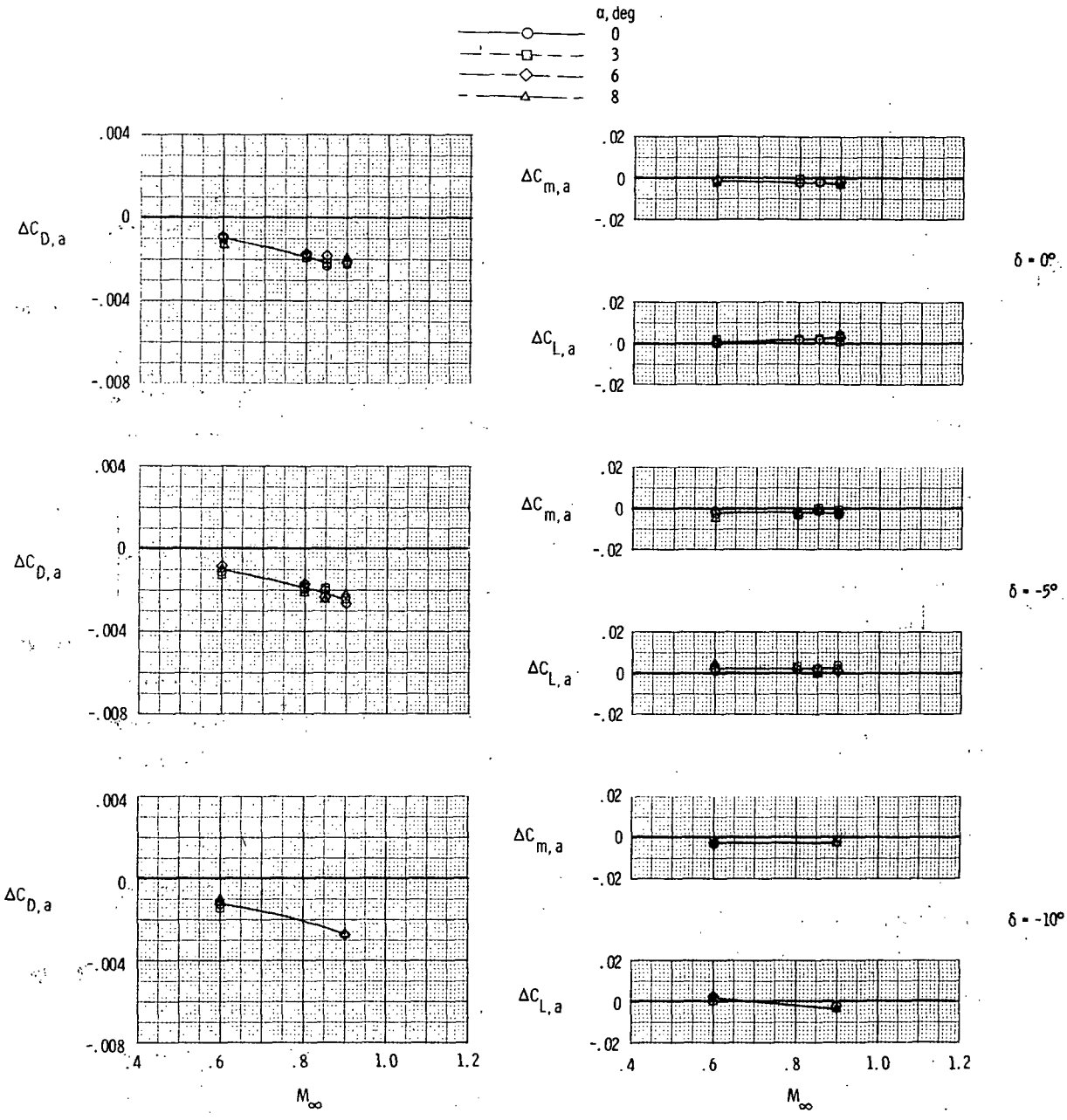

(a) Translating-flap nozzle cruise position.

Figure 19.- Effect of Mach number on incremental aerodynamic characteristics of various configurations. Increments are due to jet interference with jet operating at scheduled pressure ratios.

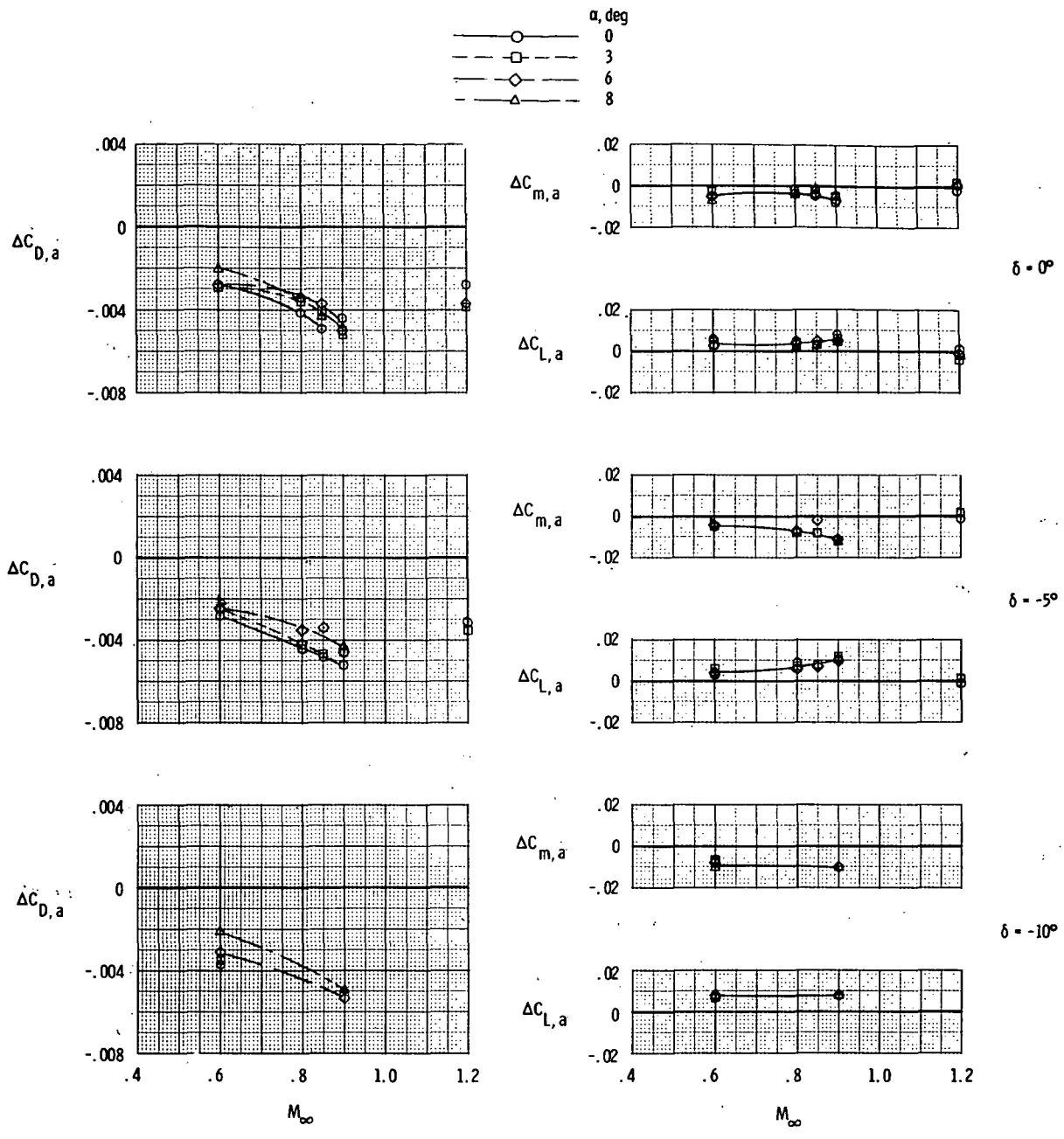

(b) Translating-flap nozzle afterburning position.

Figure 19.- Continued.

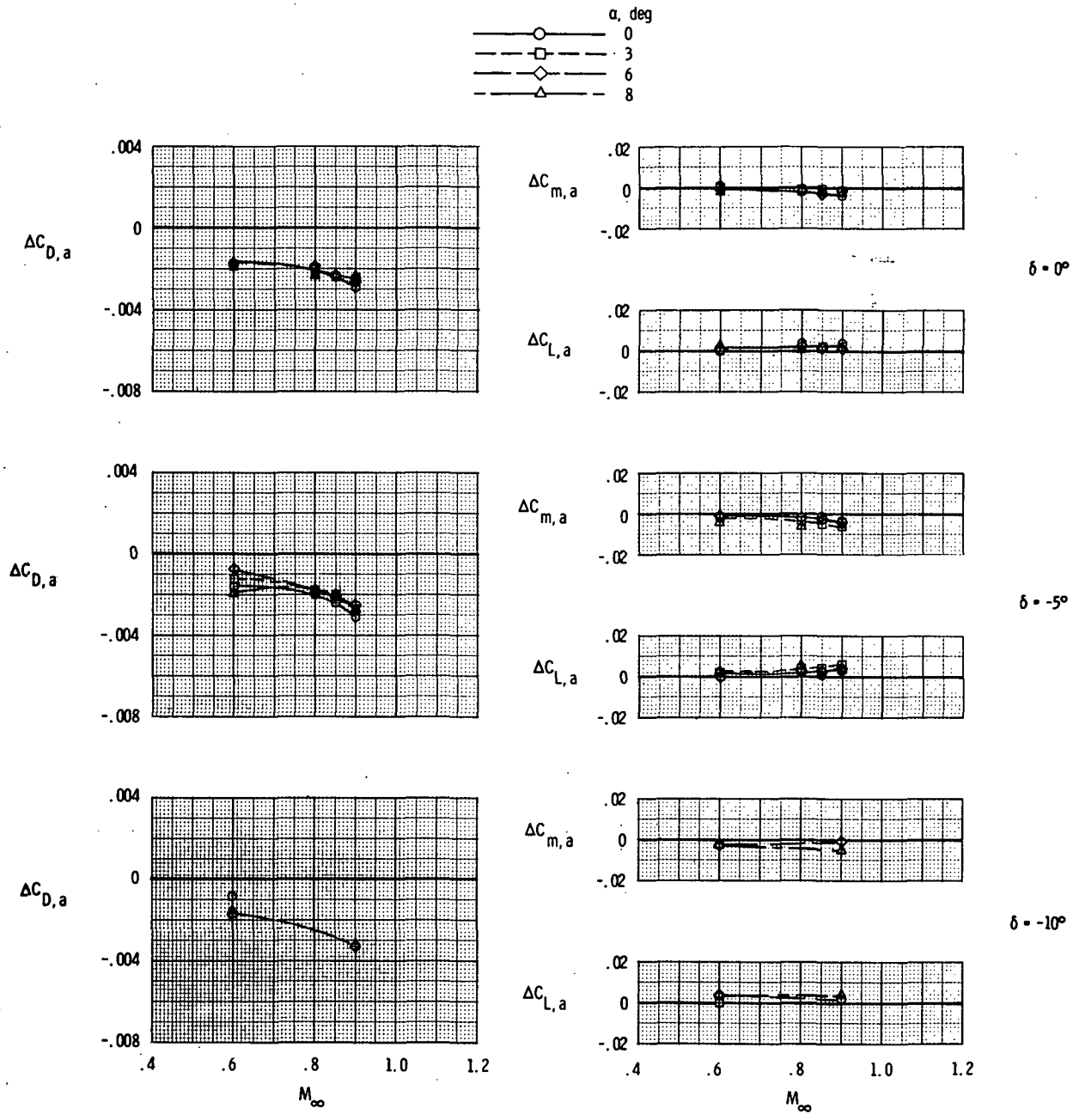

(c) Hinged-flap nozzle cruise position.

Figure 19.- Continued.

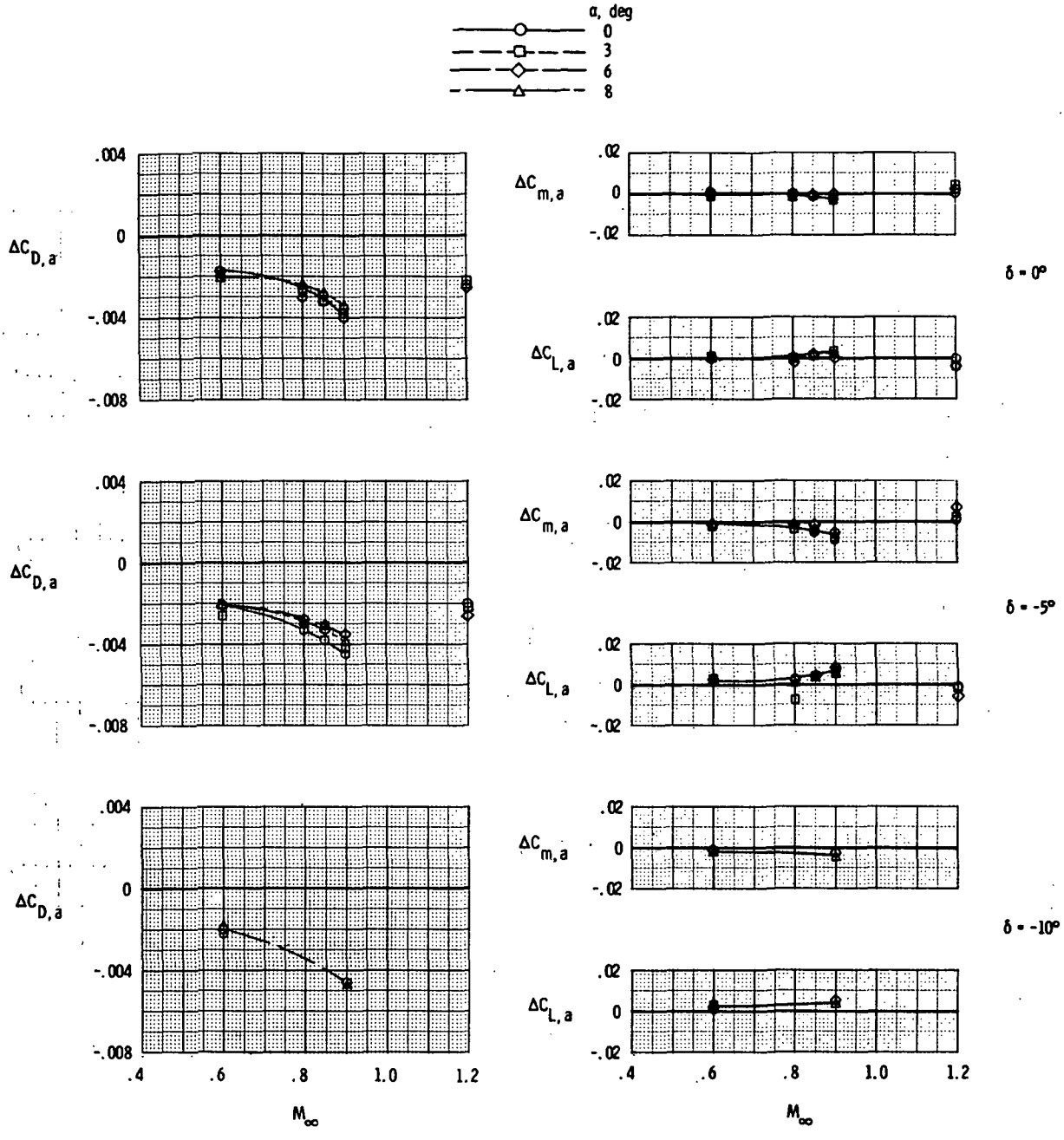

(d) Hinged-flap nozzle afterburning position.

Figure 19.- Concluded.

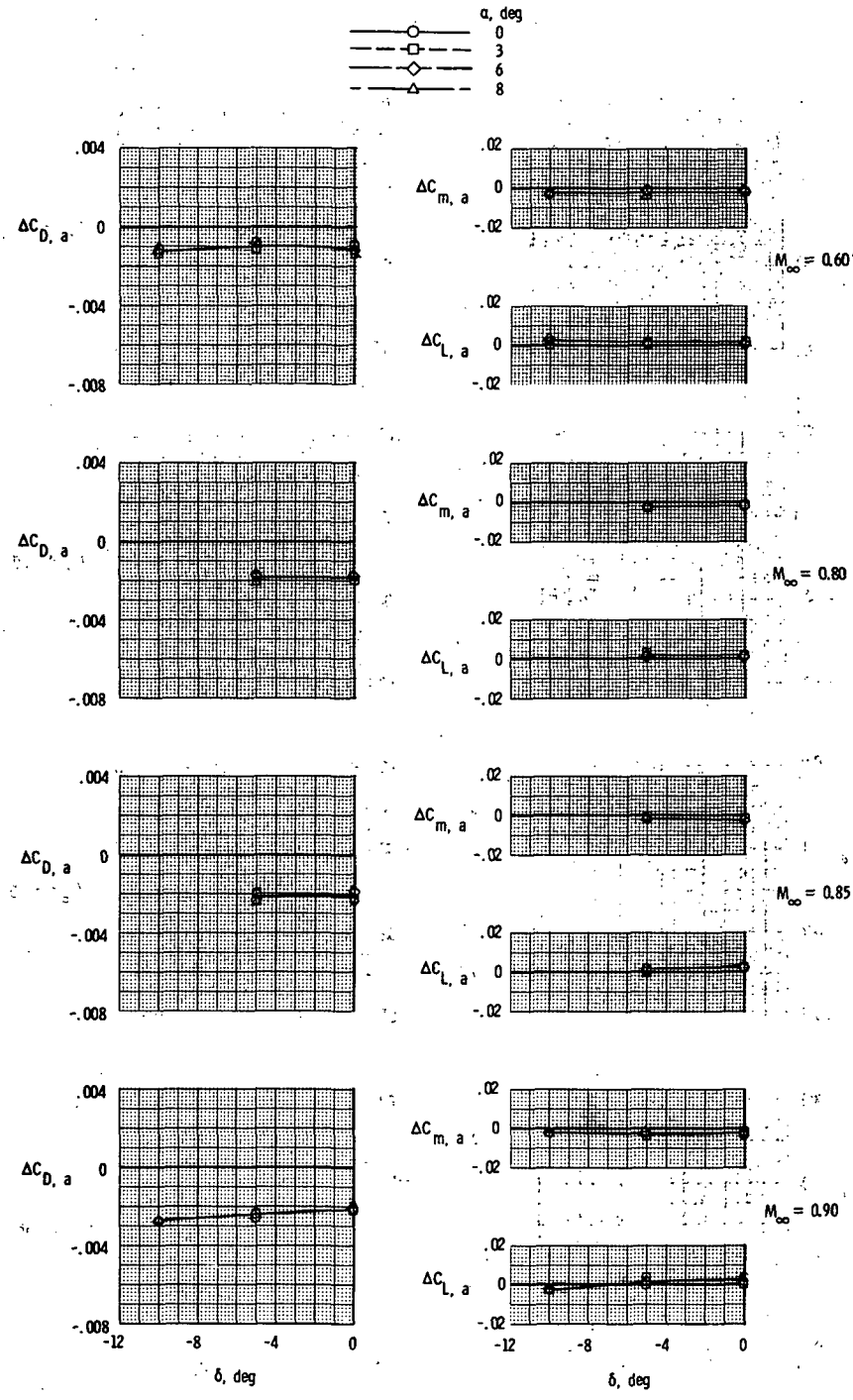

(a) Translating-flap nozzle cruise position.

Figure 20.- Effect of horizontal-tail deflection angle on incremental aerodynamic characteristics of various configurations. Increments are due to jet interference with jet operating at scheduled pressure ratios.

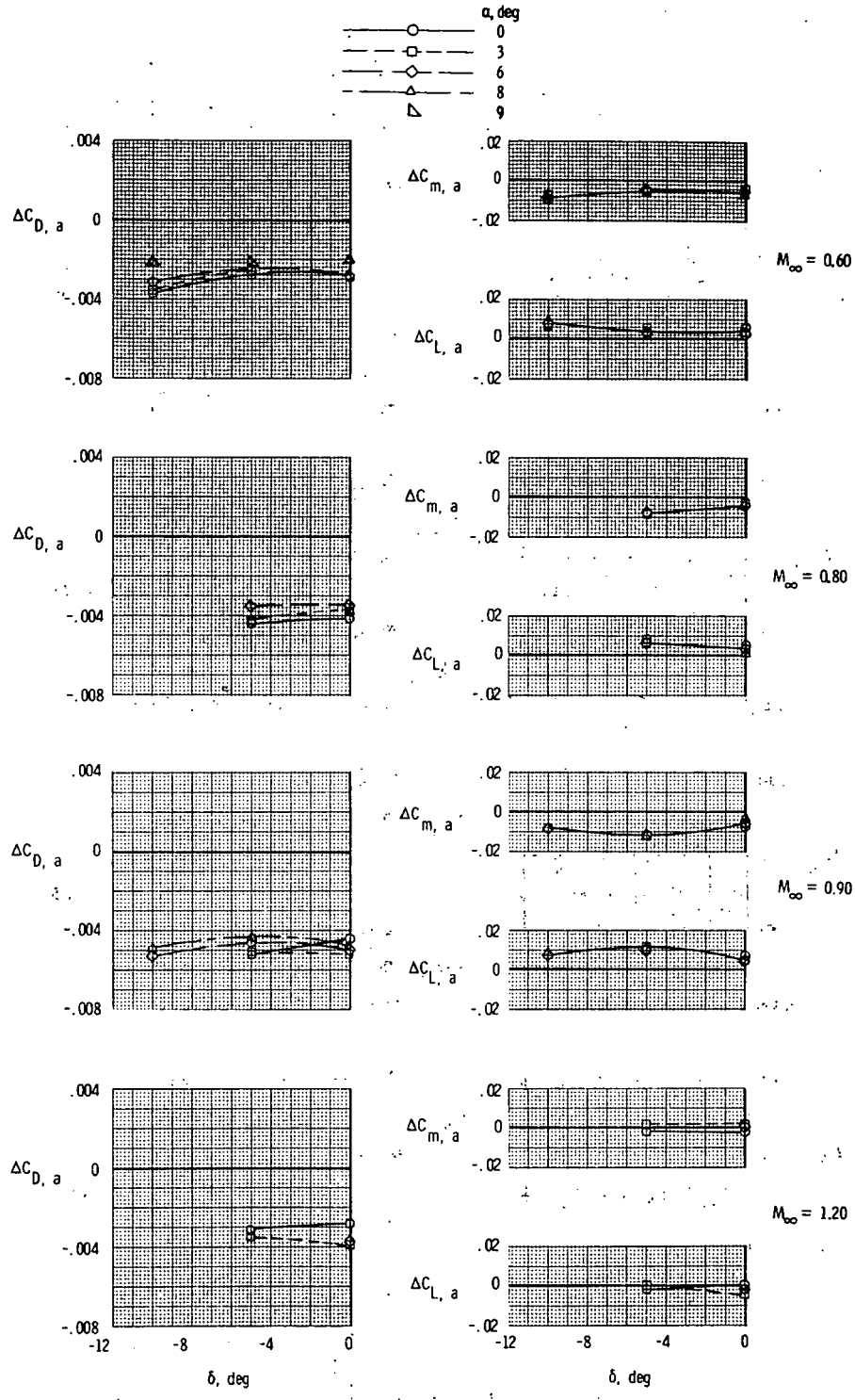

(b) Translating-flap nozzle afterburning position.

Figure 20.- Continued.

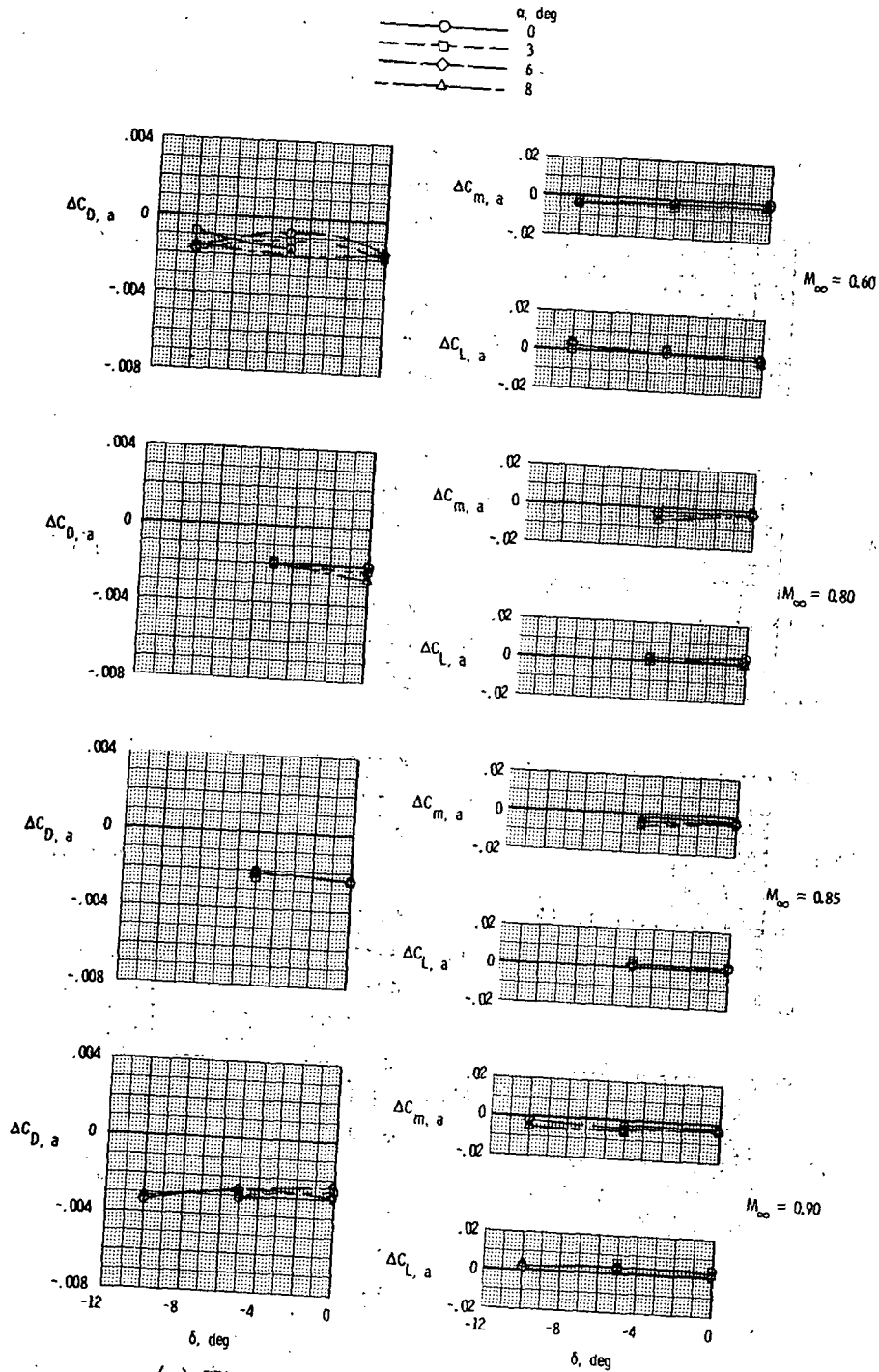

(c) Hinged-flap nozzle cruise position.

Figure 20.- Continued.

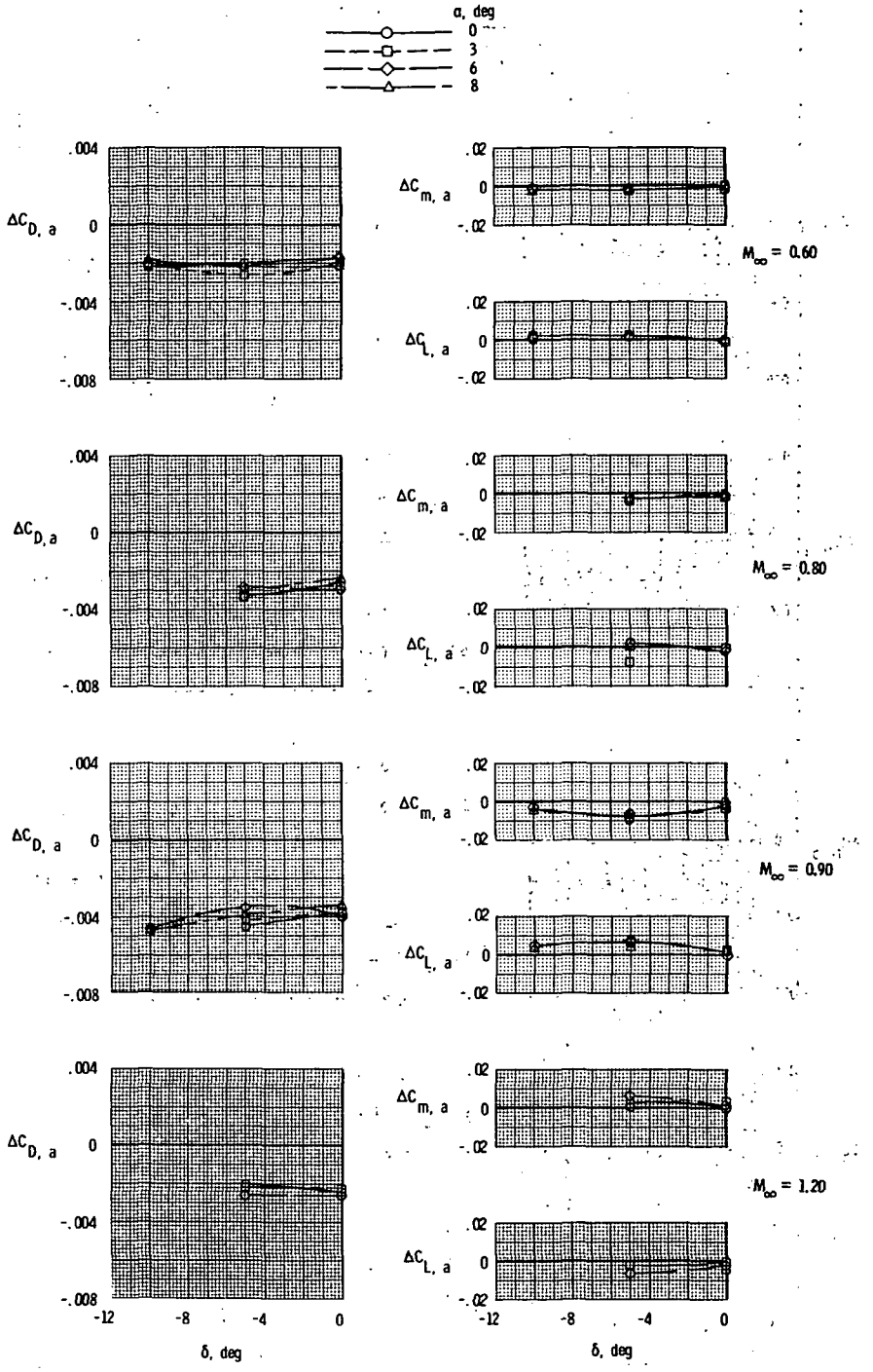

(d) Hinged-flap nozzle afterburning position.

Figure 20.- Concluded.

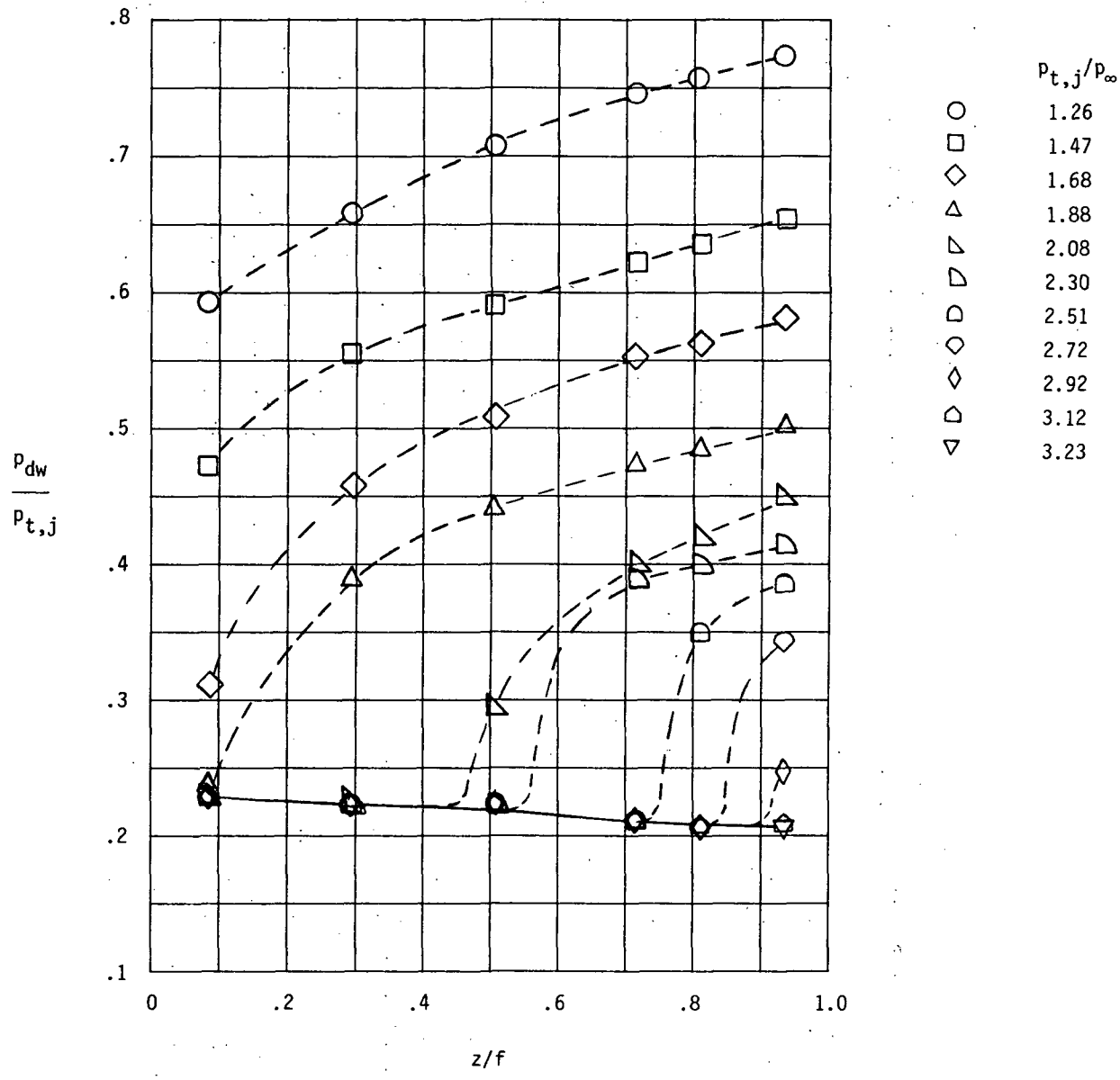

Figure 21.- Internal pressure distributions for hinged-flap nozzle in afterburning configuration exhausting into a quiescent atmosphere.

$p_{t,j}/p_\infty = 2.12$

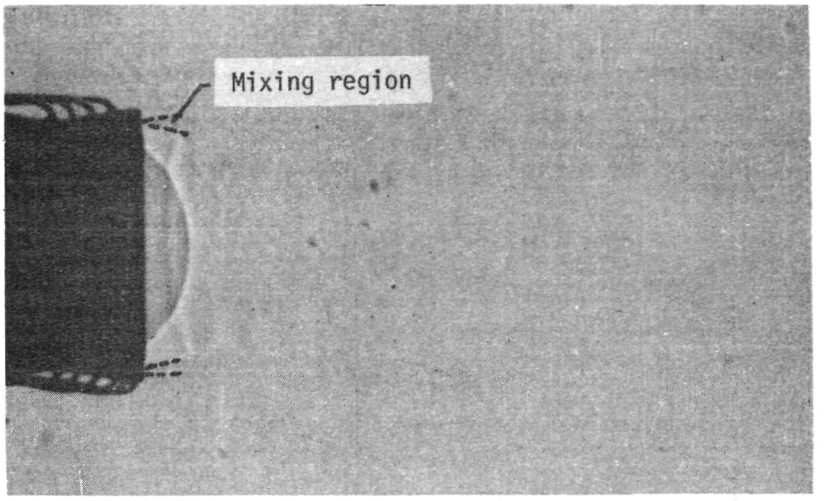

$p_{t,j}/p_\infty = 2.46$

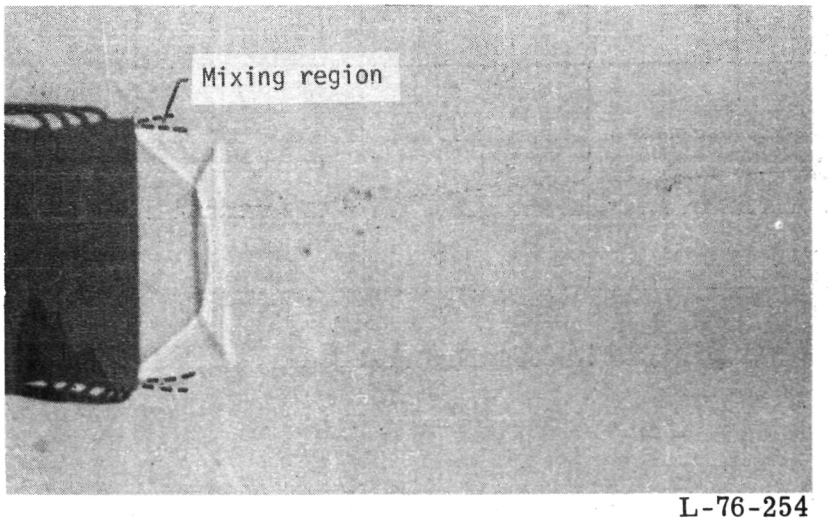

L-76-254

(a) $p_{t,j}/p_\infty = 2.12$ and 2.46.

Figure 22.- Shadowgraphs of flow exhausting into a quiescent atmosphere from hinged-flap nozzle in afterburning configuration.

$p_{t,j}/p_{\infty} = 2.80$

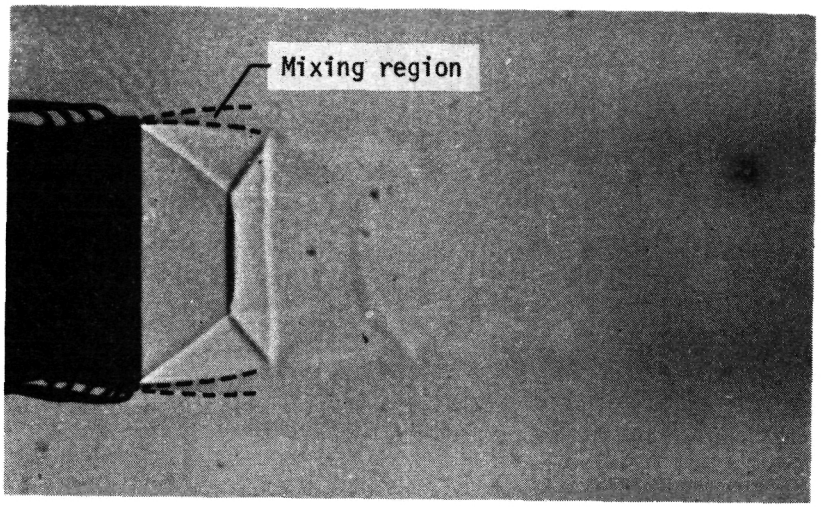

$p_{t,j}/p_{\infty} = 3.15$

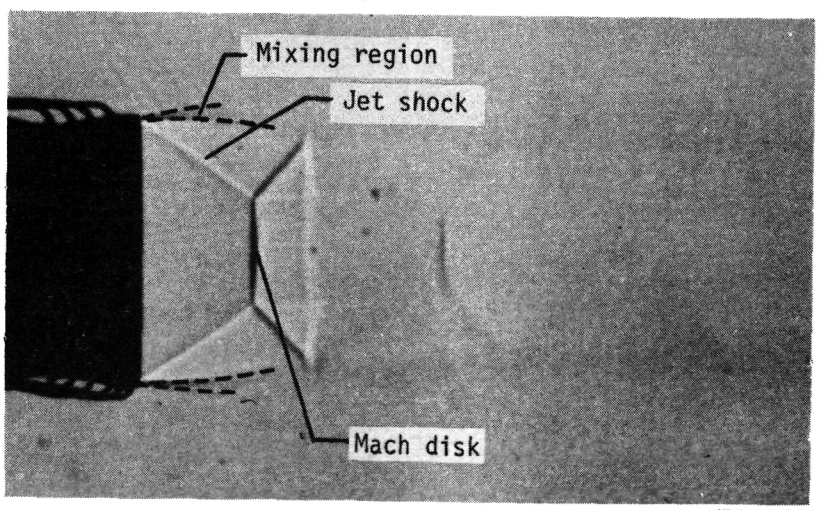

L-76-255

(b) $p_{t,j}/p_{\infty} = 2.80$ and 3.15.

Figure 22.- Concluded.

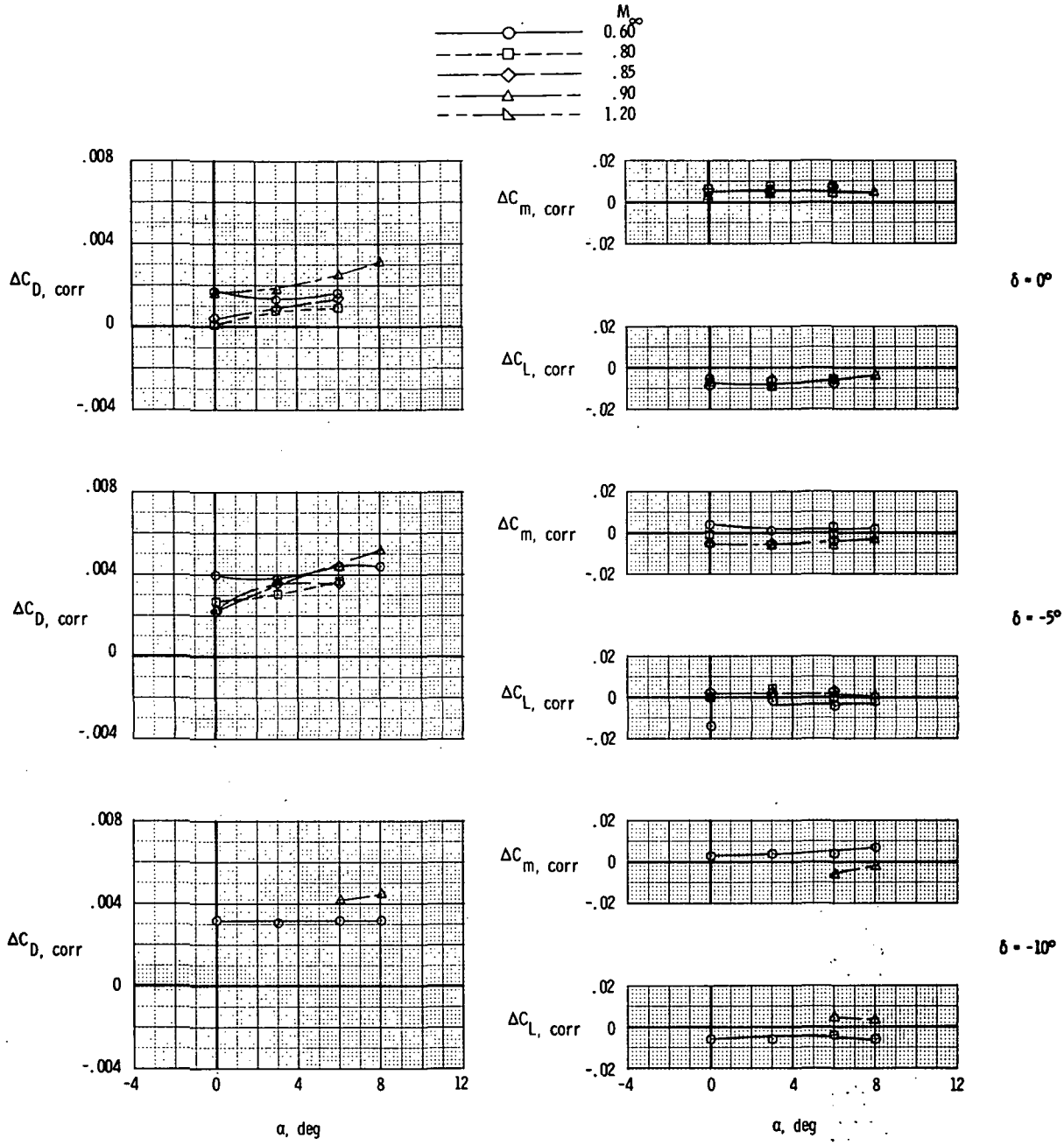

(a) Translating-flap nozzle cruise position.

Figure 23.- Effect of angle of attack on propulsion installation corrections to reference configuration. Jet pressure ratio is at scheduled values.

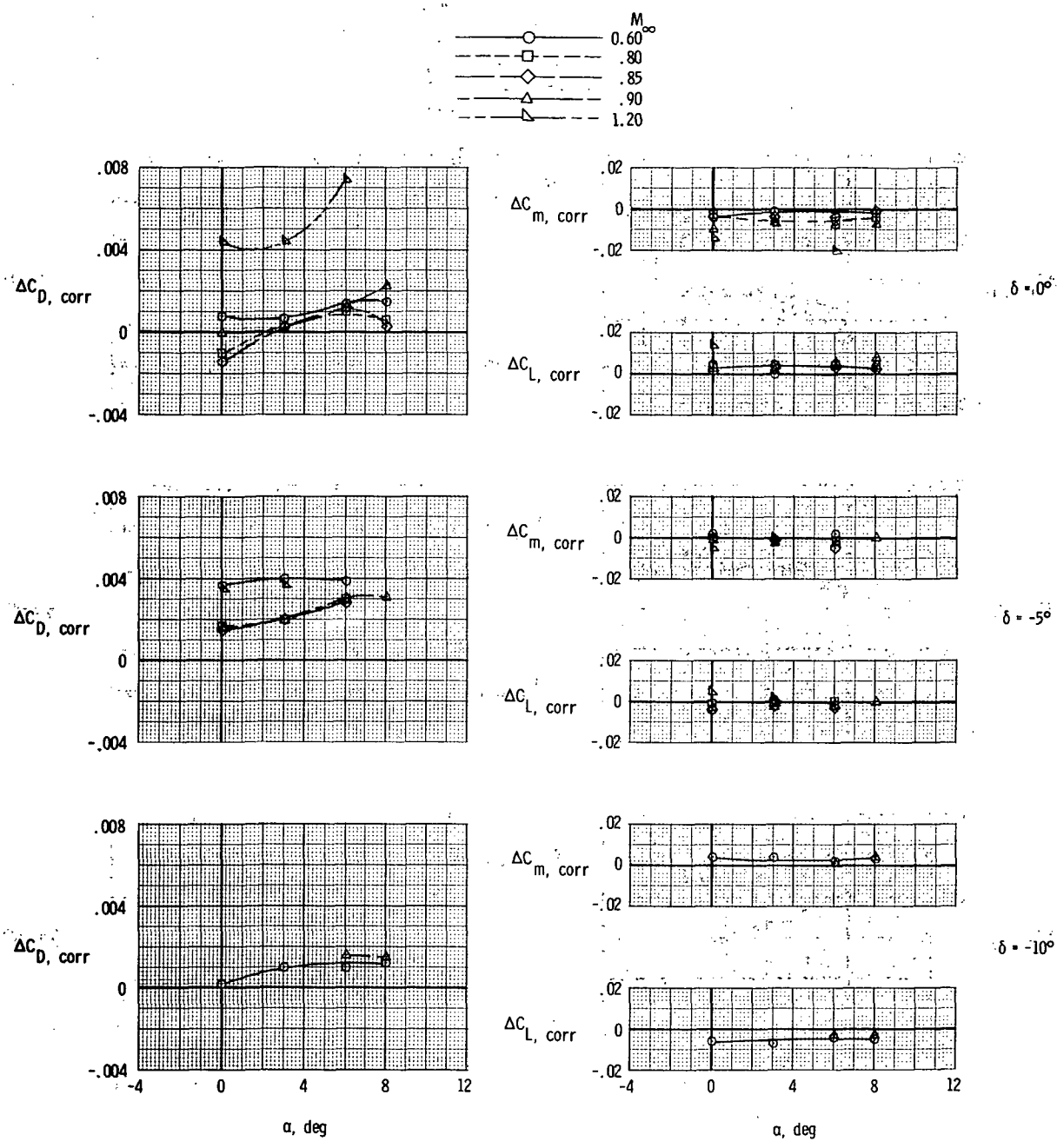

(b) Translating-flap nozzle afterburning position.

Figure 23.- Continued.

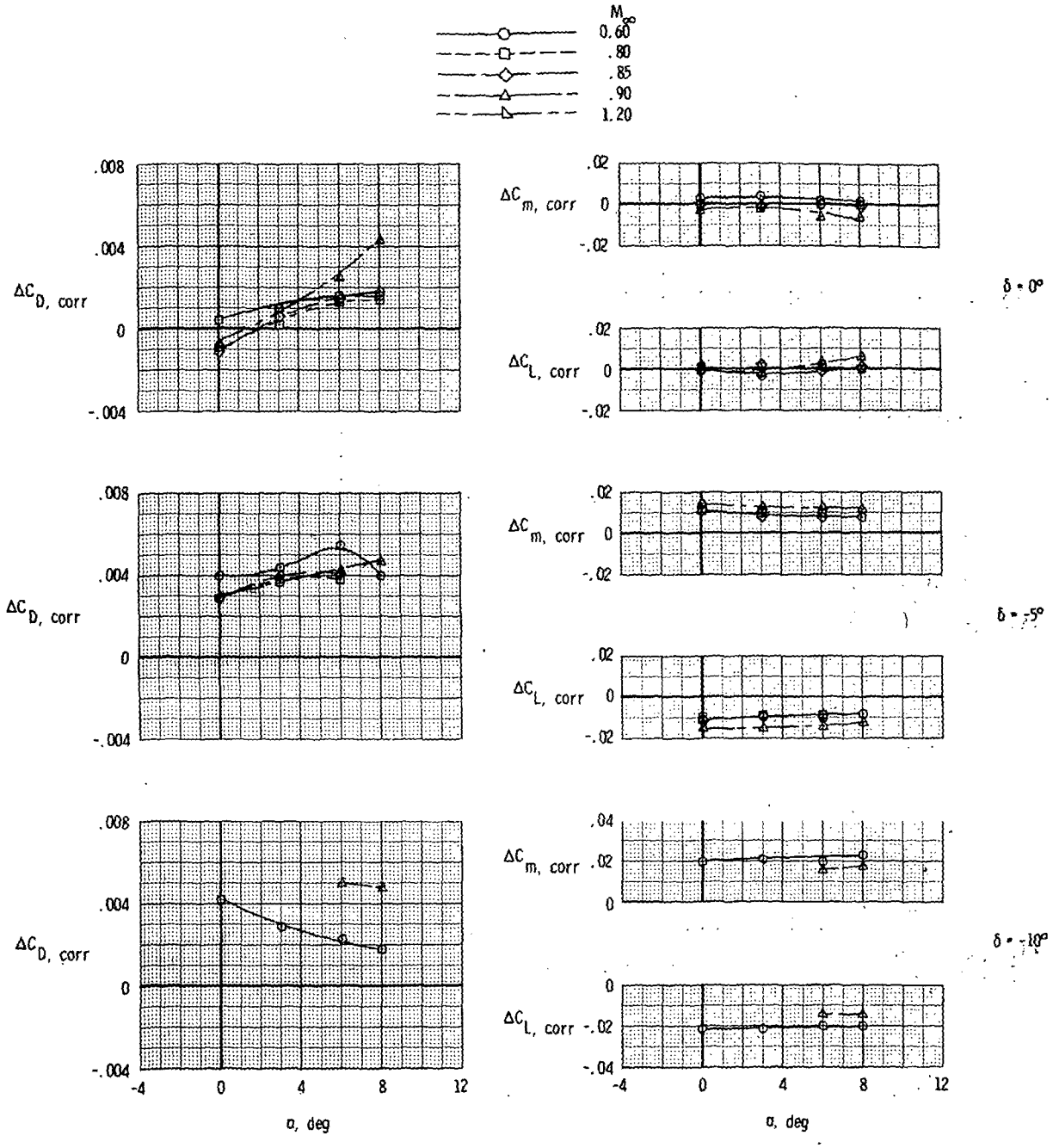

(c) Hinged-flap nozzle cruise position.

Figure 23.- Continued.

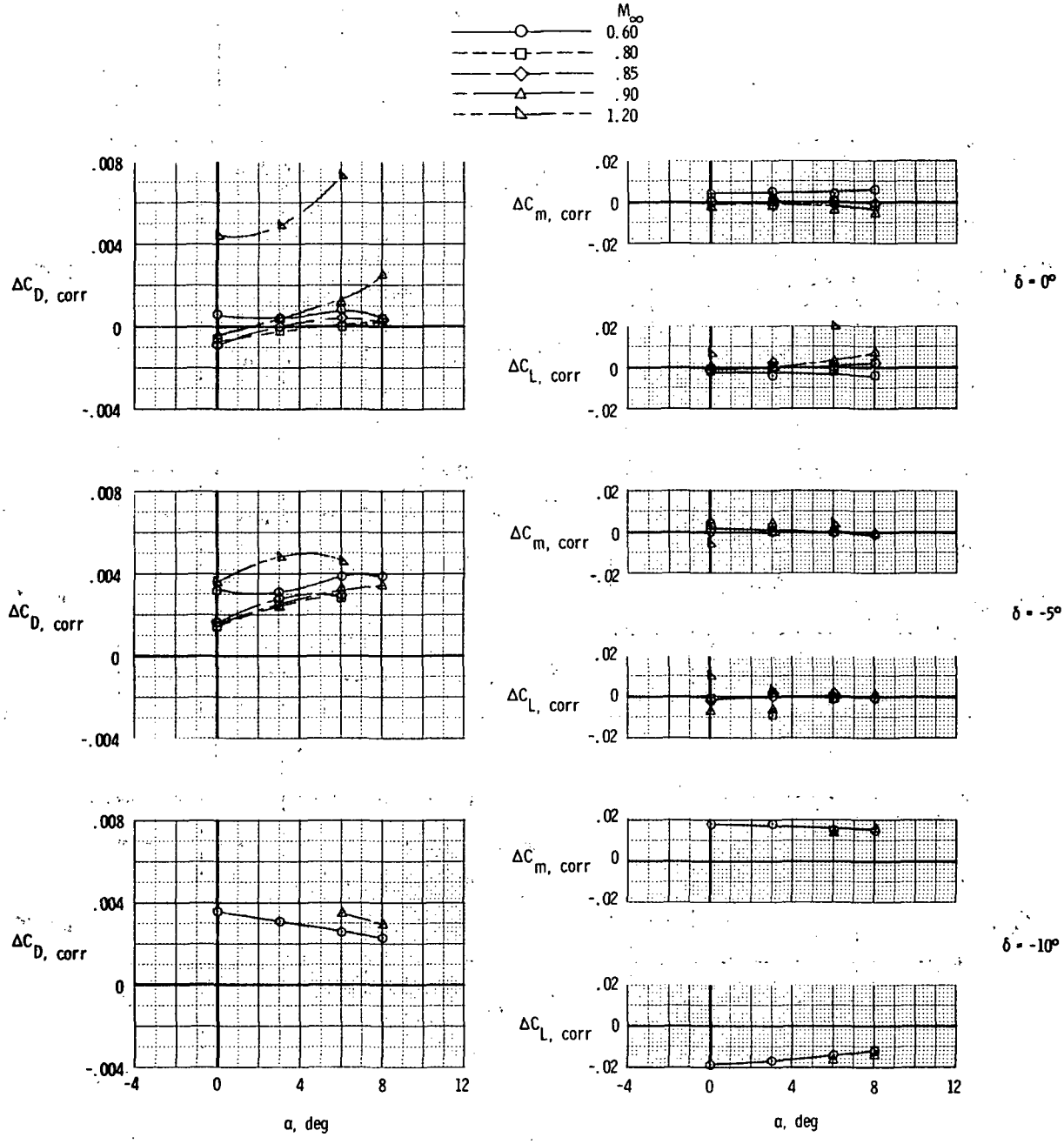

(d) Hinged-flap nozzle afterburning position.

Figure 23. - Concluded.

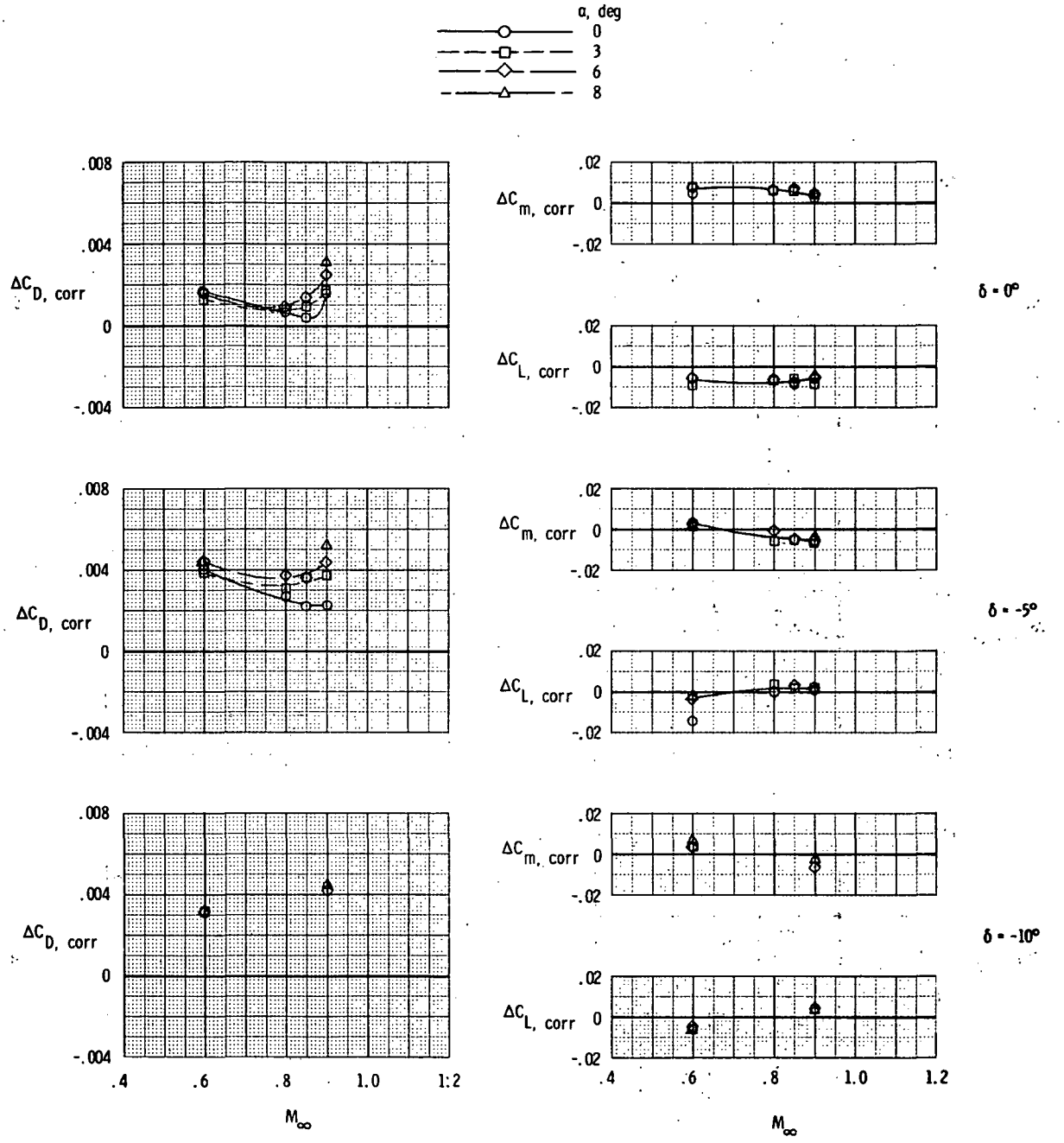

(a) Translating-flap nozzle cruise position.

Figure 24.- Effect of Mach number on propulsion installation corrections to reference configuration. Jet pressure ratio is at scheduled values.

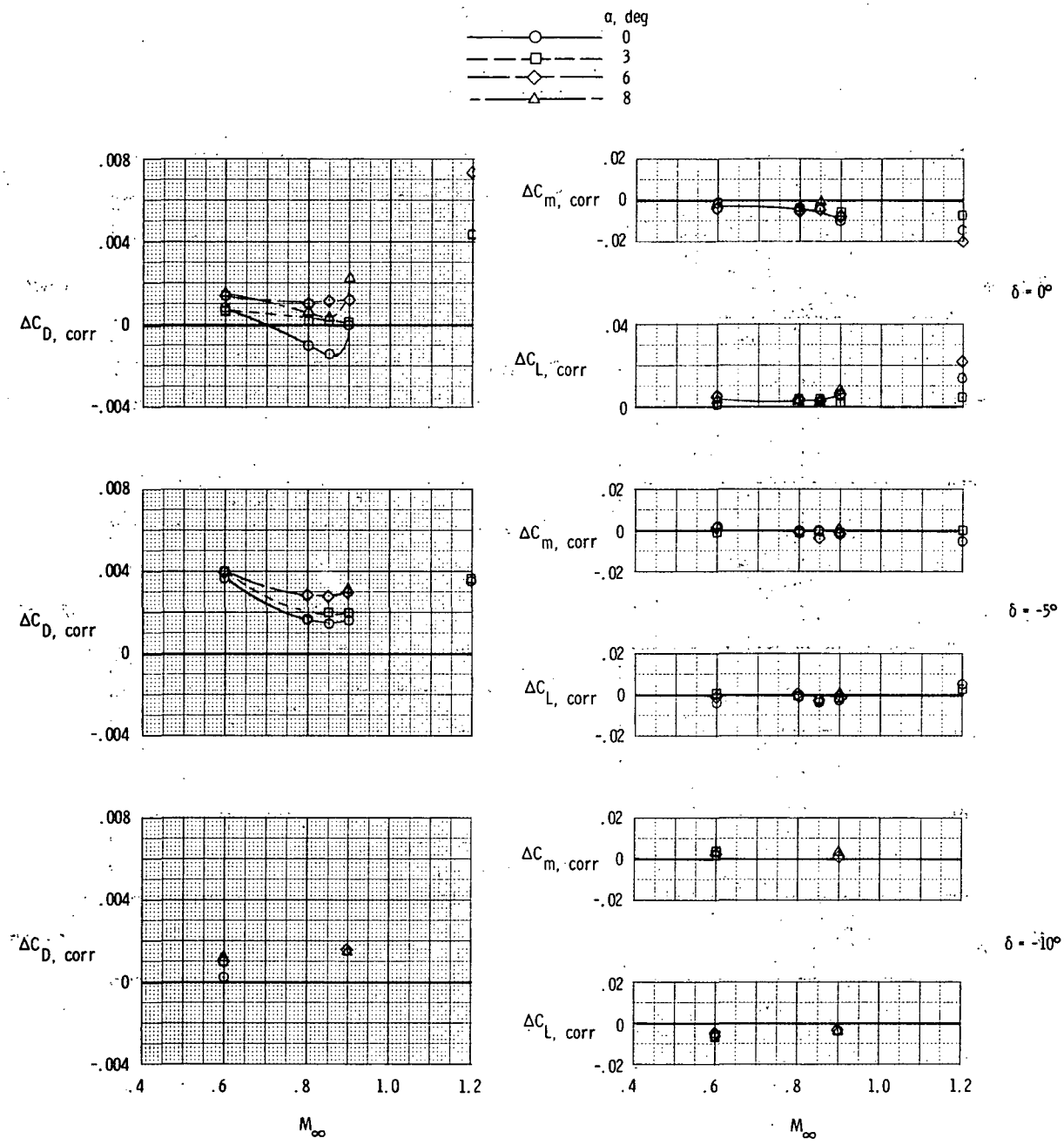

(b) Translating-flap nozzle afterburning position.

Figure 24.- Continued.

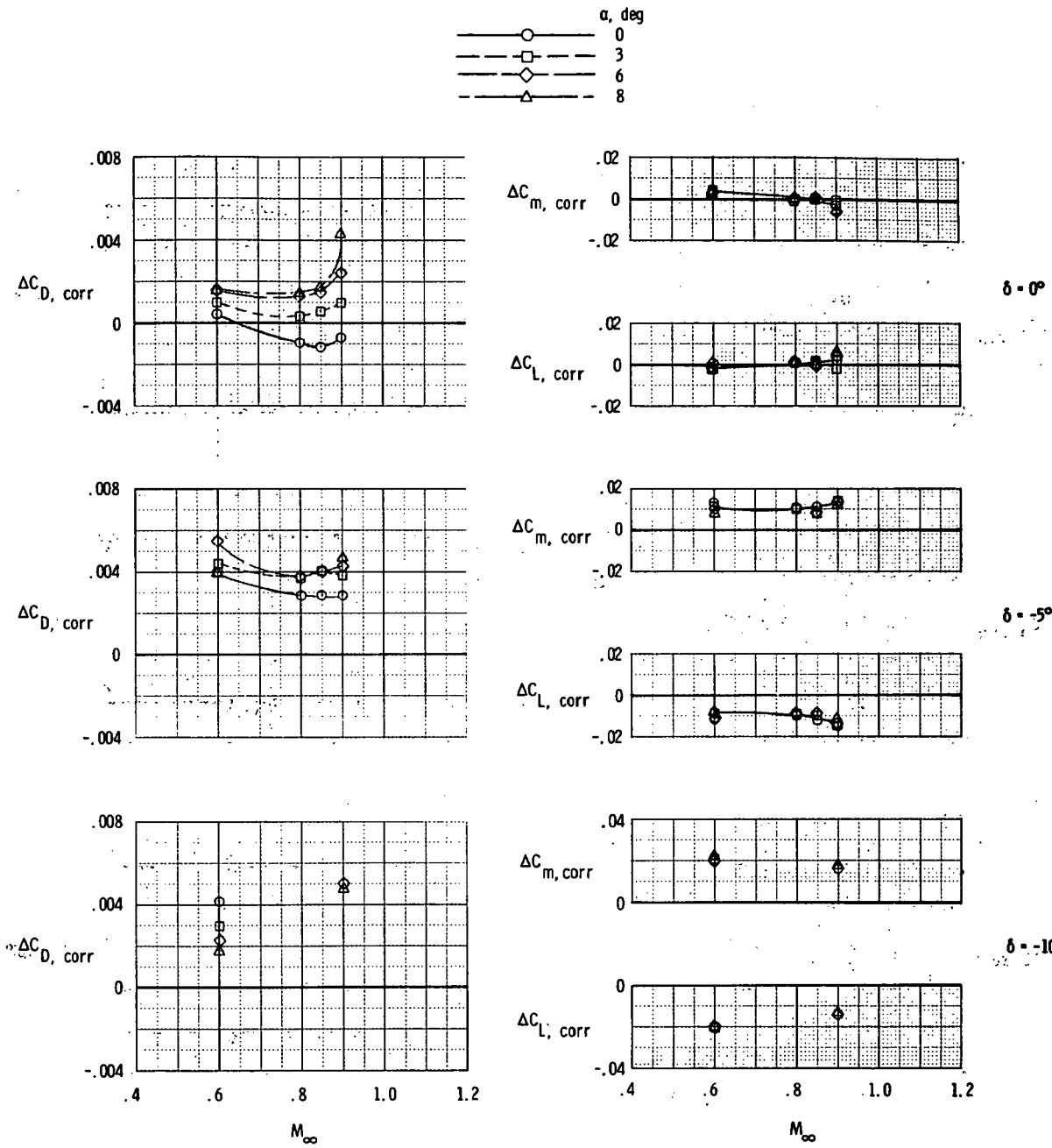

(c) Hinged-flap nozzle cruise position.

Figure 24. - Continued.

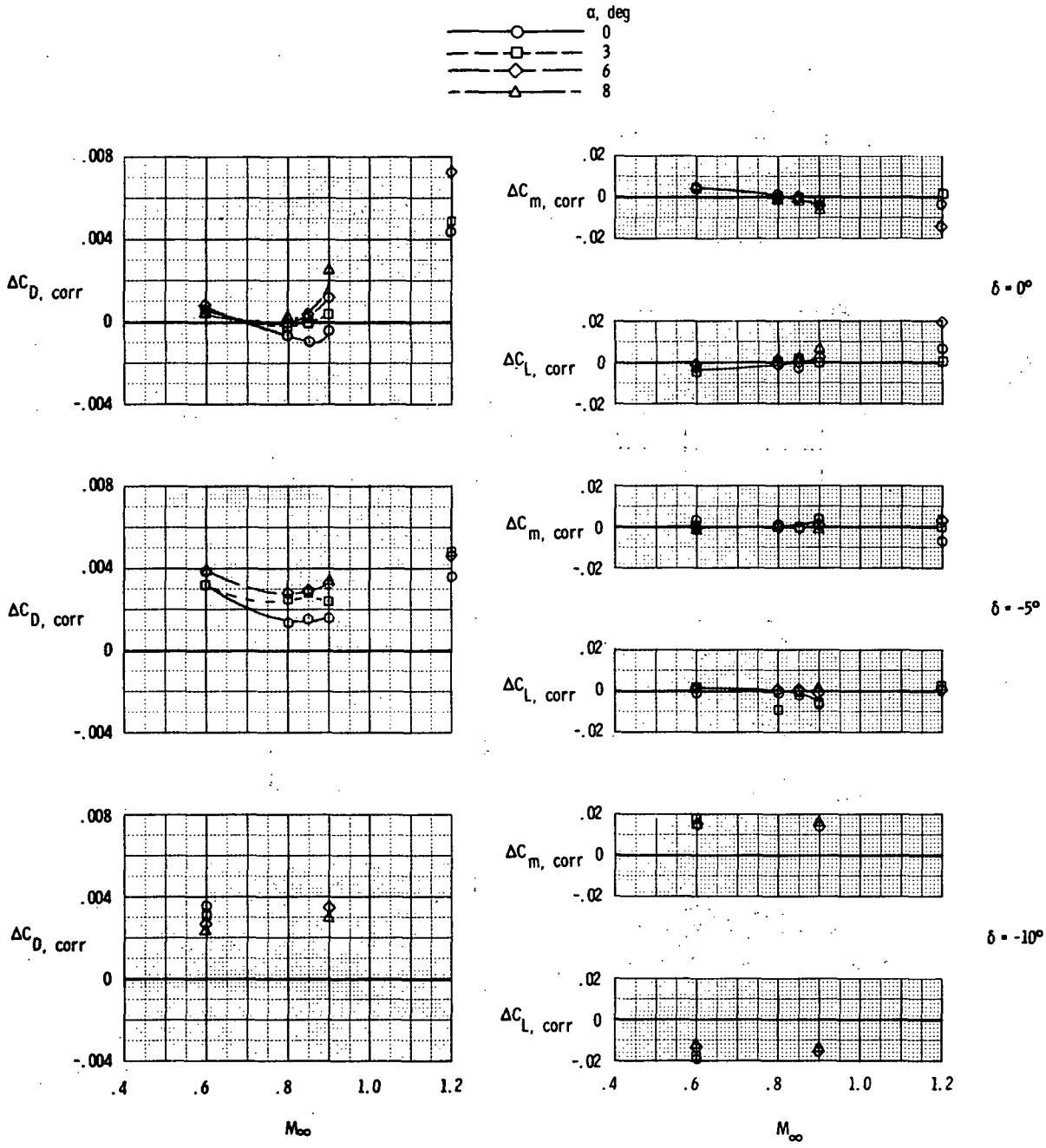

(d) Hinged-flap nozzle afterburning position.

Figure 24.- Concluded.

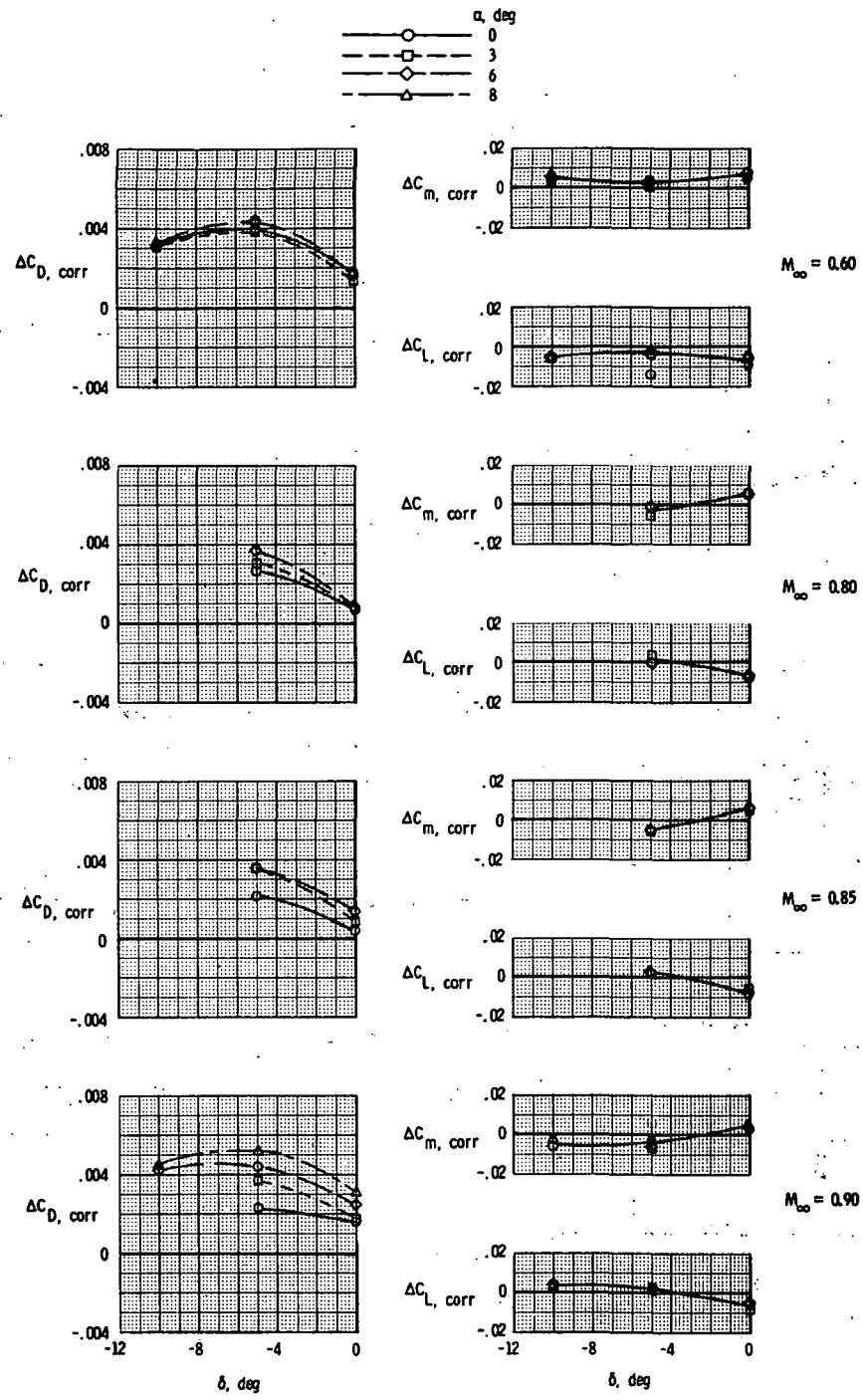

(a) Translating-flap nozzle cruise position.

Figure 25.- Effect of horizontal-tail deflection angle on propulsion installation corrections to reference configuration with simulated vertical-tail support. Jet pressure ratio is at scheduled values.

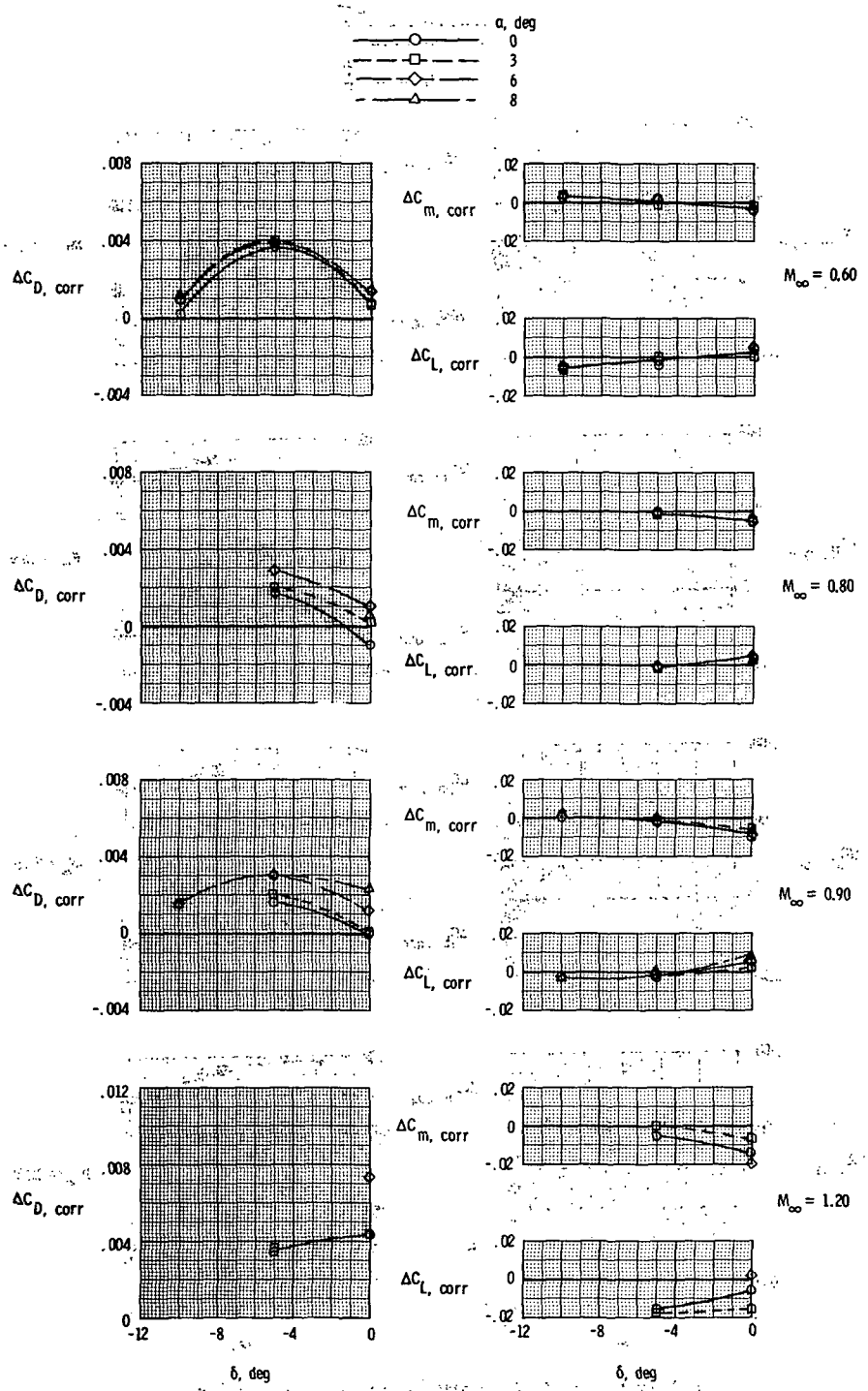

(b) Translating-flap nozzle afterburning position.

Figure 25.- Continued.

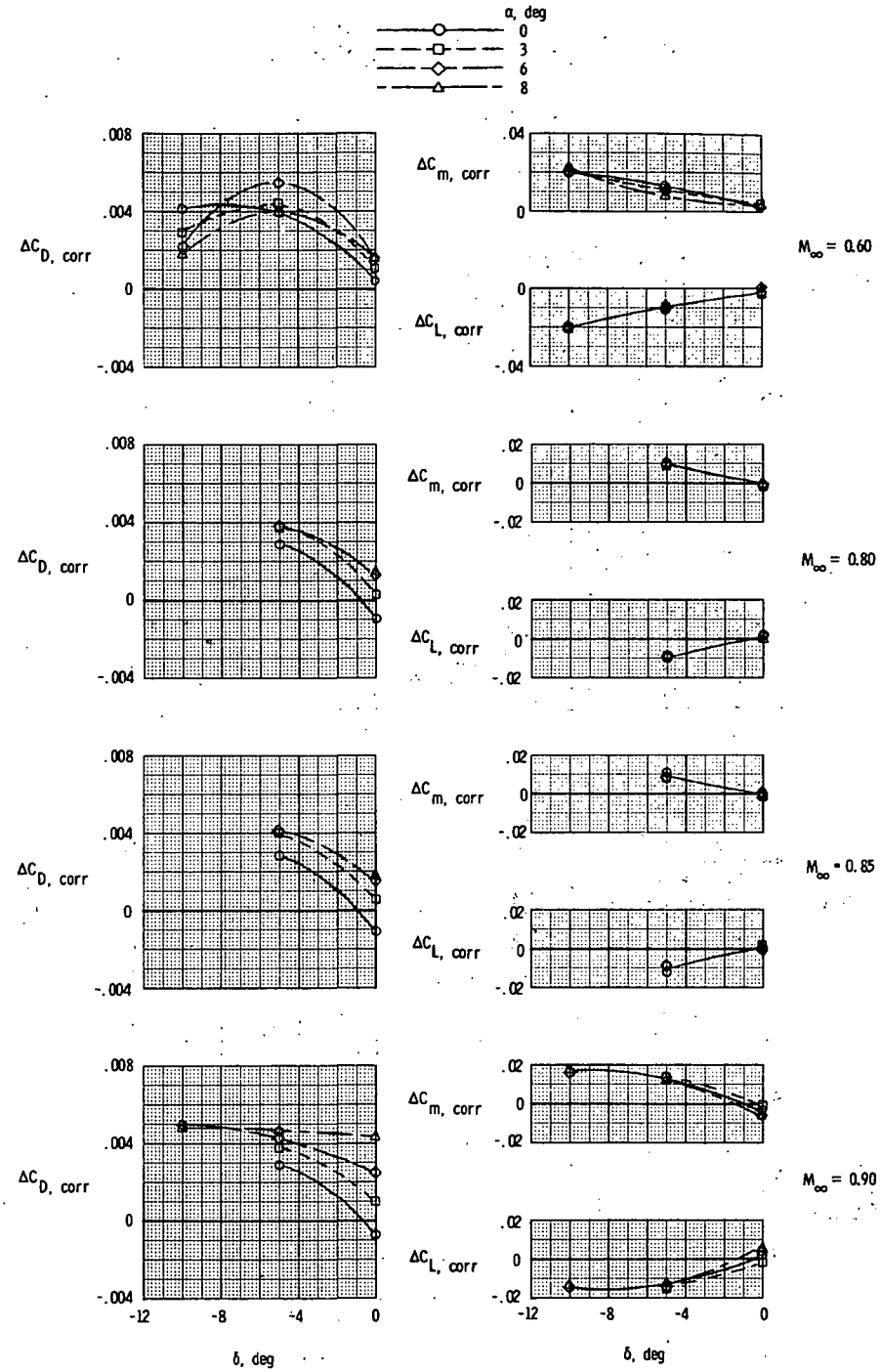

(c) Hinged-flap nozzle cruise position.

Figure 25.- Continued.

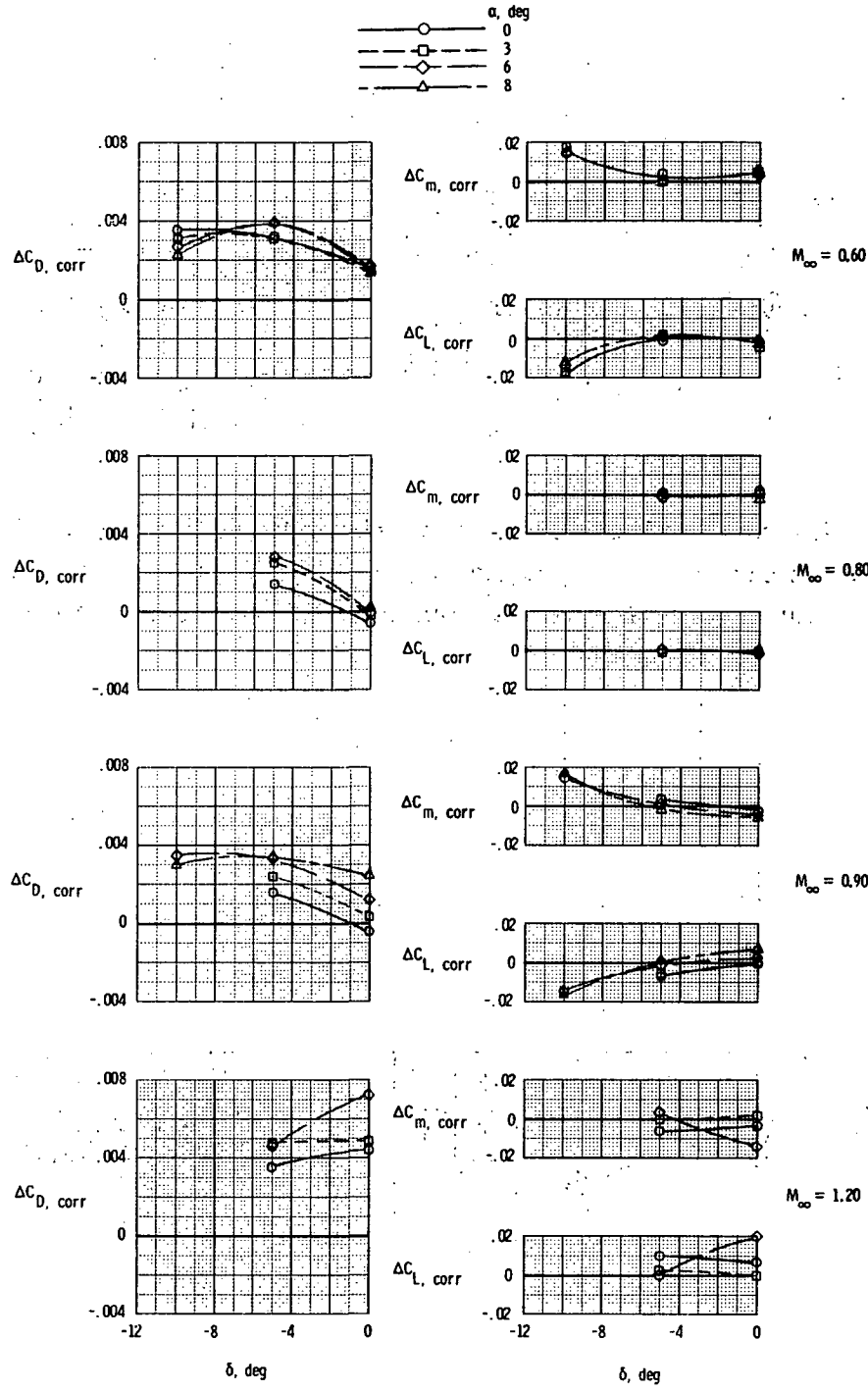

(d) Hinged-flap nozzle afterburning position.

Figure 25.- Concluded.

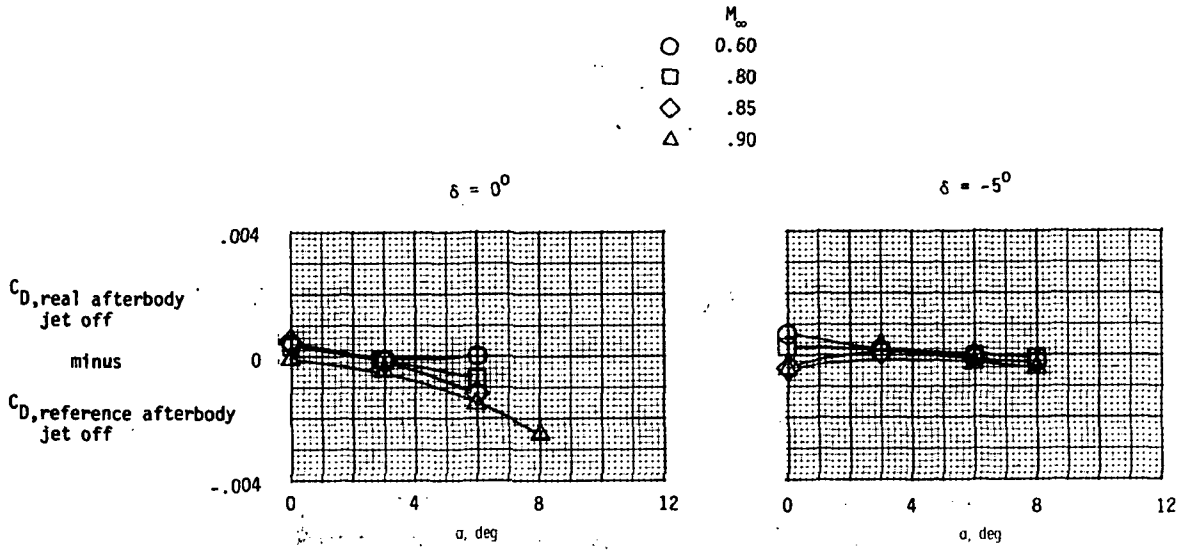

Figure 26.- Effect of afterbody shape on afterbody drag coefficients. Jet off. Realistic afterbody with translating-flap nozzles in cruise position and reference afterbody. Real vertical tail installed on reference afterbody.

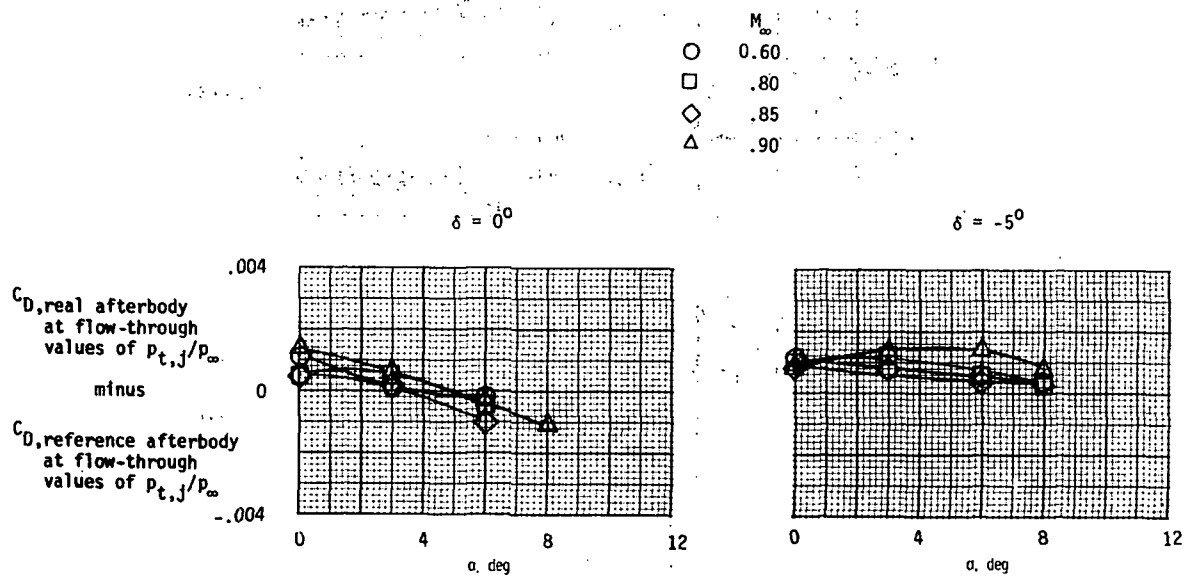

Figure 27.- Effect of afterbody shape on afterbody drag coefficient and jet interference. Jet pressure ratio at flow-through-nacelle values. Realistic afterbody with translating-flap nozzles in cruise position and reference afterbody. Real vertical tail installed on reference afterbody.

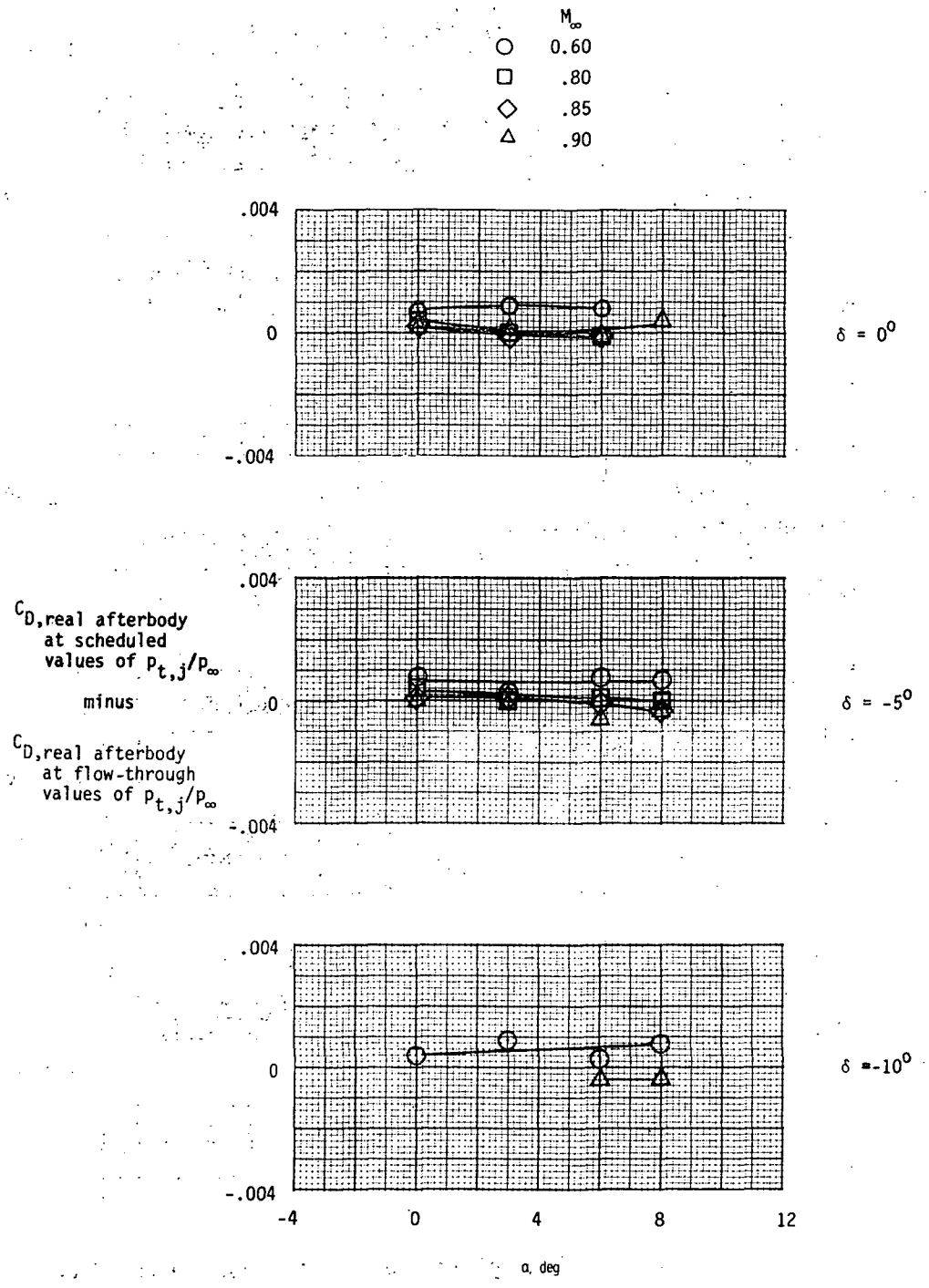

Figure 28.- Effect of jet pressure ratio on afterbody drag. Realistic afterbody with translating-flap nozzles in cruise position.

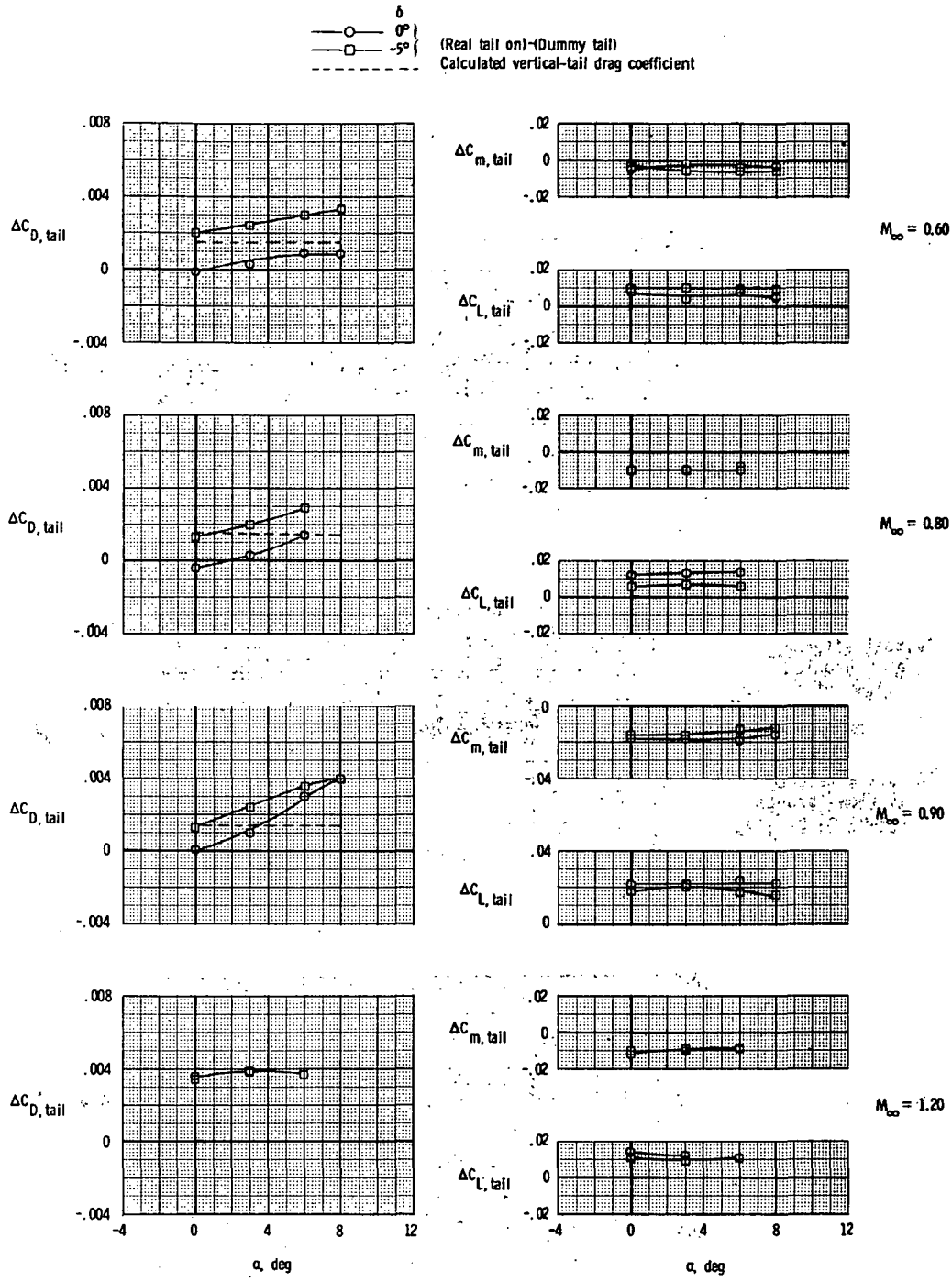

Figure 29.- Effect of vertical tail on aerodynamic characteristics of reference afterbody. Jet pressure ratio at flow-through-nacelle values.

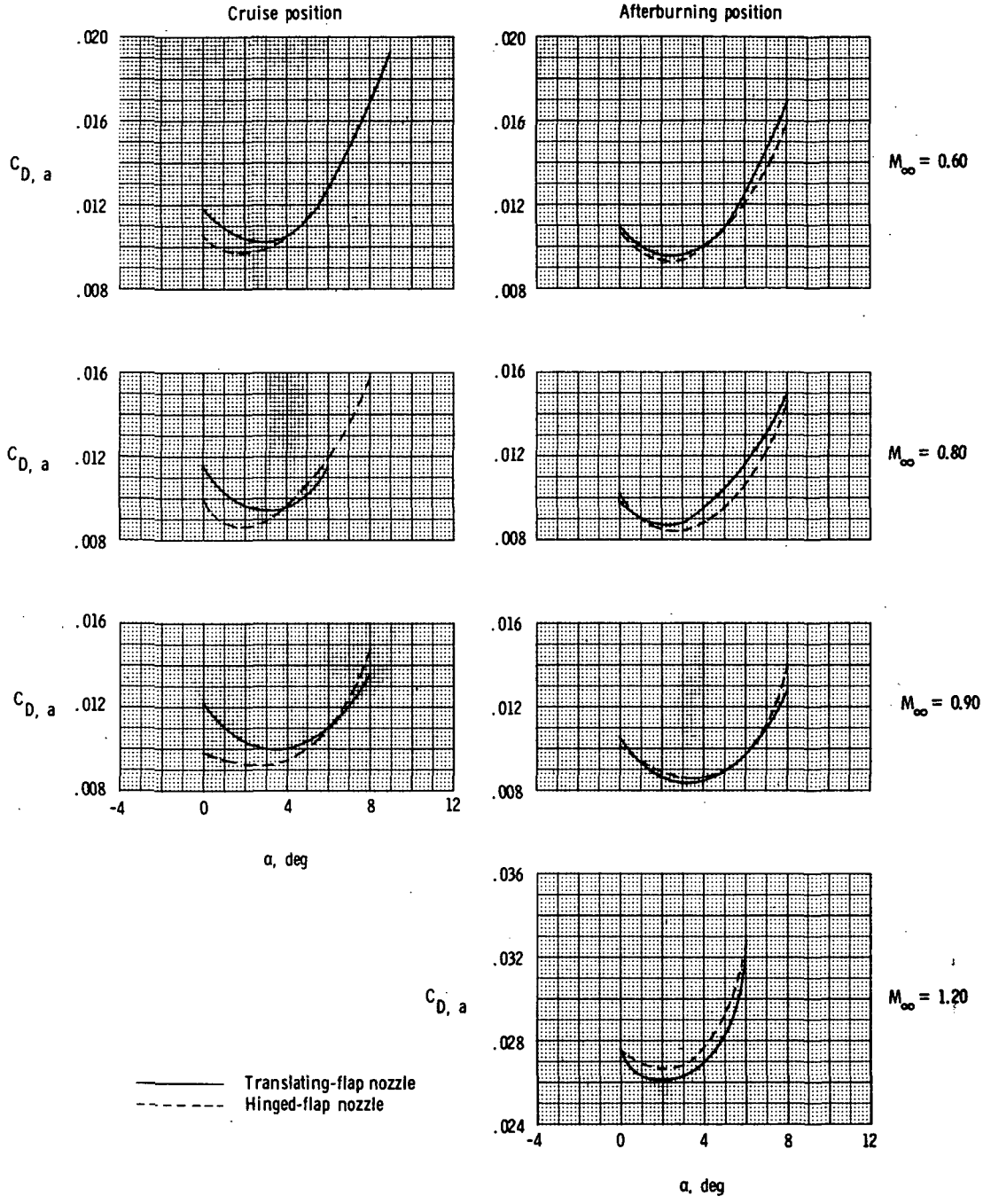

Figure 30.- Comparison of afterbody drag coefficients of translating-flap and hinged-flap nozzle configurations $\delta = 0^{o}$, jet pressure ratio at scheduled values.

*U.S. GOVERNMENT PRINTING OFFICE: 1976 - 735-004/15

NATIONAL AERONAUTICS AND SPACE ADMINISTRATION
WASHINGTON, D.C. 20546

OFFICIAL BUSINESS
PENALTY FOR PRIVATE USE $300

SPECIAL FOURTH-CLASS RATE
BOOK

POSTAGE AND FEES PAID
NATIONAL AERONAUTICS AND
SPACE ADMINISTRATION
451

U.S.MAIL

POSTMASTER : If Undeliverable (Section 158 Postal Manual) Do Not Return

"The aeronautical and space activities of the United States shall be conducted so as to contribute . . . to the expansion of human knowledge of phenomena in the atmosphere and space. The Administration shall provide for the widest practicable and appropriate dissemination of information concerning its activities and the results thereof."

—NATIONAL AERONAUTICS AND SPACE ACT OF 1958

NASA SCIENTIFIC AND TECHNICAL PUBLICATIONS

TECHNICAL REPORTS: Scientific and technical information considered important, complete, and a lasting contribution to existing knowledge.

TECHNICAL NOTES: Information less broad in scope but nevertheless of importance as a contribution to existing knowledge.

TECHNICAL MEMORANDUMS: Information receiving limited distribution because of preliminary data, security classification, or other reasons. Also includes conference proceedings with either limited or unlimited distribution.

CONTRACTOR REPORTS: Scientific and technical information generated under a NASA contract or grant and considered an important contribution to existing knowledge.

TECHNICAL TRANSLATIONS: Information published in a foreign language considered to merit NASA distribution in English.

SPECIAL PUBLICATIONS: Information derived from or of value to NASA activities. Publications include final reports of major projects, monographs, data compilations, handbooks, sourcebooks, and special bibliographies.

TECHNOLOGY UTILIZATION PUBLICATIONS: Information on technology used by NASA that may be of particular interest in commercial and other non-aerospace applications. Publications include Tech Briefs, Technology Utilization Reports and Technology Surveys.

Details on the availability of these publications may be obtained from:

SCIENTIFIC AND TECHNICAL INFORMATION OFFICE

NATIONAL AERONAUTICS AND SPACE ADMINISTRATION

Washington, D.C. 20546